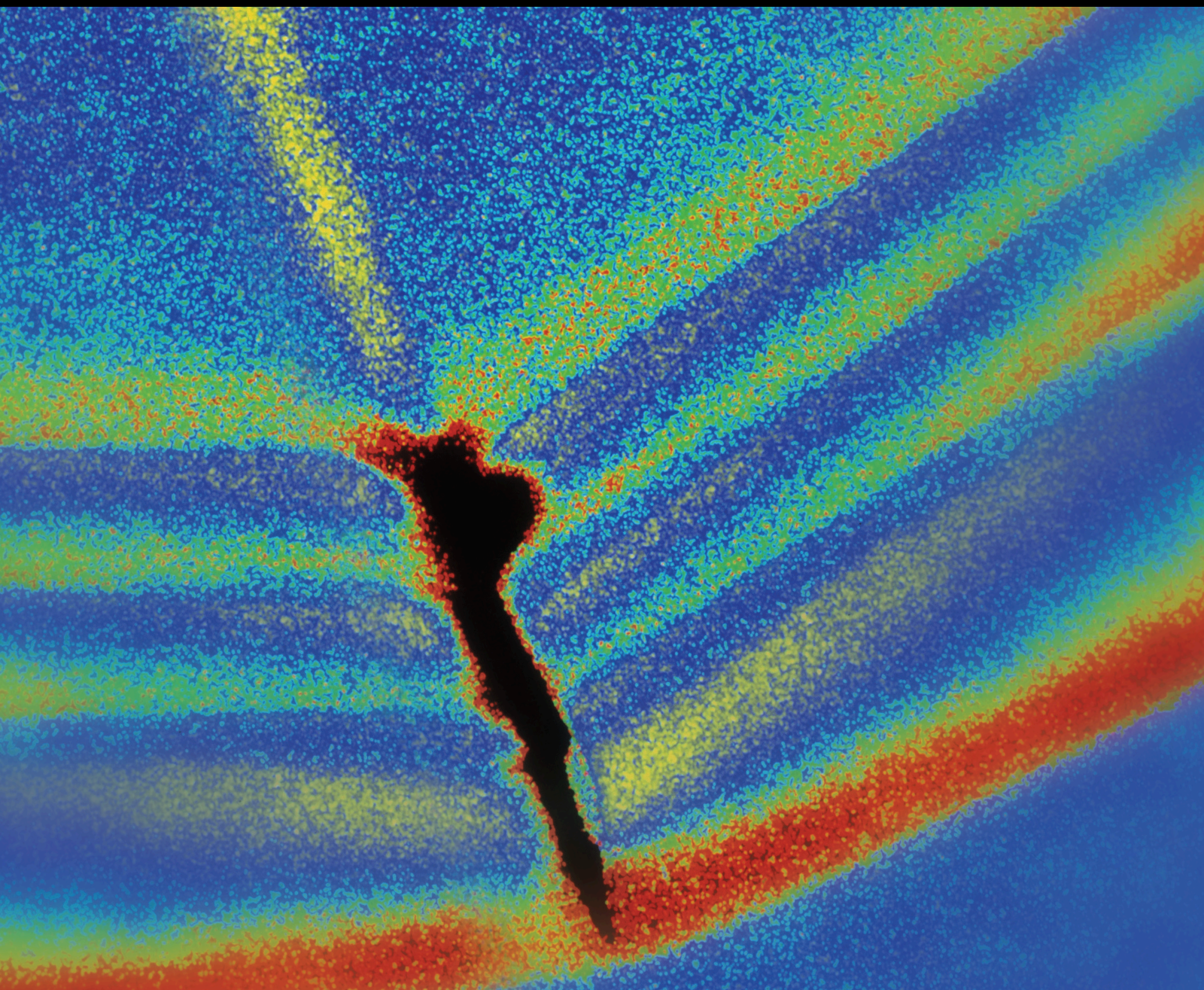


Resilient Civil Infrastructure Under Dynamic Loadings 2020

Lead Guest Editor: Xing Ma

Guest Editors: Nawawi Chouw, Mohamed ElGawady, Songye Zhu, and Xiaonong Guo





Resilient Civil Infrastructure Under Dynamic Loadings 2020

Shock and Vibration

Resilient Civil Infrastructure Under Dynamic Loadings 2020

Lead Guest Editor: Xing Ma

Guest Editors: Nawawi Chouw, Mohamed
ElGawady, Songye Zhu, and Xiaonong Guo

Chief Editor

Huu-Tai Thai, Australia

Editorial Board

Maher Abdelghani, Tunisia
Mohamed A. A. Abdelkareem, Egypt
Haim Abramovich, Israel
Desmond Adair, Kazakhstan
Manuel Aenlle Lopez, Spain
Brij N. Agrawal, USA
Ehsan Ahmadi, United Kingdom
Felix Albu, Romania
Marco Alfano, Italy
Sara Amoroso, Italy
P. Antonaci, Italy
Sumeet S. Aphale, United Kingdom
José V. Araújo dos Santos, Portugal
Jorge P. Arenas, Chile
Lutz Auersch, Germany
Matteo Aureli, USA
Azwan I. Azmi, Malaysia
Yi Bao, USA
Antonio Batista, Brazil
Mahmoud Bayat, USA
Marco Belloli, Italy
Francisco Beltran-Carbajal, Mexico
Denis Benasciutti, Italy
Marta Berardengo, Italy
Sébastien Besset, France
Giosuè Boscato, Italy
Fabio Botta, Italy
Francesco Braghin, Italy
Giuseppe Brandonisio, Italy
Francesco Bucchi, Italy
Rafał Burdzik, Poland
Salvatore Caddemi, Italy
Wahyu Caesarendra, Brunei Darussalam
Baoping Cai, China
Ivo Calì, Italy
Sandro Carbonari, Italy
Antonio Carcaterra, Italy
Cristina Castejón, Spain
Nicola Caterino, Italy
Gabriele Cazzulani, Italy
Athanasios Chasalevris, Greece
Zengshun Chen, China
Shunhua Chen, China
Guoda Chen, China

Xavier Chiementin, France
Nawawi Chouw, New Zealand
Simone Cinquemani, Italy
Ömer Cívalek, Turkey
Marco Cocconcelli, Italy
Pedro A. Costa, Portugal
Alvaro Cunha, Portugal
Giorgio Dalpiaz, Italy
Thanh-Phong Dao, Vietnam
Silvio L.T. de Souza, Brazil
Xiaowei Deng, Hong Kong
Dario Di Maio, The Netherlands
Raffaella Di Sante, Italy
Luigi Di Sarno, Italy
Xiaoxi Ding, China
Longjun Dong, China
Enrique Lopez Droguett, Chile
Farzad Ebrahimi, Iran
Mohammad Elahinia, USA
Sami El-Borgi, Qatar
Said Elias, Iceland
Selçuk Erkaya, Turkey
Cheng Fang, China
Fiorenzo A. Fazzolari, United Kingdom
Chengwei Fei, China
Shengwei Fei, China
Luis A. Felipe-Sese, Spain
Matteo Filippi, Italy
Piotr Folega, Poland
Paola Forte, Italy
Francesco Franco, Italy
Juan C. G. Prada, Spain
Roman Gabl, United Kingdom
Pedro Galvín, Spain
Jinqiang Gan, China
Shan Gao, China
Arturo García García-Perez, Mexico
Gianluca Gatti, Italy
Rozaimi Ghazali, Malaysia
Marco Gherlone, Italy
Anindya Ghoshal, USA
Gilbert R. Gillich, Romania
Antonio Giuffrida, Italy
Annalisa Greco, Italy

Jiajie Guo, China
Hassan Haddadpour, Iran
Mohammad A. Hariri-Ardebili, USA
Seyed M. Hashemi, Canada
Xue-qiu He, China
M.I. Herreros, Spain
Kazuhiko Hiramoto, Japan
Hamid Hosano, Japan
Yanzhu Hu, China
Jin Huang, China
Ahmed Ibrahim, USA
Bernard W. Ikua, Kenya
Reza Jazar, Australia
Wei Kang Jiang, China
Xingxing Jiang, China
Jiang Jin, China
Xiaohang Jin, China
Sakdirat Kaewunruen, United Kingdom
Shao-Bo Kang, China
Yuri S. Karinski, Israel
Denise-Penelope Kontoni, Greece, Greece
Jeong-Hoi Koo, USA
Mohammadreza Koopialipoor, Iran
Georges Kouroussis, Belgium
Genadijus Kulvietis, Lithuania
Simon Laflamme, USA
Mickaël Lallart, France
Luca Landi, Italy
Moon G. Lee, Republic of Korea
Qiu lemiao, China
Trupti Ranjan Lenka, India
Arcanjo Lenzi, Brazil
Marco Lepidi, Italy
Zhixiong Li, China
Shuang Li, China
Larry Kin Bong Li, Hong Kong
Jinhua Li, China
Xihui Liang, Canada
Tzu-Kang Lin, Taiwan
Xiang Liu, China
Jinxin Liu, China
Yixiang Lu, China
Zeqi Lu, China
R. Luo, China
Nuno M. Maia, Portugal
Abdollah Malekjafarian, Ireland
Stefano Manzoni, Italy






Giuseppe Carlo Marano, Italy
Stefano Marchesiello, Italy
Francesco S. Marulo, Italy
Traian Mazilu, Romania
Nur Izzi Md. Yusoff, Malaysia
Jean-Mathieu Mencik, France
Laurent Mevel, France
Letícia Fleck Fadel Miguel, Brazil
FuRen Ming, China
Fabio Minghini, Italy
Marco Miniaci, USA
Dr Mahdi Mohammadpour, United Kingdom
Rui Moreira, Portugal
Emiliano Mucchi, Italy
Peter Múčka, Slovakia
Sara Muggiasca, Italy
Tony Murmu, United Kingdom
Pedro Museros, Spain
Fehmi Najar, Tunisia
Roberto Nascimbene, Italy
M. Z. Naser, USA
Amr A. Nassr, Egypt
Sundararajan Natarajan, India
Toshiaki Natsuki, Japan
Miguel Neves, Portugal
Tuan Ngo, Australia
Sy Dzung Nguyen, Republic of Korea
Trung Nguyen-Thoi, Vietnam
Hung Nguyen-Xuan, Vietnam
Baoyu Ni, China
Gianni Niccolini, Italy
Rodrigo Nicoletti, Brazil
Nicola Nisticò, Italy
Bin Niu, China
Leilei Niu, China
Lucio Olivares, Italy
Erkan Oterkus, United Kingdom
Selda Oterkus, Scotland
Roberto Palma, Spain
Junhong Park, Republic of Korea
Annamaria Pau, Italy
Francesco Pellicano, Italy
Paolo Pennacchi, Italy
Giuseppe Petrone, Italy
Evgeny Petrov, United Kingdom
Antonina Pirrotta, Italy
Franck Poisson, France

Luca Pugi, Italy
Zhaoye Qin, China
Yi Qin, China
Virginio Quaglini, Italy
Mohammad Rafiee, Canada
Carlo Rainieri, Italy
Vasudevan Rajamohan, India
Ricardo A. Ramirez-Mendoza, Mexico
José J. Rangel-Magdaleno, Mexico
Didier Rémond, France
Dario Richiedi, Italy
Francesco Ripamonti, Italy
Fabio Rizzo, Italy
Nibaldo Rodríguez, Chile
Carlo Rosso, Italy
Riccardo Rubini, Italy
Salvatore Russo, Italy
Giuseppe Ruta, Italy
Edoardo Sabbioni, Italy
N. A. Saeed, Egypt
Filippo Santucci de Magistris, Italy
Abdullah Seçgin, Turkey
Roger Serra, France
Changqing Shen, China
Yujie Shen, China
Chengzhi Shi, USA
Bao-Jun Shi, China
Vadim V. Silberschmidt, United Kingdom
Gerardo Silva-Navarro, Mexico
marcos silveira, Brazil
Kumar V. Singh, USA
Jean-Jacques Sinou, France
Isabelle Sochet, France
Alba Sofi, Italy
Jussi Sopanen, Finland
Stefano Sorace, Italy
Silvio Sorrentino, Italy
Andrea Spaggiari, Italy
Lei Su, China
Shuaishuai Sun, Australia
Fidelis Tawiah Suorineni, Kazakhstan
Tomasz Szolc, Poland
Zhuhua Tan, China
Gang Tang, China
Chao Tao, China
Marco Tarabini, Italy
Gloria Terenzi, Italy




Mario Terzo, Italy
Hamid Toopchi-Nezhad, Iran
Carlo Trigona, Italy
Federica Tubino, Italy
Nerio Tullini, Italy
Angelo Marcelo Tusset, Brazil
Jens Twiefel, Germany
Filippo Ubertini, Italy
Marcello Vanali, Italy
Christian Vanhille, Spain
F. Viadero, Spain
M. Ahmer Wadee, United Kingdom
Jörg Wallaschek, Germany
YuRen Wang, China
Pengfei Wang, China
Bin Wang, China
Huiqi Wang, China
Gaoxin Wang, China
Weiqiang Wang, Australia
Jinjiang Wang, China
C. M. Wang, Australia
Matthew J. Whelan, USA
Wai-on Wong, Hong Kong
Tang-Bin Xia, China
Yuanping XU, China
Qilong Xue, China
Xin Xue, China
Diansen Yang, China
Jie Yang, Australia
Junyan Yi, China
Chang-Ping Yi, Sweden
Davood Younesian, Iran
Nicolo Zampieri, Italy
Chao-Ping Zang, China
Enrico Zappino, Italy
Shaojian Zhang, China
Guo-Qing Zhang, China
Hong Zhang, China
W. Zhang, China
Yongfang Zhang, China
Yaobing Zhao, China
Changjie Zheng, China
Jiaxi Zhou, China
Hongwei Zhou, China
Hongyuan Zhou, China
Chuanbo Zhou, China
Radoslaw Zimroz, Poland

Contents





Resilient Civil Infrastructure under Dynamic Loadings 2020

Xing Ma , Nawawi Chouw , Mohamed ElGawady , Songye Zhu , and Xiaonong Guo 
Editorial (1 page), Article ID 9790657, Volume 2021 (2021)

Transmitting Characteristics of Seismic Motion in Super-Deep Overburden Layer Ground

Long Wang , Zheng-quan Yang , Jian-ming Zhao , Xiao-sheng Liu , and Yan-feng Wen 
Research Article (23 pages), Article ID 8898012, Volume 2021 (2021)


Seismic Behavior of Hybrid Frame Joints between Composite Columns and Steel Beams

Liusheng Chu , Qingze Li , Jun Zhao , and Danda Li 
Research Article (16 pages), Article ID 8870582, Volume 2020 (2020)


Analysis of Lateral Dynamic Response of Caisson Foundation in Layered Clayey Soils considering Scour-Hole Dimensions

Wenbo Tu , Xiaoqiang Gu , Xianfeng Ma , and Dawei Huang 
Research Article (11 pages), Article ID 8827498, Volume 2020 (2020)


Vibration-Isolation Performance of a Pile Barrier in an Area of Soft Soil in Shanghai

X. F. Ma, M. Y. Cao, X. Q. Gu , B. M. Zhang, Z. H. Yang, and P. F. Guan
Research Article (27 pages), Article ID 8813476, Volume 2020 (2020)


Dynamic Reliability of Continuous Rigid-Frame Bridges under Stochastic Moving Vehicle Loads

Naiwei Lu , Kai Wang, Honghao Wang, Yang Liu, Yuan Luo, and Xinhui Xiao
Research Article (13 pages), Article ID 8811105, Volume 2020 (2020)



Antipenetration Performance of Honeycomb Shelter under Two Repeat Projectile Strikes

Qifan Wang, Liusheng Chu , Jie Li, Jianhu Sun, Sheng Luo, and Lei Mao
Research Article (10 pages), Article ID 8827486, Volume 2020 (2020)

Seismic Performance Analysis of Self-Centering Concentrically Braced Steel Frame Structures

Ergang Xiong , Kun Zu, and Qian Zhang
Research Article (13 pages), Article ID 8826272, Volume 2020 (2020)

Seismic Response Study of Tunnels Running underneath a Subway Station in Parallel

Fuxue Sun, Guo-bo Wang , Xiang-jun Peng, Zhou-zhou Jin, Xiao-chun Li, and Jie-lin Zhao 
Research Article (15 pages), Article ID 8822981, Volume 2020 (2020)

Editorial

Resilient Civil Infrastructure under Dynamic Loadings 2020

Xing Ma ¹, **Nawawi Chouw** ², **Mohamed ElGawady** ³, **Songye Zhu** ⁴,
and Xiaonong Guo ⁵

¹UniSA STEM, University of South Australia, Adelaide, Australia

²Department of Civil and Environmental Engineering, The University of Auckland, Auckland, New Zealand

³Department of Civil, Architectural and Environmental Engineering, Missouri University of Science and Technology, Rolla, MO, USA

⁴Department of Civil and Environmental Engineering, The Hong Kong Polytechnic University, Hong Kong, China

⁵Department of Structural Engineering, Tongji University, Shanghai, China

Correspondence should be addressed to Xing Ma; xing.ma@unisa.edu.au

Received 28 July 2021; Accepted 28 July 2021; Published 17 August 2021

Copyright © 2021 Xing Ma et al. This is an open access article distributed under the Creative Commons Attribution License, which permits unrestricted use, distribution, and reproduction in any medium, provided the original work is properly cited.

Infrastructural systems are important components in the modern society. The design and construction of resilient civil infrastructures is an effective way to reduce or even avoid large economic losses due to the downtime of the infrastructure after a strong natural or manmade hazard. Following the 2018 Special Issue on resilient civil infrastructures, this 2020 Annual Issue addresses the challenges and emerging problems in the research area of resilient infrastructural systems under dynamic loadings, e.g., wind, traffic, tsunamis, and earthquakes.

After a rigorous reviewing process, eight papers have been finally selected for publication. Three papers address the seismic behavior of structures and structural joints including “Seismic Performance Analysis of Self-Centering Concentrically Braced Steel Frame Structures” by E. Xiong et al., “Seismic Response Study of Tunnels Running underneath a Subway Station in Parallel” by F. Sun et al., and “Seismic Behavior of Hybrid Frame Joints between Composite Columns and Steel Beams” by L. Chu et al. The impact resistance of a honeycomb shelter was studied in “Anti-penetration Performance of Honeycomb Shelter under Two Repeat Projectile Strikes” by Q. Wang et al. Two papers entitled “Vibration-Isolation Performance of a Pile Barrier in an Area of Soft Soil in Shanghai” by X. F. Ma et al. and “Analysis of Lateral Dynamic Response of Caisson Foundation in Layered Clayey Soils considering Scour-Hole Dimensions” by W. Tu et al. investigate the soil-foundation interactional responses. Vehicle-induced vibration is studied

in “Dynamic Reliability of Continuous Rigid-Frame Bridges under Stochastic Moving Vehicle Loads” by N. Lu et al. Finally, L. Wang et al. present a study on “Transmitting Characteristics of Seismic Motion in Super-Deep Overburden Layer Ground.”

We hope that the publication of the Special Issue will address some of the current challenges and stimulate further research in the related field.

Conflicts of Interest

The Guest Editors of this Special Issue declare no conflicts of interest.

Xing Ma
Nawawi Chouw
Mohamed ElGawady
Songye Zhu
Xiaonong Guo

Research Article

Transmitting Characteristics of Seismic Motion in Super-Deep Overburden Layer Ground

Long Wang ^{1,2}, Zheng-quan Yang ^{1,2}, Jian-ming Zhao ^{1,2}, Xiao-sheng Liu ^{1,2},
and Yan-feng Wen ^{1,2}

¹State Key Laboratory of Simulation and Regulation of Water Cycle in River Basin, Beijing 100038, China

²Department of Geotechnical Engineering, China Institute of Water Resources and Hydropower Research, Beijing 100048, China

Correspondence should be addressed to Zheng-quan Yang; yangzhq@iwhr.com

Received 12 August 2020; Revised 5 February 2021; Accepted 10 February 2021; Published 28 February 2021

Academic Editor: Songye Zhu

Copyright © 2021 Long Wang et al. This is an open access article distributed under the Creative Commons Attribution License, which permits unrestricted use, distribution, and reproduction in any medium, provided the original work is properly cited.

Dynamic response characteristics and antiseismic performance of the structures which were constructed on the super-deep overburden layer are affected obviously by the seismic motion characteristics of the super-deep overburden layer foundation. In this paper, the seismic motion characteristics of horizontally stratified super-deep overburdenIn this paper, the seismic motion characteristics of horizontally stratified super-deep overburden based on the research results of on-site in situ tests and indoor material property tests, the horizontal shear layer method that can consider the nonlinear characteristics of dynamic soil deformation and the characteristics of seismic wave propagation in the soil is used to study the characteristics of ground motions of super-deep and thick overburden level of an earth-rock dam in China. The influence law of input ground motion characteristics and input ground motion position on seismic response analysis results of overburden ground is studied. Taking the uniform overburden layer model as an example, the coupling influence analysis of soil layer thickness and shear velocity on ground motion response are carried out, and the coupling influence law is proposed. The study shows that the seismic motion propagating characteristics of the earthquake in super-deep overburden layer is involved, inputting location of the seismic motion affects the results of ground seismic response greatly; super-deep overburden layer thickness and the soil shear wave velocity on influence law of ground motion characteristics have coupling. When the shear wave velocity of the soil layer is constant, the surface acceleration response has an inflection point with the change of the soil layer thickness; when the thickness of overburden is constant, the surface acceleration response also has an inflection point with the change of shear wave velocity of the soil layer; these inflexion values are influenced by both soil thickness and shear wave velocity.

1. Introduction

With the extensive and in-depth development of the global water conservancy and hydropower industry, the problem of strong earthquakes and deep overburden foundations has become a double challenge for hydropower project construction, and it is difficult to evade, becoming a controlling factor for the successful construction of many projects [1]. The main structure of the CCS (Coca Codo Sinclair) hydro project in Ecuador has been built on a super-deep overburden over 200 m thickness. There are several active volcanoes around the project site, and the intensity of the maximum credible earthquake is IX degree. The asphalt concrete core dam of Xiabandi hydro-junction (in Xinjiang

province of China) was constructed on the deep overburden layer which has a maximum depth of 150 m, and the basic earthquake intensity of the dam site is VIII degree. The Yele earth-rock fill dam had been constructed in the Sichuan province of China, and the maximum depth of the dam foundation overburden layer is over 400 m. The seismic fortification intensity of the dam is IX degree, and the maximum horizontal acceleration of the bedrock was determined as 441.5 gals according to the results of region earthquake hazard analysis.

The ground motion characteristics of the site with deep overburden in the river valley have an essential influence on the dynamic response characteristics of the upper earth-rock dam, gate dam, and diversion structure [1], because the

characteristics of earthquake inputting from the bedrock down overburden layer are changed greatly by the deep overburden layer. The analyzed object is the structural system that contains the structure and its near-field foundation in the dynamic analysis of hydraulic structure on deep overburden layer normally, and the size of the structure near-field foundation is limited. Because the response of local area in the structure should be paid more attention, together with the demand that the numerical element size should be coordinated with the wavelength, the scale of the structure foundation should not be too large considering the difficulty and working load of calculation. Especially when the thickness of the overburden layer in the valley is relatively large relative to the height of the structure, it is obviously inappropriate to take the soil layer within the thickness of the entire overburden layer as the near-field foundation of the calculation model. It is advisable to cutoff the foundation of the overburden layer and take only a cover layer of a certain thickness is used as the calculated near-field foundation. The seismic motion of this truncated boundary is different from the seismic motion of the bedrock surface under the soil layer. The ground seismic response analysis of the deep overburden layer should be conducted to study the influence law of overburden layer on the characteristics of the seismic motion inputted from bedrock. The seismic motion characteristics of calculation model boundary should be determined to provide seismic motion characteristic parameters for the dynamic analysis of the structure and foundation system on the deep overburden layer [2]. Besides, the application of the pseudostatic method in hydraulic structure design should be in the premise of that determining the seismic motion characteristic parameters of calculation model boundary [3].

Wang et al. [4] discussed the influence of boundary interception range on acceleration response of dam body when wave method is adopted. The results show that the acceleration response of the dam is obviously higher than that of the fluctuation method, and the vertical seismic action is more significant. The sensitivity of the fluctuation method is obviously lower than that of the vertical seismic input when the horizontal ground motion is input. Ting and Shao [5] carried out the sensitivity analysis of the thickness of overburden, the peak value of input seismic wave, and the thickness of soft soil layer in the overburden. It is concluded that the thickness of overburden, the peak value of input acceleration, and the thickness of soft soil layer are positively correlated with the attenuation of the magnification of the base surface, and the basic law of the acceleration magnification of overburden with elevation is attenuation firstly and then amplification. When there is a weak soil layer, the secondary attenuation of dynamic reaction will occur in the soil layer due to its filtering isolation. Han et al. [6] compared and analyzed the dynamic response of the lower dam for the seismic action of pulse type and nonpulse type. The results show that the impulse ground motion has a certain influence on the acceleration response of the high earth-rock dam on the deep overburden. It makes the dam body deform greatly in a very short time, which is not conducive to the dam safety. Taking into account the change of soil thickness, the

change of bedrock topography, and the influence of new structure, Yang et al. [7] studied the influence of the change of overburden structure on-site ground motion and concluded that the overburden has a significant influence on the amplitude of site ground motion. Zhu et al. [8] and Wang et al. [9] believe that the dynamic response of the dam on the deep overburden is a single relationship with the thickness of the overburden and the input of ground motion, and there is no superposition effect.

There is an earth-rock fill dam whose main body structure is constructed on the valley super-deep overburden layer in China, and it is the first case in global dam engineering fields for that the maximum thickness of this super-deep overburden layer is more than 500 m [10]. The dam is constructed on a high earthquake-intensity site in which the horizontal peak acceleration of bedrock is over 500 gal with the exceeding probability of 2.0 in 100 years. Not only the thickness of the overburden layer foundation is large but also the structure of soil layer is complicated that can be understood in the following description, and the difficulty of foundation treatment is serious. Taking this super-deep overburden layer as the basic research object, seismic motion transmitting characteristics of the overburden layer foundation have been studied deeply in the paper. The influence rules of the seismic motion characteristics of earthquake inputting from bedrock and the inputting position of the earthquake in the ground seismic response analysis on the seismic motion transmitting characteristics of soil layer have been analyzed too. Moreover, series of ground models with thickness and shear wave velocity of soil layer are different and are established based on the former real super-deep overburden layer model. The coupling influencing analysis of soil layer thickness and shear velocity on the seismic motion characteristics of ground is performed, and the coupling influencing rule is proposed in the end.

2. Analysis Methods

2.1. Summary of Ground Seismic Analysis Methods. The methods of determining ground seismic motion parameters can be classified into two types generally: one is the specification method, which is summarized based on the engineering experience, and it can be used simply and conveniently by engineers; the other is the ground seismic analysis method, in which theoretical models and calculating process are more complete, and the calculating model should be established based on the real site condition firstly. There are two types of ground seismic analysis methods, the back analysis method and the forward analysis method. The back analysis method can obtain the seismic motion parameters of the soil layer in any depth underground surface when the natural earthquake of soil layer ground free surface has been recorded and can obtain the seismic motion parameters of bedrock surface too. The forward analysis method can study the seismic motion characteristics of soil layer in any height up bedrock surface when the site earthquake of horizontal bedrock free surface has been defined by the region earthquake hazard analysis, and the seismic motion characteristics of ground surface can be obtained too.

Based on the simplification mode of the soil layer structure, the ground seismic analysis methods can be distinguished as horizontal layer shearing method, centralized mass system method, numerical analysis method (such as finite element method), and so on. Meanwhile, they also can be distinguished as time-domain analysis method and frequency-domain analysis method based on the solving method. The horizontal layer shearing method and the centralized mass system method are suitable for the ground seismic analysis of horizontally stratified soil layer under the shear horizontal waves, and they can be solved using a linear method or equivalent nonlinear method [11–13]. Using the finite element method and the other numerical analysis methods, we obtain the ground seismic analysis of soil layers in which geometry shapes are arbitrary under multidimensional earthquakes, and they can be solved using the linear method, equivalent linearization method, and real nonlinear method [14, 15].

For the horizontally stratified super-deep overburden soil layer ground in which thickness is over 500 m, it is reasonable and feasible that the ground seismic analysis of soil layer is carried out using the horizontal layer shearing method which can consider the superposition effect of the incident wave and reflected wave and the influence of super-deep soil layer on the vibration characteristics of bedrock surface under soil layer for the following reasons. Firstly, because the thickness of soil layer is large, vibration characteristics of the soil layer are influenced greatly by the superposition effect of the incident wave and reflected wave when the earthquake transmits in the ground; secondly, the real vibration characteristics of bedrock surface under soil layer are different greatly from the vibration characteristics of free bedrock surface with no soil on it (it is the site earthquake from the region earthquake hazard analysis) because the thickness of soil layer is too large; lastly, the seismic motion, which affects the vibration characteristics of super-deep overburden layer ground and the hydraulic structures on it greatly, is the horizontal shearing wave which transmits vertically from the deep crust. In this paper, the horizontal layer shearing method is the basic analysis method for ground seismic analysis to study the influencing rule of super-deep overburden layer on the seismic motion characteristics of the earthquake from bedrock under soil layer. The vibration acceleration response characteristics of soil layer are the reference object of the seismic motion characteristics analysis of overburden layer ground, which contains the acceleration amplitude and spectrum characteristics of the vibration.

2.2. Horizontal Layer Shearing Method Based on Wave Theory.

For the horizontally stratified soil layer ground, the transmitting progress of horizontal shear wave inputting from bedrock under soil layer can be represented by the schematic diagram in Figure 1. As Figure 1 shows, the site (including the semi-infinite horizontal bedrock under the soil layer) is divided into N horizontal layers, and the layers' number is 1– N from the ground surface to the half-space bedrock. The earthquake produced in deep crust transmits vertically into

the overburden layer ground foundation through the half-space bedrock and reflects back to soil layer ground and deep bedrock when it transmits to ground surface.

The $u-x$ whole coordinate system of a two-dimensional plane for a ground model is established, as shown in Figure 1, and the position coordinate of particles in the vertical direction is represented as x and the horizontal dynamic displacement of particles vibration is represented as u . Assuming soil is the material that deforms in the viscoelastic model, the relationship of u (particles' horizontal vibration displacement in a soil layer) with x (particles' vertical position coordinate) and t (time) is represented by the wave equation as equation (1) when the horizontal shear wave from bedrock underground transmits vertically in the soil layer.

$$\rho \frac{\partial^2 u}{\partial t^2} = G \frac{\partial^2 u}{\partial x^2} + \eta \frac{\partial^3 u}{\partial x^2 \partial t}, \quad (1)$$

where ρ , G , and η are the density, shearing modulus, and viscosity coefficient of soil, and the viscosity coefficient of soil can be obtained by the equation $\eta = 2G\lambda/\omega$ (λ is the damping ratio of soil and ω is the angular vibration frequency).

An irregular earthquake in time domain can be transformed into a wave group of some simple harmonic waves in frequency domain in which vibration amplitude is different. The simple harmonics with a frequency ω causes the vibrating displacement of the particle in the horizontal direction can be expressed as the following equation:

$$u(x, t) = U(x) \cdot e^{i\omega t}, \quad (2)$$

where $U(x)$ is the amplitude of particle vibration. By equations (1) and (2), the partial differential equation, as shown in equation (3) can be obtained,

$$(G + i\omega\eta) \frac{\partial^2 U}{\partial x^2} = \rho\omega^2 U, \quad (3)$$

where $U(x)$ is represented as equation (4) by solving the partial differential equation above,

$$U(x) = Ee^{ikx} + Fe^{-ikx}. \quad (4)$$

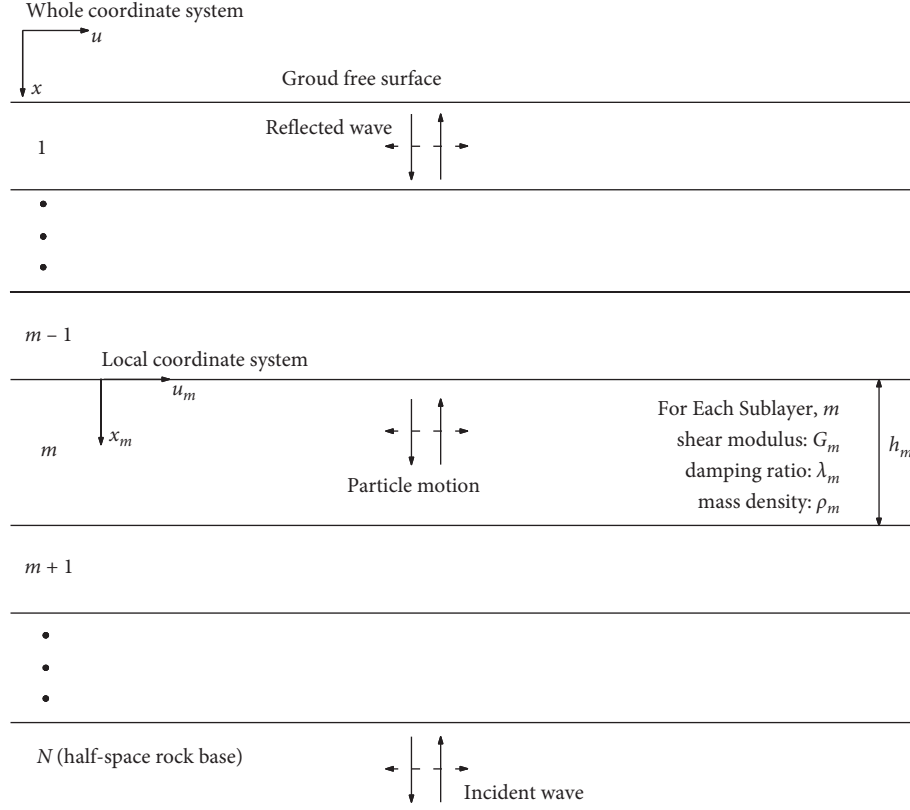
In equation (4), k is the complex wave number; it satisfies the following formula:

$$k^2 = \frac{\rho\omega^2}{G + i\omega\eta} = \frac{\rho\omega^2}{G^*}, \quad (5)$$

where G^* is the complex shear modulus.

In the general case, the values of soil shearing modulus (G) and damping ratio (λ) are correlative with the vibration frequency of soil layer (ω). Still, they are nearly constant in the frequency domains that engineers are interested in it. So, the complex shear modulus (G^*) can be represented as the following equation:

$$G^* = G + i\omega\eta = G(1 + 2i\lambda). \quad (6)$$

FIGURE 1: Two-dimensional diagram of oblique incidence of plane P wave.

By equations (2)–(6), the particles' horizontal vibrating displacement is obtained as the following equation:

$$u(x, t) = Ee^{i(kx+\omega t)} + Fe^{-i(kx-\omega t)}. \quad (7)$$

Note that in equation (7), particles' horizontal vibrating state of soil layer $u(x, t)$ can be represented by two contents: the first one is $u_1 = Ee^{i(kx+\omega t)}$; as there is increasing of time, in order to obtain the same u_1 , the x needs to be a new value smaller than former, so the expression represents the exercising results of the incident wave which transmits vertically in the negative direction along x coordinate axis; the other one is $u_2 = Fe^{-i(kx-\omega t)}$; similarly as before, the expression represents the exercising results of the reflected wave which transmits vertically in the positive direction along the x coordinate axis. The levels of vibration amplitude of incident wave and reflected wave are defined by E and F which are called as wave amplitude coefficients.

For any soil layer of the ground (the soil layer number is “ m ”), the local coordinate system $u_m - x_m$ is introduced, and the vibration displacement of soil layer top surface and bottom surface can be represented respectively as the following equations:

$$u_m(x_m = 0) = (E_m + F_m)e^{i\omega t}, \quad (8a)$$

$$u_m(x_m = h_m) = (E_me^{ik_m h_m} + F_me^{-ik_m h_m})e^{i\omega t}. \quad (8b)$$

The shear stress of any horizontal plane in the soil layer is represented as the following equation:

$$\tau(x, t) = G \frac{\partial u}{\partial x} + \eta \frac{\partial u}{\partial x} \frac{\partial u}{\partial t} = G^* \frac{\partial u}{\partial x}. \quad (9)$$

Considering equation (7), equation (9) can be represented as equation (10); furthermore,

$$\tau(x, t) = ikG^*(Ee^{ikx} - Fe^{-ikx})e^{i\omega t}. \quad (10)$$

So, the shear stress of soil layer top surface and bottom surface are represented, respectively, as the following equation:

$$\tau_m(x_m = 0) = ik_m G_m^*(E_m - F_m)e^{i\omega t}, \quad (11a)$$

$$\tau_m(x_m = h_m) = ik_m G_m^*(E_me^{ik_m h_m} - F_me^{-ik_m h_m})e^{i\omega t}. \quad (11b)$$

The stress and vibration displacement on any interface of soil layers are continuous. Based on equations (8) and (11), equations (12) and (13) are obtained,

$$E_{m+1} + F_{m+1} = E_me^{ik_m h_m} + F_me^{-ik_m h_m}, \quad (12)$$

$$E_{m+1} - F_{m+1} = \frac{k_m G_m^*}{k_{m+1} G_{m+1}^*} (E_me^{ik_m h_m} - F_me^{-ik_m h_m}). \quad (13)$$

Solving the coupled equations of (12) and (13), the relationships of E_{m+1} with E_m and F_{m+1} with F_m can be represented as equations (14) and (15),

$$E_{m+1} = \frac{1}{2}E_m(1 + \alpha_m)e^{ik_m h_m} + \frac{1}{2}F_m(1 - \alpha_m)e^{-ik_m h_m}, \quad (14)$$

$$F_{m+1} = \frac{1}{2}E_m(1 - \alpha_m)e^{ik_m h_m} + \frac{1}{2}F_m(1 + \alpha_m)e^{-ik_m h_m}. \quad (15)$$

In equations (14) and (15), α_m is the complex wave impedance ratio, and it can be represented as the following equation:

$$\alpha_m = \frac{k_m G_m^*}{k_{m+1} G_{m+1}^*} = \left(\frac{\rho_m G_m^*}{\rho_{m+1} G_{m+1}^*} \right)^{1/2}. \quad (16)$$

The shear stress in the surface of ground is 0, so the result of $E_1 = F_1$ is got based on equation (10), and the recursive relations of E_m and F_m of any soil layer in which soil layer number is m with E_1 (or F_1) are represented as equations (17a) and (17b). Based on equations (17a) and (17b), the wave amplitude coefficients of incident wave and reflected wave of all soil layers could be obtained recursively if the wave amplitude coefficient of incident wave or reflected wave of any soil layer is known.

$$E_m = e_m(\omega)E_1, \quad (17a)$$

$$F_m = f_m(\omega)E_1, \quad (17b)$$

where in equation (17), $e_m(\omega)$ and $f_m(\omega)$ are the quantities associated with the natural vibration angular frequency of the harmonic wave, and they are obtained based on the structure characteristics parameters of ground model.

The transmitting progress of earthquake waves that contain incident waves and reflected waves is shown in Figure 2. Because the incident wave cannot be influenced by the upper overburden layer on the surface of bedrock, the vibration amplitude of incident wave (E_m) is half of it on rock outcrop ($2E_m$). The vibration progress of rock outcrop should be considered same as the site earthquake, which is the vibration acceleration time history of horizontal bedrock free surface, and the site earthquake can be obtained by the region earthquake hazard analysis. The vibration amplitudes of incident wave (E_m) and reflected wave (F_m) of any soil layer " m " in the ground can be obtained recursively by the recursive relations (as equation (17)) when the amplitude of incident wave on the surface of bedrock under overburden layer (E_m) is defined based on the earthquake time history which is the result of region earthquake hazard analysis for the study site.

Furthermore, the horizontal vibration acceleration and shear stress of any soil layer in the ground are represented as equations (18) and (19), and the other characteristic quantities can be obtained recursively too.

$$\ddot{u}(x, t) = \frac{\partial^2 u}{\partial t^2} = -\omega^2 (Ee^{i(kx+\omega t)} + Fe^{-i(kx-\omega t)}), \quad (18)$$

$$\gamma = \frac{\partial u}{\partial x} = ik(Ee^{i(kx+\omega t)} - Fe^{-i(kx-\omega t)}). \quad (19)$$

3. Example Analysis for Seismic Motion Characteristics of Super-Deep Overburden Layer

One reservoir will be constructed in China, and the water-retaining structure is an earth-rock fill dam whose main body is constructed on the super-deep overburden layer in a wide valley. The thickness of valley overburden layer is large in the whole range of the dam sites, and the thickness of most ground regions around the dam is more than 500 m. Combining with many drilling data in the dam site area, we can see that soil layers of overburden layer foundation are horizontally stratified well and the thickness of soil layers along horizontal direction changes little in the range of project. The valley super-deep overburden layer foundation is constituted by seven main soil layers; those soil layers from down to up are layer ①, moraine and glacial relics stacking crushed-rock layer; layer ②, alluvial-pluvial and stacking sand layer containing crush (or pebble); layer ③-1, fluvial-lacustrine deposit sand layer containing gravel; layer ③-2, fluvial-lacustrine deposit silty clay layer; layer ③-3, fluvial-lacustrine deposit sand layer containing gravel; layer ④, modern alluvial deposit sand gravel stratum layer.

In the engineering design stage, a large number of on-site surveys were carried out, and the site soils have been transported to the laboratory used to do dynamic characteristic tests. All those achievements of site geotechnical investigation and laboratory material tests can be the basic data of ground seismic analysis [10].

3.1. Model of Ground Seismic Analysis. The soil layer of the overburden layer in the dam site area shows a good horizontal stratification, and the thickness of the soil layer along the horizontal river direction (the most dangerous direction of ground motion) changes little. Because the thickness of the foundation soil layer is large, the fluctuation effects are obvious when the earthquake transmits in the soil layer ground, and the vibration characteristics of bedrock surface are influenced obviously by the super-deep overburden soil layer on the bedrock. According to these actual conditions, considering the wave effect of horizontal seismic waves propagating on the ground, it is reasonable and feasible to use the horizontal layer shear method for ground motion analysis. Because the soil layers are horizontally stratified well in the whole range of ground, the ground seismic analysis model can be established based on the data of one typical drilling, which reveals that the thickness of soil layer is bigger than others. The typical drilling reveals that the thickness of soil layer is 566.9 m. Soil layer structure and soil features of the ground are shown as the above description and the drilling structure diagram (Figure 3), and the field cross-hole wave velocity tests have been performed to definite the shear wave velocity of soil layers further more (Figure 3).

According to the distribution of the soil layer and the shear wave speed, it is necessary to avoid the calculation model from being too large while ensuring the calculation accuracy. The soil layer thickness of the site analysis model is

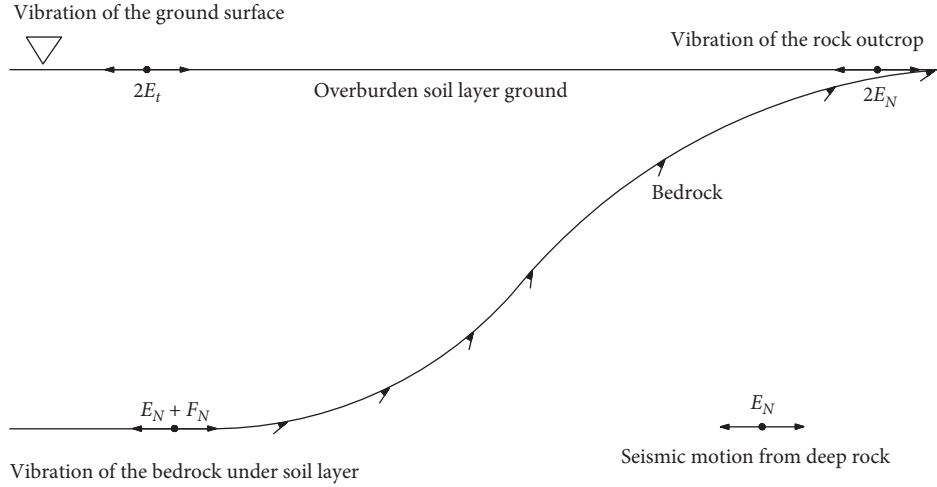


FIGURE 2: The relationship schematic diagram of soil layer's vibration and bedrock's vibration in the ground system.

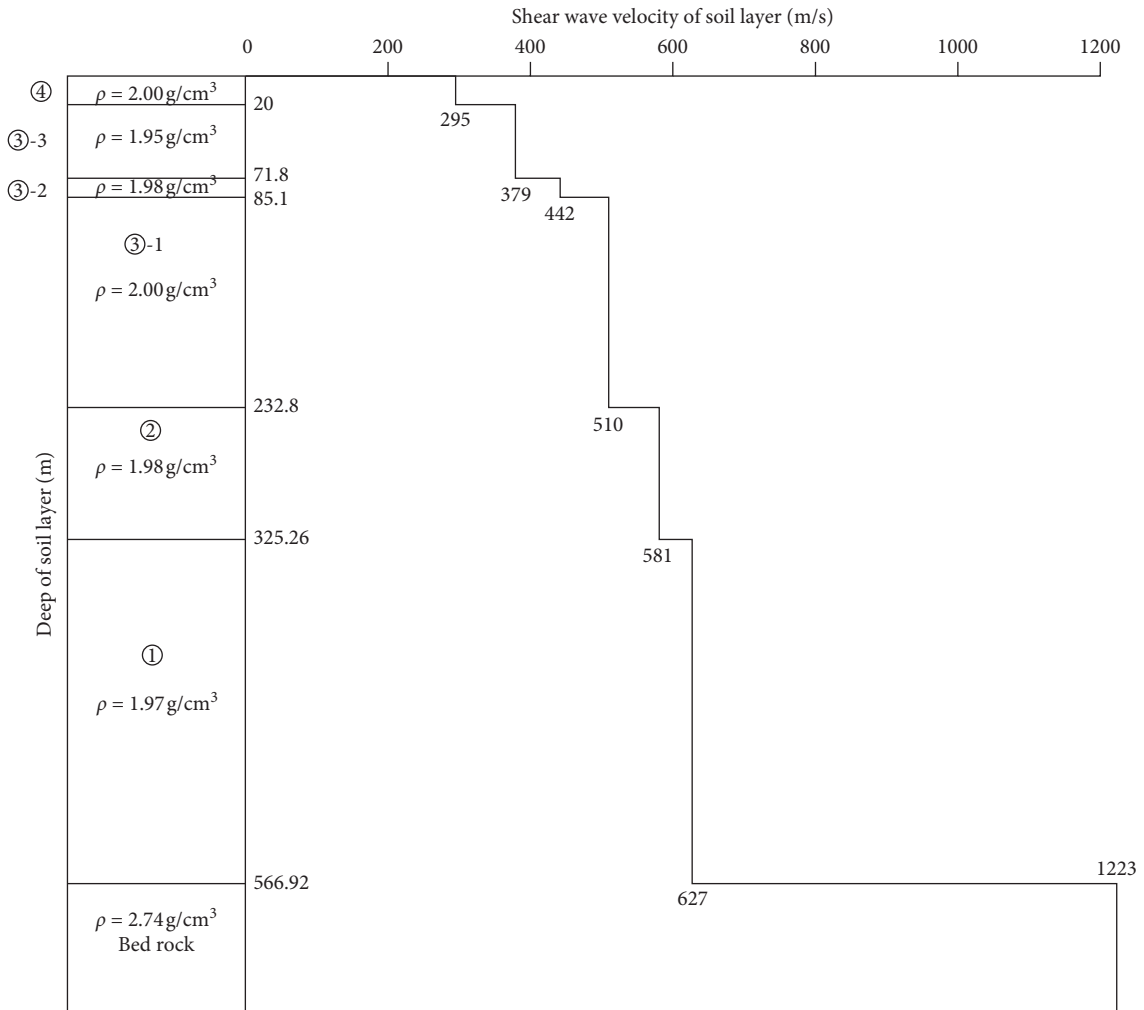


FIGURE 3: The soil layer structure of ground based on structure diagram of the typical drilling.

divided to ensure that the maximum soil layer thickness is not greater than 1/6 of the shear wave wavelength [11, 12]. Simultaneously, the component of the input ground motion of the bedrock has a significant impact on the site and the

structure on the foundation is the part with a frequency lesser than 10 Hz. Accordingly, the soil layer of the site in Figure 3 is divided into 77 sublayers, including the horizontal bedrock layer with a semi-infinite space at the bottom.

Among them, the thickness of each sublayer of the soil layer (layer ①, layer ②, and layer ③-1) with wave speed greater than 500 m/s is 8m, and the wave speed lesser than 500 m/s corresponds to 1/6 of the minimum wavelength of 50m which is 8.33 m. The thickness of each sublayer of the soil layer (layer ③-2, layer ③-3, and layer ④) with a wave velocity of 295–500 m/s is 5m, which is basically the same as 1/6 (4.91 m) of the minimum wavelength of 29.5 m corresponding to the wave velocity of 295 m/s.

3.2. Dynamic Characteristic Parameters of Soil in Ground Seismic Analysis. Soil of overburden layer is the material that deforms in visco-elastic mode, and the equivalent nonlinear visco-elastic dynamic model improved by Zhu-jiang Shen has been used to reflect the nonlinear characteristics of soil dynamic stress-strain relationship under the seismic loading [16].

The normal equivalent nonlinear visco-elastic dynamic model had been improved by Zhu-jiang Shen, and the improved model can be used more conveniently than before [11, 16]. In the improved model, the modulus decay (or damping ratio increasing) coefficient k_1 and the maximum damping ratio λ_{\max} have been used to reflect the decaying relationship of modulus and the increasing relationship of damping ratio with the increase of soil shear strain. The improved model is described using the following formulas:

$$G = \frac{G_{\max}}{1 + k_1 \gamma_c}, \quad (20)$$

$$G_{\max} = k_2 P_a \left(\frac{\sigma'_0}{P_a} \right)^n, \quad (21)$$

$$\lambda = \lambda_{\max} \frac{k_1 \gamma_c}{1 + k_1 \gamma_c}, \quad (22)$$

where P_a is the standard atmospheric pressure (101.3 kPa); σ'_0 is the mean effective stress of soil; G_{\max} is the maximum shear modulus, k_2 and n are the dynamic shear modulus coefficient and index; and γ_c is the reference shear strain, and it is calculated by

$$\gamma_c = \frac{\gamma}{(\sigma'_0/P_a)^{1/2}}, \quad (23)$$

where γ is the dynamic shear strain of soil.

There are two key variables in the equivalent nonlinear visco-elastic dynamic model, dynamic shear modulus G , and damping ratio λ which are associated with the dynamic shear strain of soil and are used to reflect the nonlinear elasticity and viscosity of soil under dynamic load. Dynamic shear modulus and damping ratio are calculated by equations (20) and (22). All four parameters of the model (k_1 , k_2 , n , and λ_{\max}) can be defined by a group of dynamic triaxial tests or resonant column tests [16].

In the improved equivalent nonlinear visco-elastic model, dynamic shear modulus coefficient k_2 and index n are used to define the maximum dynamic shear modulus G_{\max} as equation (20). Although they can be defined by approach

of the laboratory tests as in the above description, the values of k_2 and n defined by laboratory tests are difficult to reflect the actual dynamic deformation characteristics of soil in the ground comprehensively and reasonably, and they should be replaced by the results of field testing if the testing is performed carefully and generally. Firstly, the in-situ structural property of soil which has an important effect on the dynamic deformation characteristics of soil cannot be represented suitably in laboratory tests. Secondly, although some physical properties of soil (such as the natural compactness) can be represented suitably in laboratory tests through adjusting the experimental condition, the physical properties of soil are discrete in the whole range of the ground, and they can be described by limited experimental working conditions. So, the results of laboratory tests in which experimental working conditions are limited cannot reflect the real dynamic deformation characteristics of soil overall for the whole ground. The corresponding characteristic parameters defined by the method of field cross-hole wave velocity tests are representative entirely, because the shear wave velocity of soil layer is the entirety reflection of soil's dynamic deformation characteristics in field site.

Based on the above described reasons, the dynamic deformation characteristic parameters of soil (for maximum shear modulus) used in the following calculation analysis are defined based on the results of field cross-hole wave velocity tests as presented in Figure 3. In field exploration of the project, many field cross-hole wave velocity tests are performed, and the testing results are credible. The maximum shear modulus G_{\max} of soil can be calculated by equation (24) when the shear wave velocity of soil layer v_s is known,

$$G_{\max} = \rho v_s^2, \quad (24)$$

where ρ is the natural density of soil.

Because the decaying relationship of soil dynamic shear modulus (or the increasing relationship of soil damping ratio) with the increasing of soil dynamic shear strain is difficult to be determined by the method of field testing, the modulus decay (or damping ratio increasing) coefficient k_1 which reflects the relationship of dynamic shear modulus and damping ratio with dynamic shear strain and the maximum damping ratio λ_{\max} still need to be defined by the laboratory tests. Based on the equivalent nonlinear visco-elastic dynamic model improved by Zhu-jiang Shen, soil dynamic shear modulus and damping ratio of any soil layers in the ground model can be calculated using the mean effective stress state of soil in any layers which can be defined by the static finite element method, the shear wave velocity of soil layers which can be defined by the field cross-hole wave velocity tests, and the relationship parameters of dynamic shear modulus and damping ratio with the dynamic shear strain of any type soils which can be defined by the laboratory tests. The modulus decay (or damping ratio increasing) coefficient k_1 and the maximum damping ratio λ_{\max} of all soils in the ground model which is defined by the laboratory tests are shown as Table 1.

TABLE 1: Maximum damping ratio λ_{\max} and modulus decay (or damping ratio increasing) coefficient k_1 of soils in ground.

Soils	λ_{\max}	k_1
Layer ④, modern alluvial deposit sand gravel stratum layer	0.238	17.6
Layer ③-3, fluvio-lacustrine deposits sand layer containing gravel	0.278	5.5
Layer ③-2, fluvio-lacustrine deposits silty clay layer	0.293	6.3
Layer ③-1, fluvio-lacustrine deposits sand layer containing gravel	0.271	5.7
Layer ②, alluvial-pluvial and stacking sand layer containing crush (or pebble)	0.245	15.2
Layer ①, moraine and glacial relics stacking crushed-rock layer	0.240	16.0

3.3. Inputting Seismic Motion. The input seismic wave from bedrock is the site wave determined by the regional seismic hazard analysis. The site wave considers the impact of the regional seismic environment such as the geological structure of the engineering site, including the characteristics of the main potential sources and the attenuation characteristics in propagation. The uniform probability method is used to determine the seismic acceleration response spectrum of different probability levels in the engineering field, and the acceleration time history is generated accordingly. The horizontal vibration peak acceleration of the free surface of the wave bedrock of the site is 0.54 g, and the absolute acceleration response spectrum is shown in Figure 4(a). Considering the regional ground motion characteristics comprehensively, the time history of ground motion acceleration generated from the acceleration response spectrum is 82 s, as shown in Figure 4(b). It can be seen from Figure 4 that the acceleration response spectrum has a wide spectrum platform, the first characteristic period is about 0.1 s, and the second characteristic period (the falling inflection point of the response spectrum platform) is about 0.6 s. Although the ground motion lasts up to 81 s, the main body vibration occurs. In the first 40 s of the earthquake, the vibration amplitude was smaller in the later period.

3.4. Basic Calculation Results of the Ground Seismic Analysis and the Primary Analysis. Acceleration peak values of soil layers in different depths of the ground are shown in Figure 5(a), and the distribution of corresponding acceleration amplification factors along the vertical direction in the ground is shown in Figure 5(b). The acceleration amplification factors of soil layers are based on the acceleration peak value of site earthquake which is the vibration progress of rock outcrop in an earthquake (0.54 g). Comparison of the horizontal vibration acceleration time history and the corresponding acceleration spectra of soil layers at different heights in the ground is shown in Figure 6.

From Figure 5, super-deep overburden layer has a significant reducing effect on the seismic motion inputting from deep bedrock, the peak value of acceleration on the bedrock surface underground is far below to it on the bedrock outcrop (site earthquake) because of the restrictive effects of super-deep overburden layer on vibration of bedrock surface, and the vibration amplitude of soil layers in any height of the ground is lower than the bedrock surface. The vibration acceleration amplification factor of soil layers decreases first and then increases with the growth of soil layers' altitude. The acceleration

amplification factor on the ground surface is only about 0.6, and the acceleration peak value is far below the inputting value. The main reason is that the overburden layer is softer than the bedrock and the overburden layer is super deep; the super-deep soft soil layers dissipate the energy of inputting seismic motion from bedrock largely, so the vibration amplitude of soil layers is lower than it on the bedrock surface under overburden layer ground. Because the gravel-bearing sand (with silty sand) layer (layer ③-1 and layer ③-3) of the river-lacustrine facies sedimentation is interspersed with the relatively hard silty clay layer (layer ③-2) of the river-lacustrine sedimentation, as a result, the curve has a certain degree of bending abrupt change at the soil elevation.

From Figure 6, long-period components of the acceleration response spectra increase as the growth of soil layers' altitude. Shape of the response spectra curve changes from single peak type to multipeak or plateau type, and the characteristic period corresponding to the maximum value of response spectra changes bigger gradually. The second characteristic period (decreasing inflection point of response spectra platform) of response spectra is about 2.0 s on the ground surface that is larger than the value on the bedrock surface (about 0.6 s). Based on the response spectra shape on the ground surface, it can be known that vibration of the soil layer on ground surface presents a slowly sloshing station relatively to it on the bedrock surface.

Although acceleration amplitude of the seismic motion inputting from bedrock is reduced greatly because of the super-deep overburden layer, long-period components of its' acceleration response spectra change prominently, and the characteristic period of seismic motion changes larger. Long-period components of the acceleration response spectra change prominently on the ground surface, which is disadvantageous to towering structures on ground surface in which natural vibration period is relatively large, such as in the 1985 Mexican Earthquake [17]. Although Mexico City was 400 km from epicenter of the Mexican Earthquake, that is, a large distance, also lots of towering structures in the city were destroyed seriously for the earthquake, and most destroyed tower structures were constructed on the lacustrine deposits deep overburden soil layer. Although the deep soil layer reduced acceleration amplitude of the earthquake greatly (the peak value of acceleration on ground surface is only 0.15 g), but the characteristic period of earthquake increased greatly for the deep soil layer, and the characteristic period of seismic motion on the ground surface changed close to the natural vibration period of towering structures. That is the main reason for serious damage in the earthquake.

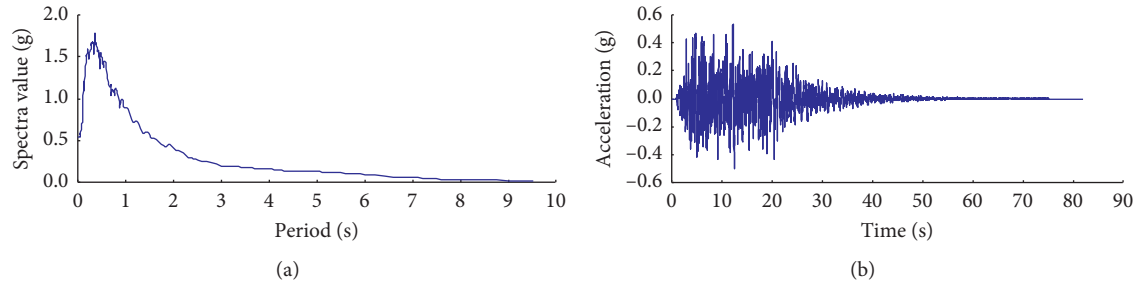


FIGURE 4: Inputting seismic motion of the ground seismic analysis. (a) Acceleration spectra (damping ratio is 0.05). (b) Acceleration time history.

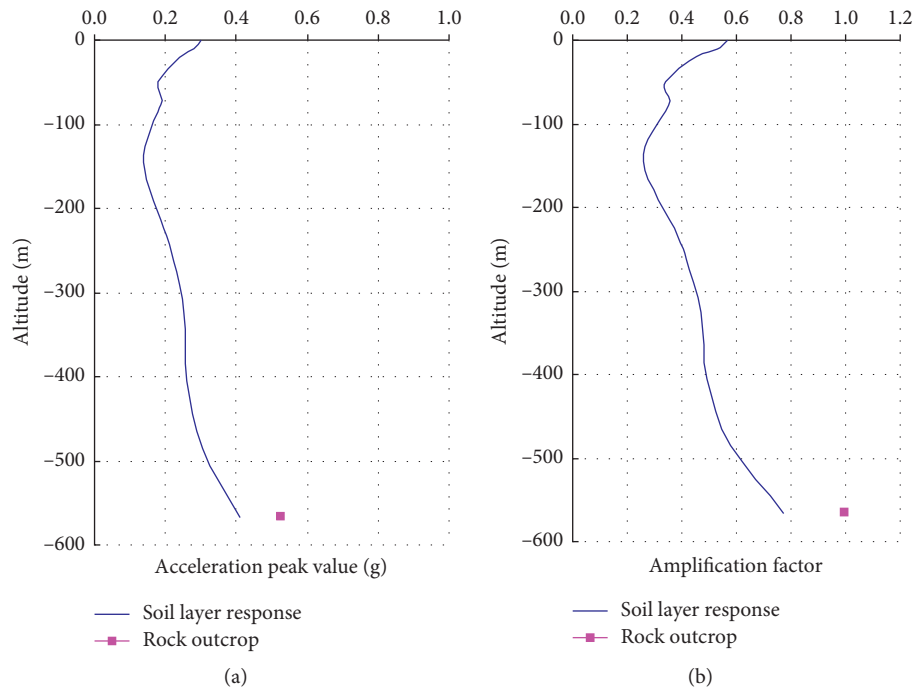


FIGURE 5: Distribution of the acceleration peak values and the corresponding amplification factors of soil layers in the ground along the vertical direction (the altitude of ground surface is 0 m and the altitude of bedrock surface is -566.9 m). (a) Acceleration peak value. (b) Acceleration amplification factor.

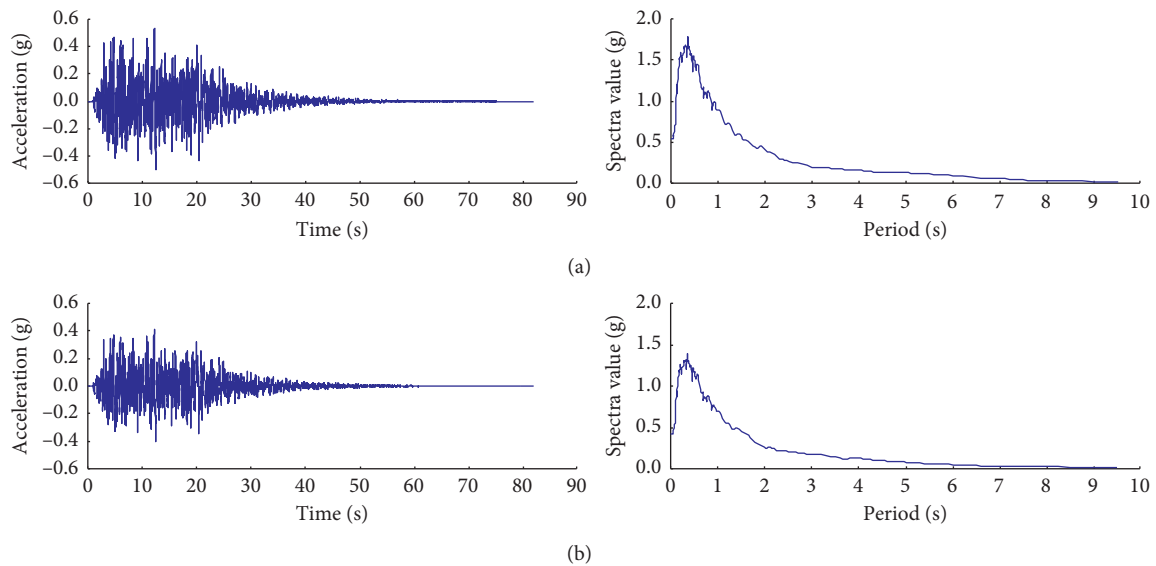


FIGURE 6: Continued.

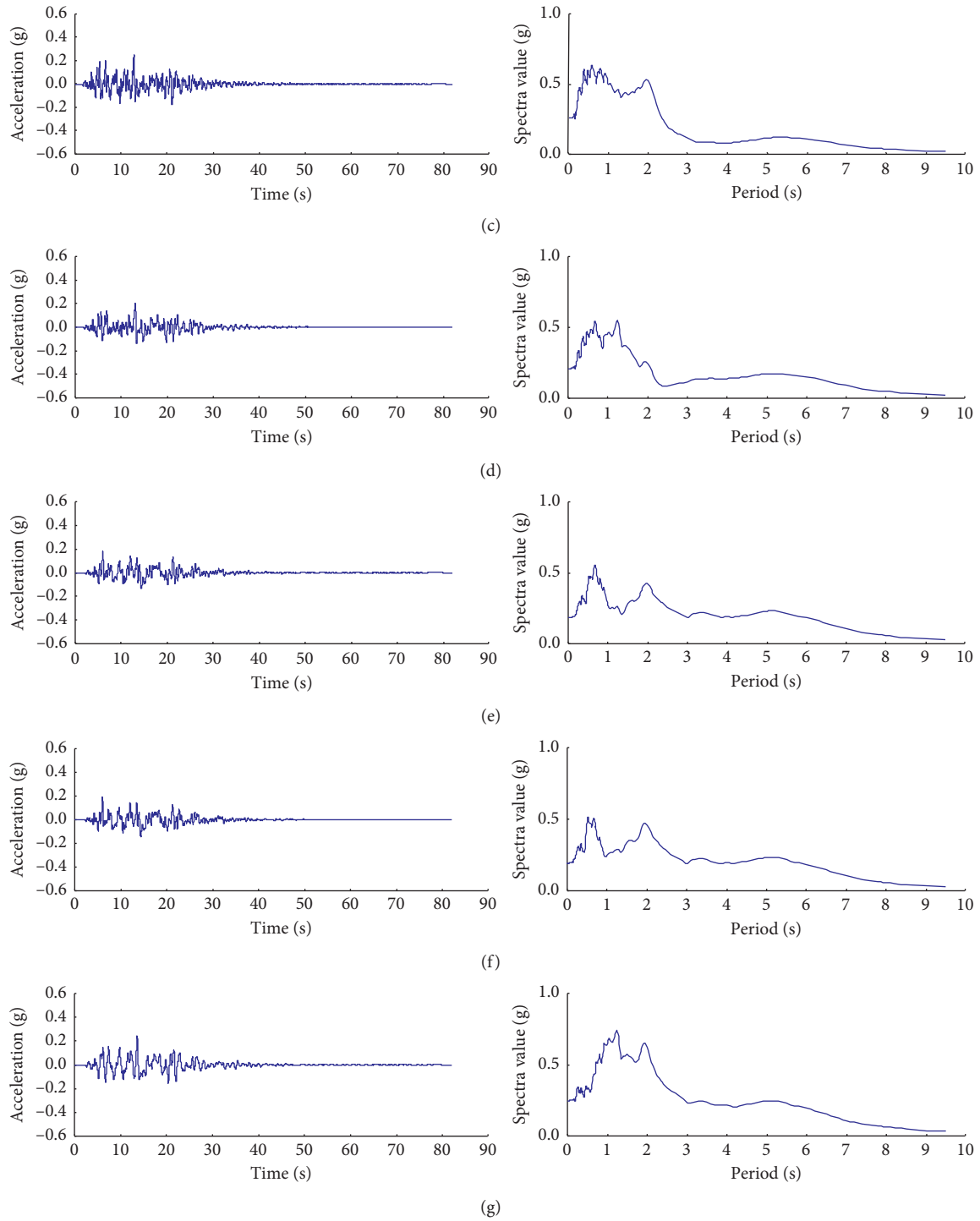


FIGURE 6: Continued.

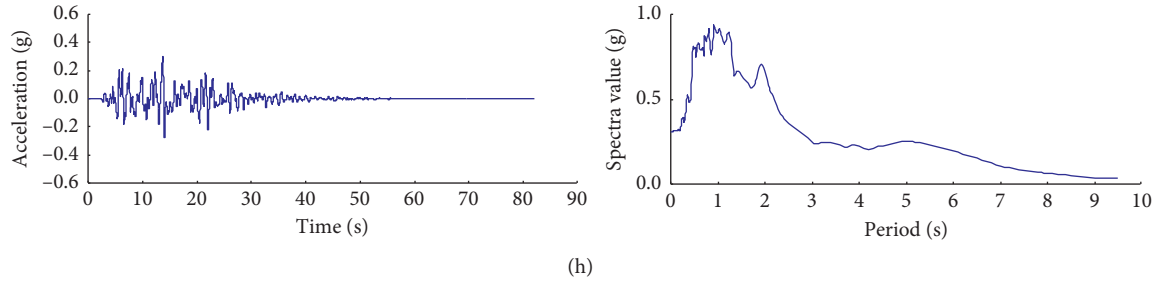


FIGURE 6: Comparison of the vibration acceleration time history and the corresponding acceleration spectra (damping ratio is 0.05) of soil layers at different altitude in the ground. (a) Inputting seismic motion (surface of the rock outcrop). (b) Surface of the bedrock under overburden layer ground (the height to bedrock surface is 0 m). (c) Surface of layer ① (the height to bedrock surface is 241 m). (d) Surface of layer ② (the height to bedrock surface is 334 m). (e) Surface of layer ③-1 (the height to bedrock surface is 481 m). (f) Surface of layer ③-2 (the height to bedrock surface is 495 m). (g) Surface of layer ③-3 (the height to bedrock surface is 546 m). (h) Surface of layer ④ (the height to bedrock surface is 566.9 m).

3.5. Impacts of Inputting Seismic Motion from Bedrock on the Ground Seismic Motion Characteristics. The seismic motion transmitting characteristics of overburden layer under earthquake from bedrock under ground is influenced dually by the structural characteristics of overburden layer ground and the seismic motion characteristics of inputting earthquake [18–23]. The influencing rule of seismic motion characteristics of inputting earthquake on seismic motion transmitting characteristics of overburden layer is studied through investigating the difference of ground seismic motion characteristics under different earthquakes. Seismic motion characteristics of the earthquake can be represented by the intensity of earthquake (seismic motion amplitude), the spectral characteristics of earthquake, and the vibration duration of earthquake.

A series seismic response analysis of the ground is conducted in condition that the acceleration peak value of earthquake is adjusted in the range of 0.1 g~0.9 g and the shape of earthquake acceleration time history becomes unchangeable (the spectral characteristics and the vibration duration of earthquake become unchangeable). Acceleration peak values and corresponding acceleration amplification factors of the soil layers in different depths of ground under earthquakes in which acceleration peak values are different, as shown in Figure 7. Acceleration response amplitude of the ground increases with the increase of the amplitude of inputting earthquake, and the difference of soil layer acceleration response amplitude under different intensity earthquakes decreases first and then increases with the growth of soil layers' altitude. Acceleration amplification factors of the soil layers decrease with the increase of the amplitude of inputting earthquake, which is caused by the nonlinear dynamic characteristics of ground soils mainly. When the amplitude of inputting earthquake is relatively low (lower than 0.2 g), the vibration amplitude of ground surface is magnified slightly contrasting with bedrock inputting (site earthquake), and the vibration amplitude of ground surface is reduced contrasting with the site earthquake when the amplitude of inputting earthquake is higher than 0.2 g. On the other hand, from the results of the response spectrum analysis, the influence of deep overburden layer ground on

the acceleration response spectra shape changes more obviously when the inputting earthquake changes strongly, and the amplification effects of soil layer on the long-period seismic motion components are outstanding in strong earthquake.

In order to investigate the influence of inputting earthquake wave shape (containing the dual influencing of earthquake spectral characteristics and vibration duration) on seismic motion transmitting characteristics of soil layer ground, the ground seismic response analysis when the ground is under the other earthquake is performed contrasting with the site earthquake of the example project. The comparative earthquake is a site earthquake of the other project and vibration duration of the earthquake is 26.0 s, and the acceleration peak value is adjusted to 0.53 g. Acceleration spectra of the earthquake and the acceleration time history, which is generated according to the acceleration spectra, are shown in Figure 8. Contrasting with Figure 5, characteristic period of acceleration spectra peak value of the comparative earthquake is below than the site earthquake of the example project. The first characteristic period is 0.1 s, but the second characteristic period (decreasing inflection point of response spectra platform) is about 0.3 s that is far lower than the site earthquake of the example project. So, short period components of the comparative earthquake are more obvious compared with the site earthquake of the example project. On the other hand, vibration duration of the comparative earthquake is shorter more than the site earthquake of the example project. The spectral characteristics and the vibration duration of two earthquakes have a significant difference.

Comparison of the acceleration amplification factor of soil layers in different heights of the ground under two different earthquakes is shown in Figure 9. From the figure, the vibration amplitude on the bedrock surface under two earthquakes is basically quite, but the vibration amplitude of soil layers induced by different earthquake waves transmitting in overburden layer ground is different obviously, and the vibration amplitude of soil layers under comparative earthquake is far below than the site earthquake of the example project. Reasons of that can be summarized as

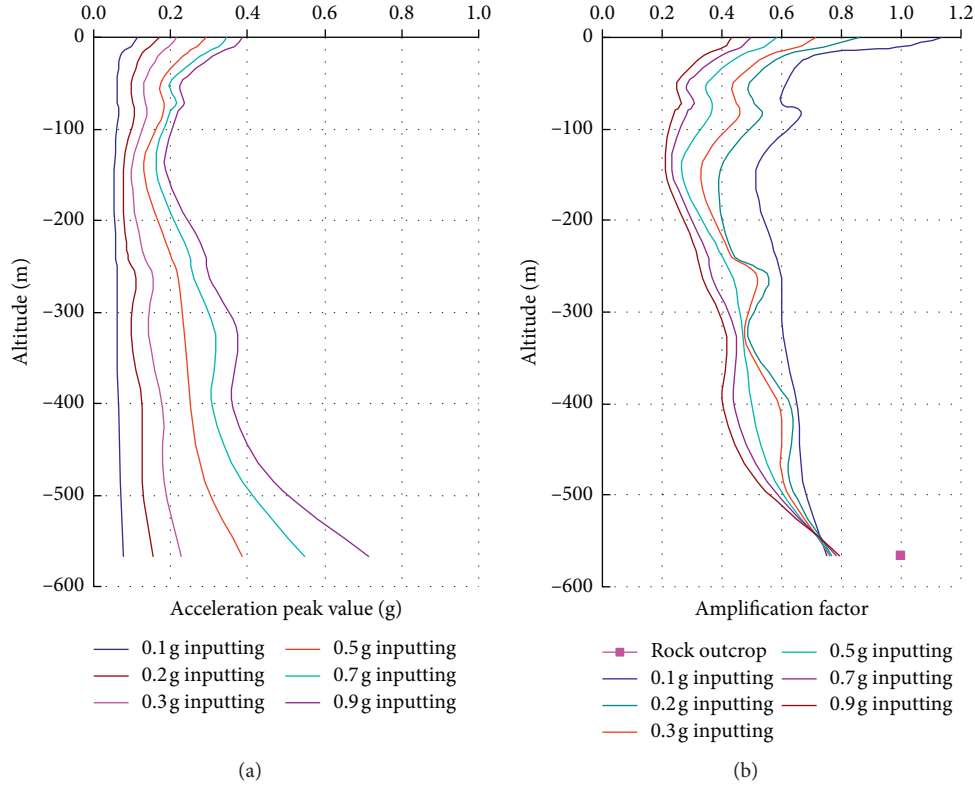


FIGURE 7: Impacts of seismic motion intensity on the site amplification effects of overburden layer. (a) Acceleration peak value. (b) Acceleration amplification factor.

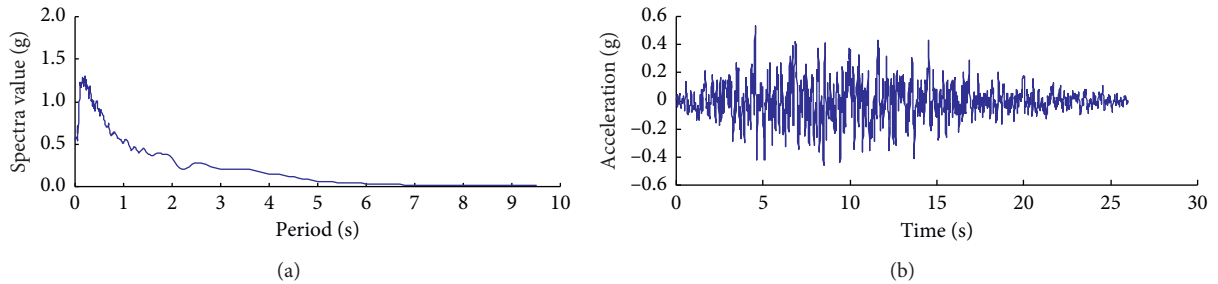


FIGURE 8: Inputting seismic motion of the contrasting analysis. (a) Acceleration spectra (damping ratio is 0.05). (b) Acceleration time history.

follows: (1) the second characteristic period (decreasing inflection point of response spectra platform) of the site earthquake of the example project is higher than the comparative earthquake and the long-period components of the earthquake are outstanding; all these seismic motion characteristics of the site earthquake of example project are adaptive with the structural characteristics of super-deep overburden layer ground system in which first natural vibration period is relatively high. When the characteristic period of the earthquake is close to the structural first natural vibration period of overburden layer ground, vibration of the ground is stronger. (2) Vibration of soil layers is the dual results of incident wave and reflected wave; vibration amplitude of soil layers is the superposition of incident wave amplitude and reflected wave amplitude. Because vibration duration of the site earthquake of the example project is

longer than the comparative earthquake, the superposition effects of soil layers vibration are more obvious when the earthquake transmits in the super-deep ground. So, the vibration amplitude of the soil layers under the site earthquake of the example project is stronger than the comparative earthquake.

3.6. Impacts of Seismic Motion Inputting Interface on Results of the Ground Seismic Response Analysis. Based on the results of ground seismic analysis for two deep soil layer grounds in which thickness is 100 m and 280 m, Guo-Xing Chen suggests that the interface of soil layers whose shear velocity is 500 m/s could be regarded as the interface of seismic motion inputting in ground seismic analysis [24]. For the typical drilling of example ground that the calculation model of

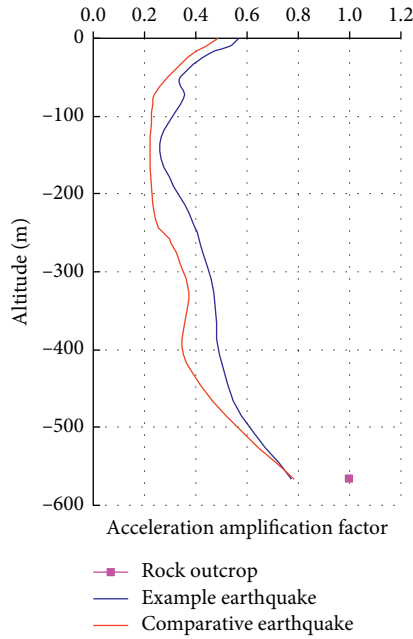


FIGURE 9: Impacts of the inputting earthquake shape on the seismic motion transmitting characteristics (containing the dual influencing of earthquake spectral characteristics and vibration duration).

ground seismic response analysis is established based on it, the interface of soil layers in which shear velocity is 500 m/s is located in the interior of layer ③-1, and depth of the interface is 128 m under the ground surface. In the following, some ground models for ground seismic response analysis for example ground are established in which seismic motion inputting interfaces are on the surface of layer ③-1 (underground depth 85.1 m), the 500 m/s shear wave velocity interface (inside layer ③-1, underground depth 128 m), the surface of layer ② (underground depth 232.8 m), and the surface of bedrock (underground depth 566.92 m). The ground seismic response analysis for these ground models under the same earthquake as before is performed to study the influencing rule of the location of seismic motion inputting interface on the results of ground seismic response analysis. Comparison of the acceleration magnified factors of soil layers along the vertical direction in the ground is shown in Figure 10 when the different interfaces have been as the seismic motion inputting interface for the ground seismic response analysis.

From Figure 10 and combining with the acceleration spectra analysis, it can be known that the acceleration response amplitude of soil layers in the ground increases greatly when the altitude of seismic motion inputting interface changes higher, and the shape of acceleration spectra is not affected obviously by the location of seismic motion inputting interface. The calculation results show that simply selecting the 500m/s shear wave velocity interface as the ground motion input interface will significantly overestimate the amplification effect of the site on the input ground motion of the bedrock. Although the soil is hard relatively when the shear velocity of soil layer is over 500 m/s or even

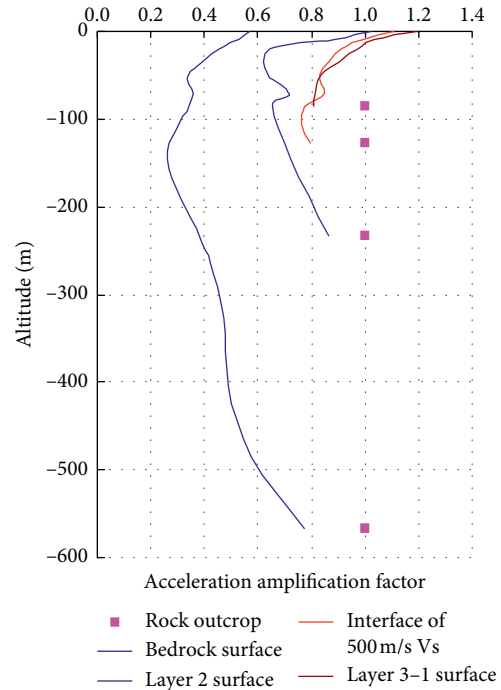


FIGURE 10: Impacts of seismic motion inputting interface on results of the ground seismic response analysis.

more higher, the visco-elastic characteristics and the dynamic deformation nonlinear characteristics of soil are still significant, so the energy dissipation effects of these hard soil layers in which shear velocity is over 500 m/s on the earthquake from the bedrock is still nonnegligible. For those super-deep overburden soil layer grounds, it is vital selecting the real hard bedrock surface under soil layer ground as the inputting interface of seismic motion in the ground seismic response analysis.

4. Ground Seismic Response

Analysis considering the Coupling

Influence of Soil Layer Thickness and Soil Shear Velocity

4.1. Research Thinking and Calculation Model. As the description of the abovementioned ground seismic response analysis theory, seismic motion transmitting characteristics of overburden layer under earthquake from bedrock under the ground is influenced dually by the structural characteristics of overburden layer ground system and the seismic motion characteristics of inputting earthquake. The above results of the ground seismic motion characteristics example analysis for the real super-deep overburden layer have shown that seismic motion characteristics of deep overburden layer ground are influenced greatly by the seismic motion characteristics of inputting earthquake (such as the seismic motion amplitude, the spectral characteristics, and the vibration duration of earthquake). For another influencing factor of seismic ground motion transmitting characteristics, the structural characteristics of overburden layer ground system are controlled mainly by two

influencing factors, the thickness of overburden layer ground and the dynamic deformation characteristics of soil. Structural geometric characteristics of the ground are influenced by the thickness of soil layer, structural material characteristics of the ground is influenced by the dynamic deformation characteristics of soil, and the structural characteristics of overburden layer ground are determined by the geometric and material characteristics of ground dually [25, 26].

As shown in the above description, the dynamic deformation characteristics of soil are represented by the maximum shear modulus of soil and its' decay characteristics with the increasing of soil shear strain, and the maximum shear modulus of soil can be represented indirectly by the values of shear wave velocity which is obtained from the field cross-hole wave velocity testing. Normally, the shear wave velocity of soil layer is not uniform along the vertical direction, and the vertical structural characteristics of the ground are widely existed. The shear wave velocity characteristics of the ground as a whole (or the hardness of whole ground) can be represented grossly by the mean shear wave velocity of the ground which is controlled dually by the shear wave velocity of all soil layers and the corresponding thickness of soil layers as shown in equation (25). The hardness of the overburden layer ground can be shown qualitatively by the mean shear wave velocity of the ground basically, and the mean shear wave velocity of the ground is used to represent the ground characteristics qualitatively in some Chinese structure antiseismic design codes [27, 28]. Although the seismic motion transmitting characteristics of overburden layer ground is influenced by the distribution characteristics of soil layer shear wave velocity along the vertical direction in the ground to a certain degree, the mean shear wave velocity of the ground is still used to judge the seismic motion characteristics qualitatively in those codes. On the other hand, because the influencing analysis of the shear wave velocity on the ground seismic motion characteristics cannot be realized easily based on the ground model which has structural features along the vertical direction in the real study work, it is necessary using the mean shear wave velocity to represent the hardness of ground in the influencing analysis of soil layer shear wave velocity (the maximum dynamic shear modulus of soil) on the ground seismic motion characteristics. The mean shear wave velocity of the ground is used to represent the shear wave velocity characteristics of the ground as a whole (or the hardness of the whole ground) in the coupling influencing analysis of the ground soil layer thickness and shear wave velocity on the ground seismic motion characteristics:

$$v_{se} = \frac{d_0}{\sum_{i=1}^n (d_i/v_{si})}, \quad (25)$$

where v_{se} is the mean shear wave velocity of ground, d_0 is the thickness of soil ground, d_i is the thickness of soil layer i , v_{si} is the shear wave velocity of soil layer i , and n is the number of soil layers in the ground model.

When the thickness of the ground is a certain value, the influence of ground shear wave velocity (or the hardness of

whole ground) on the seismic motion characteristics of the ground is investigated through the method of adjusting the mean shear wave velocity of ground. When the mean shear wave velocity of ground is a certain value, the influence of soil layer ground thickness on the seismic motion characteristics of the ground is investigated through the method of adjusting the soil layer thickness of ground. In order to investigate whether the coupling influencing of the soil layer ground thickness and shear wave velocity on the ground seismic motion characteristics have existed and find the coupling influencing rule further more, lots of calculation work conditions are designed to do the ground seismic response analysis in which thickness and shear wave velocity of the ground model are changed simultaneously.

Range of soil layer ground thickness is 5~600 m, and the thickness interval of ground models is 20 m. Some uniform ground models whose shear wave velocity characteristics are represented by the mean shear wave velocity are established. When the mean shear wave velocity is above 500 m/s, thickness of the sublayer in the ground models is 8 m. When the mean shear wave velocity is below 500 m/s, thickness of the sublayer in the ground models is 5 m, and the minimum number of ground sublayers is 10. The value of mean shear wave velocity of the uniform ground is changed uniformly from 530 m/s which is the value of mean shear wave velocity of the above example super-deep overburden layer ground, and the range of soil layer ground mean shear wave velocity is 212~1223 m/s which covers the mean shear wave velocity range of normal overburden layer grounds basically. The critical state of the uniform soil layer ground is the uniform bedrock ground when the shear wave velocity is large enough, and the shear wave velocity interval of ground models is 53 m/s. The calculation work conditions of coupling influencing analysis of soil layer ground thickness and shear wave velocity are shown as Table 2, and it gives the values of thickness and shear wave velocity of the ground models.

The soil damping characteristics and the decay characteristics of soil dynamic shear modulus with dynamic strain increasing are the important representation of soil dynamic deformation characteristics, and they are related with the shear wave velocity of soil (or maximum dynamic shear modulus). But the dynamic modulus decay (or damping ratio increasing) coefficient k_1 and maximum damping ratio λ_{\max} representing the dynamic modulus decay characteristics and the damping characteristics of soil are assumed to be unchangeable with the increasing of dynamic shear strain in order to be easy for calculation and contrastive analysis. The value of soil modulus decay (or damping ratio increasing) coefficient k_1 is 10.0 fixedly, the soil maximum damping ratio λ_{\max} is 0.255 fixedly, and the natural soil density is 2.0 g/cm³ fixedly.

In order to be easy for calculation and contrastive analysis similarly, the inputting seismic motion of ground seismic response analysis is still the site earthquake of the example project.

4.2. Basic Calculation Results Representation. Seismic motion characteristics of the grounds in which thickness and

TABLE 2: Influence of soil ground thickness and shear wave velocity on acceleration magnified factors on ground free surface.

Soil ground thickness (m)	Surface																			
	Mean shear wave velocity of ground (m/s)																			
	212	265	318	371	424	477	530	583	636	699	742	795	848	901	954	1007	1060	1113	1166	1223
5	1.707	1.425	1.161	1.109	1.049	1.008	1.008	1.024	1.030	1.028	1.024	1.021	1.018	1.016	1.014	1.012	1.011	1.010	1.009	1.009
10	1.846	1.994	1.833	1.646	1.521	1.328	1.190	1.106	1.037	1.015	1.006	0.988	0.981	0.989	0.994	0.999	1.002	1.004	1.005	1.005
20	1.323	1.637	1.783	1.762	1.637	1.780	1.723	1.611	1.419	1.288	1.252	1.214	1.151	1.076	1.052	1.033	1.013	0.996	0.991	0.989
40	0.985	1.189	1.196	1.288	1.462	1.621	1.688	1.591	1.512	1.425	1.333	1.350	1.377	1.276	1.191	1.169	1.110	1.092	1.080	1.060
60	0.721	0.890	1.019	1.191	1.254	1.201	1.251	1.356	1.495	1.548	1.524	1.456	1.379	1.304	1.234	1.202	1.135	1.111	1.120	1.096
80	0.546	0.733	0.896	1.030	1.044	1.214	1.235	1.229	1.250	1.269	1.275	1.357	1.384	1.410	1.359	1.317	1.247	1.194	1.151	1.111
100	0.443	0.572	0.752	0.911	0.994	1.026	1.066	1.219	1.235	1.221	1.236	1.198	1.182	1.194	1.237	1.276	1.272	1.262	1.210	1.177
120	0.376	0.485	0.578	0.768	0.915	0.953	1.033	1.067	1.092	1.170	1.168	1.189	1.172	1.189	1.193	1.203	1.210	1.138	1.167	1.142
140	0.334	0.457	0.588	0.597	0.781	0.912	0.920	1.016	1.004	1.010	1.076	1.083	1.088	1.095	1.097	1.102	1.108	1.112	1.108	1.076
160	0.313	0.390	0.505	0.634	0.630	0.791	0.909	0.921	0.994	1.004	1.034	1.013	1.052	1.055	1.063	1.067	1.079	1.079	1.081	1.071
180	0.310	0.362	0.465	0.538	0.644	0.655	0.799	0.902	0.915	0.964	0.983	0.986	1.002	1.019	1.030	1.053	1.071	1.077	1.078	1.070
200	0.294	0.340	0.411	0.523	0.611	0.643	0.676	0.805	0.899	0.913	0.938	0.980	0.964	0.939	0.957	1.023	1.069	1.073	1.074	1.055
220	0.259	0.338	0.387	0.475	0.546	0.651	0.629	0.692	0.809	0.894	0.905	0.916	0.959	0.953	0.927	0.921	0.985	1.010	1.040	1.033
240	0.223	0.335	0.370	0.430	0.534	0.576	0.668	0.627	0.705	0.816	0.884	0.891	0.894	0.932	0.942	0.918	0.931	0.937	0.947	0.981
260	0.196	0.321	0.360	0.410	0.486	0.569	0.628	0.671	0.645	0.722	0.812	0.874	0.877	0.875	0.907	0.908	0.904	0.907	0.912	0.917
280	0.179	0.294	0.361	0.400	0.447	0.541	0.573	0.663	0.660	0.659	0.728	0.811	0.863	0.864	0.857	0.877	0.882	0.894	0.895	0.899
300	0.171	0.260	0.359	0.383	0.426	0.497	0.581	0.598	0.678	0.640	0.664	0.735	0.808	0.850	0.848	0.847	0.865	0.872	0.879	0.882
320	0.168	0.235	0.346	0.381	0.423	0.462	0.551	0.588	0.642	0.676	0.629	0.669	0.737	0.802	0.836	0.833	0.837	0.850	0.855	0.861
340	0.163	0.215	0.324	0.381	0.406	0.443	0.509	0.589	0.591	0.666	0.669	0.640	0.673	0.735	0.795	0.822	0.816	0.827	0.835	0.842
360	0.153	0.201	0.296	0.377	0.398	0.440	0.476	0.556	0.602	0.619	0.675	0.654	0.649	0.676	0.732	0.786	0.808	0.808	0.817	0.822
380	0.137	0.190	0.271	0.367	0.397	0.429	0.456	0.519	0.595	0.596	0.644	0.675	0.633	0.654	0.678	0.733	0.777	0.794	0.800	0.808
400	0.121	0.188	0.251	0.350	0.399	0.416	0.453	0.489	0.564	0.613	0.602	0.658	0.665	0.648	0.659	0.678	0.732	0.767	0.781	0.794
420	0.114	0.187	0.234	0.326	0.394	0.412	0.449	0.469	0.528	0.601	0.605	0.619	0.665	0.646	0.652	0.658	0.681	0.728	0.755	0.772
440	0.108	0.183	0.221	0.300	0.386	0.412	0.435	0.462	0.501	0.571	0.619	0.600	0.636	0.664	0.635	0.662	0.664	0.686	0.725	0.748
460	0.100	0.176	0.209	0.283	0.372	0.412	0.426	0.463	0.482	0.537	0.604	0.616	0.602	0.647	0.652	0.643	0.659	0.667	0.690	0.723
480	0.094	0.164	0.205	0.267	0.352	0.409	0.424	0.452	0.472	0.510	0.572	0.620	0.600	0.617	0.652	0.639	0.656	0.664	0.669	0.693
500	0.090	0.150	0.204	0.252	0.330	0.401	0.424	0.442	0.473	0.497	0.541	0.603	0.622	0.601	0.626	0.649	0.630	0.655	0.666	0.668
520	0.084	0.138	0.204	0.239	0.310	0.390	0.425	0.436	0.466	0.480	0.517	0.574	0.621	0.607	0.603	0.633	0.636	0.643	0.664	0.665
540	0.080	0.128	0.202	0.228	0.296	0.374	0.422	0.434	0.456	0.480	0.503	0.545	0.602	0.624	0.599	0.614	0.638	0.638	0.649	0.661
560	0.077	0.123	0.197	0.220	0.283	0.354	0.416	0.434	0.449	0.479	0.488	0.523	0.576	0.623	0.615	0.592	0.620	0.635	0.639	0.657
580	0.074	0.117	0.189	0.218	0.269	0.335	0.405	0.435	0.445	0.470	0.485	0.513	0.549	0.603	0.620	0.600	0.594	0.619	0.622	0.641
600	0.071	0.111	0.177	0.219	0.258	0.320	0.393	0.434	0.442	0.461	0.486	0.493	0.529	0.576	0.620	0.617	0.595	0.604	0.623	0.627

shear wave velocity are different are represented by the acceleration magnified factors on ground surface (based on the site earthquake of bedrock outcrop) and the distribution of acceleration magnified factors in grounds. Table 2 shows the acceleration magnified factors of the ground on the surface in which soil layer thickness and mean shear wave velocity are different. Influencing of the ground mean shear wave velocity on the distribution of acceleration magnified factors in the ground is shown in Figure 11 when the thickness of ground soil layer is a certain value, and influencing of the ground soil layer thickness on the distribution of acceleration magnified factors in the ground is shown in Figure 12 when the mean shear wave velocity of the ground is a certain value.

As shown in Table 2, the influencing rule of soil layer ground thickness and corresponding mean shear wave velocity on the acceleration response amplitude on ground free surface is complicated, and the influencing rules of soil layer thickness and soil layer mean shear wave velocity on the acceleration response amplitude of ground are coupled. Generally, the acceleration magnified factor on ground surface increases at first and then decreases with the increasing of soil layer shear wave velocity when the soil layer thickness is a fixed value, and the inflection wave velocity value in which acceleration magnified factor on ground surface changed from increasing to decreasing increases with the increasing of soil layer thickness; all these can be represented as yellow labels in Table 2; the acceleration

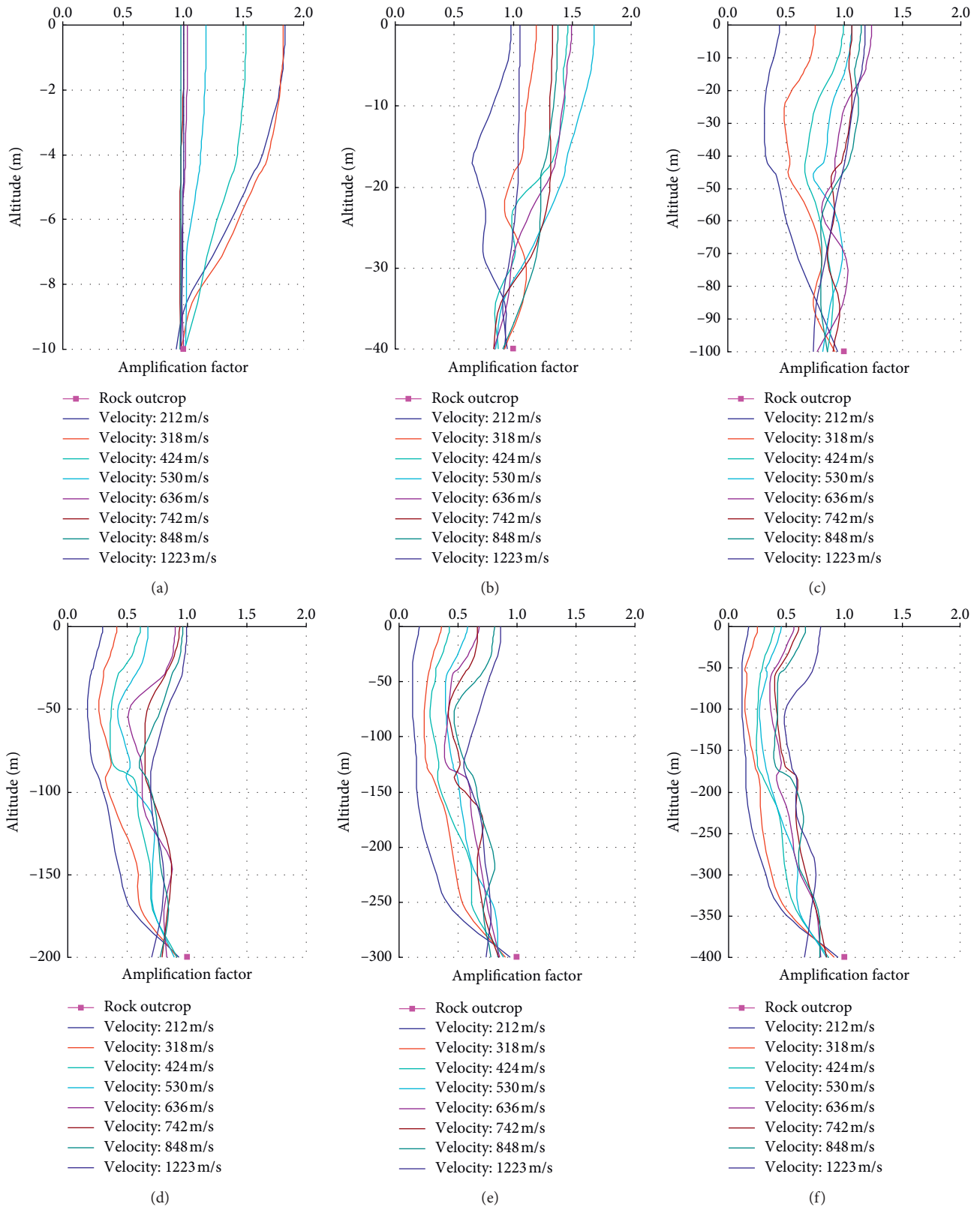


FIGURE 11: Continued.

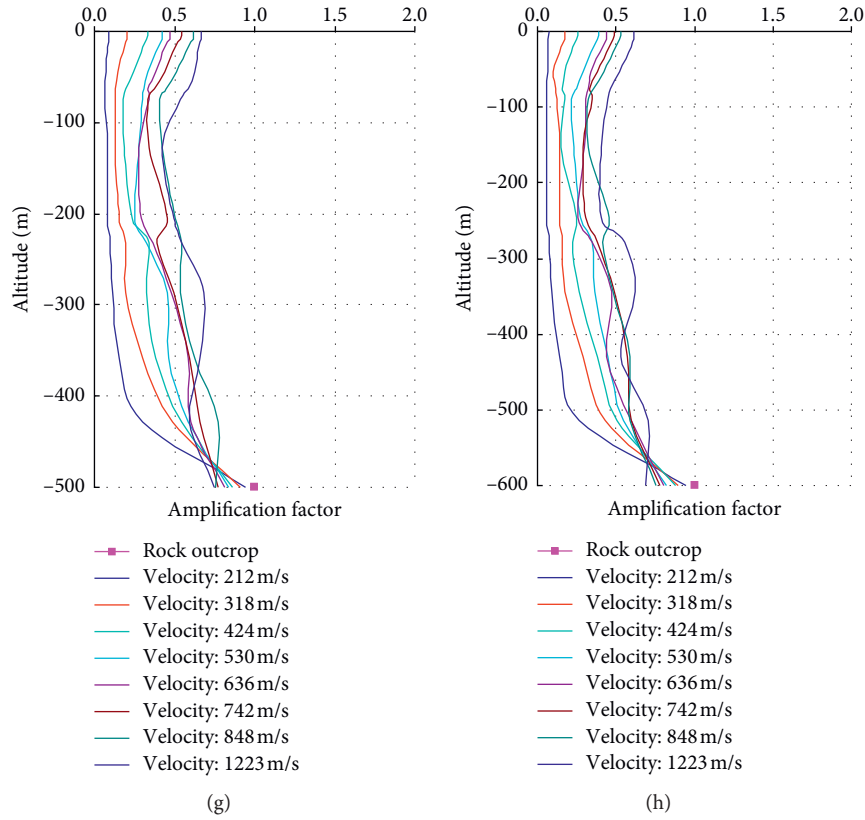


FIGURE 11: Influence of the ground mean shear wave velocity on the distribution of acceleration magnified factors in the ground when the thickness of ground is certain. (a) 10 m. (b) 40 m. (c) 100 m. (d) 200 m. (e) 300 m. (f) 400 m. (g) 500 m. (h) 600 m.

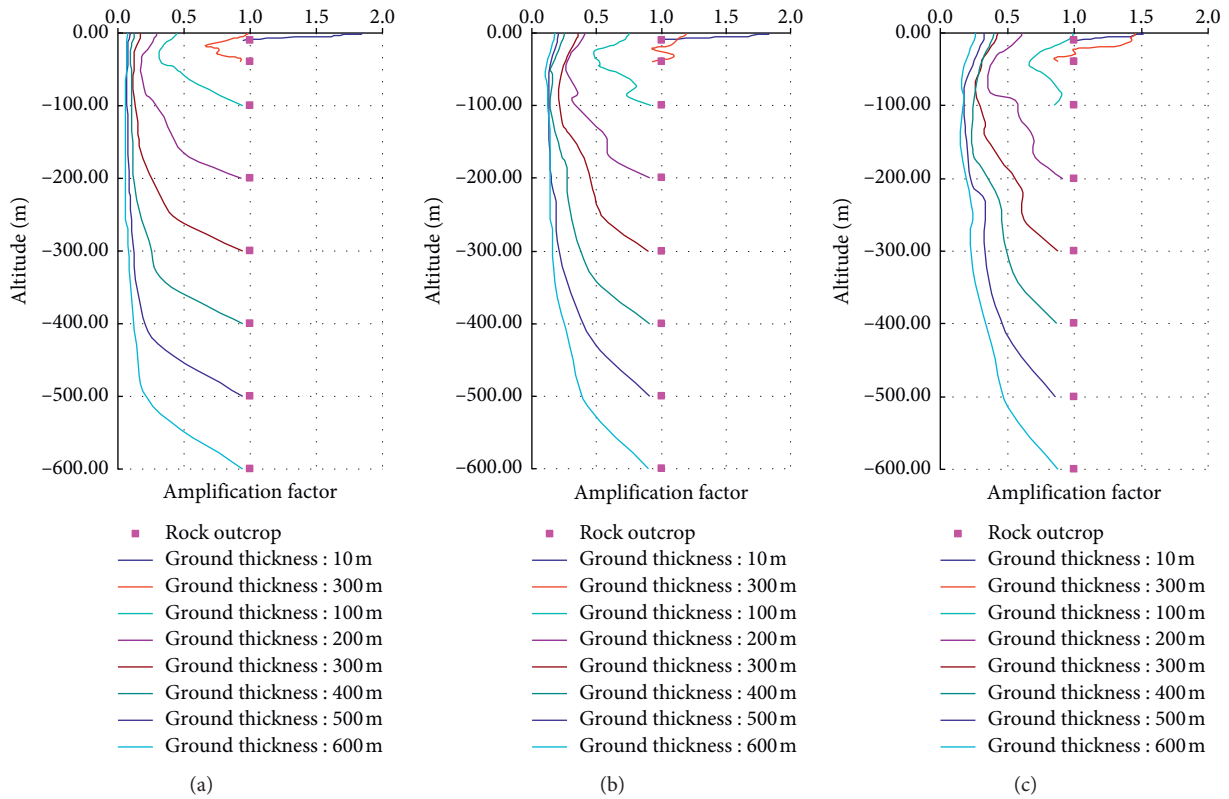


FIGURE 12: Continued.

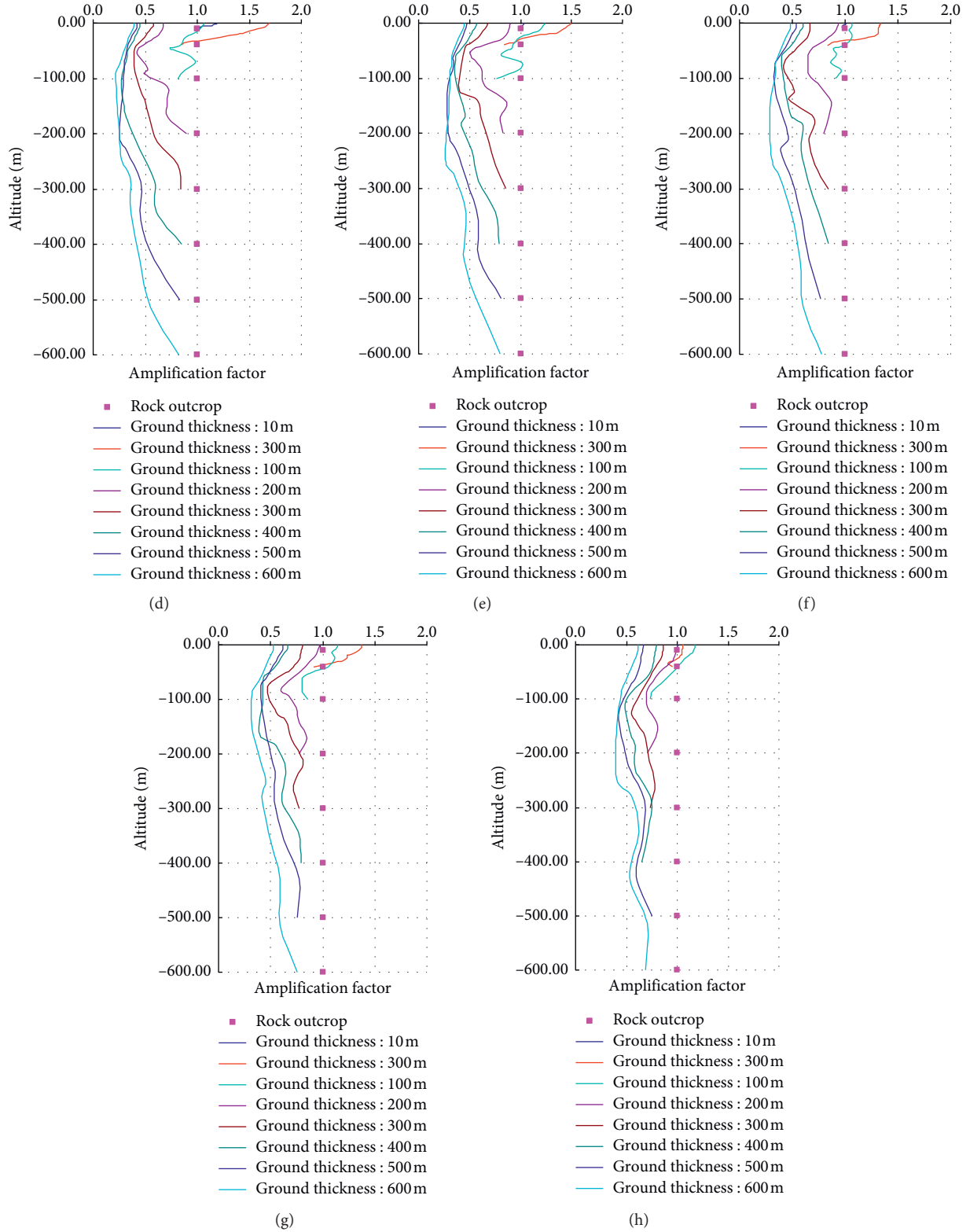


FIGURE 12: Influence of the ground thickness on the distribution of acceleration magnified factors in the ground when the mean shear wave velocity of the ground is certain. (a) 212 m/s. (b) 318 m/s. (c) 424 m/s. (d) 530 m/s. (e) 636 m/s. (f) 742 m/s. (g) 848 m/s. (h) 1223 m/s.

magnified factor on the ground surface increases at first and then decreases with the increasing of soil layer thickness when the soil layer shear wave velocity is a fixed value, and

the inflection thickness value in which acceleration magnified factor on ground surface changed from increasing to decreasing increases with the increasing of soil layer shear

wave velocity; this rule can be represented as blue labels in Table 2.

The influencing relation that the acceleration response amplitude of overburden layer ground increases at first and then decreases with the increase of ground mean shear wave velocity can be represented clearly by the distribution curves of acceleration magnified factor along the vertical direction in the grounds in which soil layer thicknesses are different as shown in Figure 11.

The acceleration magnified factor increases evenly as the altitude increases when the thickness of the soil layer ground is relatively small. But the influencing relation is different when the thickness of soil layer grounds is relatively large: the acceleration magnified factor decreases at first, then increases with the increase of altitude, and one phenomenon is found in those pictures, the distribution curves of acceleration magnified factors along the vertical direction in the grounds in which thicknesses are large present a state of irregular swinging when the ground mean shear wave velocity is relatively large.

Similarly, the influencing relation that the acceleration response amplitude of overburden layer ground increases at first and then decreases with the increasing of soil layer ground thickness can be represented clearly by the distribution curves of the acceleration magnified factor along the vertical direction in the grounds in which mean shear wave velocities are different, as shown in Figure 12.

In Table 2, (1) when the ground means shear wave velocity changes in the range of 212~1223 m/s, 1.707 is the corresponding maximum acceleration magnified factor of ground on the surface in which thickness is a certain value; (2) when the ground thickness changes in the range of 5~600 m, 1.846 is the corresponding maximum acceleration magnified factor of ground on the surface which means shear wave velocity is a certain value; (3) when the ground thickness changes in the range of 5~600 m, 0.985 is the corresponding inflexion of acceleration magnified factor of ground on the surface in which mean shear wave velocity is a certain value, and the inflexion of acceleration magnified factor is the demarcation point of acceleration response amplification and reduction on the ground surface according to the site earthquake of bedrock outcrop; (4) 1.780 is the coincidence point of (1) and (2); (5) 1.040 is the coincidence point of (1) and (3).

For the soil layer grounds in which mean shear wave velocities are relatively small, the seismic motion inputting from bedrock under the ground is magnified by the soil layer ground when the soil layer ground thickness is small relatively, and the seismic motion inputting from bedrock under the ground is reduced by the soil layer ground when the soil layer ground thickness is large relatively. But, for the soil layer grounds in which mean shear wave velocity value exceeds a certain level, the seismic motion inputting from bedrock under the ground is almost invariant along the vertical direction in ground regardless of the size of soil layer thickness, and the seismic motion inputting from bedrock under the ground is not affected obviously by the soil layer ground.

Characteristics. Variation rule of the acceleration magnified factors on ground surface with the thickness of ground is shown in Figure 13 when the mean shear wave velocity of ground is different. Figure 14 shows the comparison of the inflection point of the site with different shear wave velocities and the site thickness on the free surface acceleration magnification, including the extreme point of acceleration response and the critical point of magnification and reduction of ground vibration relative to bedrock input ground motion.

Variation rule of the acceleration magnified factors on ground surface with the mean shear wave velocity of ground is shown in Figure 15 when the thickness of ground is different. Comparison of the inflection points which are the mean shear wave velocity value corresponding the maximum value of acceleration magnified factor on ground surface is shown in Figure 16.

As shown in Figures 13 and 14 and Table 2, for the ground which means shear wave velocity is a certain value, the acceleration magnified factor on ground surface increases at first and then decreases with the increase of ground thickness, the corresponding inflection thickness increases with the increasing of ground mean shear wave velocity, and these inflection thickness values are in the range of 10~100 m. When the ground thickness is over the inflection thickness value, the acceleration magnified factor on the ground surface decreases with the increase of the ground thickness, and it is lesser than 1 when the ground thickness reaches one critical thickness which is the thickness that acceleration response amplitude on the ground surface is magnified or reduced to the inputting seismic motion from bedrock under the ground. The critical thickness of ground increases with the increase of ground mean shear wave velocity, and the maximum value of ground critical thickness is not larger than 240 m. In other words, for the uniform soil layer ground, the acceleration response amplitude on the ground surface will not be larger than the amplitude of seismic motion inputting from bedrock under the ground when thickness of the ground is over 240 m, and the amplifying effects of soil layer ground to the seismic motion inputting from bedrock under the ground is more obvious when the thickness of ground soil layer is in the range of 10~100 m.

As shown in Figures 15 and 16 and Table 2, for the ground in which soil layer thickness is a certain value, the acceleration magnified factor on ground free surface increases at first and then decreases with the increase of ground mean shear wave velocity, and the acceleration response amplitude is the biggest when the ground mean shear wave velocity is the inflection shear velocity value. The inflection shear velocity value increases with the increase of ground thickness, as shown in Table 2. But, when the ground thickness is over a certain value, the acceleration magnified factor on ground surface increases monotonously with the increasing of ground mean shear wave velocity, and the maximum value of acceleration magnified factor is obtained when the ground mean shear wave velocity is the biggest; abovementioned inflection shear velocity value has no longer existed. As the description mentioned before, the

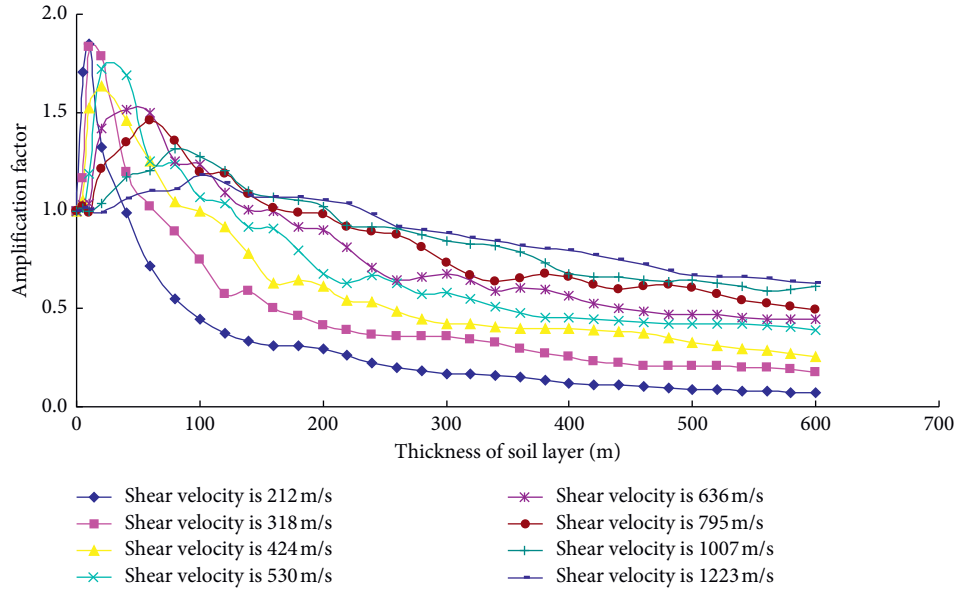


FIGURE 13: Variation rule of the acceleration magnified factors on the ground surface with the thickness of ground when the mean shear wave velocity of the ground is different.

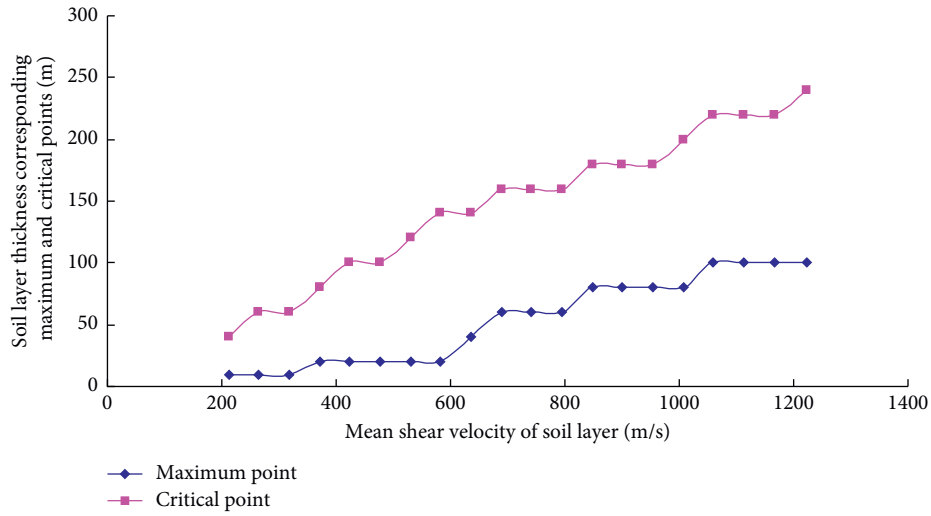


FIGURE 14: Comparison of the ground thickness corresponding the maximum points and critical points of acceleration magnified factor on the ground surface when the mean shear wave velocity of the ground is different.

acceleration response amplitude on the uniform soil ground surface will not be larger than the amplitude of seismic motion inputting from bedrock under the ground when the thickness of ground is over one certain value, and the maximum value of acceleration magnified factor on ground surface should be obtained when the ground mean shear wave velocity is the biggest. When the mean shear wave velocity of ground is big enough that reaches the level of normal bedrock layer; the vibration state on ground surface is as same as the site earthquake on bedrock outcrop.

4.4. Some Discussion on the Abovementioned Analysis Results. All abovementioned analysis and corresponding conclusions are obtained based on the ground seismic response analysis

calculation results in which calculation models are the uniform soil layer ground models, some calculation parameters are presumed to be fixed, and the inputting seismic motion is one specific site earthquake. Those factors, such as the calculation model, the calculation parameter, and the inputting seismic motion should have an important effect on the calculation results, such as the above maximum value, critical value, and some specific values of the acceleration magnified factor. But, all these simplifications and assumptions are not against the abovementioned qualitative conclusions which are based on the coupling influencing analysis of soil ground thickness and soil ground mean shear wave velocity on the ground seismic motion characteristics, and it can be verified by the other study results of the authors in [29–31].

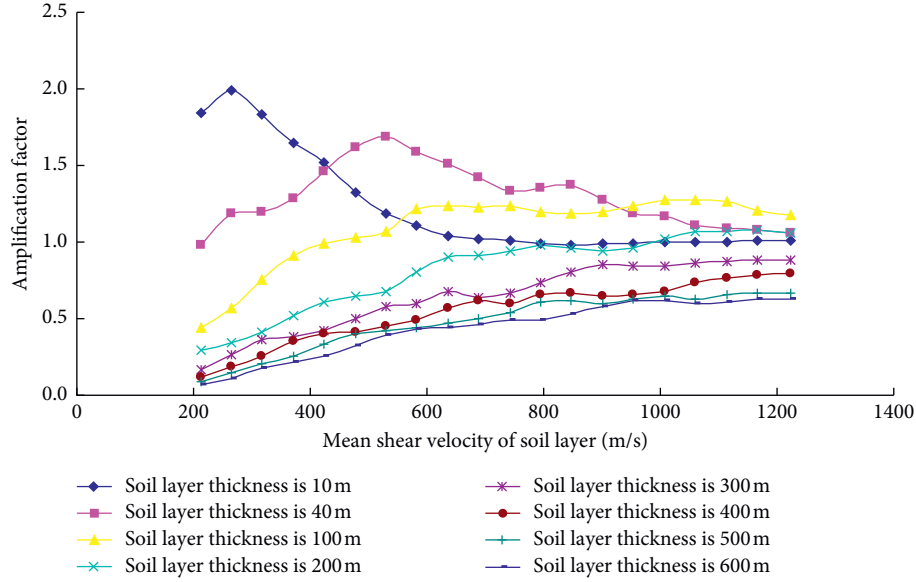


FIGURE 15: Variation rule of the acceleration magnified factors on the ground surface with the mean shear wave velocity of the ground when the thickness of the ground is different.

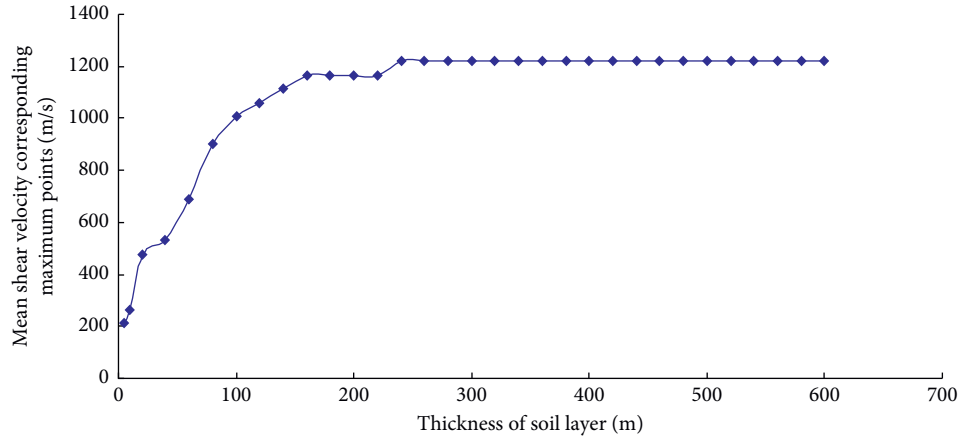


FIGURE 16: Comparison of the ground mean shear wave velocity corresponding the maximum points of acceleration magnified factor on the ground surface when the thickness of the ground is different.

For the dynamic deformation parameters of soil in ground, it produces certain influence on the calculation results that assumes the modulus decay (or damping ratio increasing) characteristic parameters and the maximum damping ratio of soils are not associated with the shear wave velocity (or maximum shear modulus) of soils. The acceleration magnified factor on ground surface and the distribution of acceleration magnified factors in the soil layer ground should be close to the horizontal half-space bedrock layer when the mean shear wave velocity of ground is large enough, that is, the limited ideal state of ground seismic response analysis, considering the influence of ground shear wave velocity. But, because the soil modulus decay (or damping ratio increasing) coefficient k_1 and the maximum damping ratio λ_{\max} have been assumed to be not changeable with the shear wave velocity and the real dynamic characteristic parameters used in calculation are different from the

ideal bedrock, the calculation results are different from the ideal state in a certain extent normally. It is not difficult to find that the limited ideal state should exist based on the changing trend of the abovementioned calculation results, and the changing trend of the abovementioned calculation results shows that the calculation results and analysis conclusions should be reliable in this paper.

5. Conclusion

Taking a real super-deep overburden layer ground which is the foundation of one earth-rock fill dam in China for example, example analysis for seismic motion characteristics of the super-deep overburden layer ground has been performed in the paper. Influencing rules of the inputting seismic motion characteristics and the seismic motion inputting location on the ground seismic response analysis

results have been investigated after the basic analysis of ground seismic response characteristics. Furthermore, coupling influencing rules of the ground soil layer thickness and the ground shear wave velocity on the ground seismic motion characteristics have been studied deeply based on the seismic response analysis of ground models in which soil layer thickness and mean shear wave velocity are adjusted in a specific range. The main study conclusions are as follows:

- (1) The horizontal layer shearing method for ground seismic response analysis which is based on fluctuation theory can consider the superposition effect of incident wave and reflected wave in the ground and the influence of deep soil layer on the natural vibration characteristics of bedrock surface under the ground; it is applicable for the ground seismic response analysis of horizontally stratified super-deep overburden layer ground.
- (2) The seismic response analysis for a super-deep overburden layer which is the foundation of one earth-rock fill dam in China is performed based on the soil dynamic characteristic parameters by field situ testing and soil laboratory testing. Inputting seismic motion of the ground response analysis is the site earthquake which is the vibration progress of the horizontal half-space bedrock layer surface based on the region earthquake hazard analysis. The calculation results of ground seismic response analysis show that the super-deep overburden layer ground has significant reducing effects on the seismic motion inputting from bedrock under the ground, and the long-period components of acceleration response spectra change more prominent on ground surface which is a disadvantage for the antiseismic performance of tower structures.
- (3) Seismic motion transmitting characteristics of the super-deep overburden layer ground is influenced by the seismic motion characteristics of inputting earthquake greatly. Magnified effects of the super-deep overburden layer ground on the seismic motion inputting from bedrock reduces with the increasing seismic motion amplitude because of the dynamic deformation nonlinear characteristics of soils. But the magnified effects of super-deep overburden layer ground on the long-period components of inputting seismic motion are enhanced with the increasing of the seismic motion amplitude oppositely.
- (4) Results of the ground seismic response analysis for super-deep overburden layer are influenced greatly by the location of seismic motion inputting interface. It will overvalue the magnified effects of overburden soil layer ground on the seismic motion inputting from bedrock greatly, taking the interface of 500 m/s shear wave velocity as the seismic motion inputting interface directly.
- (5) The acceleration response amplitude of uniform overburden layer ground increases at first and then decreases with the increase of ground shear wave velocity when the ground soil layer thickness is a certain value. There is an inflexion point of ground shear wave velocity that the acceleration response amplitude of the ground is the strongest. But this inflexion point of shear wave velocity does not exist when the ground soil layer thickness is over a certain value, and the acceleration response amplitude of the ground increases monotonously with the increase of ground shear wave velocity.
- (6) The influencing rules of ground soil layer thickness and shear wave velocity on the seismic motion characteristics of ground are coupled: the critical ground soil layer thickness of the strongest ground seismic response is influenced by the ground mean shear wave velocity, and also the critical ground shear wave velocity of the strongest ground seismic response is influenced by the ground soil layer thickness.

Data Availability

The data used to support the findings of this study are included within the article.

Disclosure

The funding sponsors had no role in the design of the study; in the collection, analyses, or interpretation of data; in the writing of the manuscript; or in the decision to publish the results.

Conflicts of Interest

The authors declare no conflicts of interest.

Authors' Contributions

Long Wang wrote the original draft; Zheng-quan Yang reviewed and edited the article; Jian-ming Zhao conceptualized the study and curated the data; Xiao-sheng Liu did formal analysis and developed the methodology; Yan-feng Wen supervised and validated the study.

Acknowledgments

This work was financially supported by the National Key Research and Development Program of China (2017YFC0404902); the National Natural Science Foundation of China under Grant no. 51509272; the Public Service Sector R&D Project of Ministry of Water Resource of China (Grant no. 201501035); and the Special Scientific Research Foundation of China Institute of Water Resources and Hydropower Research (GE0145B292017).

References

- [1] Z.-Q. Yang, *Study on Dynamic Analysis Methods Verification Using Shaking Table Model Test and Seismic Motion Input of Earth-Rock Fill Dam*, China Institute of Water Resources and Hydropower Research, Beijing, China, 2011.
- [2] C.-G. Sun and C.-K. Chung, "Assessment of site effects of a shallow and wide basin using geotechnical information-based spatial characterization," *Soil Dynamics and Earthquake Engineering*, vol. 28, no. 12, pp. 1028–1044, 2008.
- [3] Z.-Q. Yang, X.-S. Liu, X.-G. Wang, and J.-M. Zhao, "An overview on research of ground motion inputting for earth-rock fill dam," *Journal of China Institute of Water Resources and Hydropower Research*, vol. 11, no. 1, pp. 27–33, 2013.
- [4] Z.-J. Wang, H.-Y. Liu, T. Meng, and C.-U. Zhou, "Effect of seismic input method on dynamic response of high-panel rockfill dam on deep overburden," *Journal of Water Conservancy and Construction Engineering*, vol. 18, no. 3, pp. 77–81, 2013.
- [5] Y. Ting and L. Shao, "Dynamic characteristics of deep river bed covering dam foundation with soft soil layer," *Study Geotechnical Mechanics*, vol. 41, no. 1, pp. 267–277, 2020, (in Chinese).
- [6] H.-C. Han, Z.-J. Wang, C.-G. Zhou, T. Meng, and Y. Xiang, "Effect of near fault pulse earthquake on dynamic response of high earth-rockfill dam on deep overburden," *Water Conservancy and Hydropower Technology*, vol. 50, no. 3, pp. 79–84, 2013, (in Chinese).
- [7] Z.-Q. Yang, X.-S. Liu, J.-M. Zhao, Z.-H. Tian, and Y.-S. Yang, "Analysis of site seismic response considering the structural characteristics of deep overburden," *Journal of Hydropower*, vol. 34, no. 1, pp. 175–182, 2015, (in Chinese).
- [8] D.-Y. Zhu, J.-G. Dong, and Q.-B. Kuang, "Analysis on seismic response of earth-rock dam with deep overburden layer," *Northeast Water Conservancy and Hydropower*, vol. 29, no. 11, pp. 51–52, 2011, (in Chinese).
- [9] X.-N. Wang, X.-T. Zhang, W.-X. Dong, and Y.-Z. Yu, "Analysis of dynamic response to strong shock of core wall rockfill dam with deep," *Overburden Journal of Seismic Engineering*, vol. 37, no. 2, pp. 349–354, 2015, (in Chinese).
- [10] Z.-Q. Yang, Q.-W. Liu, X.-S. Liu, Y.-S. Yang, and N. Chen, "Study on dynamic deformation and strength characteristics of fine soil in super-deep overburden layer by triaxial tests," *China Earthquake Engineering Journal*, vol. 36, no. 4, pp. 824–831, 2014, (in Chinese).
- [11] I. M. Idriss and H. B. Seed, "Seismic response of horizontal soil layers," *Journal of the Soil Mechanics and Foundations Division*, vol. 94, no. 4, pp. 1003–1031, 1968.
- [12] R. Pyke, "Nonlinear soil models for irregular cyclic loadings," *Journal of Geotechnical and Geoenvironmental Engineering*, ASCE, vol. 106, no. 11, pp. 1277–1288, 1980.
- [13] Y. M. A. Hashash and D. Park, "Non-linear one-dimensional seismic ground motion propagation in the Mississippi embayment," *Engineering Geology*, vol. 62, no. 1–3, pp. 185–206, 2001.
- [14] D.-D. Jin, G.-X. Chen, and F.-f. Dong, "Large-scale two-dimensional nonlinear FE analysis on PGA amplification effect with depth and focusing effect of Fuzhou Basin," *Journal of Central South University*, vol. 21, no. 7, pp. 2894–2903, 2014.
- [15] C. Frischknecht and J. J. Wagner, "Seismic soil effect in an embanked deep alpine valley: a numerical investigation of two-dimensional resonance," *Bulletin of the Seismological Society of America*, vol. 94, no. 1, pp. 171–186, 2004.
- [16] Z.-J. Shen, *Selected Works on Soil Mechanics of Zhu-Jiang SHEN*, Tinghua University Press, Beijing, China, (in Chinese), 2005.
- [17] J. Lermo, M. Rodríguez, and S. K. Singh, "The Mexico earthquake of september 19, 1985-natural period of sites in the valley of Mexico from microtremor measurements and strong motion data," *Earthquake Spectra*, vol. 4, no. 4, pp. 805–814, 1988.
- [18] J. Penzien and M. Watabe, "Characteristics of 3-dimensional earthquake ground motions," *Earthquake Engineering & Structural Dynamics*, vol. 3, no. 4, pp. 365–373, 1974.
- [19] W. B. Joyner, R. E. Warrick, and T. E. Fumal, "The effects of Quaternary alluvium on strong ground motion in the Coyote Lake, California earthquake of 1979," *Bulletin of the Seismological Society of America*, vol. 71, no. 4, pp. 1333–1349, 1981.
- [20] D. M. Boore and W. B. Joyner, "Estimation of ground motion at deep-soil sites in eastern North America," *Bulletin of the Seismological Society of America*, vol. 81, no. 6, pp. 2167–2185, 1991.
- [21] A.-W. Elgamal, M. Zeghal, E. Parra, R. Gunturi, H. T. Tang, and J. C. Stepp, "Identification and modeling of earthquake ground response - I. Site amplification," *Soil Dynamics and Earthquake Engineering*, vol. 15, no. 8, pp. 499–522, 1996.
- [22] E. M. Rathje, A. R. Kottke, and W. L. Trent, "Influence of input motion and site property variabilities on seismic site response analysis," *Journal of Geotechnical and Geoenvironmental Engineering*, vol. 136, no. 4, pp. 607–619, 2010.
- [23] M. K. Koçkar, H. Akgün, and E. M. au, "Evaluation of site conditions for the Ankara Basin of Turkey based on seismic site characterization of near-surface geologic materials," *Soil Dynamics and Earthquake Engineering*, vol. 30, no. 1–2, pp. 8–20, 2010.
- [24] G.-X. Chen and J.-H. Chen, "A study on the influence of seismic wave inputting interface on the earthquake response of deep soft sites," *World Earthquake Engineering*, vol. 21, no. 2, pp. 36–43, 2005, (in Chinese).
- [25] L. A. Wald and J. Mori, "Evaluation of methods for estimating linear site-response amplifications in the los angeles region," *Bulletin of the Seismological Society of America*, vol. 90, no. 6B, pp. S32–S42, 2000.
- [26] S. Castellaro, F. Mulargia, and P. L. Rossi, "Vs30: proxy for seismic amplification?" *Seismological Research Letters*, vol. 79, no. 4, pp. 540–543, 2008.
- [27] C. Architecture and B. Press, "Code for Seismic Design of Buildings (GB 50011-2010)," 2010.
- [28] China Water Resource and Hydro-Powder Press, "Specification for Seismic Design of Hydraulic Structures (SL 203-97)," 1997.
- [29] Z.-Q. Yang, X.-S. Liu, J.-M. Zhao, Z.-H. Tian, and Y.-S. Yang, "Study on ground seismic response analysis considering the structural characteristics of deep overburden layer," *Journal of Hydroelectric Engineering*, vol. 33, no. 1, pp. 175–182, 2015, (in Chinese).
- [30] Z.-Q. Yang, X.-S. Liu, J.-M. Zhao, J.-Q. Zhao, N. Chen, and Q.-W. Liu, "Study on ground seismic response analysis of deep overburden layer," pp. 487–492, 2011.
- [31] Z.-Q. Yang, X.-S. Liu, X.-P. Zhou, J.-M. Zhao, and Y.-S. Yang, "Study on ground seismic motion characteristics of deep overburden layer," pp. 11487–492, 2013.

Research Article

Seismic Behavior of Hybrid Frame Joints between Composite Columns and Steel Beams

Liusheng Chu ¹, Qingze Li ¹, Jun Zhao ² and Danda Li ³

¹School of Civil Engineering, Zhengzhou University, Zhengzhou, Henan, China

²School of Mechanics and Safety Engineering, Zhengzhou University, Zhengzhou, Henan, China

³School of Natural and Built Environments, University of South Australia, Adelaide, SA, Australia 2811

Correspondence should be addressed to Jun Zhao; zhaoj@zzu.edu.cn

Received 13 April 2020; Revised 8 May 2020; Accepted 25 November 2020; Published 8 December 2020

Academic Editor: Xiaonong Guo

Copyright © 2020 Liusheng Chu et al. This is an open access article distributed under the Creative Commons Attribution License, which permits unrestricted use, distribution, and reproduction in any medium, provided the original work is properly cited.

This study presents experimental and numerical study on cyclic behavior of SRC composite columns-steel beam joints. The pseudostatic experiments were carried out on four samples with different axial loads. X-shaped shear reinforcement was added in the sample no. 4 in order to investigate its effect on the crack resistance in the joint core area. Low-frequency cyclic load was applied at beam ends to simulate the earthquake action. The failure characteristics, hysteretic behavior, stiffness degradation, shear resistance, and displacement ductility were investigated. Experimental results indicated that the failure mode of the joints was mainly shear failure, and the composite joints showed excellent seismic behavior with higher capacity and good ductility and energy dissipation ability. X-shaped shear reinforcement performed well to increase the concrete crack resistance. Shear forces from both experimental test and theoretical analysis were compared, and suggestions were given on modification of theoretical formulas. Simulation using the ABAQUS model showed good results that agreed well with the test results. Steel stress distribution and damage development were analyzed in the model. More parameters of web thickness, stiffener thickness, concrete strength, and stirrups and their influence on shear resistance were studied.

1. Introduction

SRC composite columns, a typical type of composite columns with structural steel and reinforcing steel bars embedded in reinforced concrete, having both advantageous properties of structure steel and reinforced concrete, have become widely used in high-rise buildings, large-span bridges, and transmission towers [1–4]. External concrete provides protection and restraint to internal steel and hence improves the stability of steel components. On the other hand, the existence of internal steel helps to improve stiffness and strength of column. Overall, SRC composite columns showed enhanced stiffness, stronger energy-absorption capacity, and better ductility than traditional reinforced concrete structures and steel structures. In building structure design, energy-absorption ability is also the basic requirement of its seismic performance [5].

As column-beam joints are critical for overall frame structure's strength and stiffness capacity, column-beam joints failure is the most common and direct reason for structure failure under seismic load. Overall structure's nonlinear seismic performance will be influenced by joints behavior since they are crucial parts in load-transfer and also moment distribution.

How to improve seismic performance and design procedure of column-beam joints has attracted great attention in current research. In these composite columns-steel-beam joints, the property difference between beams and columns has made the analysis more complicated. Some investigations were undertaken, and results were reported by some researchers [6–12]. Chen et al. [6] investigated shear capacity of deep structure steel-concrete beams and proposed analytical models. Cheng et al. [7] reported that load capacity of precast SRC column-beam joints was three times that of

traditional reinforced concrete joints. Chen et al. [8] proposed Park-Ang modified model for seismic performance evolution, which showed good simulation results in SRC composite joints. Xiang et al. [9] conducted tests on seismic performance on SRC joints with composite columns consisting of T-shaped structural steel section and results showed satisfying shear resistance, ductility, and overall seismic capacity. Chu et al. [10] carried out tests on the cyclic behavior of steel beam-concrete encased steel column joints with three different slab widths. Numerical simulation showed that the slab width and thickness had an important influence on the load-carrying capacity of such joints. Tao et al. [11] carried out tests on four joints specimens and, based on results from load-deflection curves, shear capacity in joint core area, strength, and stiffness degradation and ductility, they reported that seismic capacity can be improved through proper control of design to obtain better failure modes. Seo et al. [12] analyzed influencing factors on effective width of SRC column-beam joints, through comparing design methods of Deierlein, and proposed a modified formula.

In practical design, joints failure or damage is the main reason for overall building collapse or damage, even if the design is following “strong joints and weak elements” rule. Therefore, there is a need to have deep investigation on seismic performance of SRC composite columns-steel-beams joints. In this paper, the pseudostatic experiments were carried out on four specimens. Axial compression load was the main parameter of this research. In addition, based on common crack development mode in core joint area, a new joint type was proposed using X-shaped reinforcing bars in core area and discussions were developed on whether this new joint can delay concrete cracking in the joint area. Then FEM simulation was carried out using ABAQUS model and, through comparison between experimental results and simulation data, suggestions on shear capacity formulas were given.

2. Experimental Program

2.1. Specimen. The SRC composite columns-steel-beam joints studied in this paper followed “weak joints” rule and expected failure mode was shear failure at joint core area. Both structural steel elements in column and beams were in H-shaped sections, which were welded up to form sections. Due to the thin structural steel and other experimental condition limitations, welded joints were adopted for this research. Varying axial pressure ratio was applied to specimens SRC-1, SRC-2, and SRC-3 to investigate its influence on mechanical behavior of composite columns-steel-beam joints. With regard to SRC-4, X-shaped reinforcing bars were applied at core joint area to investigate if they could help to improve anticrack performance of concrete in core joint area; apart from that, all other details of SRC-4 were the same as the other three specimens.

The structural steel used in this paper was Q235 B graded with yield strength of 297 MPa and ultimate strength of 416 MPa. Vertical reinforcing bars surrounding structural steel columns were HRB335 graded with yield strength of

379 MPa and ultimate strength of 534 MPa. The stirrup bars in column were HPB300 graded with yield strength of 316 MPa and ultimate strength of 432 MPa. C30 concrete was adopted and material properties from concrete test result are listed in Table 1. The geometry details of the specimens were as follows: column height of 1.8 m, beam span of 2.4 m, concrete column cross section size of 240 mm × 240 mm, structural steel column size of 136 mm × 120 mm × 8 mm × 8 mm, and structural steel beam size of 224 mm × 100 mm × 4 mm × 4 mm. Table 2 lists the steel reinforcement details of four specimens and Figure 1 shows the geometry of the specimen and reinforcement/steel details of the joints from four specimens. X-shaped reinforcement bars of specimen SRC-4 were HPB300, which was arranged along the diagonal direction of the joint core area, as shown in Figure 2.

2.2. Loading Schemes and Measurements. Figure 3 shows test setup for specimens. Lateral supporting elements were used on top of column to avoid column instability during loading process. High-strength bolts and supporting beams were adopted at bottom end of column. Axial load was applied on top of columns via hydraulic loading. At two ends of beams, cyclic load was applied through two actuators to simulate the low-frequency cyclic seismic load. The applied load was in the form of combined displacement-control and force-control cyclic loads. The loading scheme followed instructions from JGJ101-96 [13], which is shown in Figure 4.

Prior to yield capacity of P_y and when deformation was very small, force-control loading was used and load was applied at increment of $0.2 P_y$. After the specimen reached the calculated yield load, loading was applied under displacement-control, using the horizontal displacement of beam ends Δ at calculated yield capacity as initial displacement for loading. Load was applied at increment of Δ and repeated three times at each loading level until loading bearing capacity dropped below 85% of ultimate capacity or when specimen is severely damaged. Downward load was using positive sign. During loading process, the loads at two ends of beam were in opposite directions. The main measurements consisted of applied load, beam end displacement, strain distribution, and deformation of joints. Figure 5 shows strain gauges distribution on column longitudinal and stirrup reinforcements, on beam web and column web in joint core area, and on column flanges and beam flanges.

3. Test Results and Analysis

3.1. Failure Modes of SRC-1. Figure 6 shows the crack development at different stage of loading. The first minor crack appeared when loading reached 21 kN. Beam flange reached yield strain at load of 35 kN and then beam started yielding which indicated the start of elastic-plastic stage. After the point displacement-controlled load was applied, crack started widening up at the third increment of load. Main cracks formed in the diagonal direction in joint core area. When the load reached the fourth increment and the first cycle, concrete started spalling in the joint core area and the

TABLE 1: Concrete material properties.

Sample ID	f_{cu}^k (MPa)	f_{ck} (MPa)	f_{tk} (MPa)	E_c (MPa)
H1	31.1	20.8	2.1	30165
H2	31.6	21.2	2.1	30333
H3	31.9	21.3	2.1	30419
Average	31.6	21.1	2.1	30306

TABLE 2: Cross section and steel reinforcement details.

Sample ID	Steel ratio in section (%)	Longitudinal bars in column	Reinforcement ratio (%)	Stirrup bars in column	Stirrup bars in joint	X-shaped reinforcing bars	Axial pressure ratio
SRC-1	5	4-12	0.83	·8@100	·8@60	N/A	0.1
SRC-2	5	4-12	0.83	·8@100	·8@60	N/A	0.4
SRC-3	5	4-12	0.83	·8@100	·8@60	N/A	0.7
SRC-4	5	4-12	0.83	·8@100	·8@60	Yes	0.4

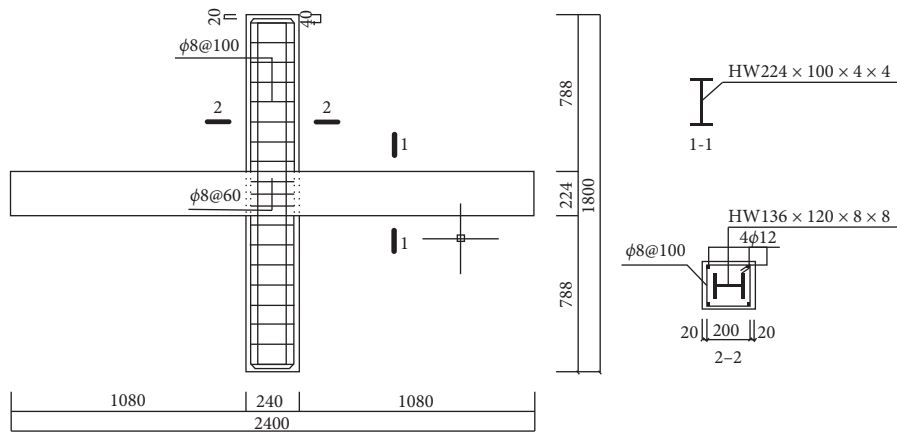


FIGURE 1: Specimen geometry and reinforcement/steel details.

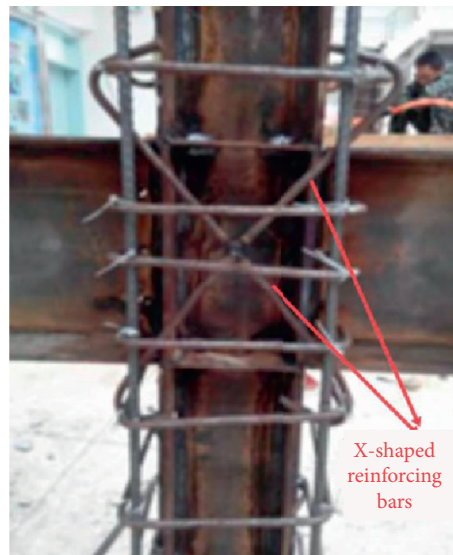


FIGURE 2: Details of X-shaped reinforcing bars and stirrups.

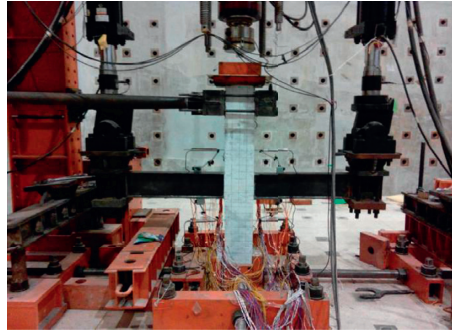


FIGURE 3: Test setup.

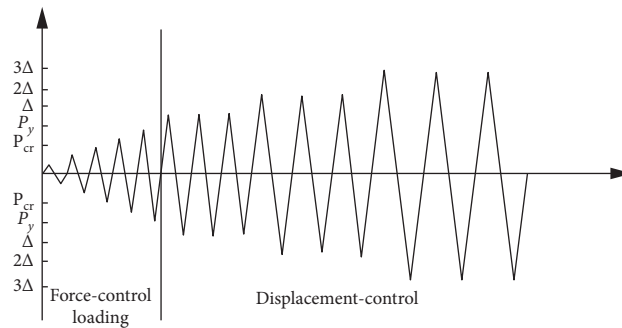


FIGURE 4: Loading scheme for cyclic tests.

rear bottom flange of the beam on left side of joint started buckling. In the second cycle, linear variable differential transformer (LVDT) dropped. When the load reached the fifth displacement increment and, in the first cycle, the front bottom flange of the beam on left side of joint started buckling, concrete started spalling in big segments and then stirrup was exposed. When load bearing capacity dropped to 85% of peak value and all cycles in fifth displacement increment finished, the test was stopped.

SRC-2 and SRC-4 showed similar failure modes to that of SRC-1, and buckling also occurred on top flange of beams. Figure 7 shows buckling on beam top flanges in SRC-4 and final failure mode of the specimen. In specimens SRC-2 and SRC-4, buckling did not appear in beam webs area and shear failure is the main failure mode of concrete in the joint core area.

With regard to SRC-3 joint, when the load reached the third displacement increment, buckling appeared on top flange of beam, which was on right side of joint. When it reached fifth increment of displacement, buckling on top flange of the beam was worsened and severe buckling in beam web area occurred (Figure 8). Due to high axial compression ratio in this specimen, the shear force in beam webs (close to joint area) was quite big; these made the specimen reach yield state very quickly. The main failure modes consisted of buckling at beam ends and shear failure at joint core area. The failure phenomena and failure modes of all specimens are shown in Table 3.

3.2. Hysteretic Curves. Figures 9–12 show hysteretic curves and envelope curves for four specimens at loading point on right-hand side of joint. All four specimens showed full hysteretic curves, which indicates good energy dissipation ability of these composite column-steel-beam joints. SRC-3 showed most full hysteretic curves, which indicates that, with higher axial compression ratio, structural steel's strong mechanical properties could be used to most potential and hence improved specimens' plastic deformation ability. The shapes of envelope curves and hysteretic curves were very close for both SRC-2 and SRC-4, which indicates that introducing X-shaped reinforcing bars can only improve crack resistance of concrete but has no impact on other mechanical performances of joints.

3.3. Envelope Curves. From Figures 9–12, it can be seen that envelope curve is in S-shape, which indicates that during loading all specimens underwent four stages: elastic stage—plastic stage—ultimate loading—final failure. Table 4 lists characteristic loading of four specimens. Combining with Figure 13, it shows positive displacement, SRC-3 showed slower increase on envelope curve compared to SRC-1 and SRC-2, while after reaching ultimate capacity, the envelope curves for SRC-1, SRC-2, and SRC-3 were very close and all see a flatter descending curve. For negative displacement, SRC-3 showed faster increase on

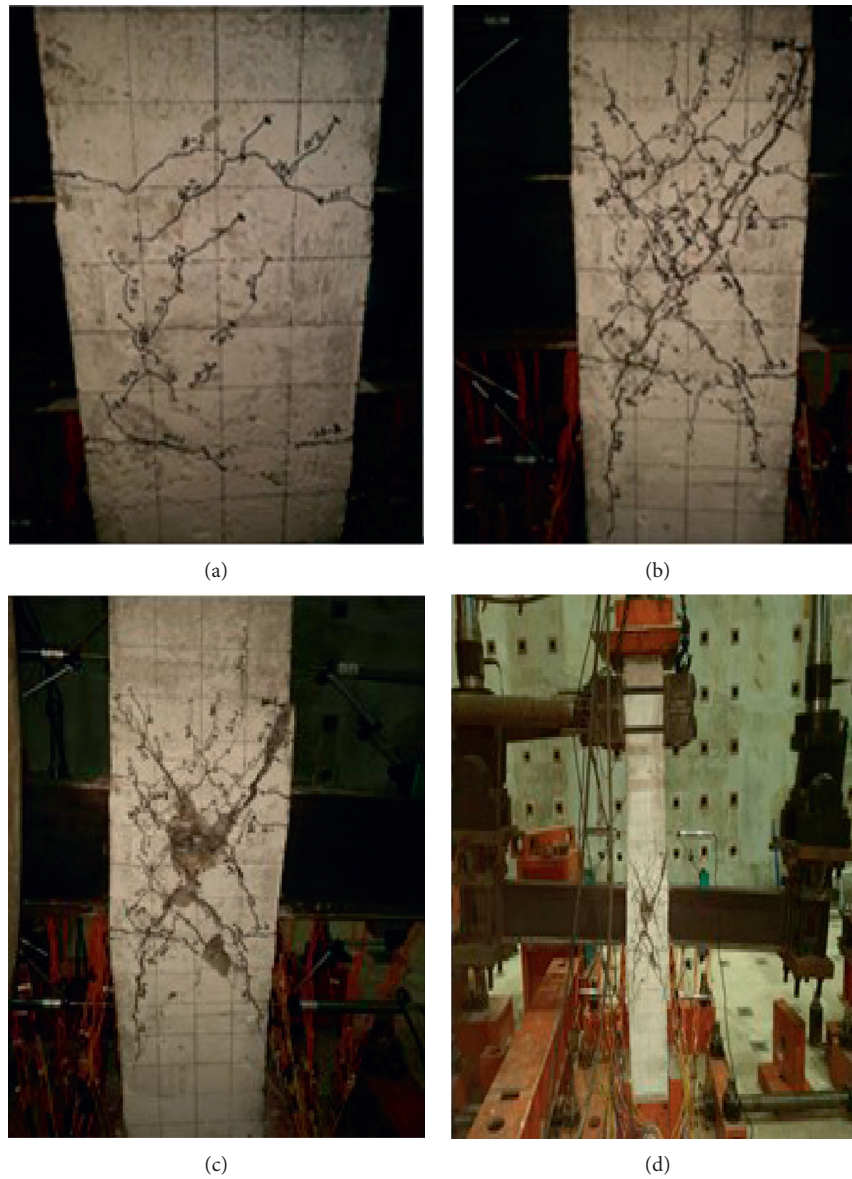


FIGURE 6: Failure modes of SRC-1. (a) Crack at yield capacity. (b) Crack development. (c) Final cracks. (d) Overall specimen at failure.

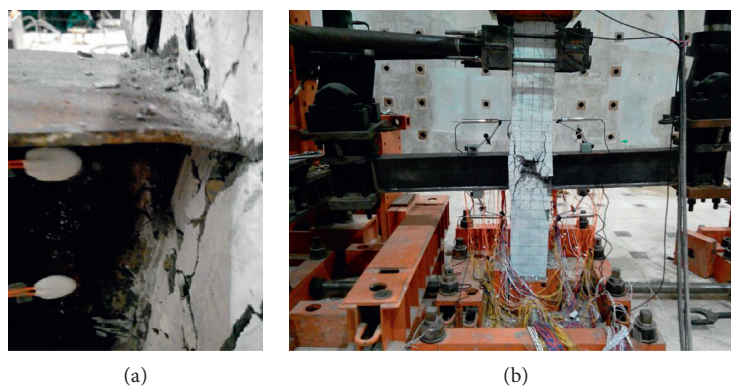


FIGURE 7: Failure modes of SRC-4. (a) Top flange buckling of beam. (b) Final failure mode.

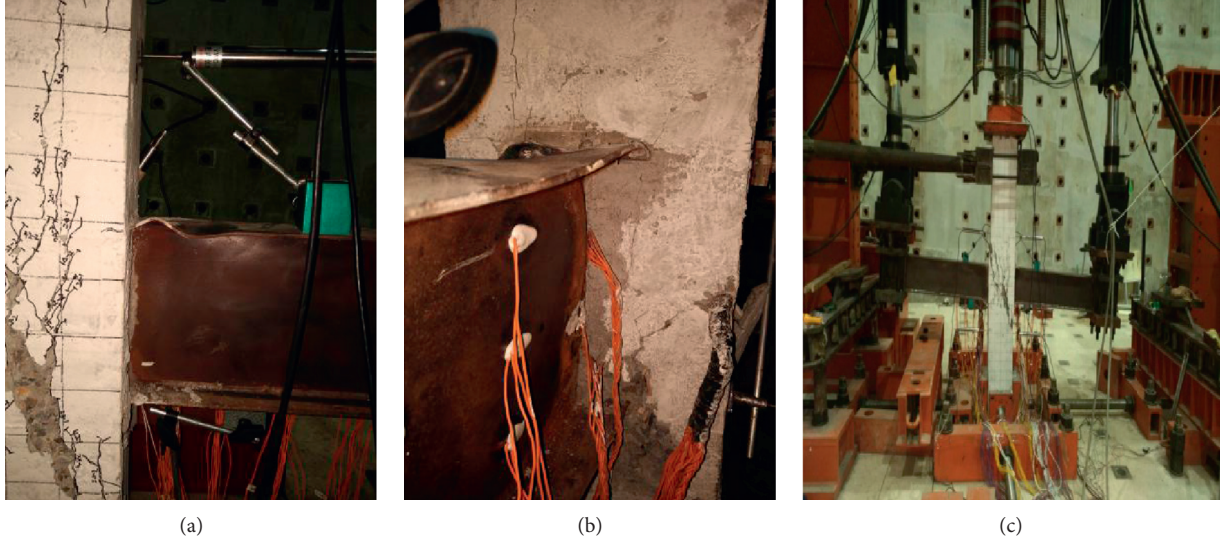


FIGURE 8: Failure modes of SRC-3. (a) Top flange buckling of beam. (b) Web buckling of beam. (c) Final failure mode.

TABLE 3: Failure modes of all specimens.

Sample ID	Details of failure	Final failure mode
SRC-1	Severe concrete spalling and shear deformation in joint, buckling in beam bottom flange	Shear failure in joint
SRC-2	Severe concrete spalling, later than that of SRC-1; shear deformation in joint, buckling in both beam top and bottom flange	Shear failure in joint
SRC-3	Severe concrete spalling, later than that of SRC-2; shear deformation in joint, buckling in both beam flanges and web	Shear failure in joint and beam flexural failure
SRC-4	Severe concrete spalling, later than that of SRC-2; shear deformation in joint, buckling in both beam top and bottom flange	Shear failure in joint

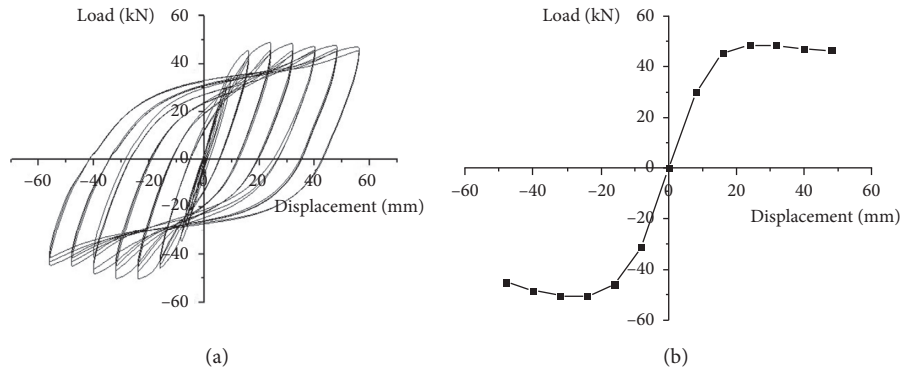


FIGURE 9: Hysteretic curve and envelope curve for SRC-1.

showed similar stiffness degradation trend, while under positive bending moment, SRC-2 showed similar trend to SRC-3 and SRC-1 showed obviously higher curve than that of SRC-2 and SRC-3.

3.6. Energy Dissipation Ability. In this paper, equivalent viscous damping coefficient [15] was used to assess specimen's energy dissipation ability. As shown in Figure 16, equivalent viscous damping coefficient can be obtained through calculation in the following equation:

$$h_e = \frac{1}{2\pi} \cdot \frac{(S_{ABC} + S_{ACF})}{(S_{OBD} + S_{OFE})}. \quad (2)$$

In this paper, only the equivalent viscous damping coefficients at ultimate capacity and at final failure point were analyzed for the three specimens and results are shown in Table 6. It can be seen from the table that the three specimens showed similar energy dissipation coefficients when the load reached ultimate capacity and all specimens showed increased coefficients at final failure points. It indicates that,

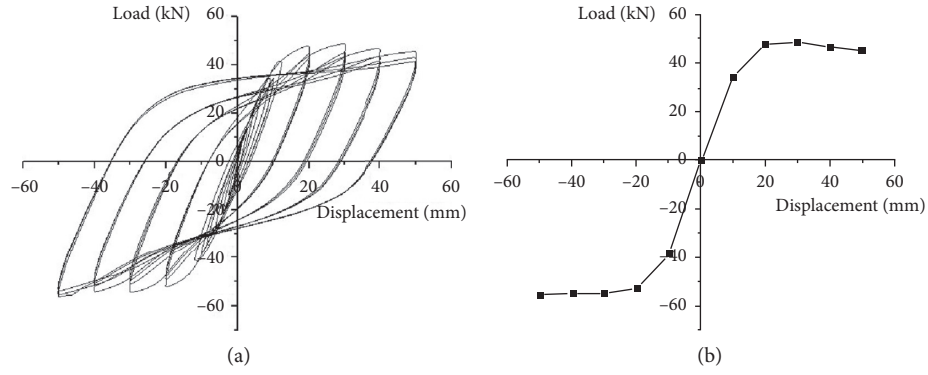


FIGURE 10: Hysteretic curve and envelope curve for SRC-2.

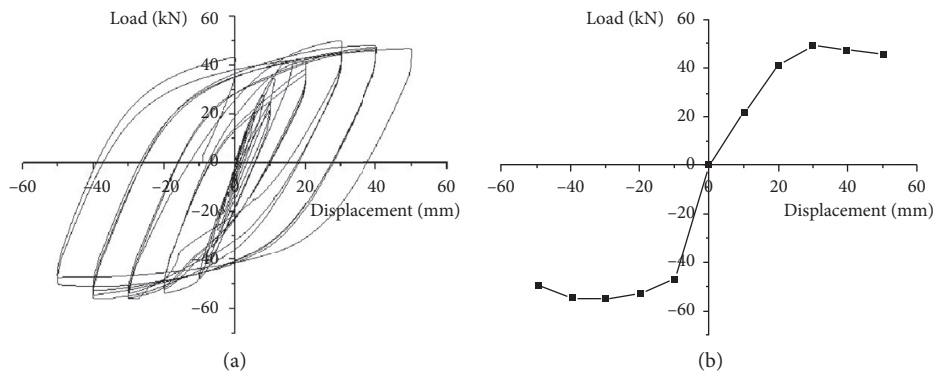


FIGURE 11: Hysteretic curve and envelope curve for SRC-3.

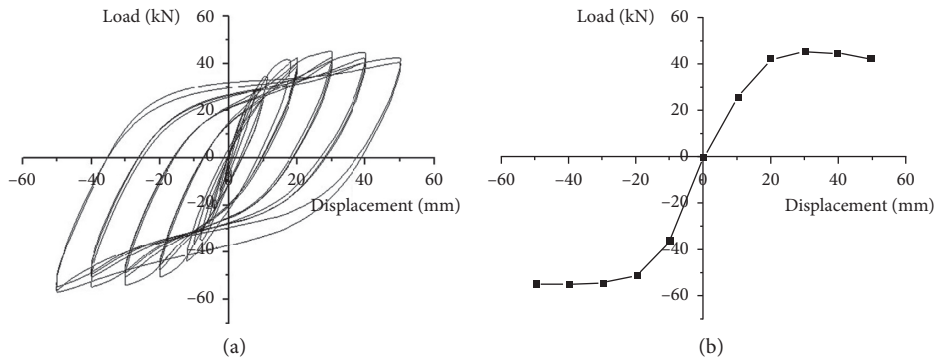


FIGURE 12: Hysteretic curve and envelope curve for SRC-4.

TABLE 4: Characteristic load.

Sample ID	Cracking load	Yielding load (kN)	Ultimate loading (kN)
SRC-1	21 kN in first cycle (positive displacement)	34.74/−34.76	48.98/−50.31
SRC-2	21 kN in first cycle (negative displacement)	41.72/−41.77	48.87/−54.59
SRC-3	28 kN in first cycle (positive displacement)	41.75/−41.80	50.21/−56.09
SRC-4	28 kN in first cycle (positive displacement)	41.32/−41.46	41.32/−41.46

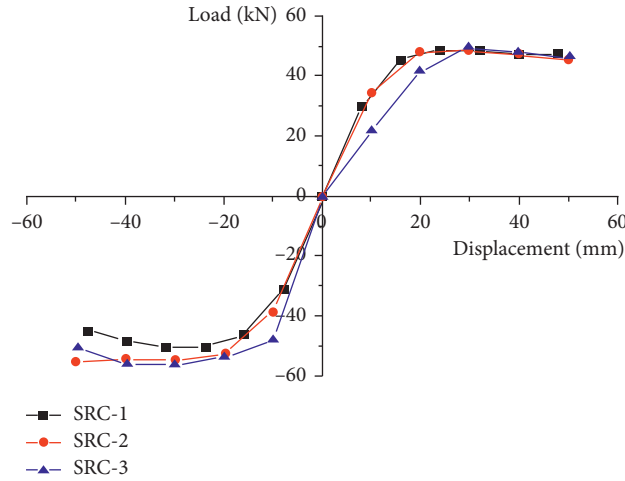


FIGURE 13: Envelope curves under varying axial compression rate.

TABLE 5: Displacement and ductility detail.

Sample ID	Displacement at yield (mm)		Yielding load (kN) (mm)		Ductility coefficient Average
	Positive	Negative	Positive	Negative	
SRC-1	9.27	8.17	31.82	31.81	3.66
SRC-2	11.67	11.21	29.71	29.92	2.61
SRC-3	12.56	10.75	29.71	29.97	2.58

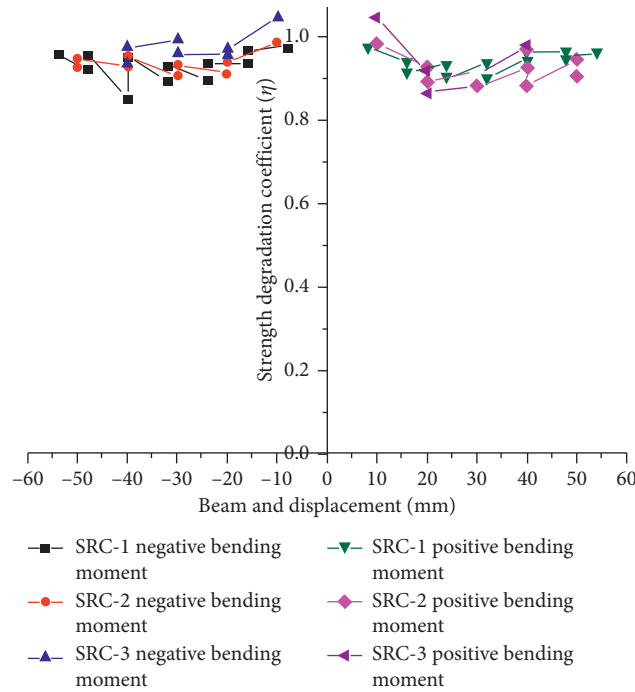


FIGURE 14: Strength degradation coefficient.

after ultimate capacity point, the load bearing capacity decreased very slowly and all joints showed good energy dissipation ability. The equivalent viscous damping

coefficient of SRC-3 is higher than those of the other two specimens by 0.1, which indicates that higher axial compression rate can help to improve energy dissipation ability.

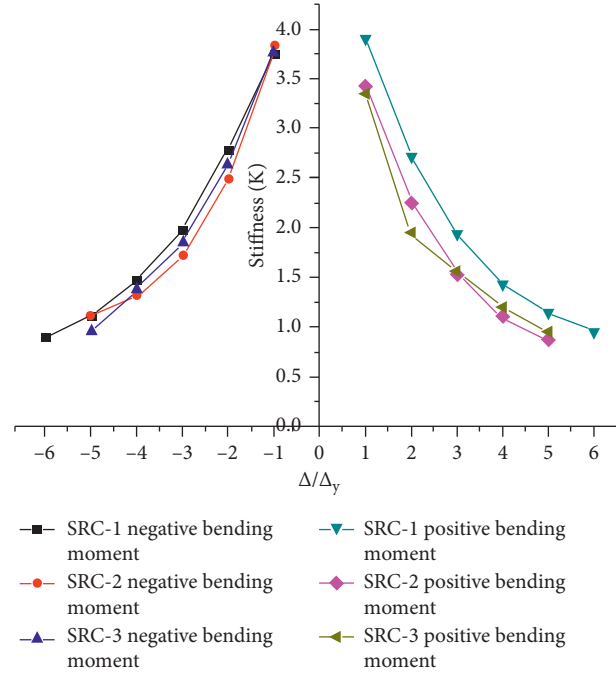


FIGURE 15: Stiffness degradation curves.

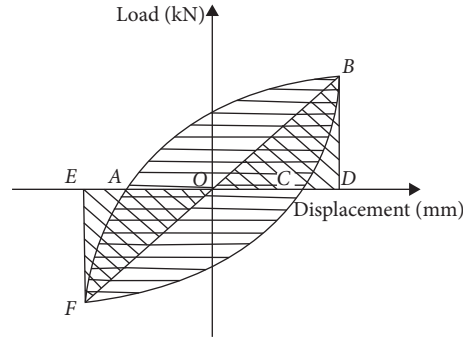
FIGURE 16: Calculation of h_e .

TABLE 6: Energy dissipation coefficients.

Sample ID	Under ultimate capacity		At failure	
	Area A	h_e	Area A	h_e
SRC-1	2300	0.23	4183	0.3
SRC-2	2257	0.24	4909	0.3
SRC-3	2196	0.22	6091	0.4

3.7. Shear Resistance Capacity. The two widely used practical codes on structural steel-concrete composite structure in China are JGJ 138-2001 [16] and YB 9082-2006 [17]. When seismic grade is not considered and only the impact from axial load is considered, the two standards provide shear resistance formula for SRC composite columns-steel-beam joints:

$$\begin{aligned}
 V = & \varphi_j \eta_j 0.25 + 0.05 \frac{N}{f_c b_c h_c} f_c b_j h_j \\
 & + f_{yv} \frac{A_{sv}}{s} h_0 - \alpha'_s + 0.58 f_a t_w h_w,
 \end{aligned} \quad (3)$$

TABLE 7: Shear capacity calculated by equation (3).

Sample ID	SRC-1	SRC-2	SRC-3
Axial compression ratio	0.1	0.4	0.7
Axial compression	140	560	980
Shear capacity of concrete	188.7	188.7	188.7
Shear capacity of stirrups	71.7	71.7	71.7
Shear capacity of structural steel	130.8	130.8	130.8
Influence factor from axial force	6.4	25.7	44.9
Shear capacity calculated from equation (3)	397.8	410.0	436.3

TABLE 8: Shear capacity calculated by equation (4).

Sample ID	SRC-1	SRC-2	SRC-3
Axial compression ratio	0.1	0.4	0.7
Axial compression	140	560	980
Shear capacity of concrete	122.7	122.7	122.7
Shear capacity of stirrups	71.7	71.7	71.7
Shear capacity of structural steel	130.8	130.8	130.8
Influence factor from axial force	12.8	51.3	89.8
Shear capacity calculated from equation (4)	338.1	376.6	415.1

TABLE 9: Comparison between theoretical values and measured values.

Sample ID	SRC-1	SRC-2	SRC-3
Testing result for shear capacity	419.1	436.6	448.7
Calculated shear capacity from equation (3)	397.8	410.0	436.3
Calculated shear capacity from equation (4)	338.1	376.6	415.1
Test result/result from equation (3)	105.4%	104.7%	102.9%
Test result/result from equation (4)	123.9%	115.9%	108.1%

$$V = \delta_j f_t b_j h_j + \frac{f_{yv} A_{sv}}{s} h_j + f_{ssv} t_w h_w + 0.1 N_c^{rc}. \quad (4)$$

In equation (4), $0.1 N_c^{rc}$ is the favorable influence of axial force.

Testing shear force is calculated through the following equation:

$$V = \frac{M_{bl} + M_{br}}{h_{b0}} \cdot \frac{1}{H} \cdot \left(H - \frac{h_{b0} L}{L_n} \right), \quad (5)$$

where H is column height, L is beam span, L_n is clear span of beam, h_{b0} is effective height of beam, and M_{bl} and M_{br} are bending moments at left and right sides of beam. Tables 7 and 8 summarize shear capacity of three specimens, and Table 9 shows comparison between theoretical values and measured values.

It can be seen from Tables 7–9 that testing results for these three specimens are all higher than calculated results from two standards. Testing results increased with axial compression ratio, which indicates that it is a proper method to include the influence from axial compression force. Testing results are more close to results from equation (3), while equation (4) showed smaller shear capacity. Comparing Tables 7 and 8, it can be seen that concrete shear capacity from equation (3) is much higher than that from equation (4), while the influence factor of axial force in equation (4) nearly doubles that from equation (3). Hence, based on the results from this paper, suggestions could be provided on modification of equation

(4), for example, increasing the calculated shear capacity of concrete and decreasing axial load.

4. Finite Element Model (FEM)

4.1. Model Setup. In order to better understand the behavior of SRC column-steel-beam structure and verify the accuracy of the experiment, ABAQUS was used to simulate the elements and loading process. With regard to concrete constitutive relationship, damage plasticity model was used to represent concrete plastic behavior. Concrete uniaxial compressive and tension stress-strain relationships suggested in GB50010-2010 [18] were employed. Concrete compressive and tensile strengths of f_{ck} and f_{tk} were from test results, which are shown in Table 1. The von Mises yield criterion and related flow rules were adopted for steel simulation and yield strength used in the model was from test results, with yield strength of 297 MPa for Q235 graded steel, 316 MPa for HPB300 graded steel, and 379 MPa for HRB335 graded steel.

Concrete was simulated through reduced linear integrated unit C3D8R. Three-dimensional Truss unit T3D2 was used for reinforcement steel simulation. Three-dimensional shell unit S4R [19] was used for structural steel simulation. Meshed structure model is shown in Figure 17.

4.2. FEM Results Analysis. Figure 18 shows FEM results and also test results from SRC-3 on load-displacement hysteretic curves. Overall, the FEM results agree well with those from the test. Figure 19 shows the final failure mode of SRC-3. It can be seen clearly that shear deformation is severe, as well as

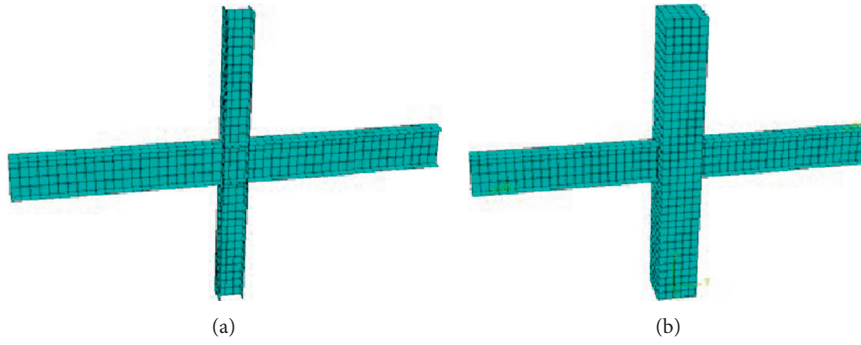


FIGURE 17: Meshed elements. (a) Joint from steel elements. (b) Joint from concrete column/steel beam.

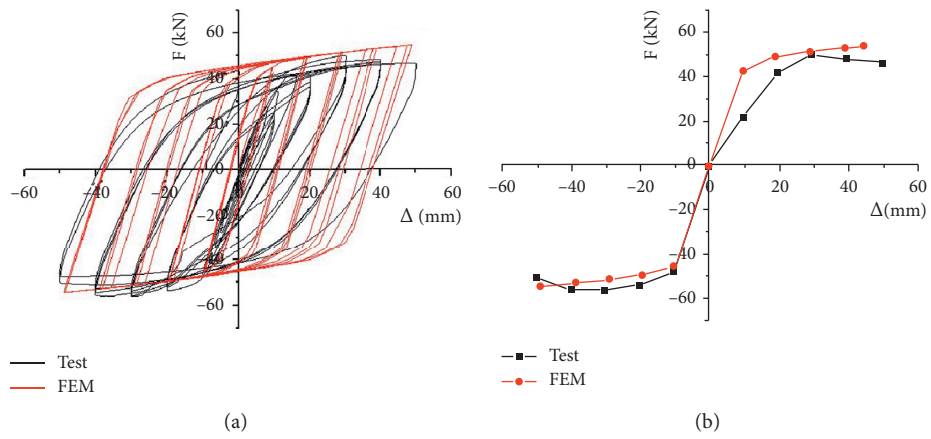


FIGURE 18: Hysteretic curve and envelope curve of SRC-3. (a) Hysteretic curve. (b) Envelope curve.

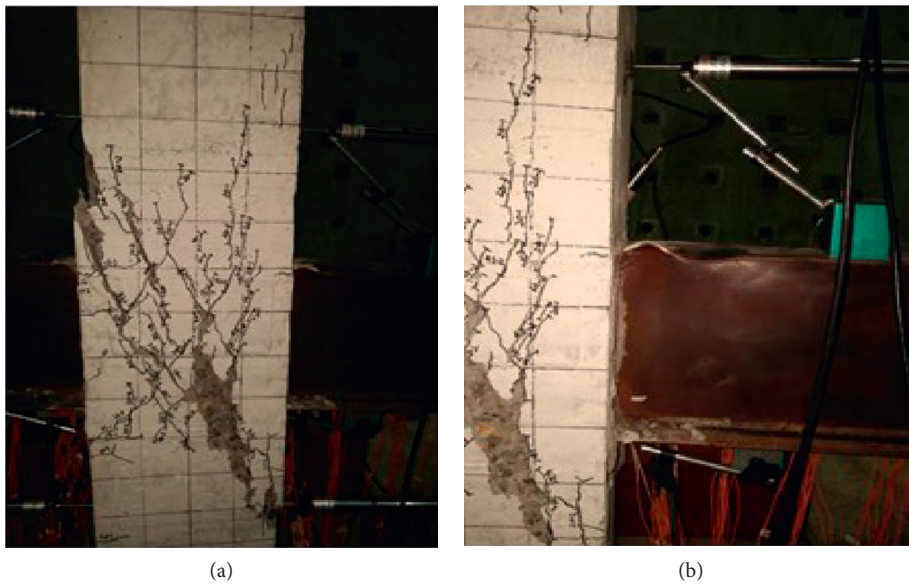


FIGURE 19: Continued.

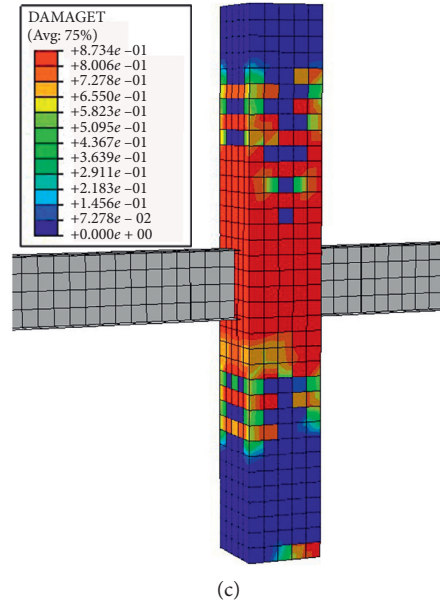


FIGURE 19: Failure mode of specimen SRC-3. (a) Final cracking. (b) Buckling in beam flange. (c) FEM result.

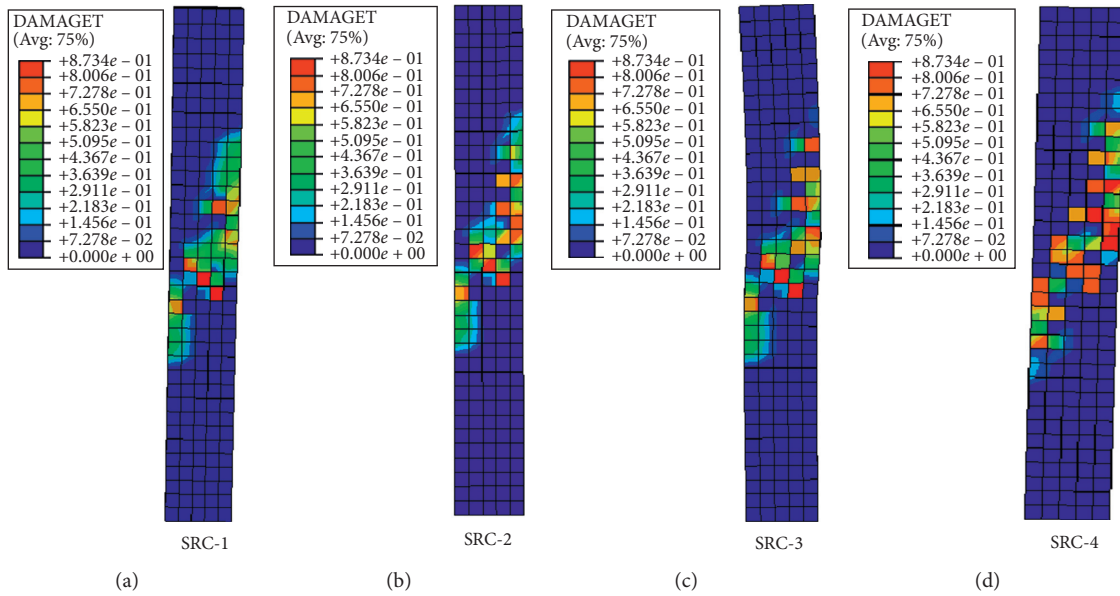


FIGURE 20: Initial cracking of concrete.

buckling and deformation in beam flanges and concrete spalling in concrete, which all agree with test phenomena. Figure 20 shows the damage contour on concrete tensile cracking from all four specimens and it can be seen from the figure that cracking load improves with increasing axial load, which indicates that increase of axial pressure ratio will improve anticracking ability and slow down crack development. SRC-4 shows obviously higher cracking load than SRC-2, which indicates that application of X-shaped rein-

forcement joint area can not only affect crack locations but also improve concrete crack resistance.

4.3. Parametric Study. Through adjustment of concrete strength, stirrup ratio, stiffener thickness, and web thickness in FEM model, their influence on joint strength capacity is analyzed. The energy dissipation ability of specimen with axial compression ratio of 0.4 was greater than that of

TABLE 10: FEM parameter analysis.

Sample ID	Concrete strength	Longitudinal bars in column	Stirrup bars in column	Stirrup bars in joint	Thickness of the stiffener (mm)	Web thickness (mm)	Axial pressure ratio
SRC-5	C30	4-12	-8@100	-8@60	N/A	8	0.4
SRC-6	C40	4-12	-8@100	-8@60	N/A	8	0.4
SRC-7	C50	4-12	-8@100	-8@60	N/A	8	0.4
SRC-8	C30	4-12	-8@100	N/A	N/A	8	0.4
SRC-9	C30	4-12	-8@100	-6@60	N/A	8	0.4
SRC-10	C30	4-12	-8@100	-8@60	N/A	8	0.4
SRC-11	C30	4-12	-8@100	-8@60	N/A	8	0.4
SRC-12	C30	4-12	-8@100	-8@60	4	8	0.4
SRC-13	C30	4-12	-8@100	-8@60	8	8	0.4
SRC-14	C30	4-12	-8@100	-8@60	N/A	4	0.4
SRC-15	C30	4-12	-8@100	-8@60	N/A	6	0.4
SRC-16	C30	4-12	-8@100	-8@60	N/A	8	0.4

TABLE 11: Beam end loads and shear from FEM.

Sample ID	Cracking load (kN)	Yielding load (kN)	Ultimate load (kN)	Shear at cracking (kN)	Shear at yielding (kN)	Ultimate shear (kN)
SRC-5	14.5	27.8	53.1	108.6	207.6	396.1
SRC-6	16.1	29.5	54.6	120.5	220.0	407.6
SRC-7	17.2	31.2	54.7	128.4	233.1	408.5
SRC-8	12.5	26.9	52.1	93.3	199.5	389.1
SRC-9	13.8	27.7	52.7	103.3	206.7	393.4
SRC-10	14.6	27.8	53.1	108.6	207.6	396.1
SRC-11	14.3	27.7	52.7	106.9	206.9	393.3
SRC-12	14.6	27.8	53.1	108.6	207.6	396.1
SRC-13	14.8	28.9	53.3	110.1	215.7	397.8
SRC-14	12.3	21.7	49.3	91.5	162.0	367.8
SRC-15	13.4	25.5	51.6	99.7	190.4	385.4
SRC-16	14.6	27.8	53.1	108.6	207.6	396.1

specimens with 0.1 axial compression ratio, while the flexural failure of steel beams was caused by high axial compression ratio of 0.7. The increase of axial compression ratio will increase the shear resistance capacity of joints, but it is only a small increase. Therefore, the axial compression ratio of 0.4 was selected for simulation.

In Table 10, concrete strengths for specimens SRC-5, SRC-6, and SRC-7 were C30, C40, and C50, respectively. There was no stirrup in SRC-8, while stirrup diameters of 6 mm and 8 mm were applied in SRC-9 and SRC-10, respectively. There was no stiffener in SRC-11, while stiffeners at thickness of 4 mm and 8 mm were applied in SRC-12 and SRC-13, respectively. Specimens SRC-14, SRC-15, and SRC-16 are with web thickness of 4 mm, 6 mm, and 8 mm, respectively. One simulated parameter was verified for every three specimens. Other parameters were the same. Table 11 lists the load and shear resistance simulation results for three different stages of the specimen.

It can be seen from Table 11 that cracking shear force and yielding shear force increase with concrete strength increasing, while ultimate shear force was not affected very much. With increasing of stirrup diameter, cracking shear force is obviously improved, while addition of stiffener in

joint area does not influence shear resistance very much. Compared with adding stiffener and stirrups, increasing web thickness can improve joint shear resistance more effectively.

Figure 21 shows that higher strength concrete makes bigger contribution to load sharing and this helps to lower the loading in structural steel web. With increase of stirrup in the joint area, this can improve shear resistance. With the increase of stiffener thickness, shear on stiffener increases and thus reduces the shear in steel web. At the same time, SRC-11 showed more severe steel buckling than the other two specimens, which indicates that adding stiffener in core area could reduce local buckling in steel flange and transfer shear to web uniformly and this finally reduces strain in web area. With web thickness increasing, the capacity and stability of joint can be obviously improved.

From the FEM results on parameter study, it can be concluded that those factors showed positive influence on improving joint shear resistance; in the order from the most obvious to the least obvious, they are web thickness, concrete strength, stirrup ratio, and stiffener thickness. Increasing web thickness is proved to be the most effective way for shear resistance improvement for SRC composite columns-steel-beam joints.

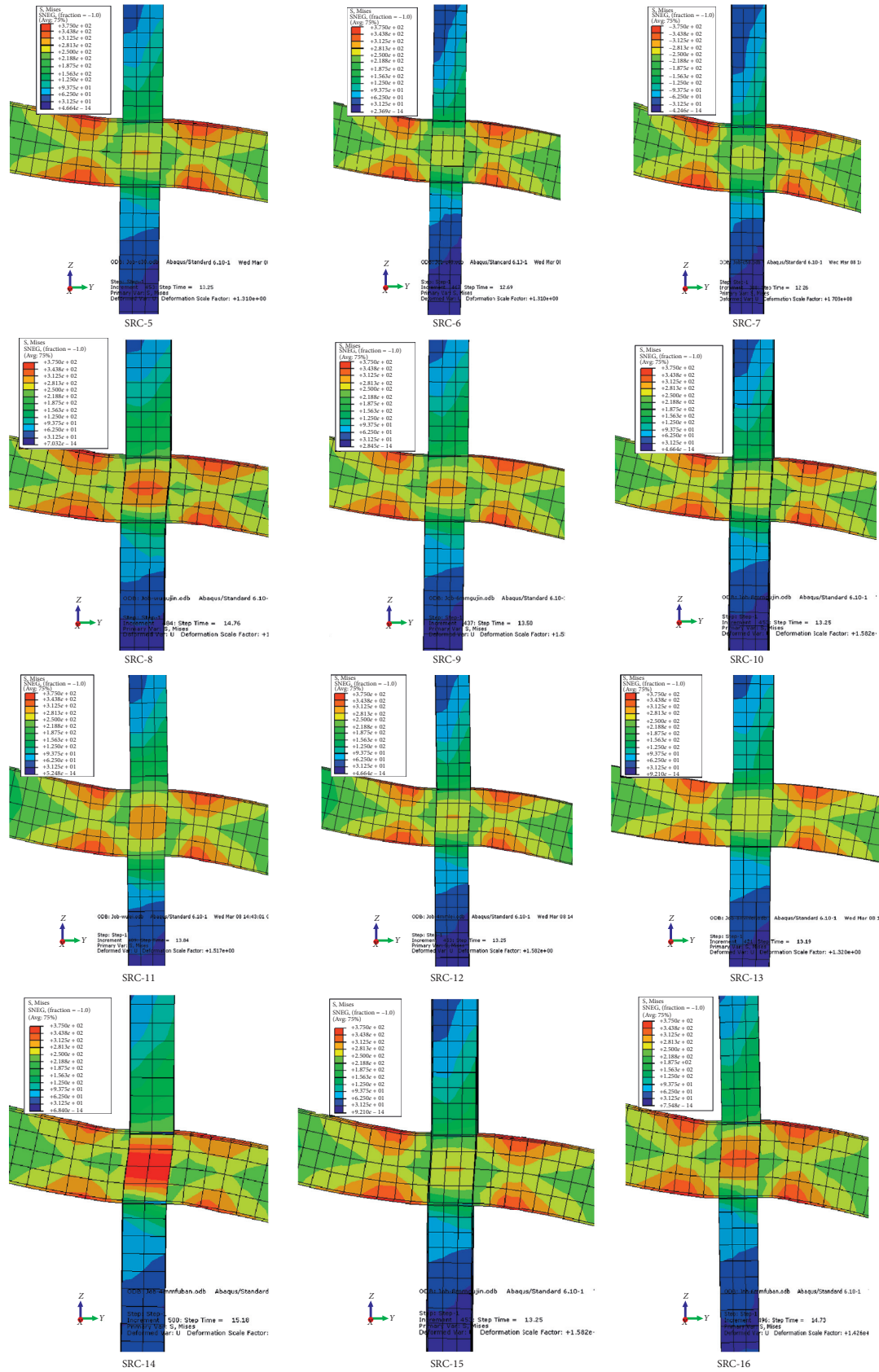


FIGURE 21: Stress distribution of specimen in ultimate state.

5. Conclusion and Future Work Recommendation

Experimental study was carried out on SRC composite columns-steel-beam joints under low-frequency cyclic loading. Results were verified by analysis result from FEM model using ABAQUS. Both experimental and FEM analysis results showed the following:

- (1) Higher axial compression ratio can improve crack resistance; however, high axial force on SRC-3 caused flexural failure of beam and then finally led to reduction in overall joint stability and load capacity in structural steel.
- (2) SRC-3 showed most full hysteretic curve among all specimens, which indicates good energy dissipation ability of SRC composite columns-steel-beam joints. With axial compression ratio increasing, ductility of joints decreased and strength degradation did not change very much, while stiffness decreased.
- (3) Adding X-shaped reinforcement in joint area could slow down concrete cracking and improve crack resistance but does not affect other mechanical properties very obviously.
- (4) Based on experimental results, suggestions could be made on modification of formula from YB9082-2006 [15] in that concrete shear capacity could be increased and positive influence from axial load could be reduced.

Data Availability

The relevant data in this paper can be obtained through relevant calculation or test.

Conflicts of Interest

The authors declare that there are no conflicts of interest regarding the publication of this paper.

Acknowledgments

This work was financially supported by the National Key R&D Program of China (2016YFE0125600), Program for Innovative Research Team of Education Ministry of China (IRT_16R67), Thousand Talents Plan in Henan Province (ZYQR201912029), and the National Natural Science Foundation of China (no. 51408556).

References

- [1] Y. Yang, Y. Xue, Y. Yu, and F. Gao, "Experimental study on seismic performance of partially precast steel reinforced concrete columns," *Engineering Structures*, vol. 175, pp. 63–75, 2018.
- [2] J. M. Ding, S. Chao, X. Zhao, and H. L. Wu, "Critical issues of structural analysis for the Shanghai center project," *Journal of Building Structures*, vol. 31, no. 6, pp. 123–131, 2010, in Chinese.
- [3] C. H. Chen, C. K. Wang, and H. Z. Su, "Experimental study on seismic behavior of full encased steel-concrete composite columns," *Journal of Structural Engineering*, vol. 140, no. 6, pp. 1–10, 2014.
- [4] J. Y. Xue, Z. P. Chen, and H. T. Zhao, *Performance, Design Method and Engineering Application of Steel Reinforced Concrete Special-Shaped Column Structure*, China Architecture & Building Press, Beijing, China, 2011, in Chinese.
- [5] L. Chu, G. Li, D. Li, and J. Zhao, "Study on progressive collapse behavior of SRC column-steel beam hybrid frame based on pushdown analysis," *Shock and Vibration*, vol. 2017, pp. 1–12, 2017.
- [6] C.-C. Chen, K.-T. Lin, and Y.-J. Chen, "Behavior and shear strength of steel shape reinforced concrete deep beams," *Engineering Structures*, vol. 175, pp. 425–435, 2018.
- [7] W. P. Cheng, L. C. Wang, Y. P. Song, and J. Wang, "Seismic behaviour of beam-column joints of precast and partial steel reinforced concrete," *Journal of Harbin Institute of Technology*, vol. 22, no. 2, pp. 108–117, 2015.
- [8] Z. P. Chen, J. J. Xu, J. Y. Xue, and N. Wang, "Deformation and energy-based seismic damage behavior of SRC specially shaped columns," *China Civil Engineering Journal*, vol. 48, no. 8, pp. 29–37, 2015, in Chinese.
- [9] P. Xiang, Z. Deng, Y. Su, H. Wang, and Y. Wan, "Experimental investigation on joints between steel-reinforced concrete T-shaped column and reinforced concrete beam under bidirectional low-cyclic reversed loading," *Advances in Structural Engineering*, vol. 20, no. 3, pp. 446–460, 2016.
- [10] L. S. Chu, D. D. Li, X. Ma, and J. Zhao, "Cyclic behaviour of concrete encased steel (CES) column-steel beam joints with concrete slabs," *Steel and Composite Structures*, vol. 29, no. 6, pp. 731–744, 2018.
- [11] M.-X. Tao, J.-S. Fan, and J.-G. Nie, "Seismic behavior of steel reinforced concrete column-steel truss beam hybrid joints," *Engineering Structures*, vol. 56, pp. 1557–1569, 2013.
- [12] S.-Y. Seo, Y. Hyun-Do, and S.-H. Kim, "Structural resistance of SRC column-steel beam joint developed for innovative," *Construction of Buildings, Journal of Iron and Steel Research*, vol. 18, no. A1, pp. 924–928, 2011.
- [13] C. Standard, *Specifying of Testing Methods for Earthquake Resistant Building (JGJ101-96)*, Architecture & Building Press, Beijing, China, 1996.
- [14] J. G. NIE, Y. Huang, and J. S. Fan, "Experimental study on load-bearing behavior of rectangular CFST frame considering composite action of floor slab," *Journal of Building Structures*, vol. 32, no. 3, pp. 99–108, 2011, in Chinese.
- [15] R. Liu, *Experimental Studies on the Seismic Behavior of Cast-In-Situ Hollow Floor Slab-Column Strengthened Connections*, Henan University of Technology, Zhengzhou, China, 2016, in Chinese.
- [16] C. Standard, *Technical Specification for Steel Reinforced Concrete Composite Structures (JGJ138-2001)*, Architecture & Building Press, Beijing, China, 2001.
- [17] C. Standard, *Technical Specification of Steel-Reinforced Concrete Structures (YB9082-2006)*, Architecture & Building Press, Beijing, China, 2006.
- [18] C. Standard, *Code for Design of Concrete structures (GB50010-2010)*, Architecture & Building Press, Beijing, China, 2015.
- [19] L. Fang, B. Zhang, G. F. JIN, K. W. LI, and Z. L. Wang, "Experimental study and finite element analysis on seismic behavior of steel reinforced concrete cross-shaped columns," *Journal of Central South University(Science and Technology)*, vol. 46, no. 3, pp. 1027–1033, 2015, in Chinese.

Research Article

Analysis of Lateral Dynamic Response of Caisson Foundation in Layered Clayey Soils considering Scour-Hole Dimensions

Wenbo Tu ¹, Xiaoqiang Gu ^{2,3}, Xianfeng Ma ^{2,4} and Dawei Huang ¹

¹School of Civil Engineering and Architecture, East China Jiaotong University, Nanchang 330013, China

²Department of Geotechnical Engineering, Tongji University, Shanghai 200092, China

³Key Laboratory of Geotechnical and Underground Engineering of Ministry of Education, Tongji University, Shanghai 200092, China

⁴School of Civil Engineering, Kashi University, Kashi 844006, China

Correspondence should be addressed to Xianfeng Ma; xf.ma@tongji.edu.cn

Received 6 September 2020; Revised 24 September 2020; Accepted 4 October 2020; Published 17 October 2020

Academic Editor: Xing Ma

Copyright © 2020 Wenbo Tu et al. This is an open access article distributed under the Creative Commons Attribution License, which permits unrestricted use, distribution, and reproduction in any medium, provided the original work is properly cited.

As a cross-sea or river deep-water foundation, it is clear that the caisson foundation will be subjected to significant lateral dynamic loads due to winds or waves and suffer from scouring under its long-term effect. In order to obtain the scour effect on the dynamic response of the foundation, an analytical model describing the scour-hole effect in terms of scour depth, scour width, and slope angle was constructed. Combined with the nonlinear Winkler theory, a method for the dynamic response of the caisson foundation considering the scour-hole dimensions was proposed. Comparisons against the results from the dynamic FEM demonstrate the reliability of this method. The effects of the scour width, slope angle, and scour depth on the dynamic response of the caisson were discussed. The results show that the scour depth affects the dynamic displacement and resonant frequency of the foundation most, whereas the scour width does less and the slope angle does the least; the dynamic response of caisson can be approximated as the case of the slope angle 5° and the scour width $5B$ when the slope angle is less than 5° and the scour width is greater than $5B$, respectively; the effects of scour width and slope angle on the dynamic response of caisson have the similar change pattern in the displacement and resonant frequency when the scour depth is different. However, the effect of amplitude on dynamic response shows a nonlinear increase trend when the scour depth is relatively large.

1. Introduction

Caisson is a common foundation type which is suitable for bridge engineering. It is widely used in cross-river and cross-sea bridges because of its strong integrity and large bearing capacity, such as the Shanghai-Nantong Yangtze River Bridge in China, the Brooklyn Bridge in the United States, and the Akashi Strait Bridge in Japan [1]. Comparing with the traditional foundation on land, the working environment of caisson foundation is more complicated. The caisson foundation not only needs to withstand the upper vertical load but also needs to withstand the horizontal dynamic load such as wind, wave currents, and possible earthquakes. Research has also shown that the mechanism of lateral interaction is more complicated than that of vertical

interaction and the lateral load takes more significant effect on the characteristics of foundation than vertical load [2]. Therefore, more strict requirements are put forward for the horizontal dynamic performance of the caisson foundation during the design and construction. In addition, the caisson foundation easily suffers from scouring due to the huge size resulting in a drastic change in the water crossing section. Take the caisson foundation used in the Taizhou Yangtze River Bridge as an example—the length, width, and height of the caisson is 58.2 m, 44.1 m, and 76 m, respectively. According to the field measurement data, the maximum local scour depth reaches 17.4 m about one year after the completion of construction, and the scour depth comes to a new peak value of 46.6 m according to the laboratory tests when the factors such as water velocity, flow, and angle are

taken into account [3, 4]. Obviously, such a huge scour depth value will inevitably cause significant changes in the bearing performance and dynamic characteristics of the foundation and may even cause the damage of bridge foundation. Based on the statistics data of 584 bridge accidents from 1813 to 2018 [5], it is concluded that about 30% of bridge collapses are related to natural disasters, and bridge scouring caused by floods is the most common case. Therefore, it is necessary to study the changes in the characteristics of the caisson foundation before and after scouring.

In recent years, there is a growing concern on the characteristics of caisson foundation before and after scouring. Liu et al. [6] studied the horizontal bearing characteristics of the suction caisson after scouring in layered clay soils. Zhang et al. [7] conducted a laboratory test to investigate the lateral response of the caisson and its dependence on the characteristics of the applied cyclic load and scouring. However, these methods for analyzing the scour effect mentioned above focused on the static behavior of the foundation, and the dynamic behavior of the foundation was not involved. Tu et al. [8, 9] discussed the influence of scouring on dynamic impedance and resonant characteristics of the caisson, but the scour pattern is assumed to be of layer distribution mode. Nevertheless, it is well recognized that scour holes formed around the caisson usually involve certain shapes and sizes [10, 11], and the static and dynamic characteristics of the foundation is affected by the shape and size of scour holes [12, 13]. Yang et al. [14] analyzed the effect of scour-hole dimensions on the response of laterally loaded piles based on the modified strain wedge method. Zhang et al. [15] used Mindlin's solution to analyze the influence of the scour-hole dimension on the horizontal bearing characteristics of a single pile. However, the caisson is different from the pile foundation; hence, Mindlin's solution cannot be directly used for scour analysis due to the large size of the caisson foundation. To get a better understanding of the scour effect, it is necessary to study the dynamic characteristics of foundations in combination with the dimension of scour holes.

The objective of this paper is to propose a simplified model for the analysis of laterally loaded caisson foundations under scouring, which can account for the effects of scour-hole dimensions on the dynamic performance of foundations. In order to verify the proposed simplified model for the lateral vibration of the scoured caisson, 3D finite element simulations are conducted and good agreements are obtained between the results of the numerical method and the theoretical model. Finally, to provide a reference for engineering application, the influence of the scour depth, scour width, and scour slope angle of scour holes on the dynamic characteristics of the caisson foundation are studied based on the proposed model.

2. Lateral Dynamic Analysis Model for the Scoured Caisson

2.1. Analysis Model for Caisson in Layered Soils. Based on the Winkler dynamic analysis theory, a two-dimensional plane analysis model of caisson in a homogeneous elastic

foundation without any scouring can be established, as shown in Figure 1 [16]. Here, the caisson is assumed to be a rigid embedded foundation. For a caisson subjected to the harmonic horizontal load Q_0 and moment M_0 at the top center of the foundation, the lateral dynamic equilibrium equation can be expressed as

$$[M_b] \begin{Bmatrix} \ddot{u}_b \\ \ddot{\theta}_b \end{Bmatrix} + [C_b] \begin{Bmatrix} \dot{u}_b \\ \dot{\theta}_b \end{Bmatrix} + [K_b] \begin{Bmatrix} u_b \\ \theta_b \end{Bmatrix} = \begin{Bmatrix} Q_0 \\ Q_0 D + M_0 \end{Bmatrix}, \quad (1)$$

where D is the height of the foundation, and u_b and θ_b are the horizontal displacement and the rotation angle of the base center of the foundation. $[M_b]$, $[K_b]$, and $[C_b]$ are the mass dynamic matrix, stiffness matrix, and damping matrix of the foundation, respectively. They can be rewritten as

$$\begin{aligned} [M_b] &= \begin{bmatrix} m & mh_1 \\ mh_1 & J_c + mh_1^2 \end{bmatrix}, \\ [K_b] &= \begin{bmatrix} K_{hh} & K_{hr} \\ K_{rh} & K_{rr} \end{bmatrix}, \\ [C_b] &= \begin{bmatrix} C_{hh} & C_{hr} \\ C_{rh} & C_{rr} \end{bmatrix}, \end{aligned} \quad (2)$$

where m is the mass of caisson foundation, h_1 is the distance from the center of gravity to the base surface of the caisson, and J_c is the mass moment of inertia of the caisson. K_{hh} , K_{rr} , and K_{hr} (K_{rh}) are the horizontal dynamic stiffness, rocking dynamic stiffness, and coupled horizontal-rocking dynamic stiffness of caisson, respectively. C_{hh} , C_{rr} , and C_{hr} (C_{rh}) are the horizontal dynamic damping, rocking dynamic damping, and coupled horizontal-rocking dynamic damping of caisson, respectively:

$$\begin{aligned} K_{hh} &= K_h + \sum_{i=1}^n k_{xi} d_i, \\ K_{hr} &= K_{rh} = \sum_{i=1}^n k_{xi} d_i z_i, \\ K_{rr} &= K_r + \sum_{i=1}^n \left[k_{xi} d_i \left(z_i^2 + \frac{1}{12} d_i^2 \right) + k_{ri} d \right], \\ C_{hh} &= C_h + \sum_{i=1}^n c_{xi} d_i, \\ C_{hr} &= C_{rh} = \sum_{i=1}^n c_{xi} d_i z_i, \\ C_{rr} &= C_r + \sum_{i=1}^n \left[c_{xi} d_i \left(z_i^2 + \frac{1}{12} d_i^2 \right) + c_{ri} d \right], \end{aligned} \quad (3)$$

where z_i is the distance from the center of layer i to the soil surface, d_i is the thickness of soil layer i , and d is the embedment depth of the caisson. K_h , C_h and K_r , C_r are the horizontal and rotational spring stiffness and damping

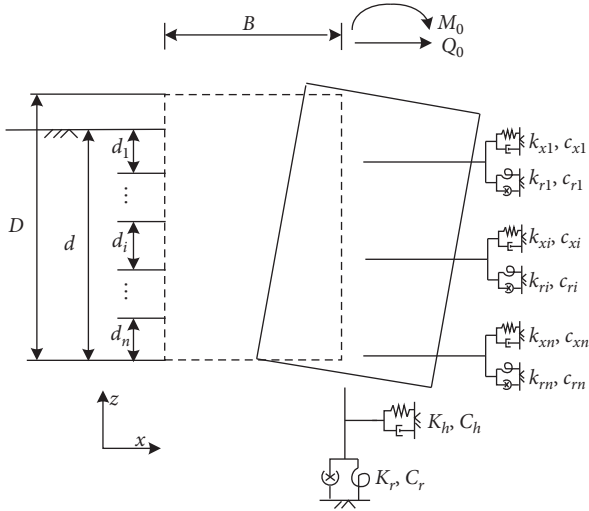


FIGURE 1: Dynamic Winkler model for the lateral vibration of the caisson.

coefficient of the concentrated springs with respect to the bottom of the caisson, respectively. k_{xi} , c_{xi} and k_{ri} , c_{ri} are the stiffness and damping coefficient of the distributed horizontal and rocking springs of layer i (i ranges from 1 to n), respectively. k_{xi} , c_{xi} and k_{ri} , c_{ri} are given in Appendix A in detail.

2.2. Simplified Method considering the Scour-Hole Dimensions. During the analysis of the scour effect, most of the studies assume that the loss of soil around the foundation is distributed in a plane mode. In reality, the scour pattern is in irregular shape, which is significantly affected by some

factors, such as the water velocity and foundation type. Generally, the scour pattern at a certain state can be approximated by scour depth S_d , scour width S_w , and scour slope angle θ , as shown in Figure 2 [12, 15]. According to the symmetry of the model, the illustration of stress loss around the caisson is shown in Figure 3.

For a caisson embedded in clay, the mean effective stress σ'_m at a certain point before scouring can be determined as

$$\sigma'_m = \frac{(1 + 2K_0)\gamma'_0 h_0}{3}, \quad (4)$$

where γ'_0 and h_0 are the effective unit weight of soil and the embedded depth, respectively. K_0 is the coefficient of earth pressure at rest.

According to Figure 3, with the formation of the scour hole, the mean effective stress at a certain state can be expressed as

$$\sigma'_{ms} = \sigma'_m - \sigma'_{ul}, \quad (5)$$

where σ'_{ms} is the mean effective stress after scouring, and σ'_{ul} is the stress loss caused by the unloading of the soil when the scour hole is formed.

Based on the plane strain hypothesis, the stress loss of the point of interest around the caisson shaft after scouring can be calculated by the superposition principle. It can be approximately expressed as the sum of the stress loss caused by the triangular scour hole “abc” and the quadrilateral scour hole “bcde,” as shown in Figure 3. Then, taking point “a” as the origin of coordinates to establish local coordinates, the vertical stress loss and lateral stress loss of the point of interest can be given as [17]

$$\sigma'_z = \frac{2\gamma'_0 S_d h_0^3}{\pi} \int_{S_d/\tan\theta}^{2S_w+S_d/\tan\theta} \frac{1}{[(S_w + S_d/\tan\theta - x)^2 + h_0^2]^2} dx + \frac{2\gamma'_0 h_0^3 \tan\theta}{\pi} \int_0^{S_d/\tan\theta} \frac{x}{[(S_d/\tan\theta)^2 + h_0^2]^2} dx, \quad (6)$$

$$\sigma'_x = \frac{4\gamma'_0 S_d h_0}{\pi} \int_{S_w+S_d/\tan\theta}^{S_d/\tan\theta} \frac{(S_w + S_d/\tan\theta)^2}{[(S_w + S_d/\tan\theta - x)^2 + h_0^2]^2} dx + \frac{4\gamma'_0 h_0 \tan\theta}{\pi} \int_0^{S_d/\tan\theta} \frac{(S_d/\tan\theta - x)^2 x}{[(S_d/\tan\theta - x)^2 + h_0^2]^2} dx, \quad (7)$$

where σ'_z and σ'_x are the vertical and lateral stress loss of the point of interest, respectively. S_d , S_w , and θ are the scour depth, scour width, and scour slope angle of the scour hole, respectively. x is the coordinate of the location from point “a” to “d,” as shown in Figure 3.

The mean effective stress σ'_{ms} after scouring obtained by putting equations (4)–(7) together can be expressed as

$$\sigma'_{ms} = \frac{(1 + 2K_0)\gamma'_0 h_0}{(3 - (\sigma'_z + 2\sigma'_x))/3}. \quad (8)$$

With the formation of the scour hole, the soil around the caisson also changed from a normal consolidated state to an overconsolidated state. As the change of the gravity of soil is limited, the OCR can be expressed as

$$\text{OCR} = \frac{\gamma'_0 h_0}{\gamma'_0 h_0 - \sigma'_z}. \quad (9)$$

In the meantime, the stress loss of the soil around the caisson will also cause a change in void ratio, and the change value in void ratio Δe is given as

$$\Delta e = e_{0s} - e_0 = -\kappa \ln\left(\frac{\sigma'_{ms}}{\sigma'_m}\right), \quad (10)$$

where e_0 and e_{0s} are the void ratio before and after scouring, respectively; and κ is the swelling index from an isotropic consolidation test.

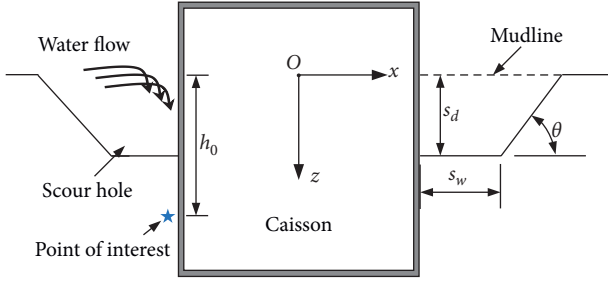


FIGURE 2: Illustration of the scour hole around the caisson foundation.

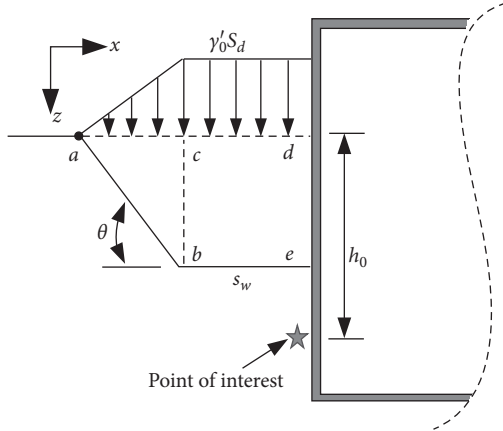


FIGURE 3: Illustration of scour-hole stress loss.

By putting equations (4) and (8) together, Δe can be rewritten as

$$\Delta e = -\kappa \ln \left[\frac{(1 + 2K_0)\gamma'_0 h_0 - (\sigma'_z + 2\sigma'_x)}{(1 + 2K_0)\gamma'_0 h_0} \right]. \quad (11)$$

In addition, the shear modulus of soil is related to the mean effective stress, void ratio, and overconsolidation ratio (OCR). For normally consolidated clay, it can be taken as [18, 19]

$$G_0 = 3230 \frac{(2.97 - e_0)^2}{1 + e_0} (\text{OCR})^k (\sigma'_m)^{0.5}, \quad (12)$$

where k is the parameter related to the plasticity index, equal to 0.18 as suggested in [19].

After scouring, the shear modulus of soil can be rewritten as

$$G_{0s} = 3230 \frac{(2.97 - e_{0s})^2}{1 + e_{0s}} \left(\frac{\gamma'_0 h_0}{\gamma'_0 h_0 - \sigma'_z} \right)^k (\sigma'_{ms})^{0.5}. \quad (13)$$

Generally, the soil around the caisson foundation shows nonlinear characteristics in practical engineering. In order to consider the nonlinear characteristics of the soil with the change of soil strain and the change of cyclic loading and unloading, the hyperbolic stress-strain relationship model was introduced to modify the proposed model:

$$\tau(\gamma) = \frac{G_0 \cdot \gamma}{G_0 \cdot \gamma / (S_u + 1)}, \quad (14)$$

where G_0 is the shear modulus of soil, $\tau(\gamma)$ is the shear stress, and S_u is the undrained shear strength. γ is shear strain of soil, which can be approximated by the following equation [20]:

$$\gamma = \frac{1 + \nu}{2.5B} y, \quad (15)$$

where y is the lateral displacement of the foundation, ν is Poisson's ratio of soil, and B is the diameter of the foundation.

The hysteretic curves of shear stress and strain obtained by Masing's rules are used to simulate the loading, reloading, and unloading, which is expressed as

$$\tau \pm \tau_{ur} = \frac{\gamma \pm \gamma_{ur}}{1/G_0 + |\gamma \pm \gamma_{ur}|/(2\tau_f)}, \quad (16)$$

where γ_{ur} and τ_{ur} are the current shear strain and shear stress at the onset of unloading or reloading, and τ_f is the shear stress at failure, given as [19]

$$\tau_f = \left[\left(\frac{1 + K_0}{2} \sigma'_v \sin \varphi' + c \cos \varphi' \right)^2 - \left(\frac{1 - K_0}{2} \sigma'_v \right)^2 \right]^{0.5}, \quad (17)$$

where σ'_v is the vertical effective stress of soil, and c and φ' are the cohesive force and effective internal friction angle of soil, respectively.

The key to calculating the dynamic stiffness matrix $[K_b]$ and damping matrix $[C_b]$ is to determine the stiffness coefficient k_{xi} , k_{ri} and the damping coefficient c_{xi} , c_{ri} , which are closely related to the shear modulus of soil. Once the soil parameters, such as the effective unit weight of soil γ'_0 and void ratio e_0 , are determined, the stiffness coefficients k_{xi} , k_{ri} and the damping coefficients c_{xi} , c_{ri} at a certain scour state with scour depth S_d , scour width S_w , and scour slope angle θ can be re-examined by equation (13). Then, the dynamic response of a caisson subjected to the lateral load can be calculated based on the proposed model.

3. Verification of the Proposed Model

A numerical simulation presented herein demonstrates the application of the proposed method for the lateral response of the caisson. The height, embedded depth, and diameter of the caisson are 120 m, 70 m, and 90 m, respectively, embedded in cohesive soil stratum. Young's modulus, Poisson's ratio, and mass density of the concrete caisson are 36 GPa, 0.3, and 2600 kg/m³, respectively. The thickness of the top, bottom, and side walls of caisson are 3.0 m. The density, initial void ratio, Poisson's ratio, and undrained shear strength of soil around the caisson are 1600 kg/m³, 0.7, 0.49, and 100 kPa, respectively. It is assumed that the scour depth S_d , the scour width S_w , and the scour slope angle θ around the caisson foundation are 20 m, 18 m, and 30°, respectively. According to the symmetry principle, half of the meshing model is depicted in Figure 4, where the model sizes are

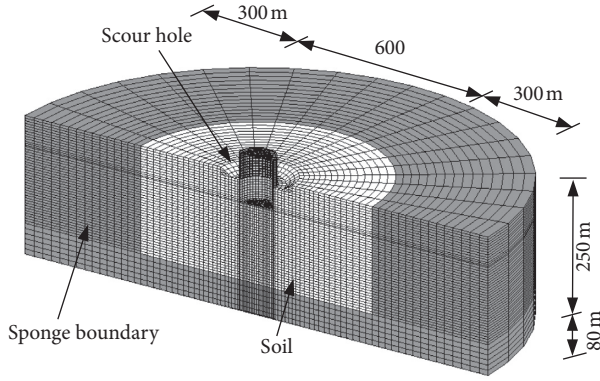


FIGURE 4: FEM model of caisson foundation.

marked. During the dynamic finite element calculation, the boundary processing is an important factor affecting the accuracy of the results. Here, the sponge boundary is adopted to attenuate the wave reflection in the dynamic finite element analysis, which was proposed by Varun et al. [21]. The gray elements enveloping the soil and caisson elements are the sponge boundary elements. It is believed that the purpose of attenuating the wave reflection can be achieved by changing the Rayleigh damping parameters within the sponge layer and the thickness of the sponge boundary layer [21]. Based on this fundamental, the Rayleigh damping parameters are selected 10.5 and 0.0105, and boundary thickness in this example is determined as 300 m. Then, the resulting amplitude reduction of P wave and S wave with frequency can be described by the curves in Figure 5. It can be seen that the higher the frequency, the more the energy of the wave being absorbed by the sponge boundary.

In order to consider the soil nonlinearity around the caisson, a hyperbolic stress-strain curve has been used in the simplified theoretical model. However, the constitutive model of soil in the finite element method (FEM) is usually selected as ideal elastoplastic, which is different from the hyperbolic stress-strain relationship used in the theoretical model. Therefore, the hyperbolic stress-strain characteristics in the FEM are simulated by the method of importing yield stress and plastic strain, and the hyperbolic hardening law can be defined by a multisegment line [22]. The yield stress and corresponding plastic strain within the embedded depth of the caisson before and after scouring are shown in Table 1.

Here, the caisson subjected to lateral harmonic loads 200 MN is used to compare the dynamic responses by considering the soil nonlinearity effect. The dynamic response curves of the top displacement of the caisson before and after scouring at different frequencies are calculated by the FEM. Comparison with the theoretical results are shown in Figure 6. It can be seen that the result of the simplified method is slightly larger than the FEM results, but the trend of the theoretical results is close to that of the FEM results, which indicates the rationality of the simplified method. In the meantime, the dynamic displacement of the caisson foundation before and after scouring both have a resonance peak value under the different frequencies of vibration loads.

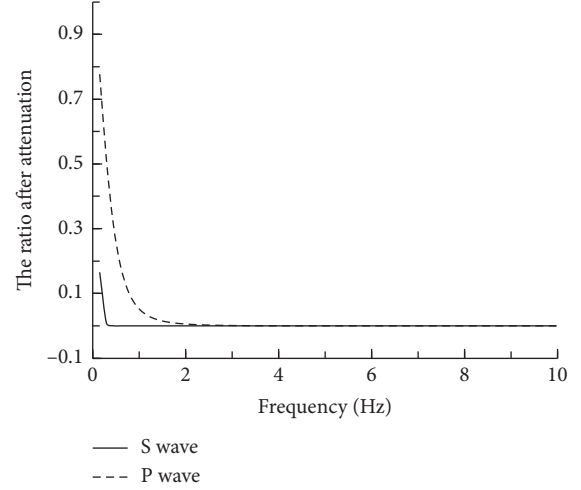
FIGURE 5: Absorption of S and P waves at the sponge boundary.

TABLE 1: Yield stresses and corresponding plastic strains at different embedded depths.

Yield stress (kPa)		40	120	160	195
Before scouring $\int d\epsilon^p$	0–20 m	$2.8e-5$	$5.1e-4$	0.0018	0.021
	20–40 m	$1.4e-5$	$2.6e-4$	$9.2e-4$	0.011
	40–60 m	$1.1e-5$	$2.0e-4$	$7.2e-4$	0.009
	Below 60 m	$9.9e-6$	$1.8e-4$	$6.4e-4$	0.008
After scouring $\int d\epsilon^p$	0–20 m	$2.5e-5$	$4.5e-4$	0.0016	0.019
	20–40 m	$1.3e-5$	$2.5e-4$	$8.8e-4$	0.010
	Below 40 m	$1.1e-5$	$2.0e-4$	$7.3e-4$	0.009

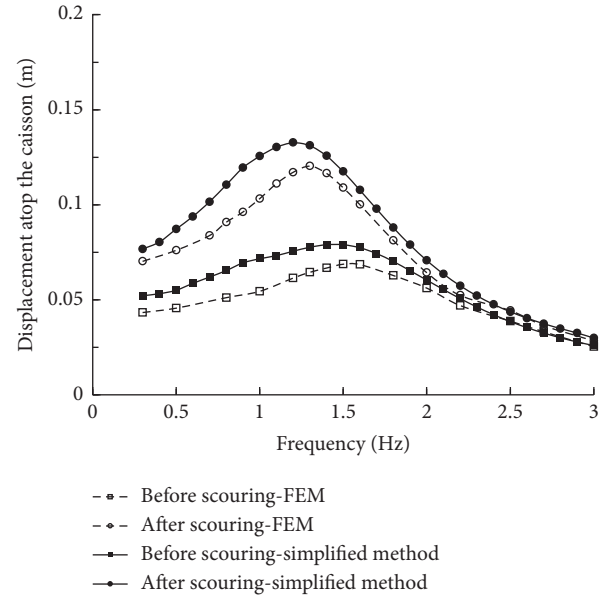


FIGURE 6: Dynamic response of caisson before and after scouring.

Notice that the displacement amplitude after scouring shows an increasing trend compared with that before scouring, while the resonant frequency shows a decreasing trend. The maximum displacement deviation between the results of the

simplified method and the FEM after scouring is about 13.3%. This is partly attributed to the limitation of the plane strain assumption in considering three-dimensional problems, which slightly magnifies the stress loss caused by the scour hole. Finally, time histories of lateral displacement atop the caisson when the frequency equals to 1.4 Hz before scouring and the frequency equal to 1.2 Hz after scouring have been extracted to make a further comparison between the FEM and the proposed simplified method, as shown in Figures 7 and 8. These comparisons show that the simplified method agrees well with the FEM, ensuring the reliability of the simplified method.

4. Simulation of the Scour Holes and Parametric Study

In order to further explore the effect of the scour hole on the lateral dynamic characteristics of the caisson foundation, the caisson foundation adopted in the FEM is used for analysis. A parametric study was conducted to evaluate the effects of scour depth, scour width, and scour slope angle on the responses of the caisson. The scour width varied from $0.2B$, B , $5B$ to $10B$, whereas the scour depth ($S_d = 0.3d$) and scour-hole slope angle ($\theta = 30^\circ$) were kept unchanged. Four scour slope angles ($\theta = 1^\circ$, 5° , 10° , and 30°) were considered to evaluate their effects on the responses of caisson when the scour depth was $0.3d$ and the scour width was $0.2B$. Three scour depths ($S_d = 0.15d$, $0.3d$, and $0.45d$) were investigated when the scour width was $0.2B$ and the scour-hole slope angle was 30° . The corresponding working conditions of scouring are summarized in Table 2. Here, $S_w = 0.2B$ (18 m), $\theta = 30^\circ$, and $S_d = 0.3d$ (20 m) were selected as reference values.

4.1. Effect of Scour Width. Figure 9 shows the dynamic lateral displacement atop the caisson after scouring as a function of the frequency computed by the simplified method at four different scour widths. It can be seen that the dynamic displacement increased significantly with scour width at an accelerating rate. The percentage increases in the peak value of the displacement compared with the no scouring condition are 70.1%, 112.7%, 141.7%, and 146.8% when scour width varied from $0.2B$ to $10B$. The total amplitude change in the peak displacement caused by the scour width is about 76.7%. It can also be found that the resonant frequency of the foundation changes very little under different scouring widths. The resonant frequency and the peak value of the displacement when the scour width was $5B$ are basically the same as when the scour width was $10B$, which indicates that the effect of the scour width was found to be the same as that at complete removal of the soil layer when the scour width was greater than $5B$. This phenomenon can also be observed from the stress-strain hysteresis curves of the surface soil around the caisson under different scour widths, as shown in Figure 10. The stress-strain curve gradually slopes downward as the scour width increases, and the peak value of curves approached a constant when the scour width exceeded $5B$. Therefore, it can be known that the traditional

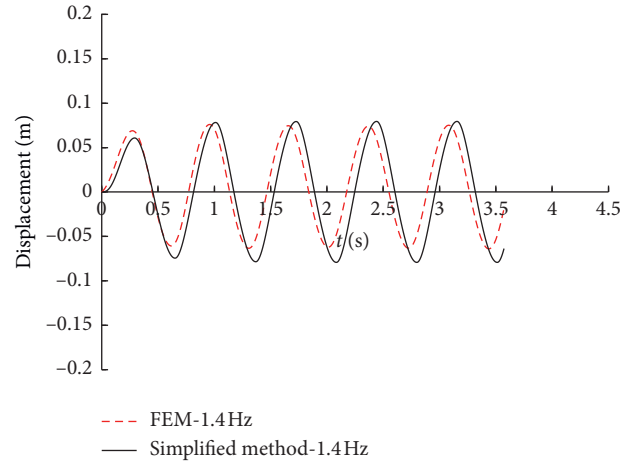


FIGURE 7: Time histories of lateral displacement atop the caisson before scouring.

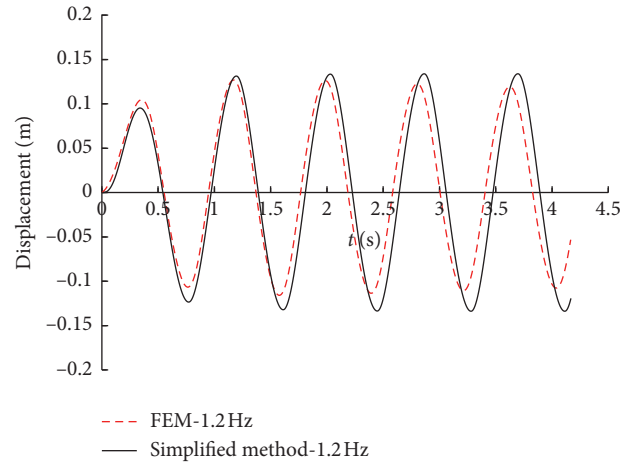


FIGURE 8: Time histories of lateral displacement atop the caisson after scouring.

TABLE 2: Working conditions of scouring.

Working conditions		S_d	S_w	θ
Variation of scour width	W1	$0.3d$	$0.2B$	30°
	W2	$0.3d$	B	30°
	W3	$0.3d$	$5B$	30°
	W4	$0.3d$	$10B$	30°
Variation of scour slope angle	A1	$0.3d$	$0.2B$	1°
	A2	$0.3d$	$0.2B$	5°
	A3	$0.3d$	$0.2B$	10°
	A4	$0.3d$	$0.2B$	30°
Variation of scour depth	S1	$0.15d$	$0.2B$	30°
	S2	$0.3d$	$0.2B$	30°
	S3	$0.45d$	$0.2B$	30°

method of completely removing the soil layer is conservative for the scouring analysis. The percentage difference of the peak value of the dynamic displacement atop the caisson between case W1 and case W4 can reach 45.4%.

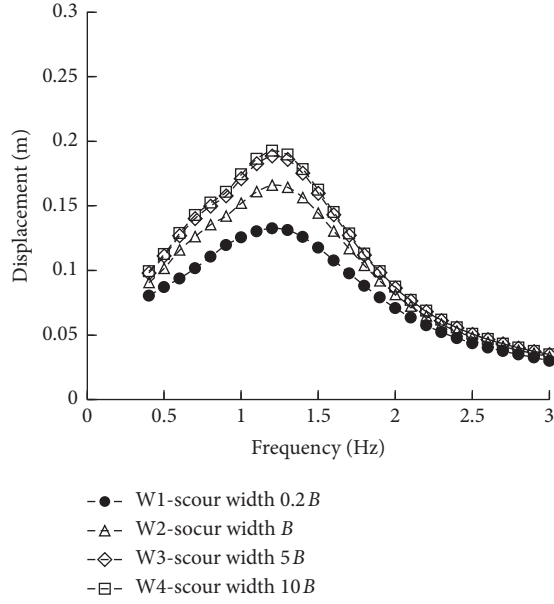


FIGURE 9: Dynamic response of caisson foundation under different scour widths.

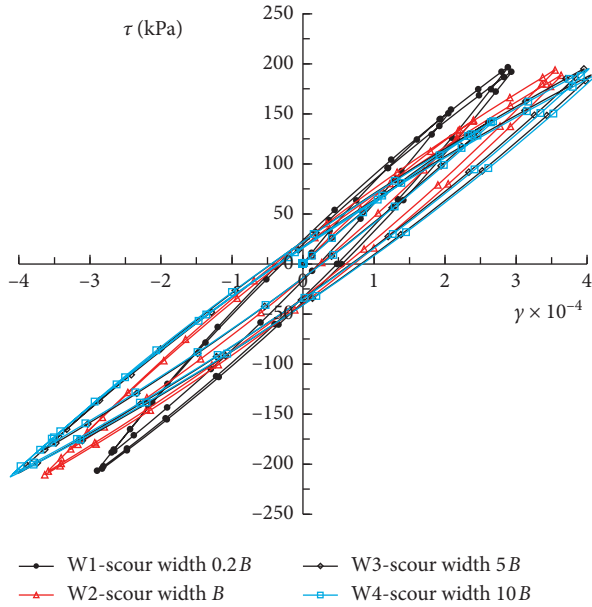


FIGURE 10: Stress-strain hysteresis loops of the surface soil under different scour widths.

4.2. Effect of Scour Slope Angle. The effects of the scour-hole slope angle on the dynamic lateral displacement atop the caisson are shown in Figure 11. An increase in the scour-hole slope angle decreased the dynamic response of the caisson. The percentage increases in the peak value of the displacement compared with the no scouring condition are 70.1%, 90.5%, 111.7%, and 129.4% when the scour slope angle varied from 30° to 1°. A decrease in the slope angle from 30° to 1° results in an increase in the displacement by approximately 59.3%. This stems from the fact that a smaller scour-hole slope angle means less overburden soil remaining

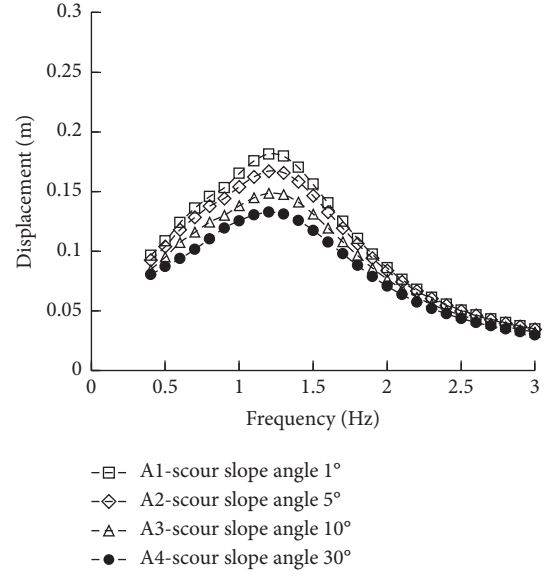


FIGURE 11: Dynamic response of caisson foundation under different scour slope angles.

above the post scour groundline, consequently, more soil resistance is induced. Similar to the previous comparisons, it can also be found that the dynamic response of case A1 almost coincided with that of case A2, and the maximum difference of displacement between case A1 and case A2 is 17.7%, which is relatively small for practical engineering. It can be concluded that the scour slope angle effect could be ignored when the scour slope angle was smaller than or equal to 5°. Compared with the effects of the scour slope angle, the variation of the dynamic response caused by the effect of scour width becomes more notable when scour depths are the same. This similar trend also reflected in the stress-strain hysteresis curves of the soil around the caisson, as shown in Figure 12. The smaller the scour slope angle is, the soil stress-strain hysteresis curve gradually slopes downward, that is, the increase in the strength of soil nonlinearity.

4.3. Effect of Scour Depth. The effects of the scour depth on the dynamic lateral displacement atop the caisson are shown in Figure 13. Here, three different scour depths 0.15d, 0.3d, and 0.45d are discussed. Considering the effect of scour depth on the resonant frequency, the value of resonant frequency gradually decreases with the increase in the scour depth around the caisson, which is different from the effect of the scour width and scour slope angle on the resonant frequency of the foundation; and the percentage increases in the peak value of the displacement compared with the no scouring condition are 14.4%, 70.1%, and 242.1% when scour depth varied from 0.15d to 0.45d. It shows an obvious nonlinear increasing trend compared with the effect of scour width and scour slope angle. The main reason for this phenomenon is that the soil loss around the caisson leads to the weakening of the lateral restraint of foundation, and the change of the stress state of the remaining soil may be the

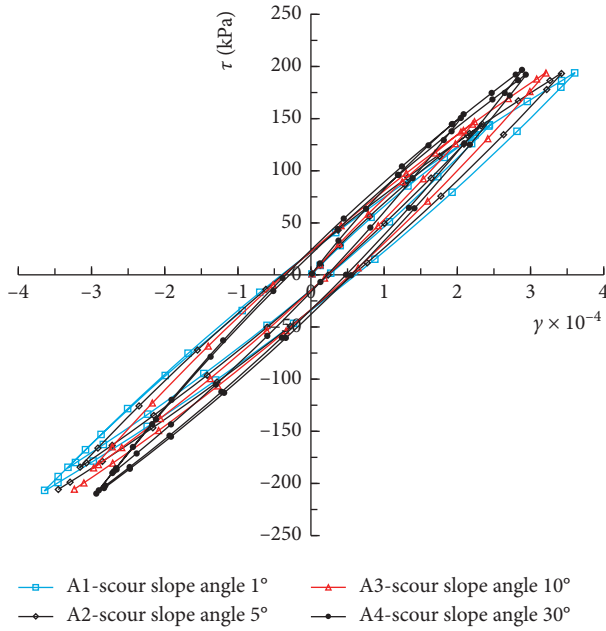


FIGURE 12: Stress-strain hysteresis loops of the surface soil under different scour slope angles.

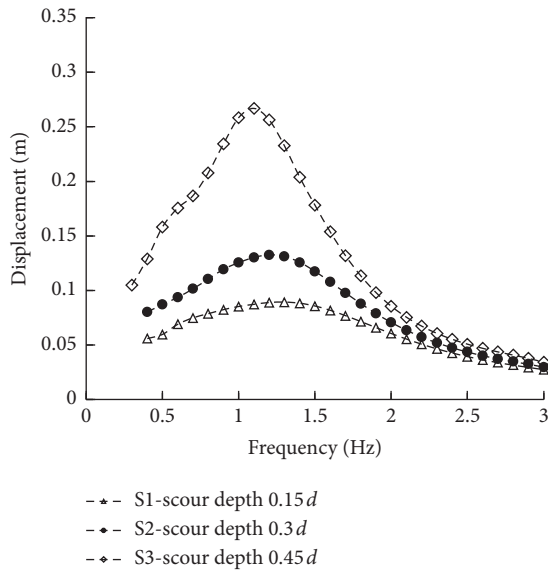


FIGURE 13: Dynamic response of caisson foundation under different scour depths.

second important factor resulting in the increase in the displacement. Figure 14 shows the stress-strain hysteresis curves of the soil around the caisson under different scour depth. It can be seen that the strength of soil nonlinearity is the other factor affecting the dynamic response of the foundation. The greater the scour depth, the larger the strength of the soil nonlinearity around the foundation and the greater the displacement response of the foundation.

From the above analysis, it can be drawn that the scour depth is the most important factor among the three scour-hole dimensions (scour depth, scour width, and scour slope angle) influencing the dynamic responses of the laterally

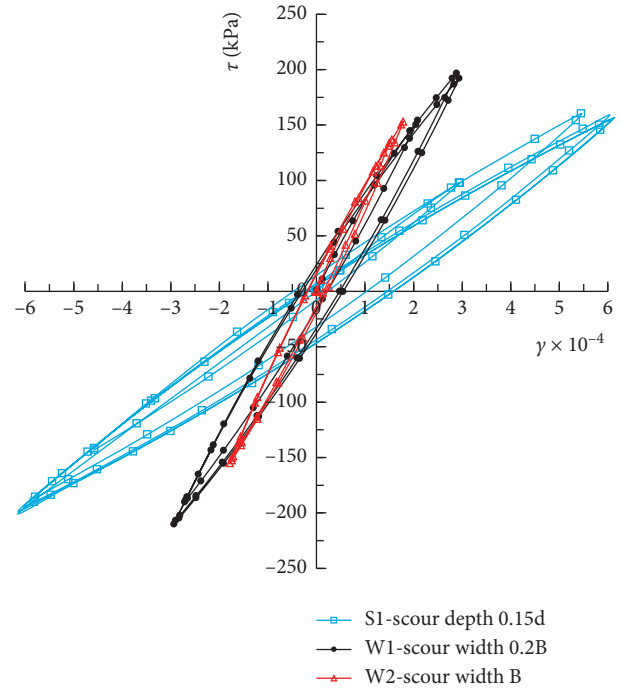


FIGURE 14: Stress-strain hysteresis loops of the surface soil under different scour depths.

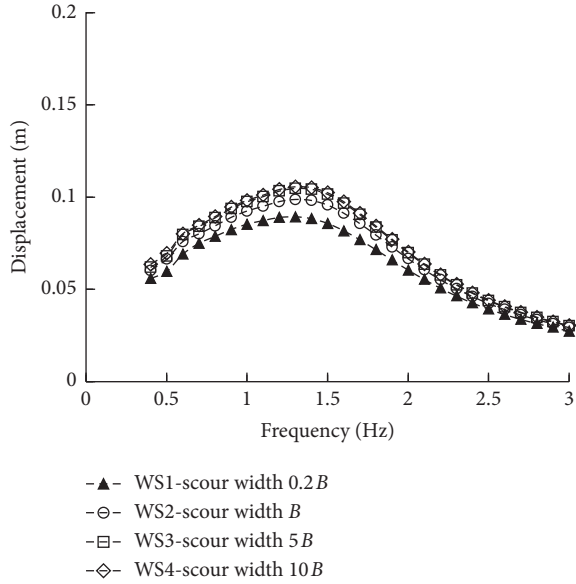
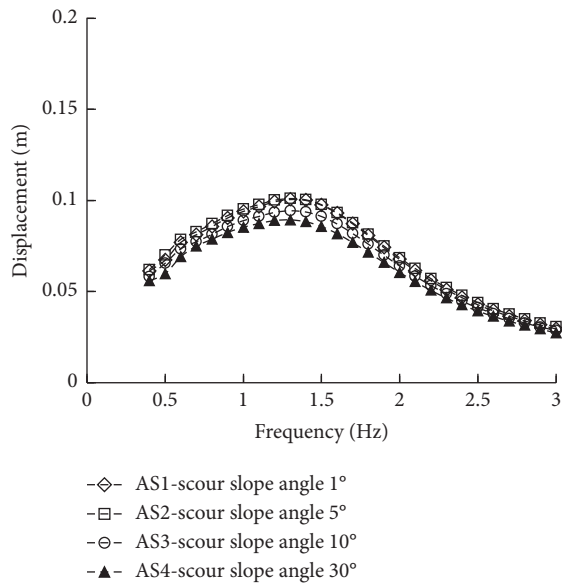
loaded foundation. Obviously, it should be worth paying more attention on the effect of scour depth on the dynamic response of the foundation. Whether the effect of the scour slope angle and the scour width on the dynamic characteristics of foundation is still affected by the scour depth should be further investigated. Therefore, the effect of scour slope angle and scour width on the dynamic characteristics of foundation are discussed when the scour depth is $0.15d$ (10 m). The working conditions are summarized in Table 3.

The lateral dynamic displacement of the caisson as a function of frequency under different scour widths and scour slope angles are shown in Figures 15 and 16. Compared with Figures 9 and 11, the overall trend of the results is roughly consistent with the change pattern given in Figures 15 and 16; however, the variation amplitude of dynamic responses is significantly reduced with the change of scour width and scour slope angle when scour depth is at a low value. The degree of displacement increase became more notable under a higher scour depth. This is mainly attributed to the small change in the stress state of the soil around the caisson. In the meantime, it can also be found that the scour width effect could be ignored when the width was greater than or equal to $5B$ and the scour slope angle effect could be ignored when the scour slope angle was less than or equal to 5° .

It is worth noting that there are two major limitations that need to be addressed for the simplified method. First, a gap will occur between the caisson foundation and soil, and this effect was not considered in this simplified method. Second, the proposed model for evaluating the dynamic response of the caisson is based on the plane strain hypothesis, as well as the scour hole around the caisson foundation. More accurate analysis needs to be studied

TABLE 3: Working conditions with scour depth at $0.15d$.

Working conditions	S_d	S_w	θ
Variation of scour width	WS1	$0.15d$	$0.2B$
	WS2	$0.15d$	B
	WS3	$0.15d$	$5B$
	WS4	$0.15d$	$10B$
Variation of scour slope angle	AS1	$0.15d$	$0.2B$
	AS2	$0.15d$	$0.2B$
	AS3	$0.15d$	$0.2B$
	AS4	$0.15d$	$0.2B$

FIGURE 15: Effect of scour width on the dynamic response of caisson foundation ($S_d = 0.15d$).FIGURE 16: Effect of slope angle on the dynamic response of caisson foundation ($S_d = 0.15d$).

further through a three-dimensional model. However, given its simplicity, the proposed method can still obtain the dynamic response of the scoured caisson foundation from a qualitative perspective.

5. Conclusions

In this paper, the dynamic characteristics of the caisson foundation before and after scouring have been studied. A simplified method was developed to evaluate the effects of the scour-hole dimensions on the responses of the laterally loaded caisson in layered soils. The influence of three factors of the scour-hole dimension on the dynamic characteristics of the foundation is discussed. The following conclusions can be drawn:

- (1) Scour depth is the most important factor influencing the dynamic displacement and resonant frequency of the laterally loaded caisson foundation, whereas the scour width does less and the slope angle does the least. An increase in scour depth significantly increases the lateral displacement and decreases resonant frequency of foundation.
- (2) An increase in scour width and scour slope angle correlates with an increase in dynamic displacement of the caisson at first, and then the peak value of displacement remains constant with the increase in the scour width and scour slope angle. It can also be found that the effect of scour width could be ignored when the width was greater than or equal to $5B$ and the effect of scour slope angle could be ignored when the scour slope angle was less than or equal to 5° .
- (3) The overall trend of the result is roughly consistent with the change pattern when scour depth is at different values, and it is found that the degree of displacement increases more significantly when the scour depth is at a larger value.

Appendix

The stiffness and damping coefficient of the distributed horizontal and rocking springs of soil k_{xi} , c_{xi} and k_{ri} , c_{ri} can be given as [16]

$$k_{xi} = \frac{1}{d} (K_{hh} - K_h). \quad (\text{A.1})$$

$$c_{xi} = \frac{1}{d} (C_{hh} - C_h), \quad (\text{A.2})$$

$$k_{ri} = \frac{1}{d} \left(K_{rr} - K_r + \frac{1}{3} d^2 K_h - \frac{1}{3} d^2 K_{hh} \right), \quad (\text{A.3})$$

$$c_{ri} = \frac{1}{d} \left(C_{rr} - C_r + \frac{1}{3} d^2 C_h - \frac{1}{3} d^2 C_{hh} \right), \quad (\text{A.4})$$

where

$$K_{hh} = \frac{4GB}{2-v} I_{tw}, \quad (\text{A.5})$$

$$C_{hh} = \frac{B}{2V_s} \cdot K_{hh} \cdot c_{hc}, \quad (\text{A.6})$$

$$K_{hr} = K_{rh} = \frac{1}{3} dK_{hh}, \quad (\text{A.7})$$

$$C_{hr} = C_{rh} = \frac{1}{3} dC_{hh}, \quad (\text{A.8})$$

$$K_{rr} = k_{rc} \cdot \frac{GB^3}{3(1-v)} \Gamma_w, \quad (\text{A.9})$$

$$C_{rr} = \frac{B}{2V_s} \cdot \frac{GB^3}{3(1-v)} \Gamma_w \cdot c_{rc}, \quad (\text{A.10})$$

$$I_{tw} = 1 + 0.21 \left(\frac{d}{B} \right)^{0.5} + 1.43 \left(\frac{d}{B} \right)^{0.8} + 0.30 \left(\frac{d}{B} \right)^{1.3}, \quad (\text{A.11})$$

$$c_{hc} = \left(0.68 + 0.57 \sqrt{\frac{2d}{B}} \right), \quad (\text{A.12})$$

$$\Gamma_w = 1 + 2.25 \left(\frac{d}{B} \right)^{0.6} + 7.01 \left(\frac{d}{B} \right)^{2.5}, \quad (\text{A.13})$$

$$k_{rc} = 1 - \frac{\mu_1}{1 + (\mu_1^2/\mu_2^2)}, \quad (\text{A.14})$$

$$c_{rc} = \frac{\mu_1}{\mu_2} (1 - k_{rc}) + 0.32 \frac{d}{B}, \quad (\text{A.15})$$

$$\mu_1 = 0.33 + 0.4 \left(\frac{d}{B} \right)^2, \quad (\text{A.16})$$

$$\mu_2 = 0.4 + 0.12 \left(\frac{d}{B} \right)^2, \quad (\text{A.17})$$

where G , v , and V_s are the shear modulus, Poisson's ratio, and shear wave velocity of soil.

Data Availability

Data used to support the findings of this study are included within the manuscript.

Conflicts of Interest

The authors declare that there are no conflicts of interest regarding the publication of this paper.

Acknowledgments

This work was financially supported by the National Natural Science Foundation of China (Grant nos. 51808220 and 51822809), the Natural Science Foundation of Jiangxi Province (Grant nos. 20192BAB216036 and 20192ACBL21003), and the Shanghai Municipal Science and Technology Major Project (Grant no. 2017SHZDZX02).

References

- [1] F. Liang, C. Wang, M. Huang, et al., "Scale effects on local scour configurations around caisson foundation and dynamic evolution," *China Journal of Highway and Transport*, vol. 29, no. 9, pp. 59–67, 2013, in Chinese.
- [2] G. Dai, H. Dai, Y. Yang, et al., "Computation method and bearing characteristics of lateral bearing single pile foundation under scour condition," *China Journal of Highway and Transport*, vol. 31, no. 8, pp. 104–112, 2018, in Chinese.
- [3] C. Chen, "Model experiment and study on local scour of large scale floating open caisson foundation," *Highway*, vol. 12, pp. 18–21, 2010, in Chinese.
- [4] Z. Lu, Z. Gao, and C. Yang, "Experimental study on local scour during large caisson foundation construction," in *Proceedings of the 14th China Ocean Engineering Symposium*, Huhehaote, China, August 2009, pp. 260–267, in Chinese.
- [5] W. Peng, J. Shen, X. Tang, et al., "Review, analysis, and insights on recent typical bridge accidents," *China Journal of Highway and Transport*, vol. 32, no. 12, pp. 1139–1146, 2019, in Chinese.
- [6] J. Liu, X. Chen, Z. Zhu, et al., "Investigation of scour effects on lateral behaviors of suction caisson," *Marine Georesources and Geotechnology*, vol. 37, no. 2, pp. 142–151, 2019.
- [7] C. Zhang, X. Zhang, M. Huang, et al., "Responses of caisson-piles foundations to long-term cyclic lateral load and scouring," *Soil Dynamics and Earthquake Engineering*, vol. 119, pp. 62–74, 2019.
- [8] W. Tu, M. Huang, X. Gu, and H.-P. Chen, "Nonlinear dynamic behavior of laterally loaded composite caisson-piles foundation under scour conditions," *Marine Georesources and Geotechnology*, pp. 1–16, 2020.
- [9] W. Tu, M. Huang, X. Gu, H.-P. Chen, and Z. Liu, "Experimental and analytical investigations on nonlinear dynamic response of caisson-pile foundations under horizontal excitation," *Ocean Engineering*, vol. 208, Article ID 107431, 2020.
- [10] M. Zhao, X. Zhu, L. Cheng, and B. Teng, "Experimental study of local scour around subsea caissons in steady currents," *Coastal Engineering*, vol. 60, pp. 30–40, 2012.
- [11] F. Liang, C. Wang, and X. Yu, "Widths, types, and configurations: influences on scour behaviors of bridge foundations in non-cohesive soils," *Marine Georesources and Geotechnology*, vol. 37, no. 5, pp. 578–588, 2019.
- [12] F. Li, J. Han, and C. Lin, "Effect of scour on the behavior of laterally loaded single piles in marine clay," *Marine Georesources and Geotechnology*, vol. 31, no. 3, pp. 271–289, 2013.
- [13] F. Liang, X. Liang, H. Zhang et al., "Seismic response from centrifuge model tests of a scoured bridge with a pile-group foundation," *Journal of Bridge Engineering*, vol. 25, no. 8, pp. 1–13, 2020.
- [14] X. Yang, C. Zhang, M. Huang, and J. Yuan, "Lateral loading of a pile using strain wedge model and its application under scouring," *Marine Georesources and Geotechnology*, vol. 36, no. 3, pp. 340–350, 2018.

- [15] H. Zhang, S. Chen, and F. Liang, "Effects of scour-hole dimensions and soil stress history on the behavior of laterally loaded piles in soft clay under scour conditions," *Computers and Geotechnics*, vol. 84, pp. 198–209, 2017.
- [16] M. Huang, W. Tu, and X. Gu, "Time domain nonlinear lateral response of dynamically loaded composite caisson-piles foundations in layered cohesive soils," *Soil Dynamics and Earthquake Engineering*, vol. 106, pp. 113–130, 2018.
- [17] J. B. Kennedy, J. T. Laba, and M. A. Mossaad, "Reinforced earth retaining walls under strip load," *Canadian Geotechnical Journal*, vol. 17, no. 3, pp. 382–394, 1980.
- [18] J. Yang and X. Q. Gu, "Shear stiffness of granular material at small strains: does it depend on grain size?" *Géotechnique*, vol. 63, no. 2, pp. 165–179, 2013.
- [19] B. O. Hardin and V. P. Drnevich, "Shear modulus and damping in soils: design equations and curves," *Journal of Soil Mechanics and Foundations Division*, vol. 98, no. 7, pp. 667–692, 1972.
- [20] T. Kagawa and L. M. Kraft, "Lateral load deflection relationships of piles subjected to dynamic loadings," *Soils Foundation*, vol. 20, no. 4, pp. 19–36, 1980.
- [21] D. A. Varun, D. Assimaki, and G. Gazetas, "A simplified model for lateral response of large diameter caisson foundations-Linear elastic formulation," *Soil Dynamics and Earthquake Engineering*, vol. 29, no. 2, pp. 268–291, 2009.
- [22] M. Huang, J. Yu, and C. Zhang, "P-y curves of laterally loaded piles in clay based on strain path approach," *Chinese Journal of Geotechnical Engineering*, vol. 37, no. 3, pp. 400–409, 2015, in Chinese.

Research Article

Vibration-Isolation Performance of a Pile Barrier in an Area of Soft Soil in Shanghai

X. F. Ma,^{1,2,3} M. Y. Cao,² X. Q. Gu ,^{2,3} B. M. Zhang,² Z. H. Yang,⁴ and P. F. Guan⁴

¹School of Civil Engineering, Kashi University, Kashi 844006, China

²Department of Geotechnical Engineering, Tongji University, Shanghai 200092, China

³Key Laboratory of Geotechnical and Underground Engineering of Ministry of Education, Tongji University, Shanghai 200092, China

⁴Shanghai Tunnel Engineering & Rail Transit Design and Research Institute, Shanghai 200092, China

Correspondence should be addressed to X. Q. Gu; guxiaoqiang@tongji.edu.cn

Received 29 August 2020; Revised 16 September 2020; Accepted 22 September 2020; Published 7 October 2020

Academic Editor: Xing Ma

Copyright © 2020 X. F. Ma et al. This is an open access article distributed under the Creative Commons Attribution License, which permits unrestricted use, distribution, and reproduction in any medium, provided the original work is properly cited.

Environmental vibration caused by traffic can affect the normal operation of precision instruments, and vibration-isolation measures should be taken to reduce such negative effects. The engineering background of this paper is a hard-X-ray tunnel under construction in Shanghai, China. First, field vibration measurements are used to study the characteristics of the ground traffic, maglev, subway, and other vibration sources near the tunnel, as well as the laws governing the propagation of vibration waves in the surface and soil layer. The finite-element modelling is then used to establish a two-dimensional numerical model for the field conditions, and the numerical results are compared with the field vibration measurements to validate the applicability of the numerical model for assessing the effects of environmental vibration. Finally, how the parameters of a pile-barrier vibration-isolation system, a vibration-isolation measure used widely for tunnels, influence its performance is studied. The results show the following: with increasing distance from the vibration source, the amplitude of the vibration acceleration decreases gradually, and the high-frequency part of the vibration wave is attenuated rapidly, whereas the low-frequency part is attenuated very little. The vibration-isolation effect of the pile barrier is directly proportional to the elastic modulus of the pile body, the pile length, and the hollow ratio of the pile, and inversely proportional to the stiffness of the filling material. The pile diameter, pile row number, and row spacing have little influence on the vibration-isolation effect. Increasing the pile diameter attenuates the acceleration amplitude somewhat around 10 Hz but has no effect on it around 5 Hz. Overall, the present numerical method is well suited to evaluating environmental vibration problems.

1. Introduction

With high-speed railways being constructed at a growing rate and speeds increasing on existing railways, vibrations due to traffic loads such as rail transit and high-speed trains are having increasing impacts on the surrounding environment. Vibrations due to traffic loads impact greatly the normal lives and work of residents, the structural safety of old buildings, and the production and use of precision instruments and equipment in factories and universities [1–4]. In particular, the effects of such vibrations on some precision instruments and equipment are to produce inaccurate readings, reduce accuracy, shorten service life, and even

prevent normal operation. Therefore, vibrations due to traffic loads require urgent solutions as far as precision instruments and equipment are concerned. Examples include (i) the laboratories of the University of Washington Physics and Astronomy Building affected by light rail [5], (ii) medical buildings to be built above existing subways in Atlanta [6], and (iii) the influence of Beijing Metro Line 4 on precision equipment in the Physics Laboratory of Peking University [7]. Failure to treat vibrations due to traffic loads effectively will lead to immeasurable economic and scientific losses; therefore, it is very important to study the laws governing the propagation of vibration waves induced by traffic loads and propose vibration-reduction solutions.

There have been various previous studies of the characteristics of vibration waves induced by traffic loads and the main measures for alleviating the vibration intensity due to such loads [8–15]. Chen et al. [16] studied the response characteristics of train vibration acceleration in seasonal frozen soil near Daqing in China. Through vibration tests on a subway tunnel in Shanghai in China, Wei et al. [17] concluded that traffic loads mainly induce vertical vibrations. Schillemans [18] used a two-dimensional (2D) finite-element (FE) model to study railway vibration response and proposed vibration-reduction measures. Gardien et al. [19] analyzed the laws governing the propagation of subway vibrations in the Netherlands and studied how different model parameters influenced the calculation results. Liao et al. [20] studied the vibration-isolation effect of piles, found it to be related to the stiffness of piles, and concluded that the vibration-isolation effect of soft piles was better than that of hard piles.

Although the aforementioned research led to some meaningful conclusions, the previous studies generally involved only one vibration source and were focused mostly on the vibration responses of buildings above ground; there has been relatively little research on the vibration responses of underground tunnels with multiple vibration sources. Herein, the vibration-isolation performance of a pile barrier in an area of soft soil is studied based on a hard-X-ray free-electron laser facility under construction in Shanghai. The hard-X-ray tunnel is located in Zhangjiang Science City, which is adjacent to a maglev, metro line 16 (viaduct part), the Luoshan Road viaduct, and Luoshan Road. The vibrations in the surrounding environment are complex, and the aforementioned research results do not meet the needs of the project fully. Therefore, it is necessary to study vibration-isolation measures under the conditions of multiple vibration sources in a soft-soil area.

This paper begins with field vibration measurements being used to study the characteristics of the ground traffic, elevated road traffic, maglev, subway, and other vibration sources, as well as the laws governing the propagation of vibration waves in the surface and soil layer. Next, a numerical model of the field measurements is constructed, and its feasibility is assessed. Finally, a dynamic 2D numerical model of the maglev, Luoshan Road viaduct, Luoshan Road, and hard-X-ray tunnel is established to analyze how various parameters of the pile-barrier system influence its vibration-isolation effect.

2. Field Vibration Measurements

2.1. Problem Outline. The hard-X-ray free-electron laser facility is a major Chinese science and technology infrastructure project with the largest investment and longest construction period in China to date. The hard-X-ray tunnel is located in Zhangjiang Science City and has a buried depth of approximately 30 m and an outer diameter of 7 m. The main sources of vibration near the tunnel are a maglev, metro line 16, Luoshan Road viaduct traffic, and Luoshan Road ground traffic. Being sensitive equipment, the hard-X-ray free-electron laser equipment may be affected by

environmental vibrations; therefore, it is necessary to study the characteristics of the ground traffic, maglev, subway, and other vibration sources and the laws governing the propagation of traffic vibration waves in the surface and soil layer.

2.2. Layout of Measuring Points and Measurement Instruments. Two groups of field vibration measurements were carried out. The first group is used to study the characteristics of the ground traffic, maglev, subway, and viaduct traffic near the hard-X-ray tunnel. The detailed locations of the measurement points are given in Table 1, and the site layout is shown in Figure 1. In the second group of field tests, the laws governing the propagation of vibration waves on the surface and in the soil layer are studied by monitoring the propagation of vibration waves induced by the maglev in the soil. The detailed locations of the test points are given in Table 2, and the layout of the field tests is shown in Figure 2. The 941 B high-sensitivity acceleration sensor manufactured by the Institute of Engineering Mechanics of the China Earthquake Administration was used in the field vibration measurements. Because the vibrations induced by traffic loads are mainly vertical vibrations [16, 17], this paper focuses on the vertical vibration acceleration due to traffic loads near the hard-X-ray tunnel.

2.3. Analysis of Field Measurement Results

2.3.1. Characteristics of Vibration Sources around Hard-X-Ray Tunnel. In this study, the SeismoSignal software was used to filter and eliminate trend terms from the field vibration measurement data. In the first group of field measurements, the vertical acceleration time histories of the maglev, metro line 16 (viaduct part), Luoshan Road viaduct traffic, and Luoshan Road ground traffic were collected, and the frequency-domain information corresponding to the acceleration time histories was obtained by Fourier transform. The results are shown in Figures 3–6, and the comparison of the vibration acceleration data of the different vibration sources is summarized in Table 3. According to the calculation results, the vibration acceleration amplitudes of the maglev and metro line 16 are the largest, followed by that of the Luoshan Road viaduct traffic, with that of the Luoshan Road ground traffic being the smallest. The vibration acceleration amplitudes of the maglev, metro line 16 (viaduct part), and Luoshan Road viaduct traffic are concentrated mainly at medium and high frequencies, whereas that of the Luoshan Road ground traffic is concentrated mainly at low frequency.

2.3.2. Propagation and Attenuation Laws of Vibration Waves in Soil. The second group of field measurements measured the propagation and attenuation of vibration waves generated by the maglev in the soil. The distance between each measuring point and the maglev and the buried depth of each measuring point are given in Table 2, and the obtained acceleration time histories and their corresponding Fourier transform spectra are shown in Figures 7–14. Comparing the

TABLE 1: Positions of measurement points in the first group of tests.

GI	GI-1	GI-2	GI-3	GI-4
Distance between measuring point and hard-X-ray tunnel (m)	92	221	305	368
Buried depth (m)	0	0	0	0

Note: the measurement points are used to collect the vibration accelerations as follows: ground traffic on Luoshan Road (GI-1); traffic on Luoshan Road viaduct (GI-2); maglev (GI-3); metro line 16 (viaduct part) (GI-4).



FIGURE 1: Layout of measurement points in the first group of field measurements. (a) GI-1. (b) GI-2. (c) GI-3. (d) GI-4.

TABLE 2: Positions of measurement points in the second group of measurements.

GII	GII-8	GII-7	GII-6	GII-5	GII-4	GII-3	GII-2	GII-1
Distance between measuring point and hard-X-ray tunnel (m)	34	94	160	221	221	221	221	221
Buried depth (m)	0	0	0	0	47.8	34.6	19.1	4.5

vibration time histories and frequency spectra of measurement points GII-5–GII 8 (see Figures 7–10) shows that (i) the amplitude of the vibration acceleration decreased gradually with increasing distance from the vibration source, (ii) the vibration wave was attenuated most obviously in the high-frequency part, and (iii) the attenuation in the low-frequency part was very small. For example, once the vibration wave had travelled 160 m, its part above 40 Hz had largely disappeared and it was basically concentrated below 30 Hz. Comparing the vibration time histories and frequency spectra of measurement points GII-1–GII 5 (see Figures 10–14) shows that the vibration acceleration decreased gradually with increasing depth. For example, once the vibration wave had reached a depth of 47 m, the vibration acceleration amplitude was only 20% of that at the surface.

3. Numerical Analysis

In this part of the study, finite-element (FE) simulation was used to investigate the second group of field measurements. The results of the numerical simulations are compared with the data obtained from the field measurements to verify the effectiveness of the numerical method in simulating environmental vibrations.

3.1. FE Calculation Model. The size of the FE numerical model and the arrangement of the measuring points were established in strict accordance with the actual conditions of the second group of field measurements. The FE model is shown in Figure 15. To meet the required calculation accuracy, the size of the FE model should be 1–1.5 times the

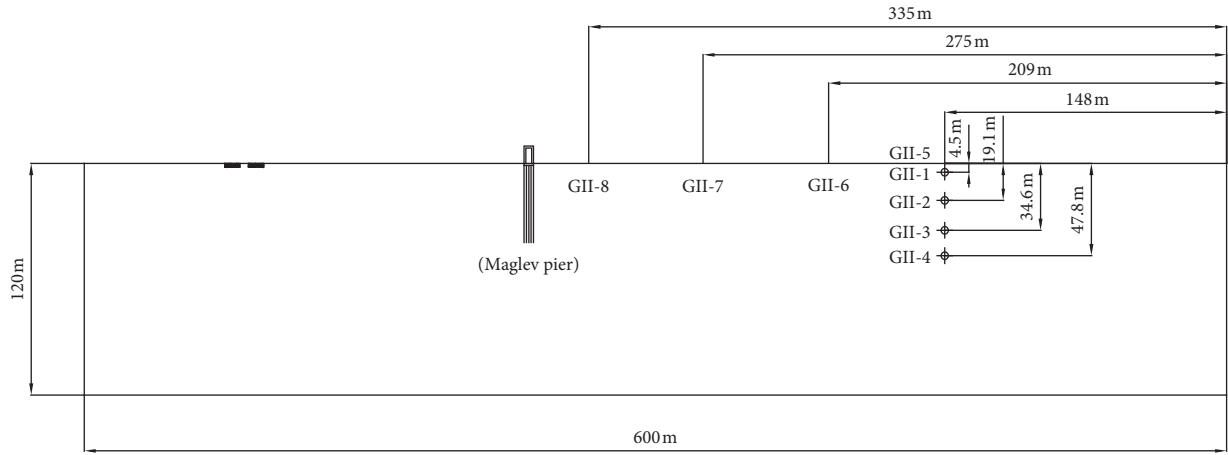


FIGURE 2: Layout of monitoring points in the second group of field measurements.

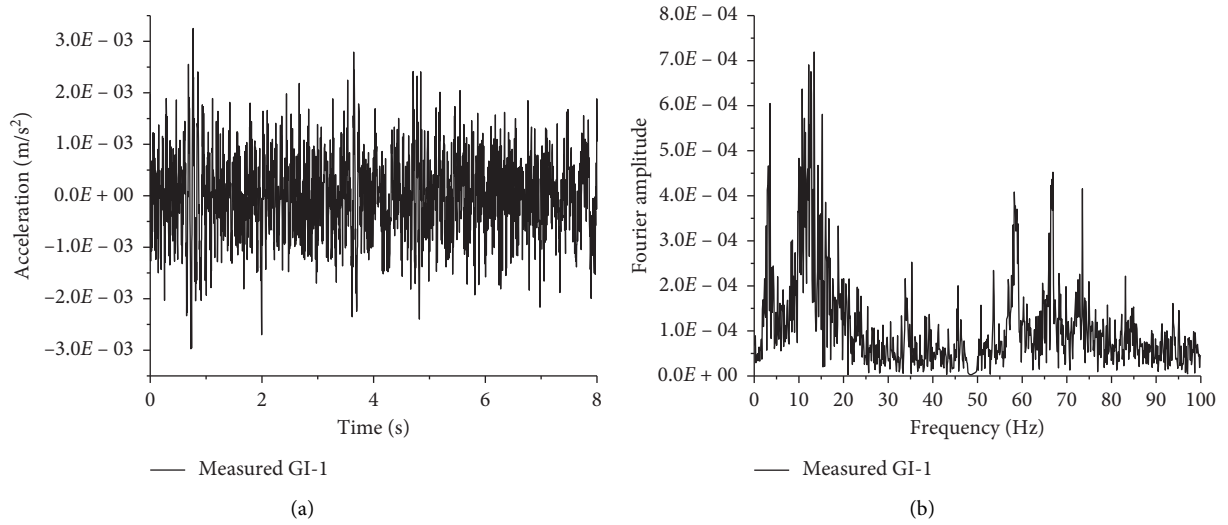


FIGURE 3: Acceleration: (a) time history and (b) frequency spectrum of GI-1.

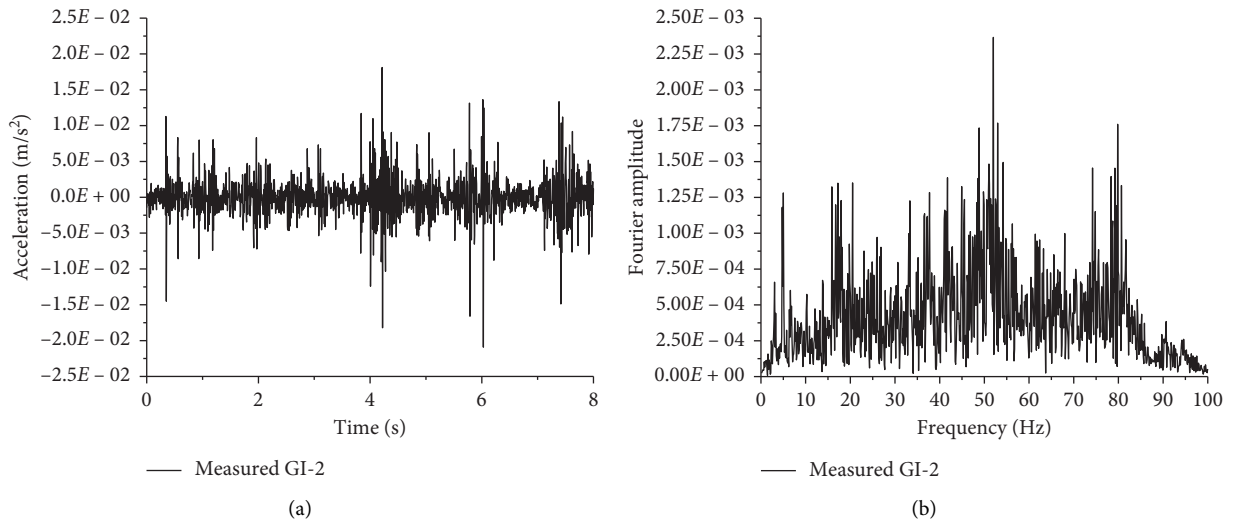


FIGURE 4: Acceleration: (a) time history and (b) frequency spectrum of GI-2.

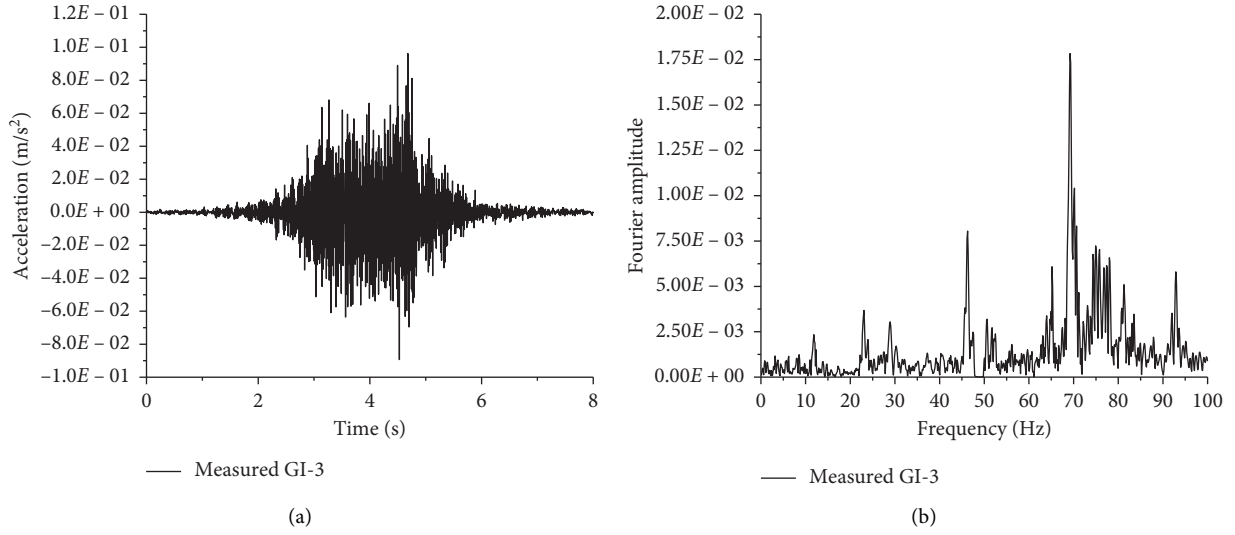


FIGURE 5: Acceleration: (a) time history and (b) frequency spectrum of GI-3.

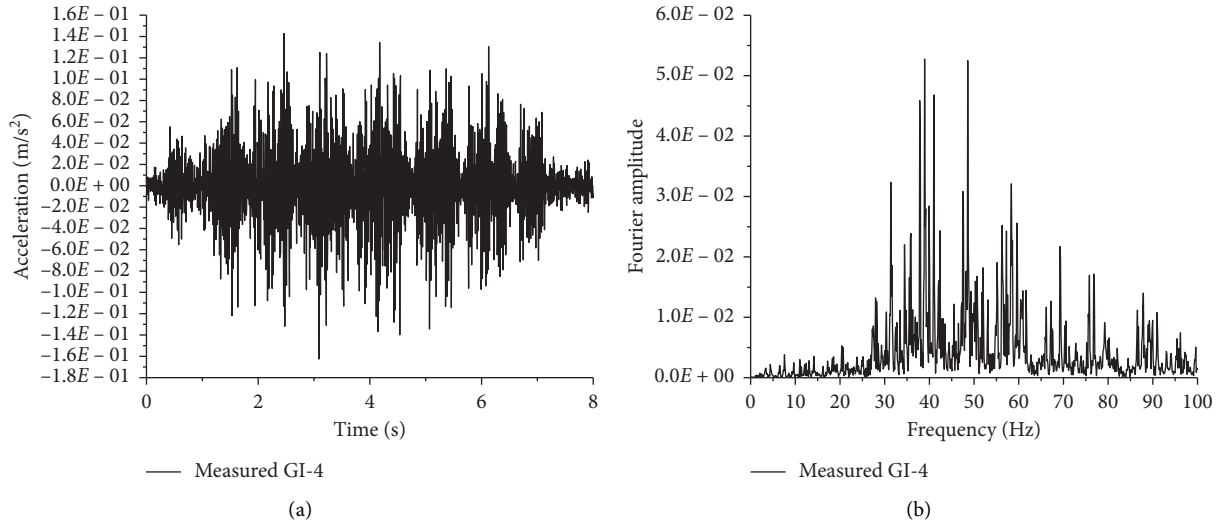


FIGURE 6: Acceleration: (a) time history and (b) frequency spectrum of GI-4.

TABLE 3: Comparison of vibration acceleration data of different vibration sources.

Measuring point	Acceleration amplitude (m/s^2)	Frequencies of amplitude (Hz)
GI-1	0.002	10–20, 55–75
GI-2	0.02	20, 52, 80
GI-3	0.14	30–60
GI-4	0.1	70

shear wavelength of interest [21]. According to the field survey data, the maximum wave velocity in the soil layer is 375 m/s (see Table 4), and the field vibration measurements show that the acceleration amplitude is attenuated slowly at 5 Hz (see Figures 7–14), so the shear wavelength of interest is approximately 75 m. Combined with the actual site conditions, the size of the soil FE model was set as $600 \text{ m} \times 120 \text{ m}$.

3.2. Model Material Parameters. For vibrations due to traffic loads, the order of magnitude of the soil strain is generally 10^{-5} or less [22], in which case, the soil is in the elastic state [23] and so the elastic model is adopted in the soil model. The physical and mechanical parameters of the soil are selected according to the field survey data (see Table 4). The in situ shear wave velocities of the soil are measured by suspension logging technique during the site investigation

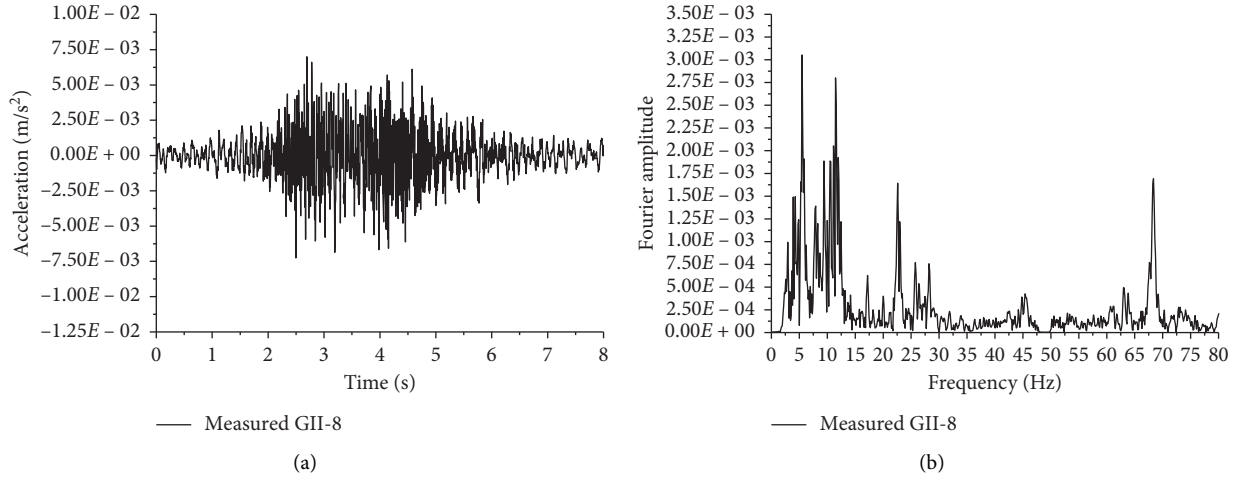


FIGURE 7: Acceleration: (a) time history and (b) frequency spectrum of GII-8.

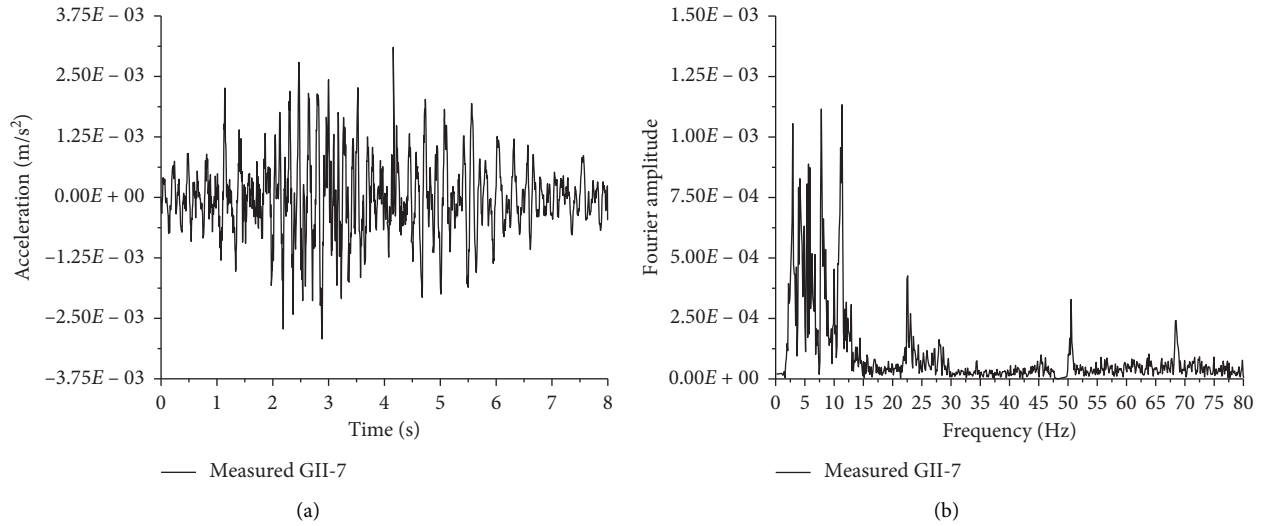


FIGURE 8: Acceleration: (a) time history and (b) frequency spectrum of GII-7.

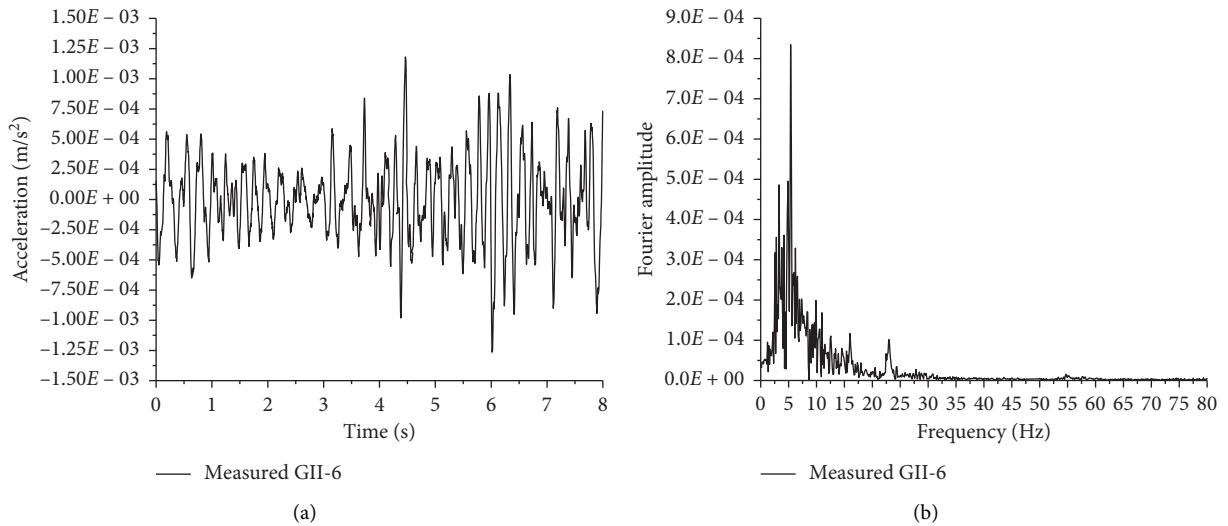


FIGURE 9: Acceleration: (a) time history and (b) frequency spectrum of GII-6.

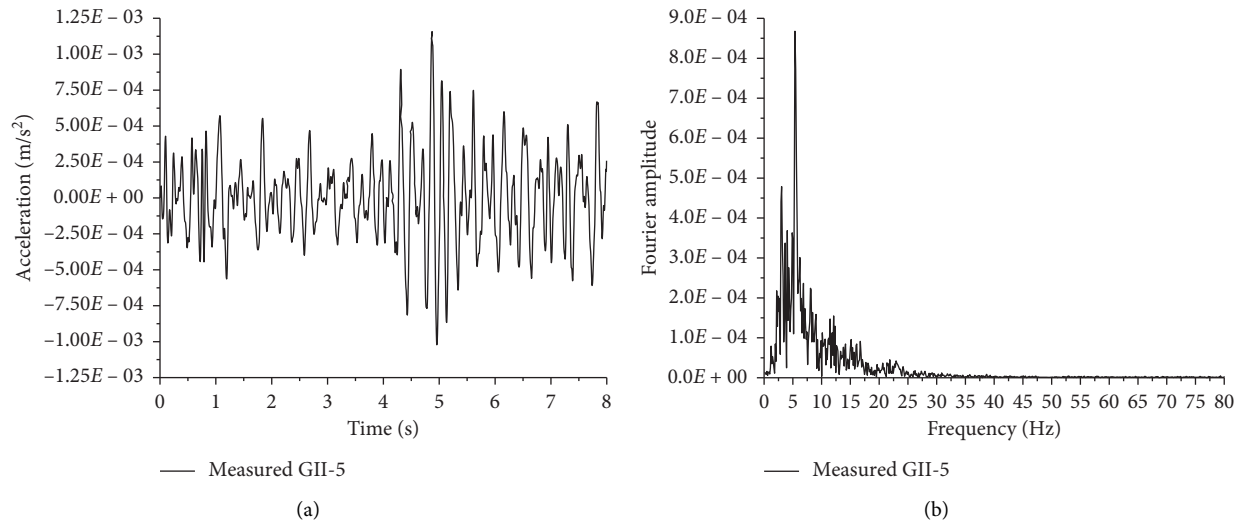


FIGURE 10: Acceleration: (a) time history and (b) frequency spectrum of GII-5.

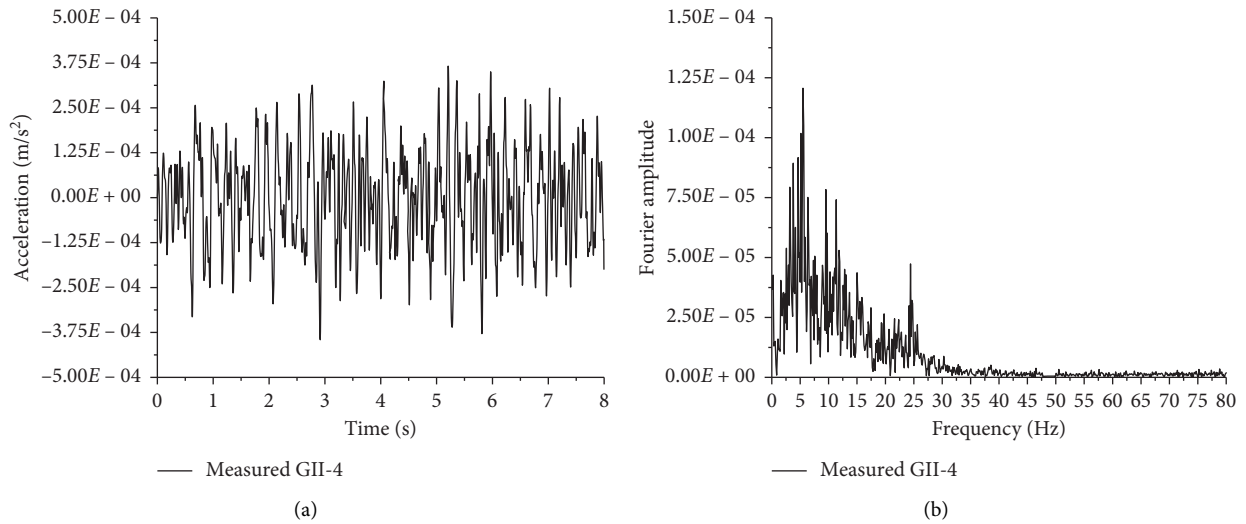


FIGURE 11: Acceleration: (a) time history and (b) frequency spectrum of GII-4.

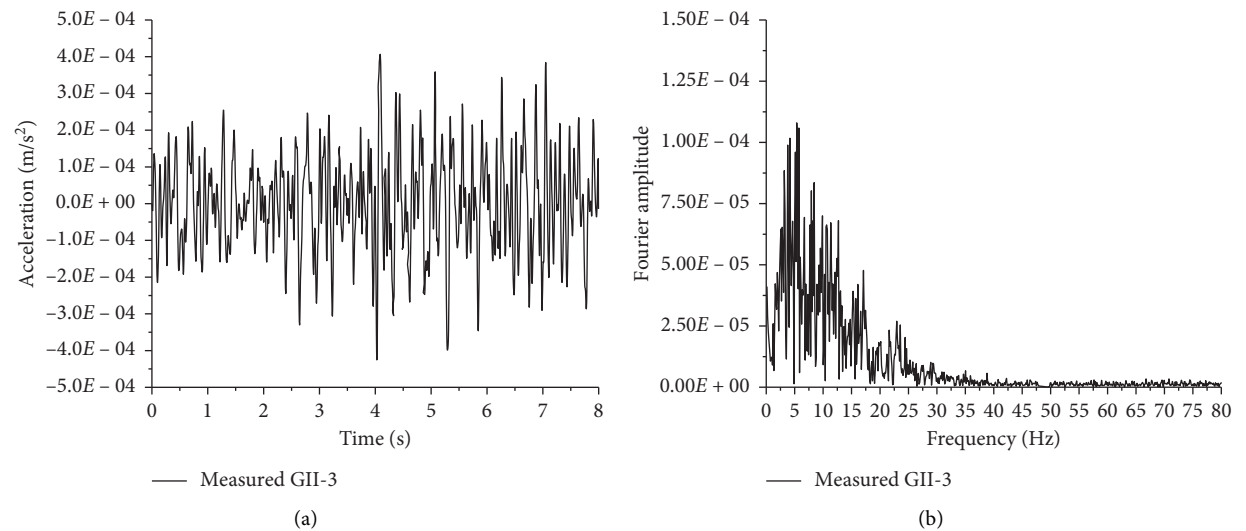


FIGURE 12: Acceleration: (a) time history and (b) frequency spectrum of GII-3.

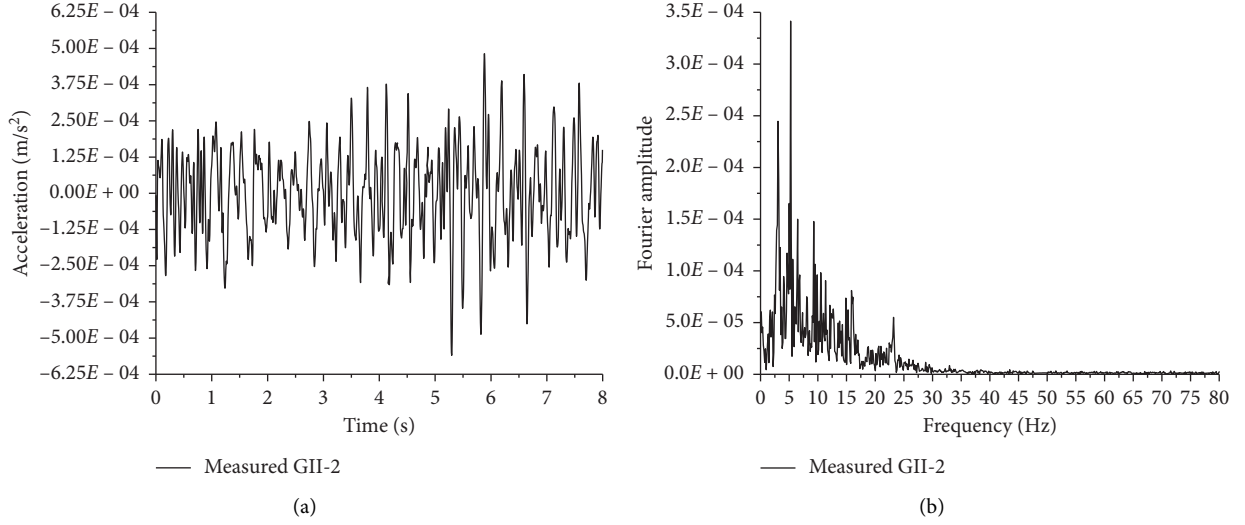


FIGURE 13: Acceleration: (a) time history and (b) frequency spectrum of GII-2.

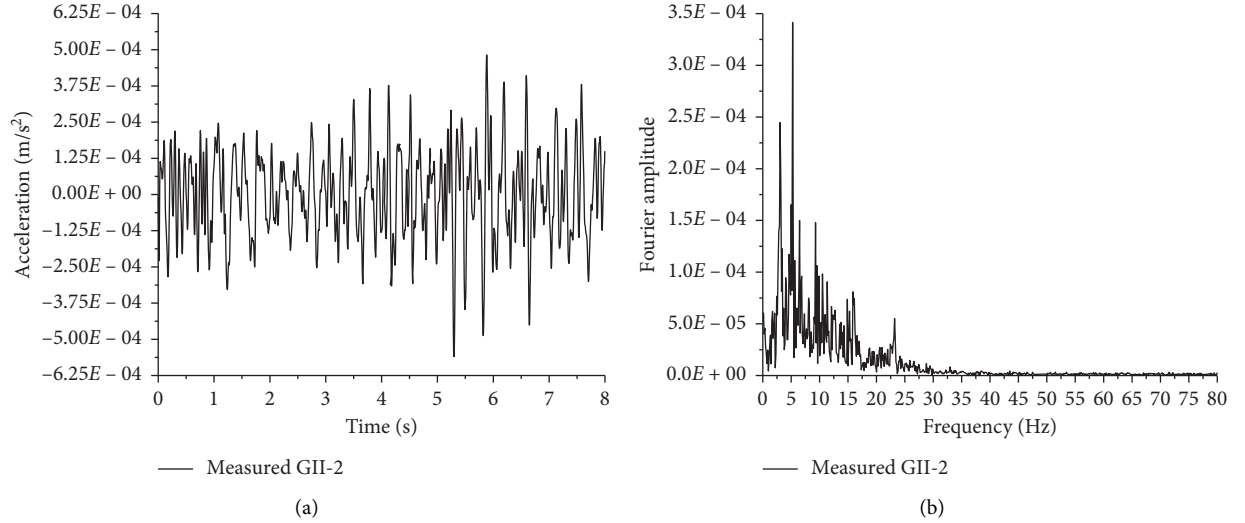


FIGURE 14: Acceleration: (a) time history and (b) frequency spectrum of GII-1.

and the dynamic shear modulus is calculated as follows [24]:

$$G_d = \rho V_s^2 \quad (1)$$

where G_d is the dynamic shear modulus; V_s is the shear wave velocity of soil; and ρ is the natural density of the soil, which is obtained from the in situ undisturbed soil through laboratory experiments.

The conversion relations between elastic modulus and shear modulus, shear wave velocity, and longitudinal wave velocity are as follows [25]:

$$G_d = \frac{E}{2(1+\nu)}, \quad (2)$$

$$\frac{V_p}{V_s} = \sqrt{\frac{2(1+\nu)}{1-2\nu}},$$

where E is the dynamic elastic modulus; ν is Poisson's ratio; and V_p is the p wave velocity of soil.

The calculation parameters of the maglev viaduct, the pile cap, and the pile foundation are as follows: elastic modulus $E = 30,000$ MPa; Poisson's ratio $\nu = 0.176$; density $\rho = 2500$ kg/m³. In this study, the Rayleigh damping model was used in the 2D dynamic model, and the Rayleigh damping coefficients α and β are given by

$$\begin{cases} \alpha = \frac{2\omega_i\omega_j(\xi_i\omega_j - \xi_j\omega_i)}{\omega_j^2 - \omega_i^2}, \\ \beta = \frac{2(\xi_j\omega_j - \xi_i\omega_i)}{\omega_j^2 - \omega_i^2}, \end{cases} \quad (3)$$

where $\xi_{i,j}$ is the damping ratio corresponding to frequency $\omega_{i,j}$. To obtain the values of α and β , undisturbed soil was

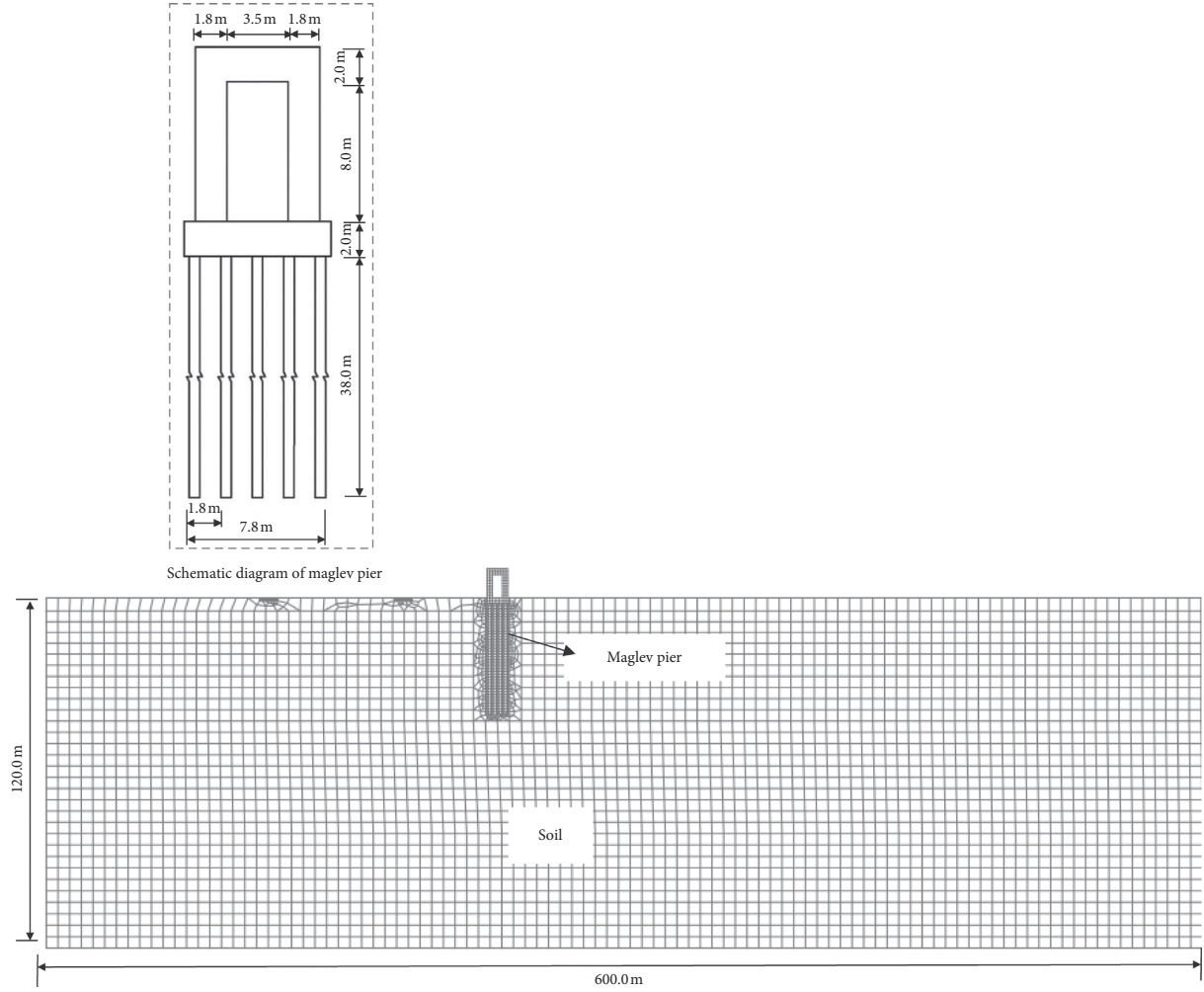


FIGURE 15: Finite-element (FE) model.

TABLE 4: Physical and mechanical soil parameters.

Soil	Thickness (m)	Dynamic elastic modulus (MPa)	Dynamic shear modulus (MPa)	Shear wave velocity (m/s)	p wave velocity (m/s)	Poisson's ratio	Density $\text{kg}\cdot\text{m}^{-3}$
Silty clay	4.5	85.41	32.11	130.0	363.62	0.33	1900.00
Mucky clay	14.7	94.23	34.90	140.0	420.00	0.35	1780.43
Clayey silt	23	160.83	60.92	180.0	487.44	0.32	1880.20
Fine silty sand 1	38.5	490.46	187.20	300.0	787.73	0.31	2080
Fine silty sand 2	39.3	744.46	295.42	375.0	859.23	0.26	2100.78

subjected to a resonant column test to obtain its damping ratio ξ . The relationship between damping ratio and strain obtained from testing the dynamic characteristics of undisturbed soil is shown in Figure 16, from which it can be seen that when the vibration strain is 10^{-5} , the soil damping ratio is 0.02. Because of the complexity of the damping ratio with frequency, it is assumed that the damping ratio is constant in a certain frequency range of interest. Figure 5 shows that the main vibration frequency band of the maglev is 10–70 Hz, so the $\omega_{i,j}$ values are taken as

$$\begin{cases} \omega_i = 10 \times 2\pi \frac{\text{rad}}{\text{s}}, \\ \omega_j = 70 \times 2\pi \frac{\text{rad}}{\text{s}}, \\ \xi_i = \xi_j = 0.02. \end{cases} \quad (4)$$

The Rayleigh damping coefficients $\alpha = 2.198$ and $\beta = 7.96 \times 10^{-5}$ are calculated by combining equations (3) and (4). When using the finite-element method to analyze

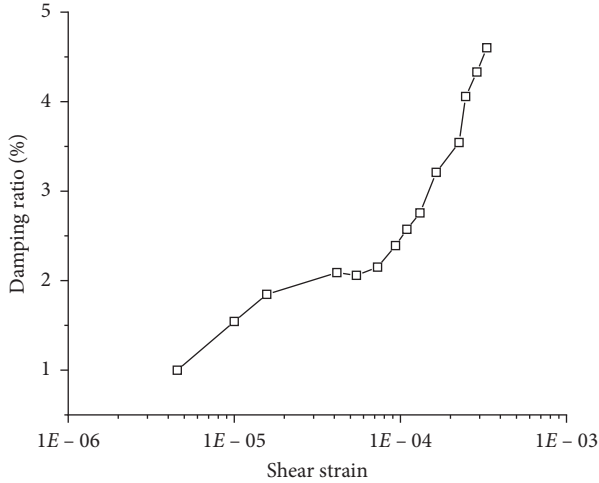


FIGURE 16: Variation of damping ratio with dynamic shear strain.

the structure-ground dynamic interaction, an artificial boundary usually needs to be applied on the selected calculation area to simulate the radiation damping of the continuous medium, so that the scattered wave does not reflect when passing through the artificial boundary from the inside of the finite calculation area. The artificial boundary of the finite-element model in this paper can be equivalent to a parallel spring-damper system in which the spring stiffness K_B and damping coefficient C_B can be expressed as follows [26]:

Normal boundary:

$$\begin{aligned} K_{BN} &= \alpha_N \frac{G}{R}, \\ C_{BN} &= \rho V_P. \end{aligned} \quad (5)$$

Tangential boundary:

$$\begin{aligned} K_{BT} &= \alpha_T \frac{G}{R}, \\ C_{BT} &= \rho V_S, \end{aligned} \quad (6)$$

where K_{BN} and K_{BT} are the normal and tangential spring stiffness, respectively; C_{BN} and C_{BT} are the normal and tangential damping coefficients of the damper, respectively; R is the distance from the wave source to the artificial boundary point; and α_N and α_T are artificial boundary parameters. As suggested by Gu [27], the recommended values of α_N and α_T are 1.33 and 0.67, respectively. It should be noted in equations (5) and (6) that the parameter R is expressed by the shortest distance from the vibration source to the artificial boundary. However, in actual problems, the scattering source is not a point source, but line source or area source with spatial distribution. Therefore, the determined spring stiffness in equations (5) and (6) is generally larger.

3.3. Analysis of Results. To verify the correctness of the numerical calculations, the numerical results are compared with the field measurement data in terms of the vibration

displacements and the time histories and frequency spectra of the vibration accelerations. These comparisons are shown in Figures 17–25.

Figures 17(a)–24(a) show that the calculated acceleration time histories of GII-7 and GII-8 agree well with the measured field data. However, the calculated acceleration time history of the measuring point far away from the vibration source (e.g., GII-3 and GII-4) is consistent with the measured field data only in the part in which the acceleration amplitude is concentrated; this fact may be related to there being vibration sources other than the maglev in the field measurements.

Figures 17(b)–24(b) show that the calculated acceleration frequency spectrum at each measurement point is basically consistent with the field test data. The calculation results of GII-7 and GII-8 near the vibration source differ considerably from the field measurement data in the low-frequency part; this difference may be related to the fact that R waves are not attenuated on the surface when the latter is acted on by a linear vibration source. The calculated acceleration frequencies of the measuring point far away from the vibration source (e.g., GII-3 and GII-4) are smaller than the field vibration test data; again, this difference may be related to there being vibration sources other than the maglev in the field measurements.

Figure 25(a) shows that the numerically calculated maximum and root mean square (RMS) displacements within 100 m from the vibration source are slightly larger than the field measured data; again, this difference may be related to the fact that R waves are not attenuated on the surface when the latter is acted on by a linear vibration source. However, when the distance from the vibration source exceeds 100 m, the numerically calculated maximum and RMS displacements are close to the field measurement results. Generally speaking, the numerically calculated maximum and RMS displacements of the ground measurement points (GII-5–GII-8) are consistent with the attenuation trend of the field measurement data: with increasing distance from the vibration source, maximum and RMS displacements both decrease gradually.

Figure 25(b) shows that when the depth of the measuring point is less than 35 m, the numerically calculated maximum and RMS displacements are not consistent with the field measured data. However, when that depth exceeds 35 m, the numerically calculated results are relatively close to the field measured data. Generally speaking, the numerically calculated maximum and RMS displacements of the measuring points varying with depth (GII-1–GII-5) are consistent with the field measurement data regarding the attenuation trend: with increasing depth, maximum and RMS displacements both decrease gradually. The numerically calculated results show that the FE numerical method can simulate well the environmental vibration caused by traffic. The subsequent research reported herein analyzes the laws governing the influences of pile material, hollow ratio of the pile, filling material, pile length, pile diameter, and other parameters on the vibration isolation of the pile barrier based on the FE numerical method.

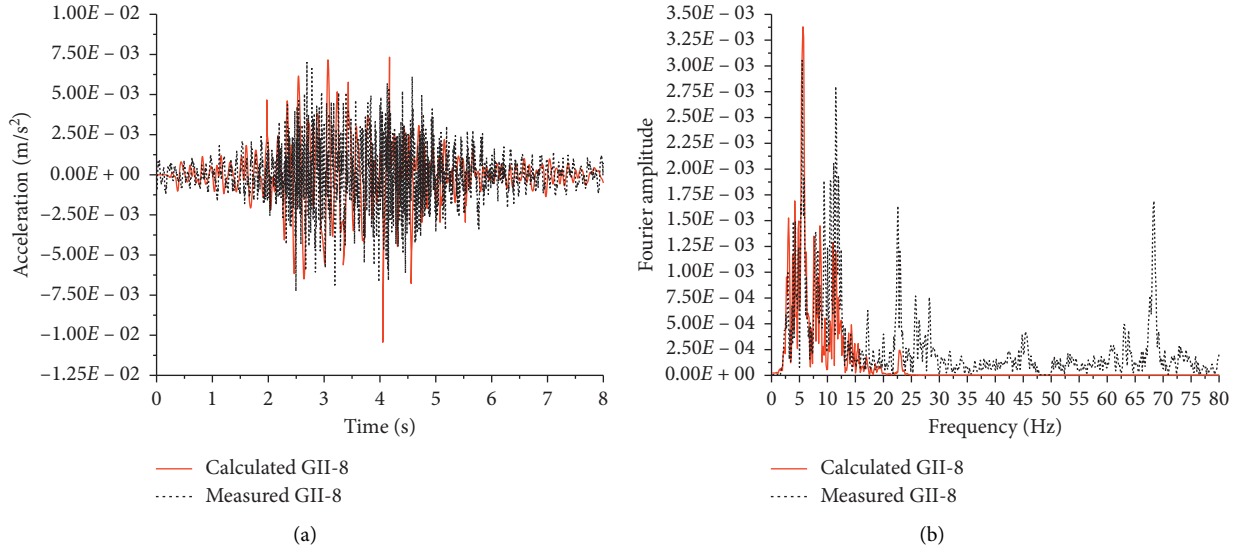


FIGURE 17: Comparison of numerical and field results (GII-8): (a) acceleration time history; (b) frequency spectrum.

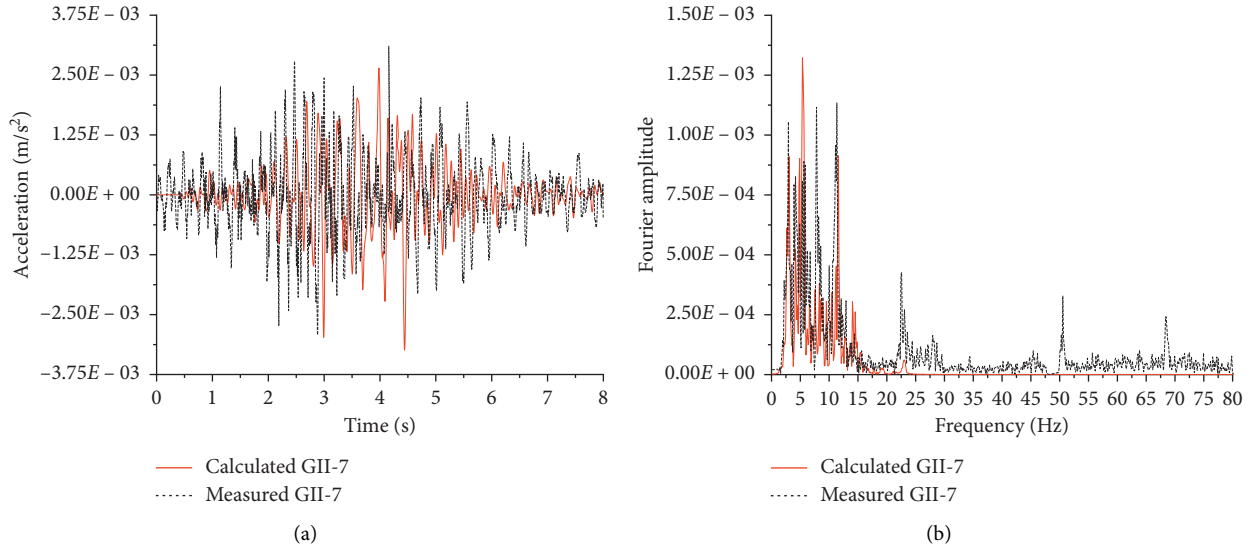


FIGURE 18: Comparison of numerical and field results (GII-7): (a) acceleration time history; (b) frequency spectrum.

4. Analysis of Vibration-Isolation Performance of Pile Barrier

As a kind of passive isolation barrier system, pile-barrier vibration isolation can eliminate or prevent the adverse effects caused by vibration [28, 29]. This section reports on an extensive numerical parametric investigation of a pile-barrier vibration-isolation system with various pile materials, hollow ratio of the pile, filling materials, pile lengths, pile diameters, vibration-isolation positions, pile spacing, and row numbers to study how each parameter influences the vibration isolation of the pile barrier.

4.1. FE Calculation Model. A 2D model of the maglev, Luoshan Road viaduct, Luoshan Road, and hard-X-ray

tunnel was established to study how the pile parameters influence the vibration-isolation effect. The FE model is shown in Figure 26. The outer diameter of the hard-X-ray tunnel model is 7 m, the inner diameter is 6.3 m, and the buried depth is 30 m. The inner and outer rings in the tunnel model are set as a lining layer and a grouting layer, respectively, and the monitoring point is located in the middle of the tunnel floor (see Figure 26). The calculation parameters of the structural model are given in Table 5. See Section 3 for the settings of the soil calculation parameters and FE model, which are not repeated here. The measured acceleration time-history data for the Luoshan Road traffic, Luoshan Road viaduct traffic, and maglev are filtered and used as the load for the numerical calculations, as shown in Figure 27. The calculations were performed first with no pile-barrier vibration-isolation measures in place, after

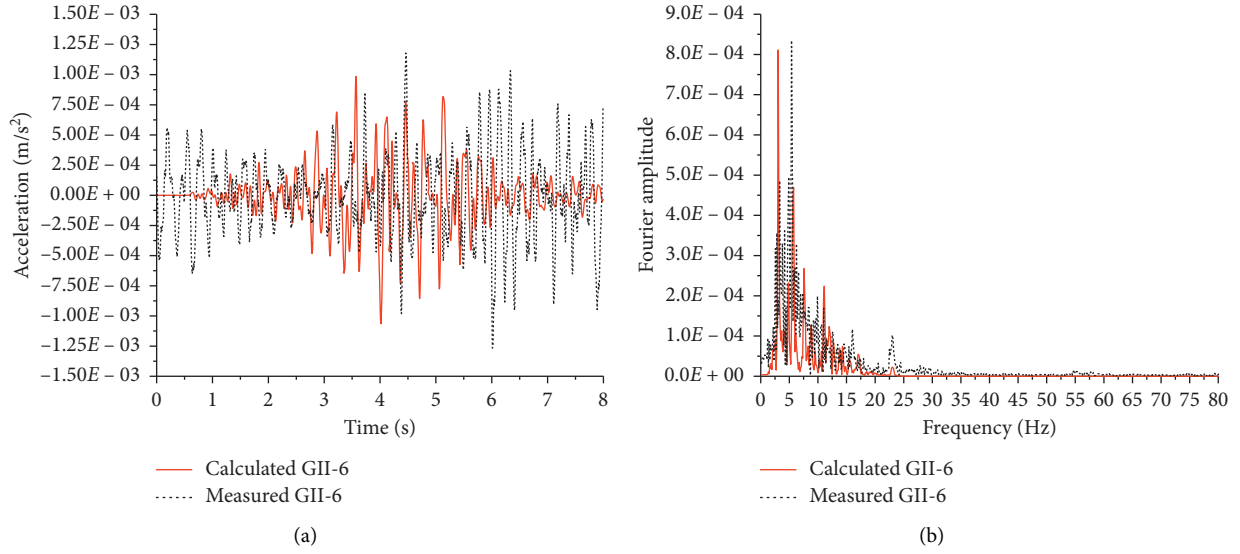


FIGURE 19: Comparison of numerical and field results (GII-6): (a) acceleration time history; (b) frequency spectrum.

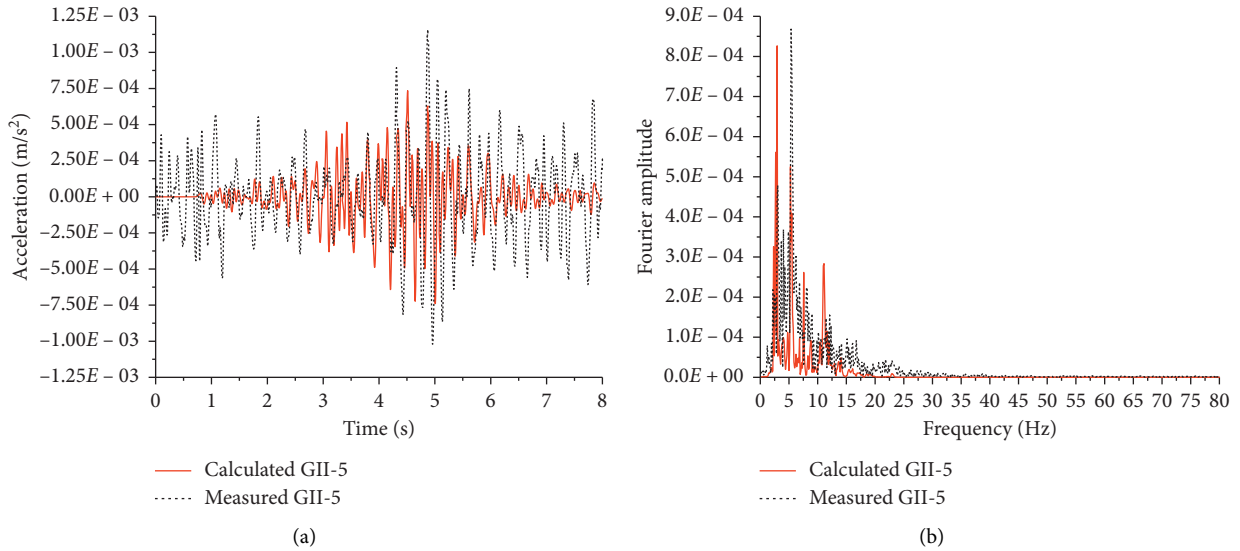


FIGURE 20: Comparison of numerical and field results (GII-5): (a) acceleration time history; (b) frequency spectrum.

which an extended numerical parametric analysis was performed to study how different pile materials, hollow ratio of the pile, filling materials, pile lengths, pile diameters, pile row numbers, and row spacing affect the vibration isolation of the pile barrier. Details of the parametric analysis are given in Table 6.

4.2. Calculation Results with No Pile Barrier Vibration Isolation. Figure 28 shows the vibration acceleration and displacement time histories and the acceleration frequency spectrum of the tunnel-floor monitoring point obtained from the numerical calculations with no vibration-isolation measures. The numerical calculations show that the maximum and RMS vibration displacements are 1086.64 and

280.95 nm, respectively. The frequency spectrum (see Figure 28(b)) shows that the vibration amplitude is concentrated mainly in the low-frequency part when it propagates to the bottom of the tunnel. Therefore, an effective way to reduce the tunnel vibration displacement is to block the vibration wave effectively in the low-frequency band.

4.3. Influence of Pile Material on Vibration Isolation Effect. In the FE simulation, concrete piles of different strength are set to study how the pile material influences the vibration-isolation performance of the pile barrier. The parameter selection of different pile materials and the calculated maximum and RMS vibration displacements of the monitoring point are shown in Group I of Table 6, and the

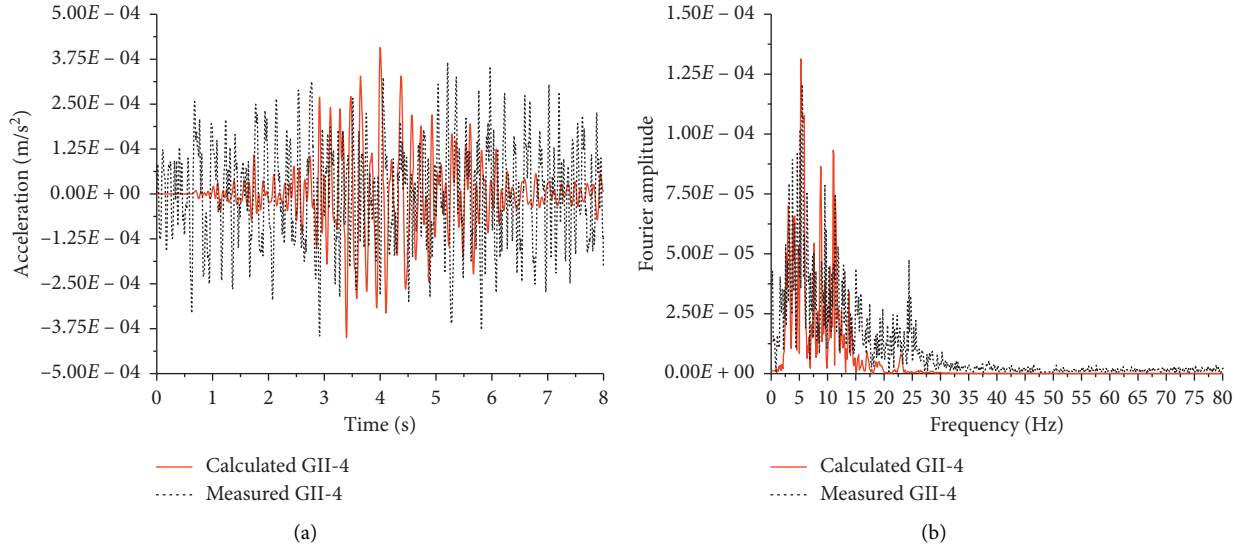


FIGURE 21: Comparison of numerical and field results (GII-4): (a) acceleration time history; (b) frequency spectrum.

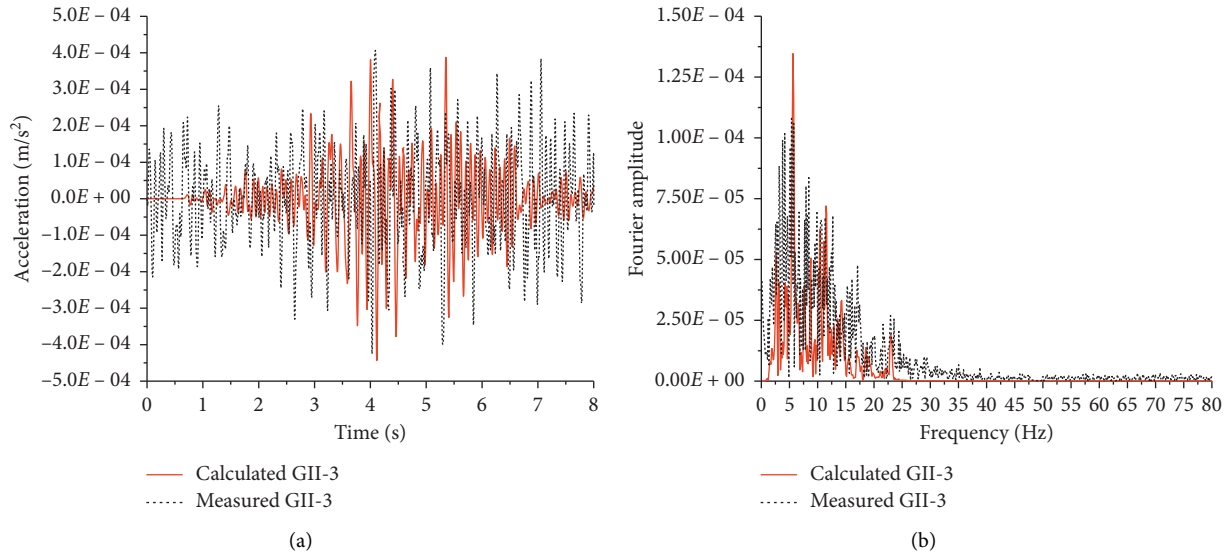


FIGURE 22: Comparison of numerical and field results (GII-3): (a) acceleration time history; (b) frequency spectrum.

frequency-spectrum comparison for different pile body materials and without vibration-isolation measures is shown in Figure 29. The calculation results show that the vibration-isolation effect is better with increasing pile stiffness when the other conditions remain unchanged. They also show that the vibration-isolation effect of foam plastic and foam concrete with a small elastic modulus is much poorer than that of concrete with a large elastic modulus, but the vibration-isolation effects of concrete piles of different strengths are mostly the same. The vibration-isolation measures adopted in engineering must consider comprehensively the vibration-isolation effect and cost. Therefore, if there is no strength requirement for the piles used for vibration isolation, it is recommended to choose row piles with C20 concrete.

4.4. Influence of Hollow Ratio (r) and Filling Material on Vibration Isolation Effect. Groups II and III of Table 6 investigate how the hollow ratio (r) of the pile and filling material influence the vibration-isolation effect. The calculated maximum and RMS vibration displacements of the monitoring points are shown in the same groups. The frequency-spectrum comparisons between different hollow ratios and filling materials and without vibration-isolation measures are shown in Figures 30 and 31, respectively. The calculation results show that with increasing hollow ratio of the pile, the vibration-isolation capacity improves. For example, the calculated maximum and RMS vibration displacements of piles with a hollow ratio of 0.39 are 48.96% and 34.36%, respectively, of those of solid piles. The calculation results also show that with increasing elastic

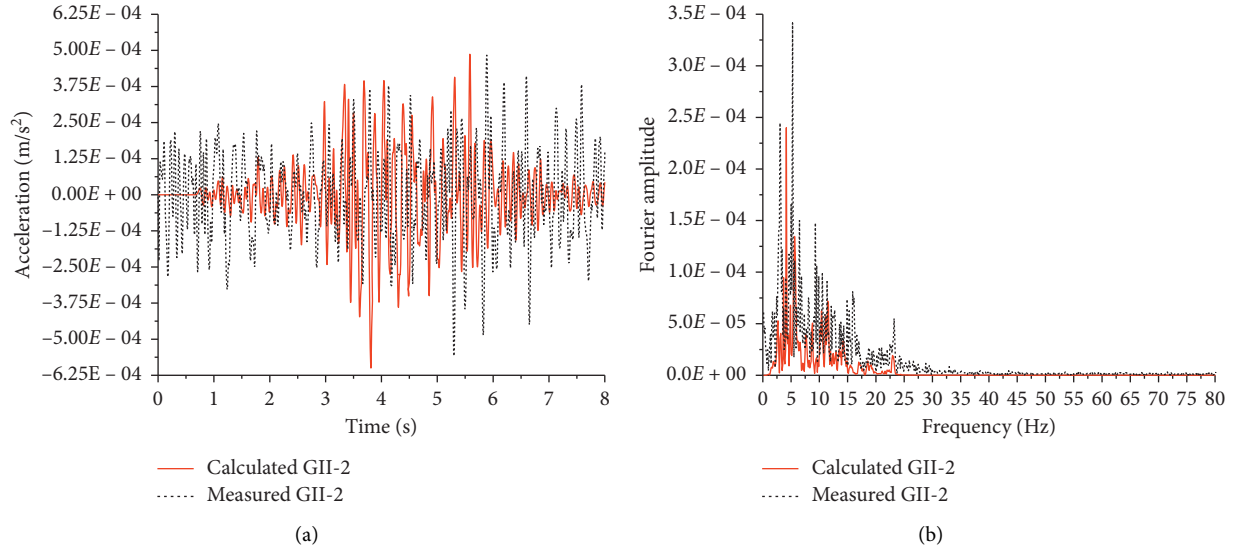


FIGURE 23: Comparison of numerical and field results (GII-2): (a) acceleration time history; (b) frequency spectrum.

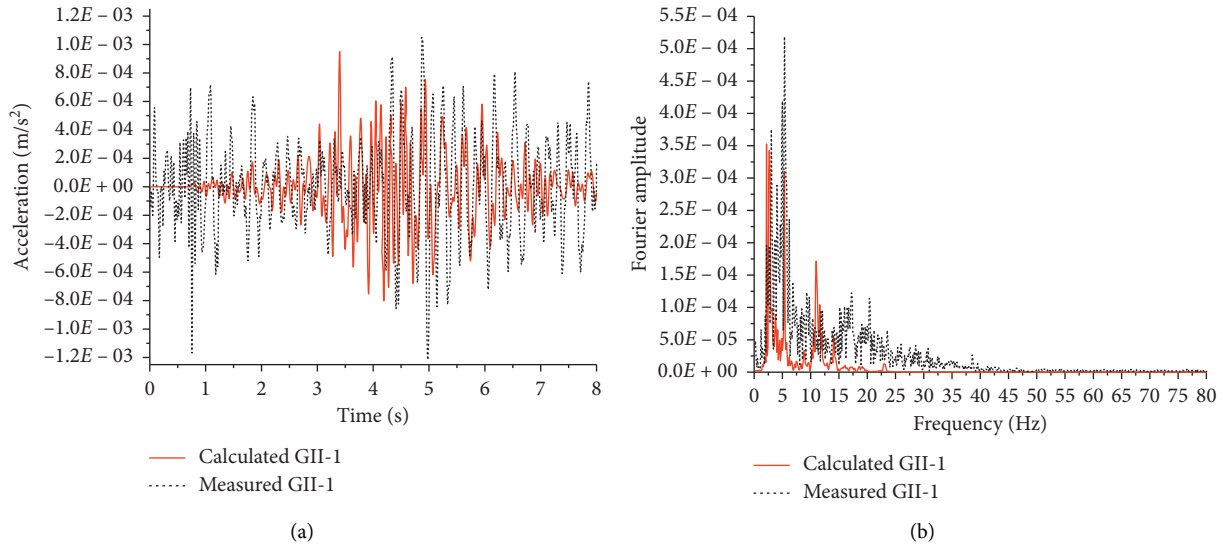


FIGURE 24: Comparison of numerical and field results (GII-1): (a) acceleration time history; (b) frequency spectrum.

modulus of the filler in the piles, the vibration-isolation capacity decreases gradually.

4.5. Influence of Pile Length (L) and Pile Diameter (D) on Vibration Isolation Effect. Groups IV and V of Table 6 explore the effects of the pile length and diameter. The calculated maximum and RMS vibration displacements of the monitoring points are shown in the same groups. The frequency-spectrum comparison between different pile lengths and diameters and without vibration-isolation measures is shown in Figures 32 and 33, respectively. The calculation results show that the vibration-isolation capacity of the pile barrier increases with increasing pile length. For example, when the pile length is increased from 10 m to 40 m, the maximum and RMS vibration displacements are reduced by

11% and 15.7%, respectively. The calculation results also show that the pile diameter has little influence on the vibration-isolation effect of the piles. Figure 33 shows that increasing the pile diameter has little effect on the acceleration amplitude around 5 Hz but affects it somewhat around 10 Hz.

4.6. Influence of Distance from Hard-X-Ray Tunnel (d) on Vibration Isolation Effect. Group VI of Table 6 shows the effect of the distance from the hard-X-ray tunnel. The calculated maximum and RMS vibration displacements of the monitoring points are shown in the same group. The frequency-spectrum comparison between different distances from the hard-X-ray tunnel and without vibration-isolation measures is shown in Figure 34. According to the calculation

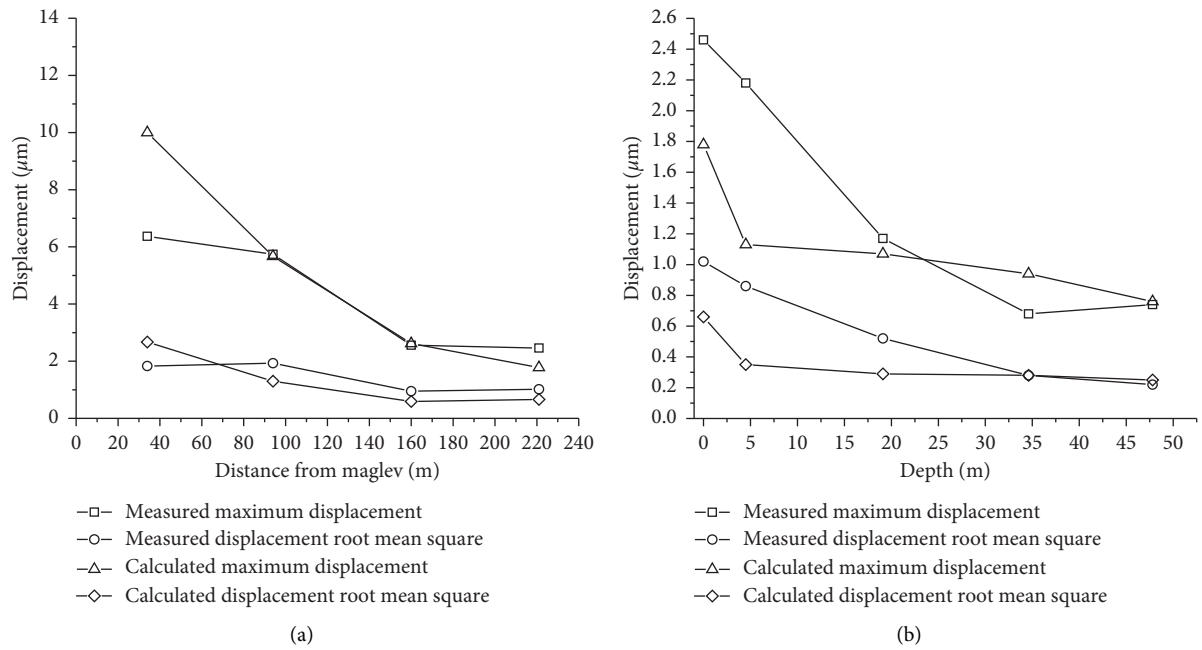


FIGURE 25: Comparison of numerical and field results: relationships between vibration displacement and (a) distance of surface measuring points from maglev (GII-5–GII-8) and (b) the measuring points varying with depth (GII-1–GII-5).

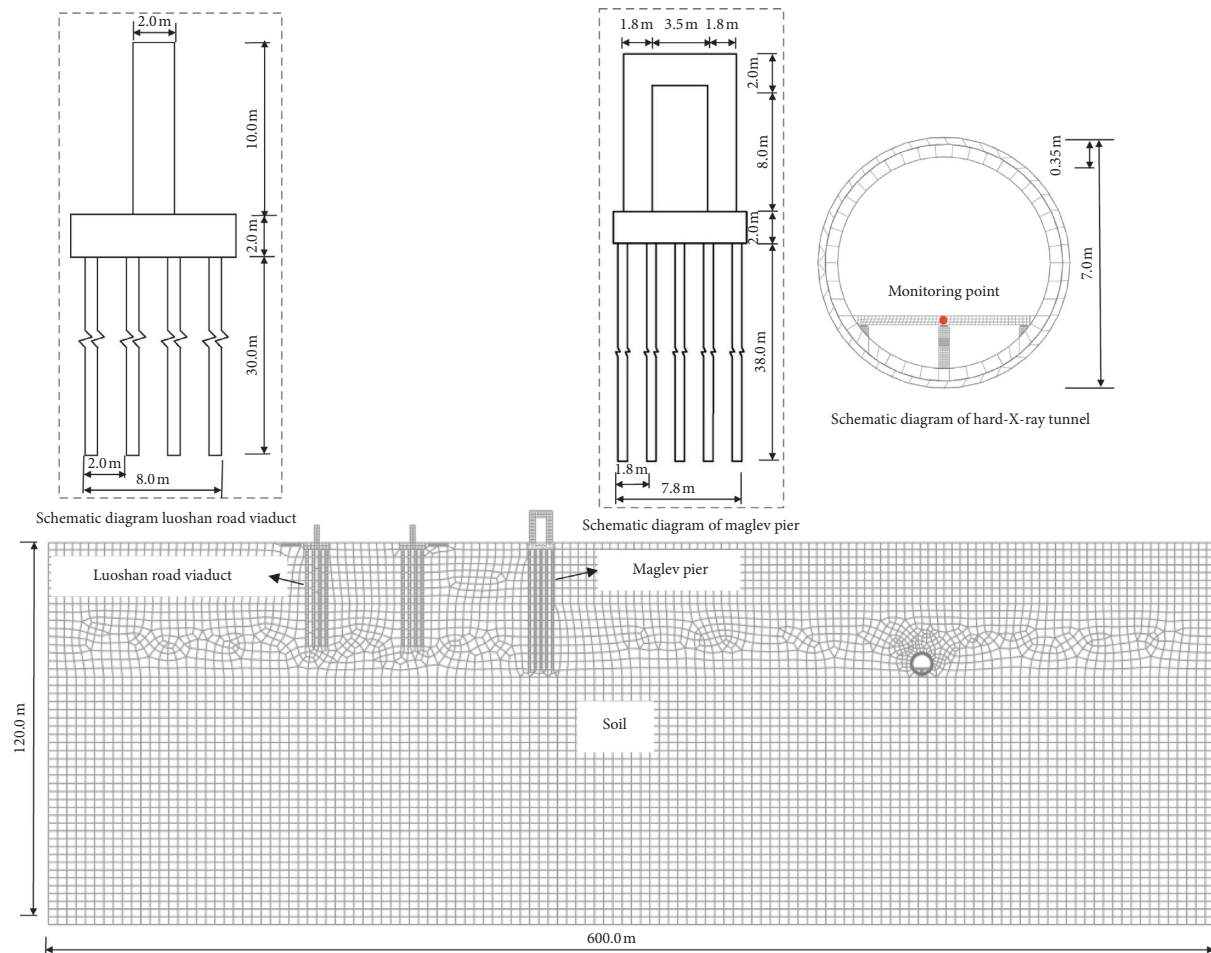


FIGURE 26: FE model.

TABLE 5: Calculation parameters of the structural model.

Structure	Elastic modulus (MPa)	Poisson's ratio	Density (kg/m^3)
Pier, pile cap, pile	30,000	0.176	2500
Tunnel grouting layer	30	0.2	2600
Tunnel lining layer	34,500	0.2	2500
Subgrade	1500	0.3	1200

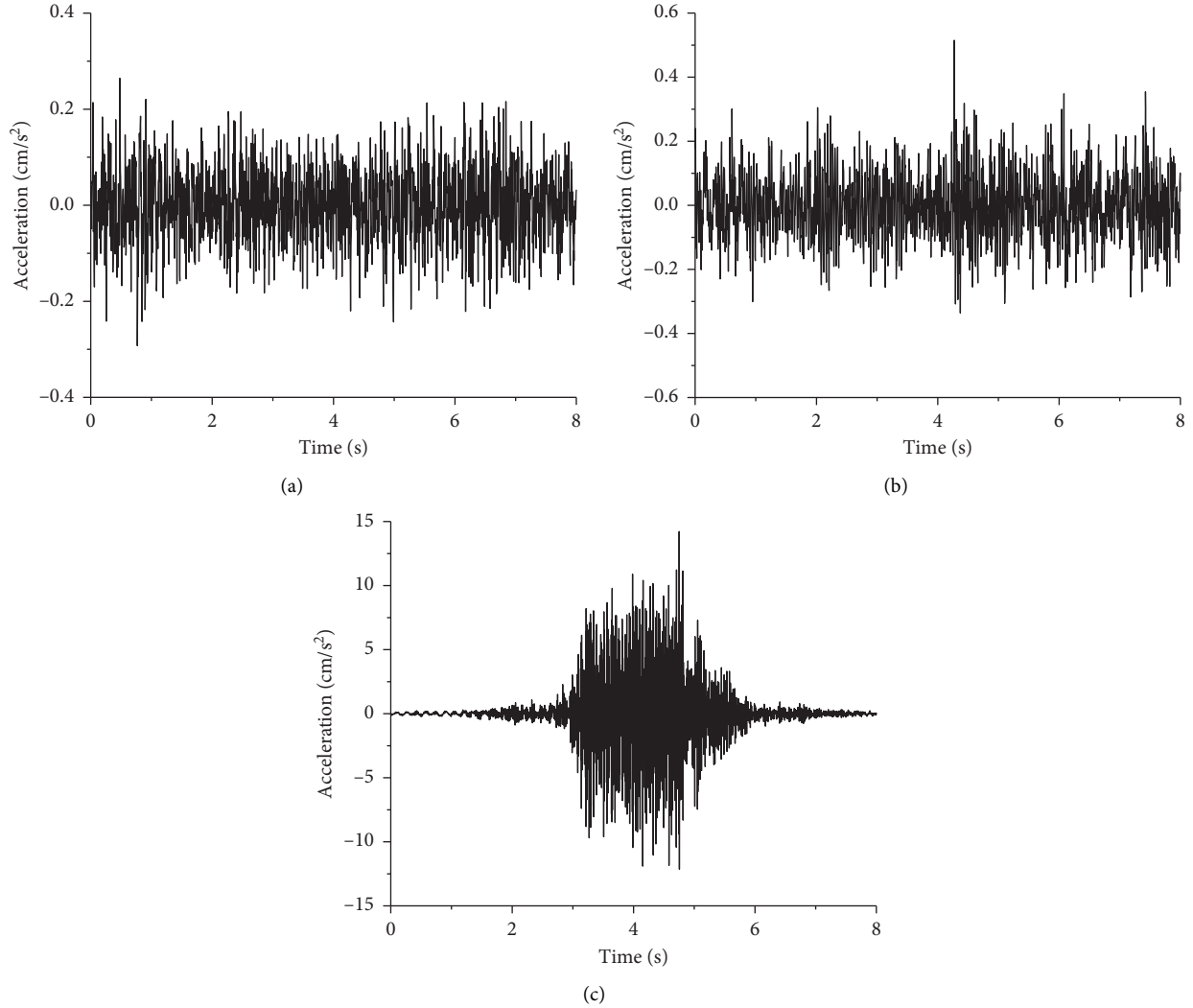


FIGURE 27: Acceleration time-history curves of vibration source: (a) Luoshan Road traffic, (b) Luoshan Road viaduct traffic, and (c) maglev.

results, the vibration-isolation effect of the piles is no better if the piles are closer to the tunnel. Therefore, the vibration-isolation position of the pile barrier in practical engineering should be considered according to the actual working conditions.

4.7. Influence of Pile Row Number (n) and Row Spacing (c) on Vibration Isolation Effect. Groups VII and VIII of Table 6

evaluate the influences of pile row number and row spacing. The frequency-spectrum comparisons between different pile row numbers and row spacing and without vibration-isolation measures are shown in Figures 35 and 36, respectively. The calculation results show that the vibration-isolation ability of the pile barrier improves gradually with increasing pile row number and decreasing row spacing, but generally speaking, the influences of pile row number and row spacing on the vibration-isolation effect are small.

TABLE 6: Summary of parametric investigation.

Group	Variable		Other key parameters/configuration		Maximum displacement (nm)	RMS displacement (nm)	Note
I	Pile body material	Foam plastics	ρ (kg/m ³) 700 E (MPa) 2000 ν 0.38	$D = 0.8$ actm; $D_0 = 0.8$ m; $L = 45$ m; $n = 1$; $d = 20$ m	950.41	208.59	Effect of pile body material
		C20 concrete	P (kg/m ³) 2500 E (MPa) 26,000 ν 0.2				
		C30 concrete	P (kg/m ³) 2500 E (MPa) 30,000 ν 0.2		825.02	190.27	
		C40 concrete	P (kg/m ³) 2500 E (MPa) 33,000 ν 0.2				
		C50 concrete	P (kg/m ³) 2500 E (MPa) 35,000 ν 0.2		828.87	190.29	
		Foam concrete	P (kg/m ³) 800 E (MPa) 400 ν 0.21				
		0	D (m) 0.8 D_0 (m) 0.8		865.29	191.57	
		0.39	D (m) 0.8 D_0 (m) 0.65				
II	Hollow ratio (r)	0.25	D (m) 0.8 D_0 (m) 0.6	$\rho = 2500$ kg/m; $E = 26,000$ MPa; $\nu = 0.2$; $L = 45$ m; $n = 1$; $d = 20$ m	506.84	133.37	Effect of hollow ratio, r
		0.19	D (m) 0.8 D_0 (m) 0.575				
		0.14	D (m) 0.8 D_0 (m) 0.55		511.35	134.12	
		0.06	D (m) 0.8 D_0 (m) 0.5				
		Loose field soil	ρ_0 (kg/m ³) 1000 E_0 (MPa) 50 ν_0 0.3		765.61	159.64	
		Dense field soil	ρ_0 (kg/m ³) 1900 E_0 (MPa) 100 ν_0 0.3				
		Foam	ρ_0 (kg/m ³) 45 E_0 (MPa) 2.94 ν_0 0.3		565.77	134.29	
		Cement-soil	ρ_0 (kg/m ³) 1850 E_0 (MPa) 1000 ν_0 0.2				
IV	Pile length, L (m)	10	$D = 0.8$ m; $D_0 = 0.8$ m; $\rho = 2500$ kg/m; $E = 26,000$ MPa; $\nu = 0.2$; $n = 1$; $d = 20$ m	979.58	227.42	Effect of pile length, L	
		20		938.49	219.07		
		30		918.67	217.26		
		40		872.22	191.74		
		50		836.84	187.94		
		60		836.84	186.92		
V	Pile diameter, D (m)	0.3	$D_0 = 0.8$ m; $\rho = 2500$ kg/m; $E = 26,000$ MPa; $\nu = 0.2$; $n = 1$; $d = 20$ m	881.9	195.8z	Effect of pile diameter, D	
		0.4		879.35	195.03		
		0.5		873.6	192.9		
		0.6		870.36	192.35		
		0.7		867.26	192.02		
		0.8		865.29	191.57		

TABLE 6: Continued.

Group	Variable	Other key parameters/configuration	Maximum displacement (nm)	RMS displacement (nm)	Note
VI	Distance from hard-X-ray tunnel, d (m)	$D = 0.8$ m; $D_0 = 0.8$ m; $\rho = 2500$ kg/m; $E = 26,000$ MPa; $\nu = 0.2$; $L = 45$ m; $n = 1$	5	182.34	Effect of the distance from hard-X-ray tunnel, d
			10	180.69	
			20	191.57	
			30	191.83	
			40	177.78	
			50	167.26	
			60	185.32	
VII	Pile row number, n	$D = 0.8$ m; $D_0 = 0.8$ m; $\rho = 2500$ kg/m; $E = 26,000$ MPa; $\nu = 0.2$; $L = 45$ m; $C = 2.5$	1	191.57	Effect of pile row number, n
			2	189.2	
			3	186.3	
			4	184.36	
VIII	Row spacing, c (m)	$D = 0.8$ m; $D_0 = 0.8$ m; $\rho = 2500$ kg/m; $E = 26,000$ MPa; $\nu = 0.2$; $L = 45$ m; $n = 2$	2	187.69	Effect of row spacing, c
			2.5	189.2	
			3	191.62	
			4	192.96	
			5	193.42	
			6	195.92	

Note: D and D_0 are the outer diameter and inner diameter of the tunnel, respectively.

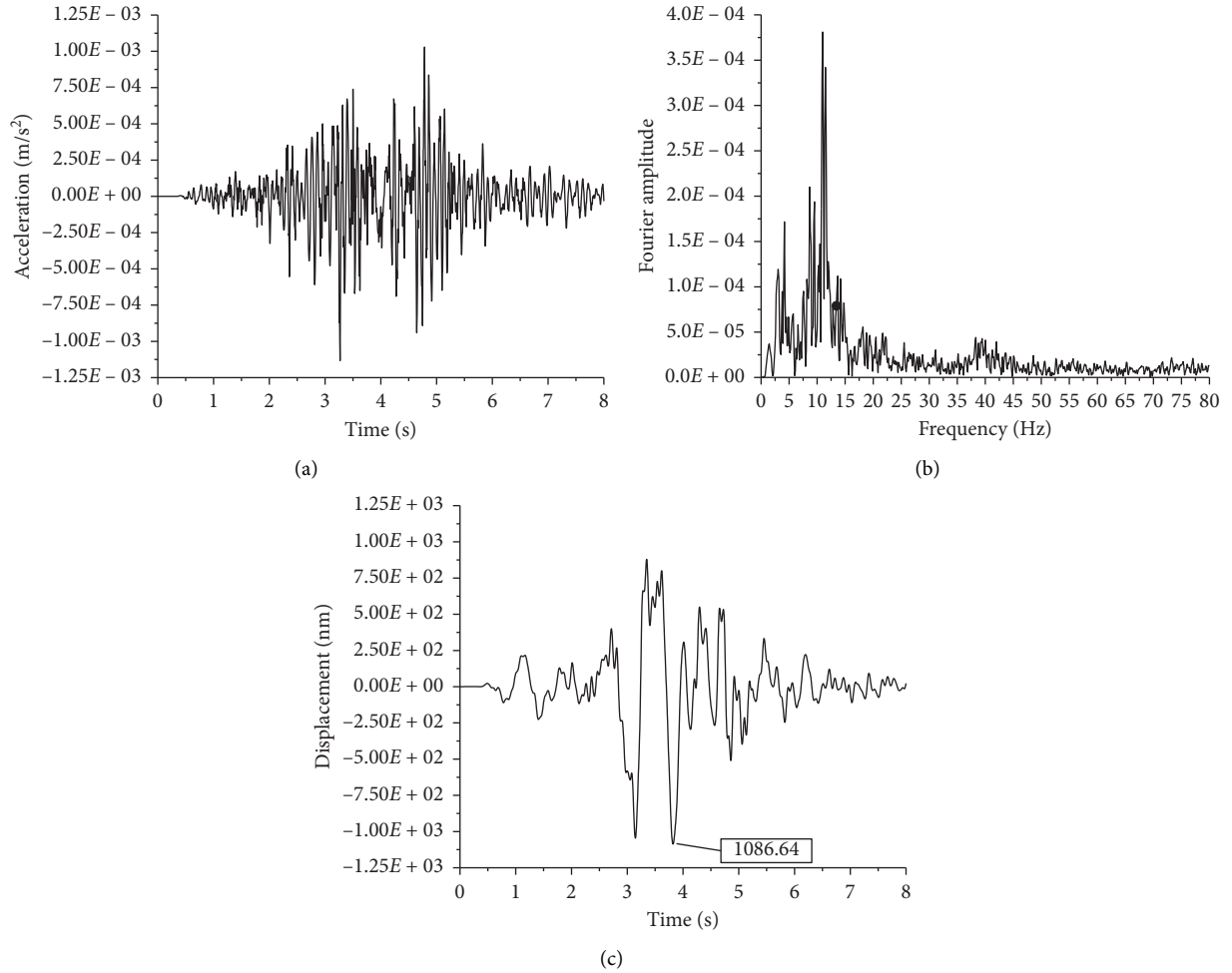


FIGURE 28: Numerical calculation results with no vibration-isolation measures: (a) acceleration time history, (b) frequency spectrum, and (c) displacement time history.

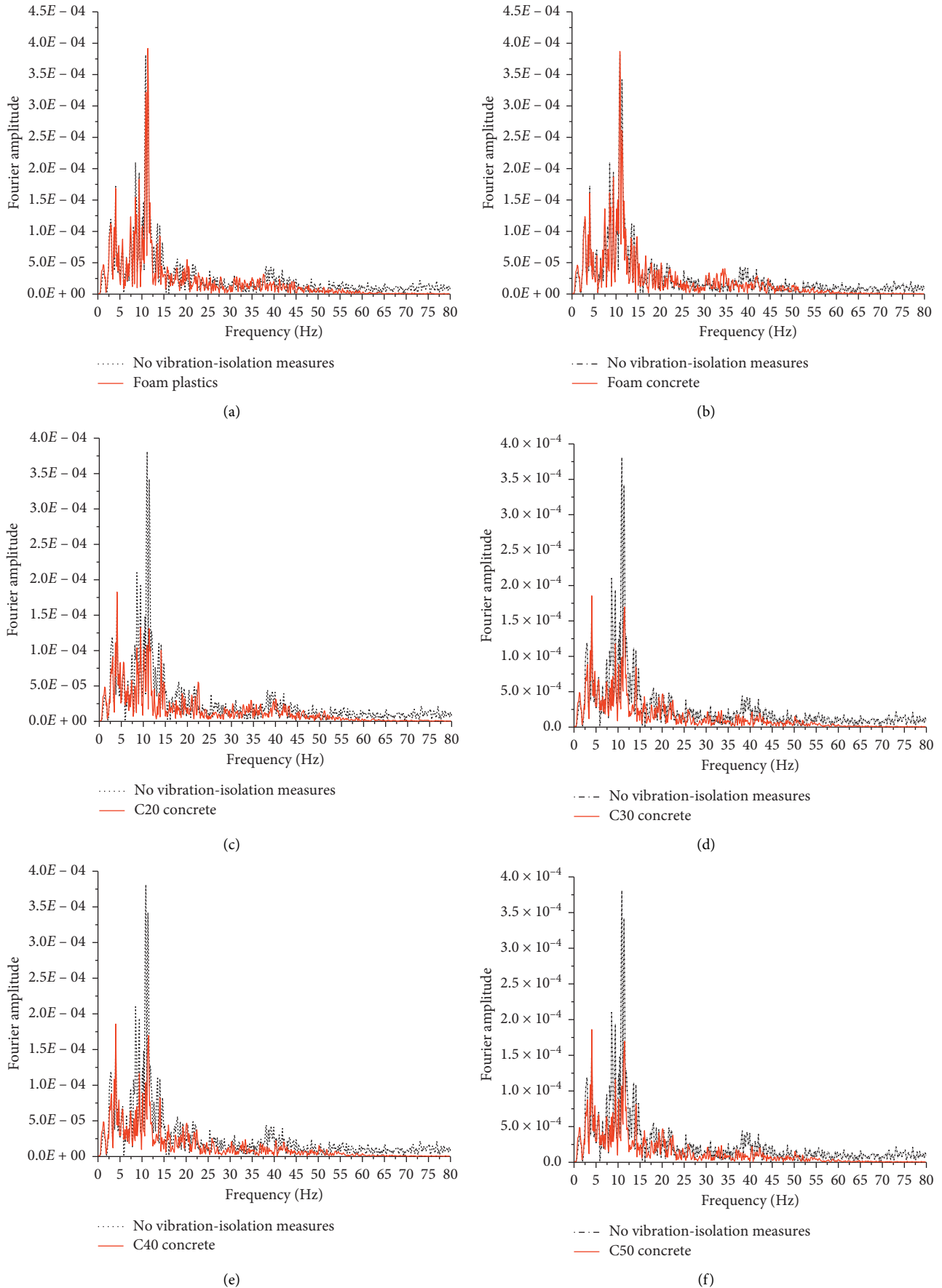


FIGURE 29: Influence of pile material on vibration-isolation effect (comparison of frequency spectra).

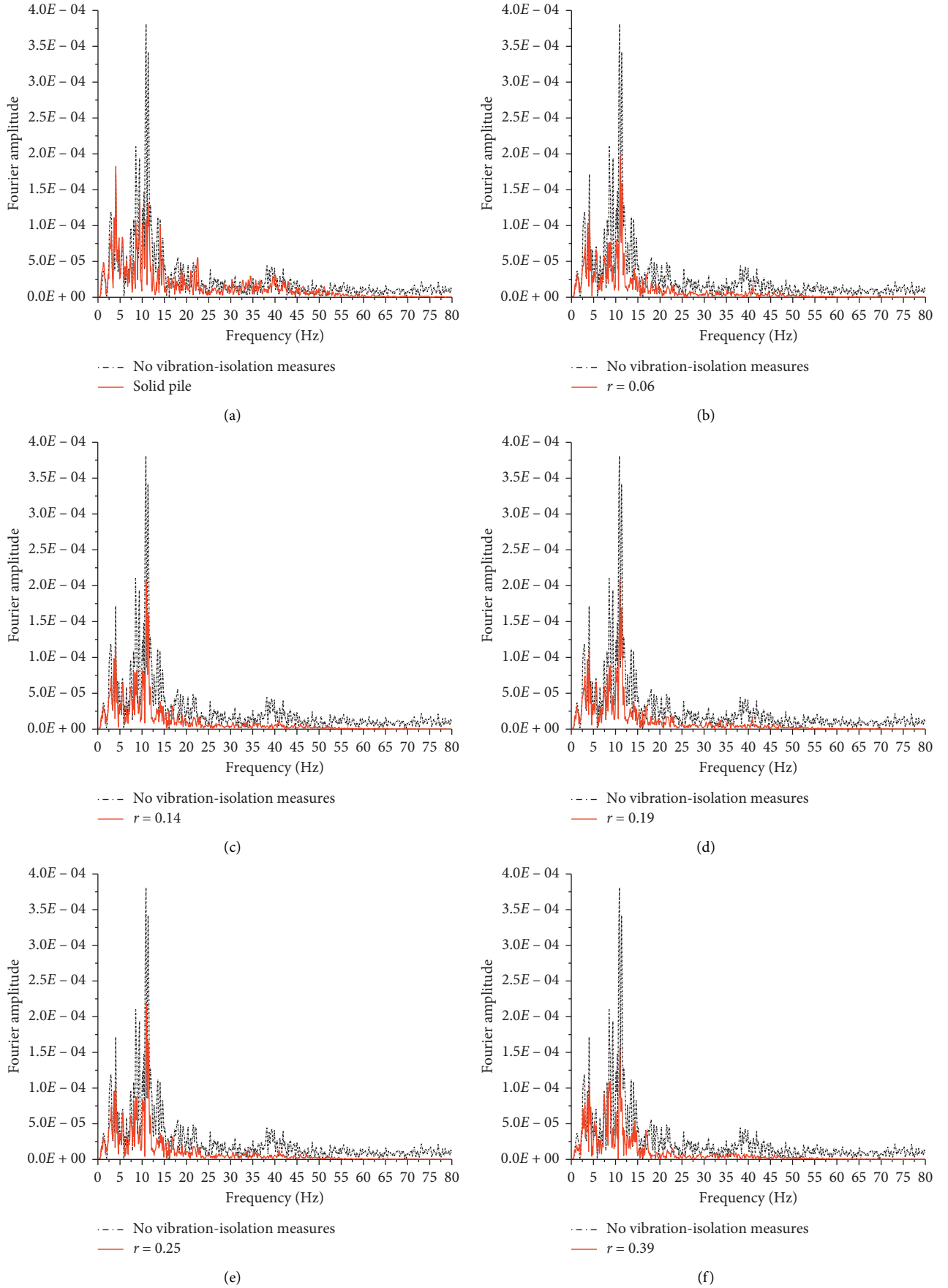


FIGURE 30: Influence of hollow ratio (r) on vibration-isolation effect (comparison of frequency spectra).

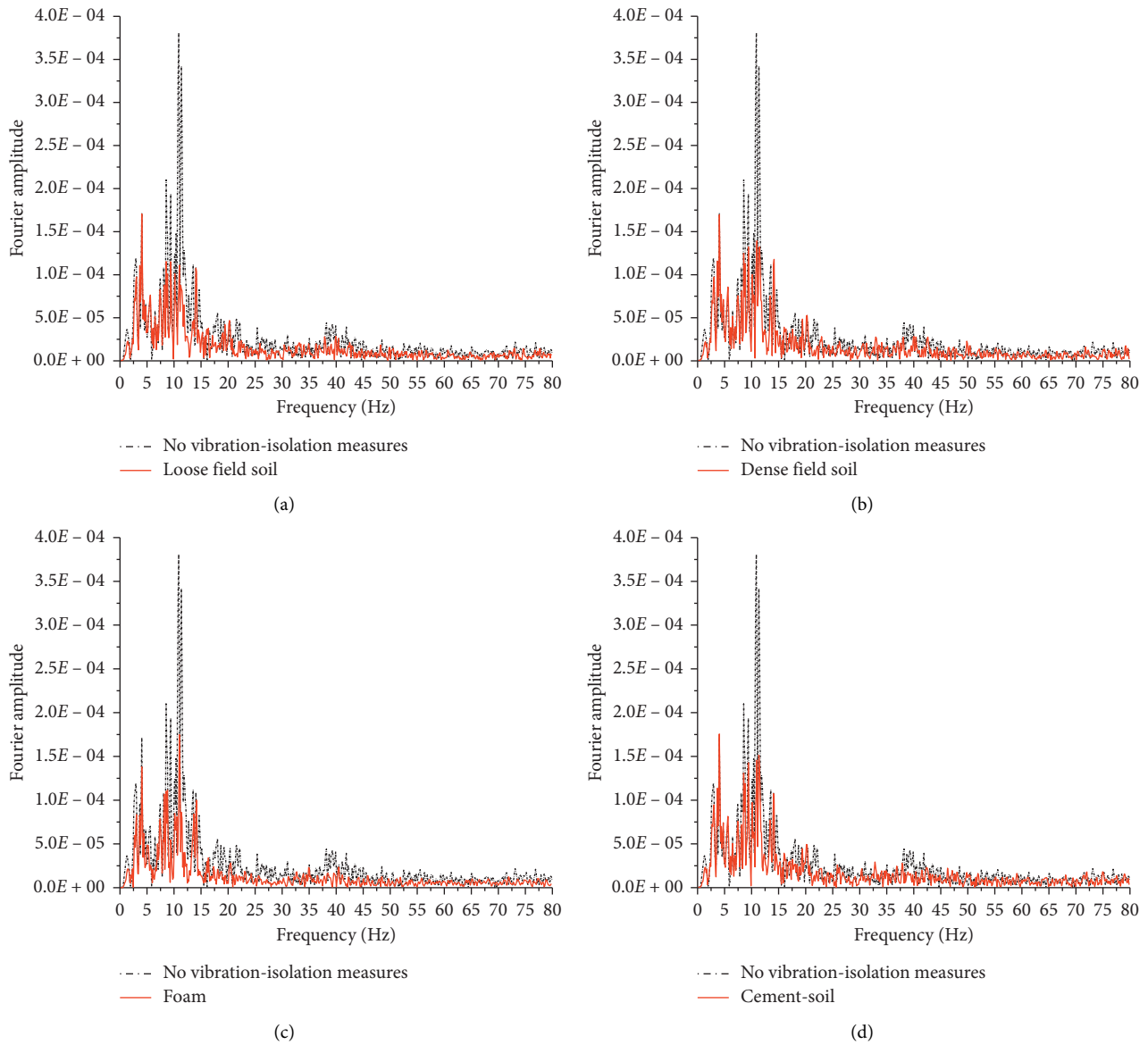


FIGURE 31: Influence of filling material on vibration-isolation effect (comparison of frequency spectra).

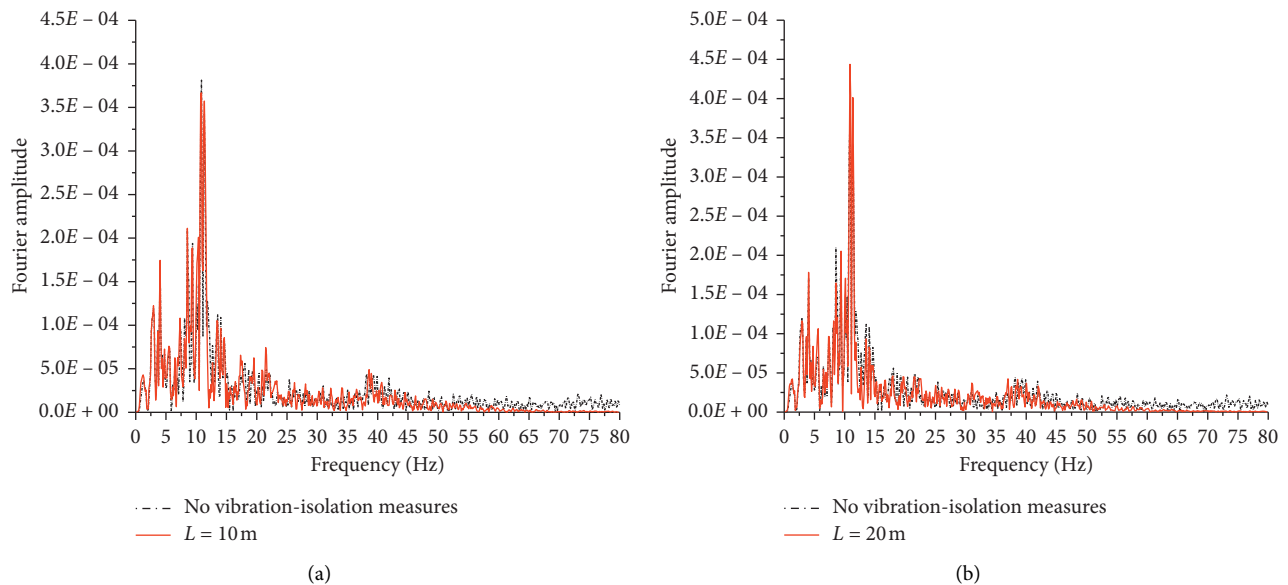
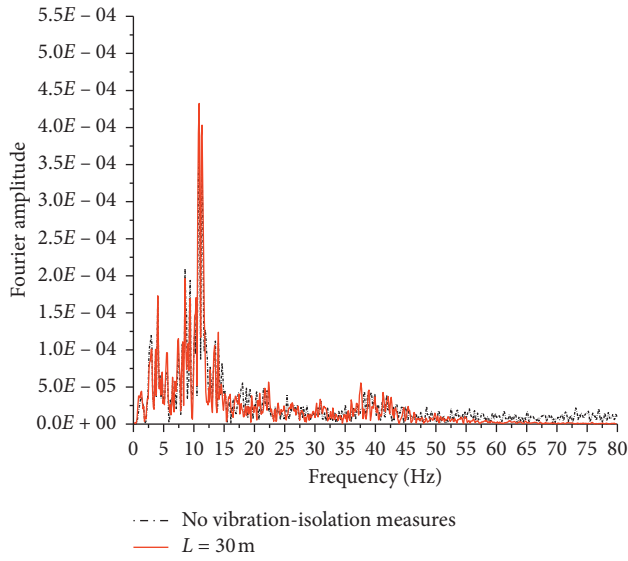
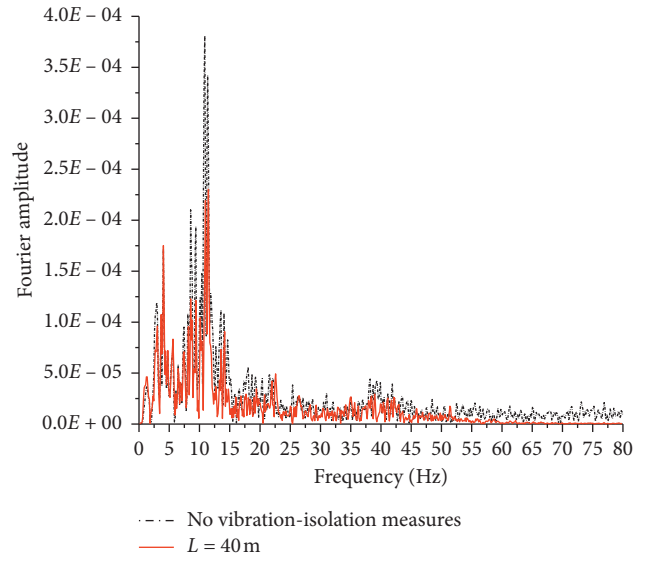


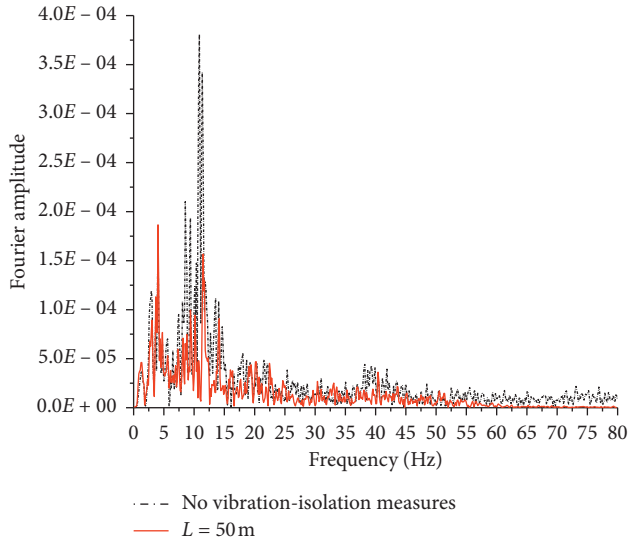
FIGURE 32: Continued.



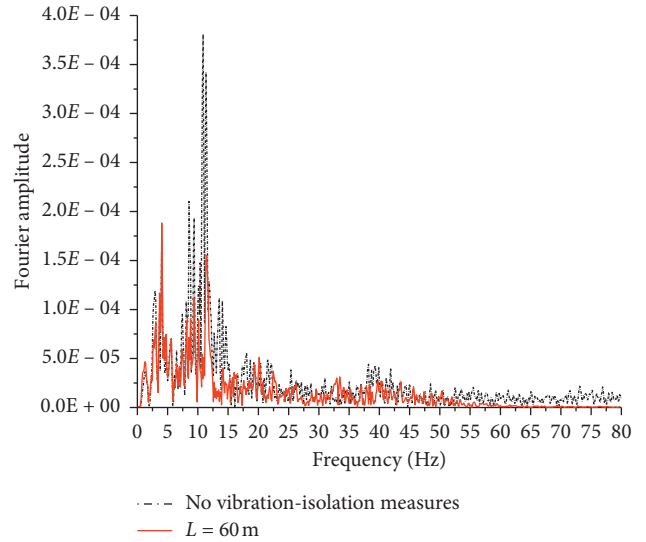
(c)



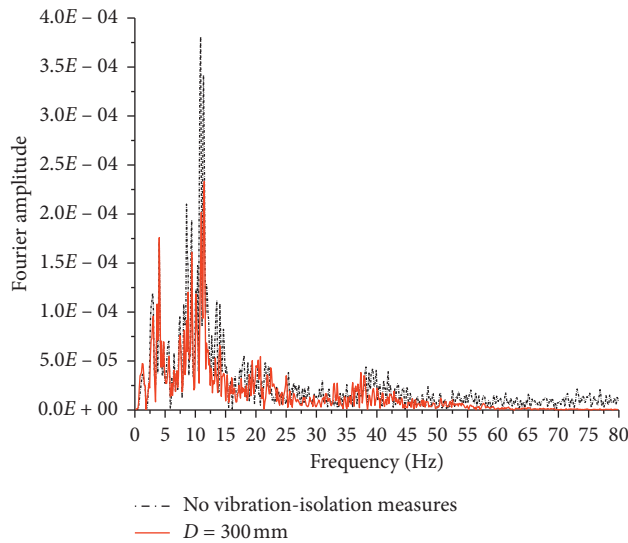
(d)



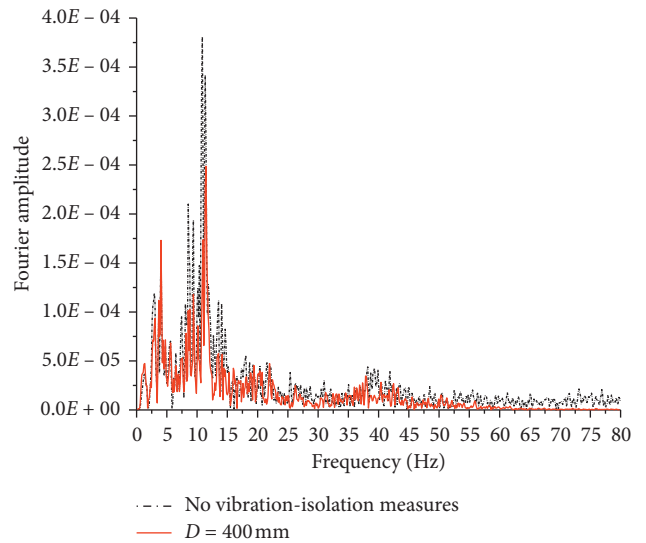
(e)



(f)

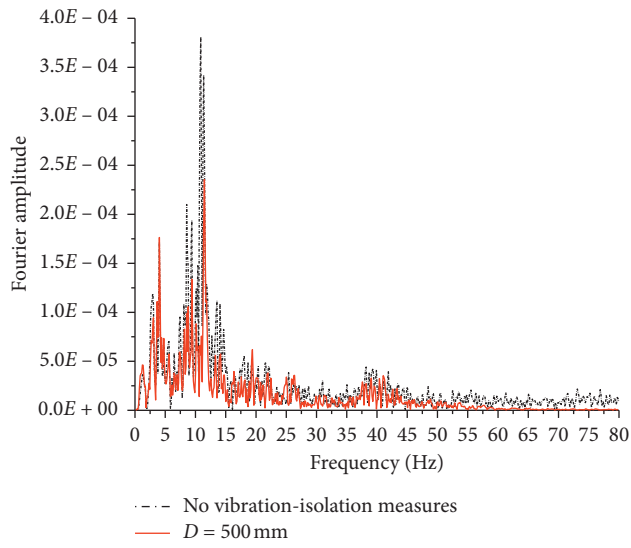
FIGURE 32: Influence of pile length (L) on vibration-isolation effect (comparison of frequency spectra).

(a)

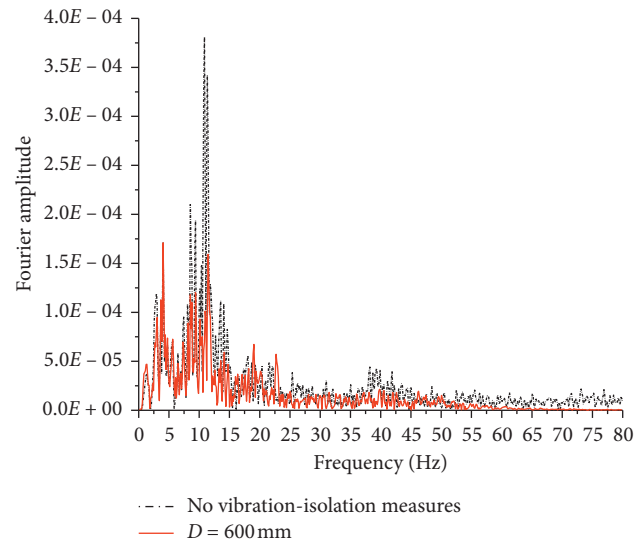


(b)

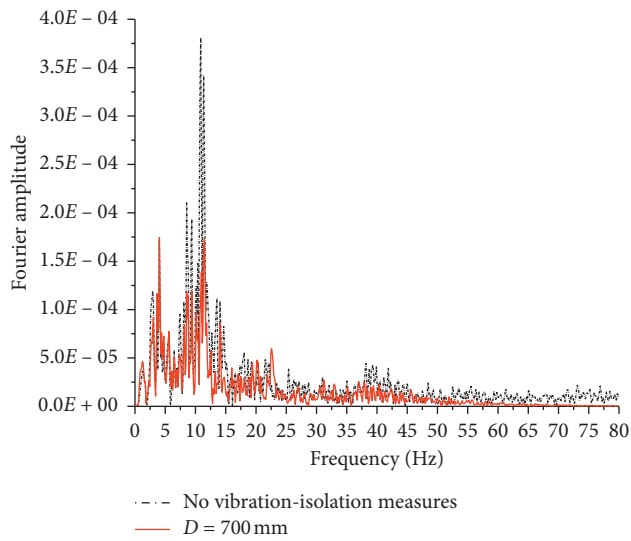
FIGURE 33: Continued.



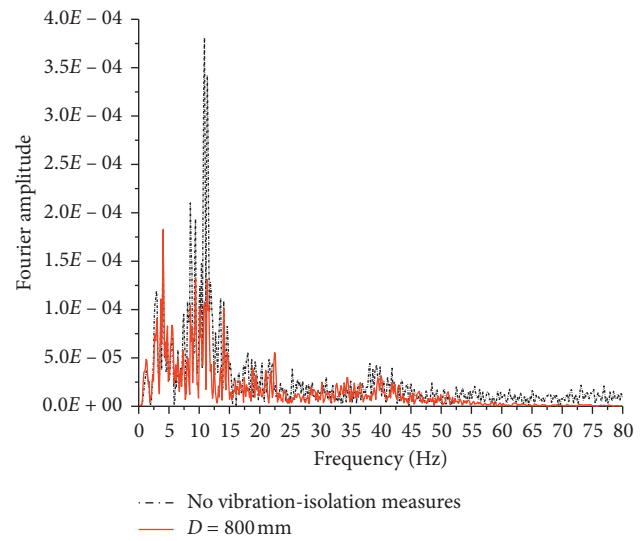
(c)



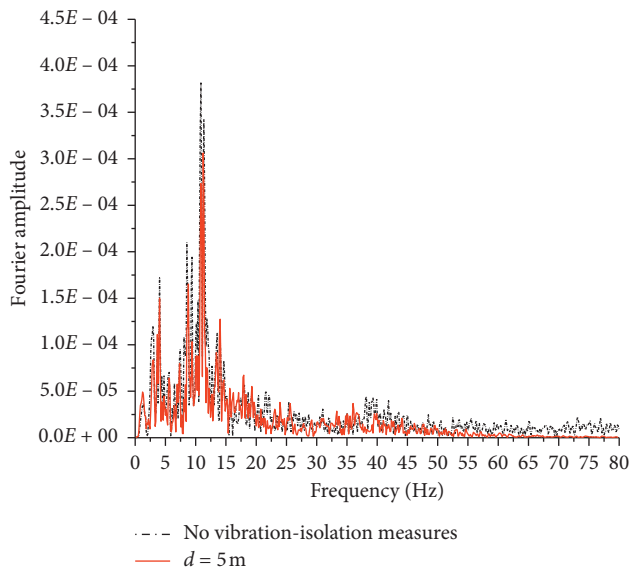
(d)



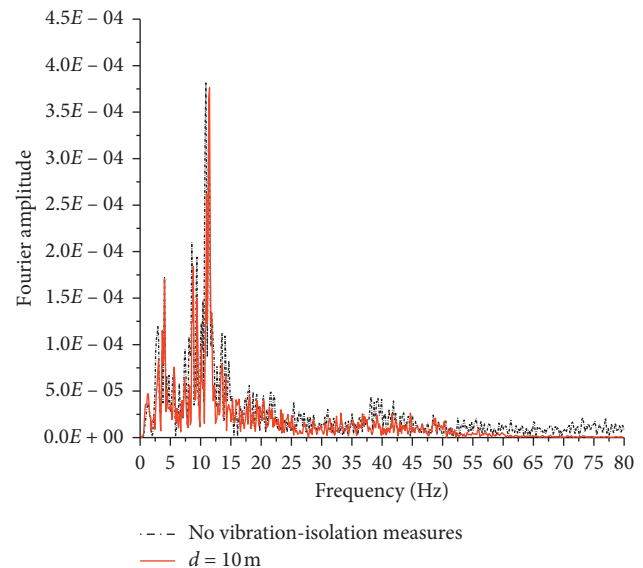
(e)



(f)

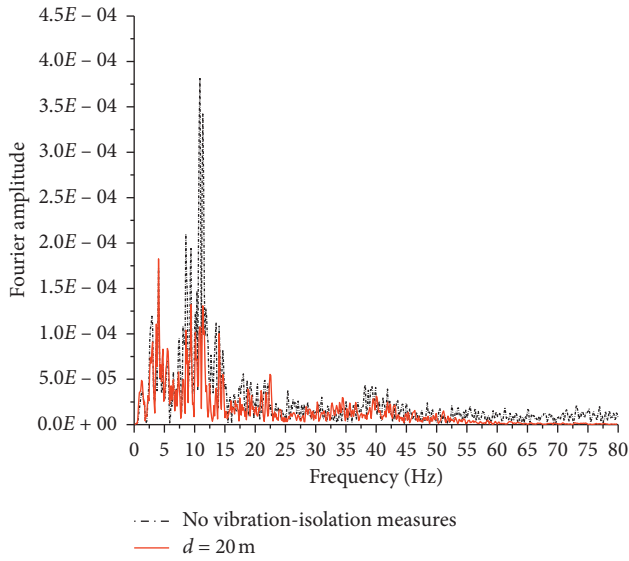
FIGURE 33: Influence of pile diameter (D) on vibration-isolation effect (comparison of frequency spectra).

(a)

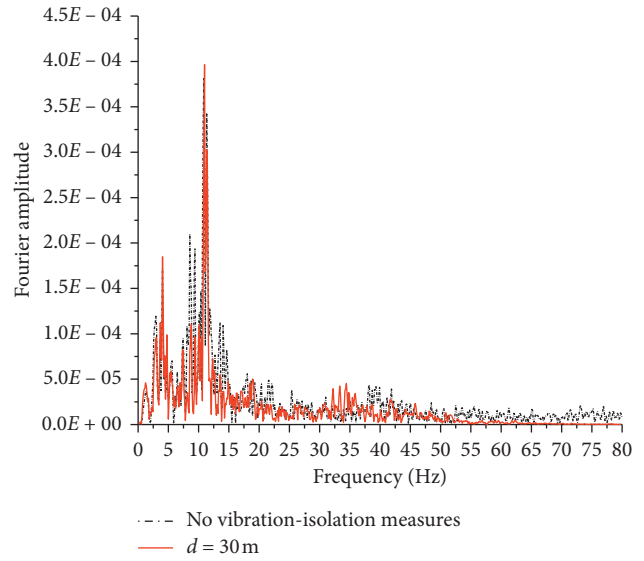


(b)

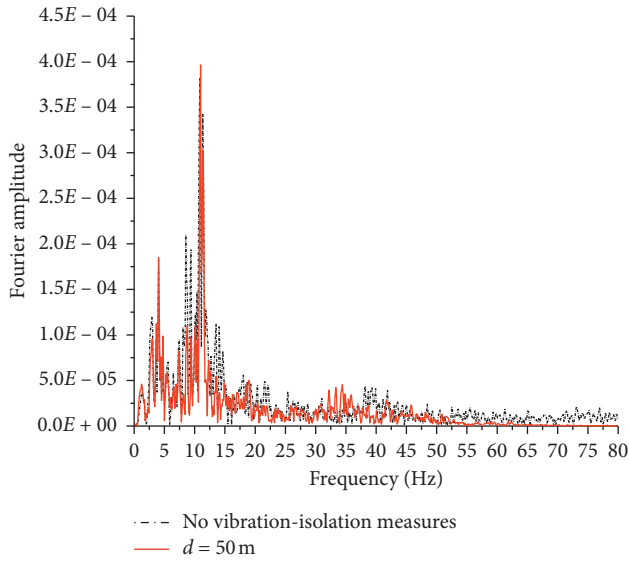
FIGURE 34: Continued.



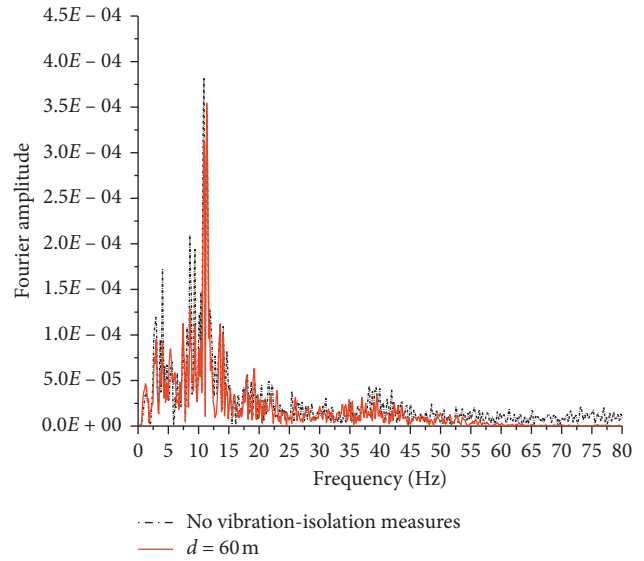
(c)



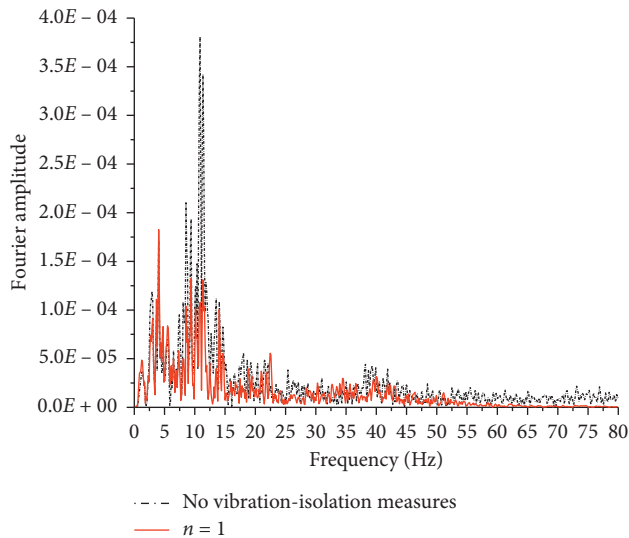
(d)



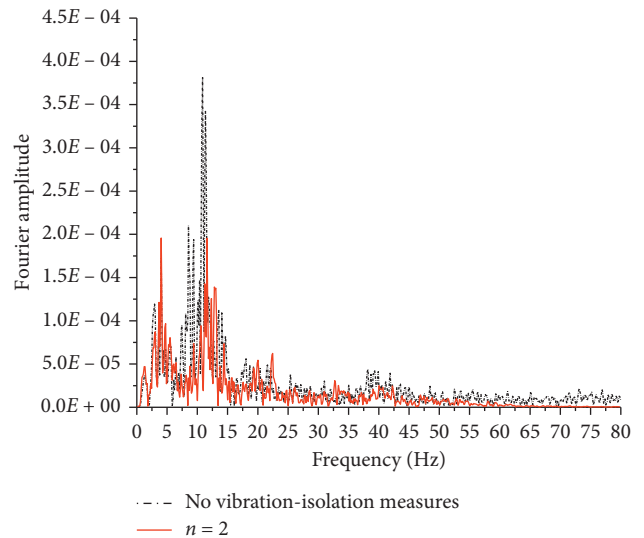
(e)



(f)

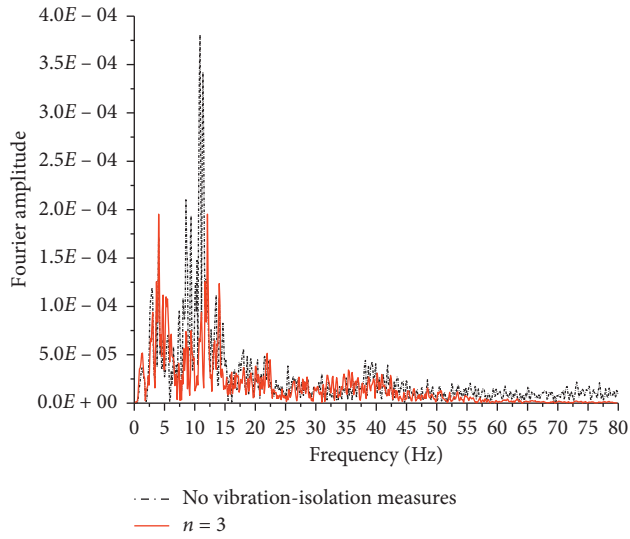
FIGURE 34: Influence of distance from hard-X-ray tunnel (d) on vibration-isolation effect (comparison of frequency spectra).

(a)

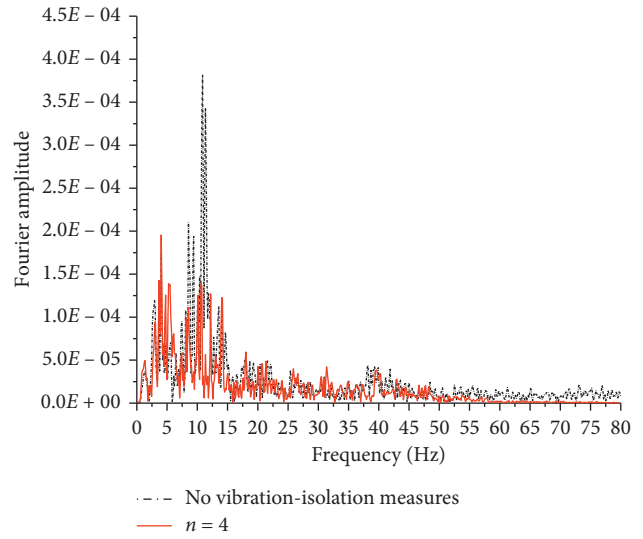


(b)

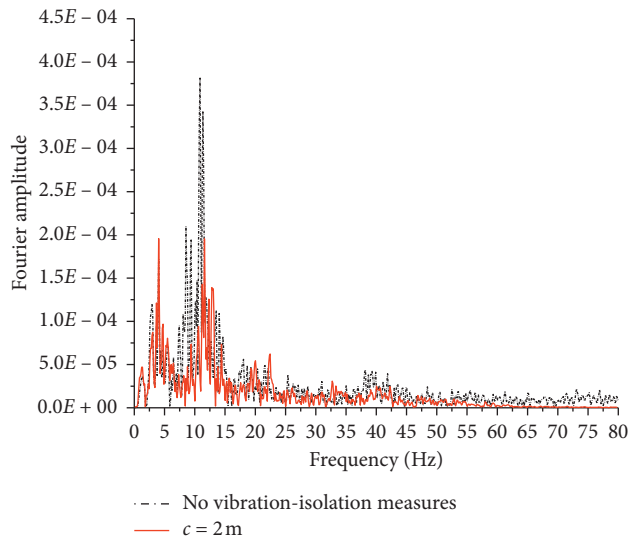
FIGURE 35: Continued.



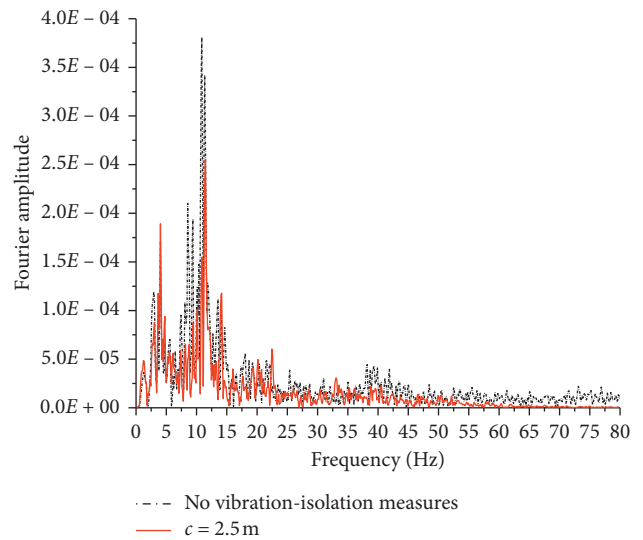
(c)



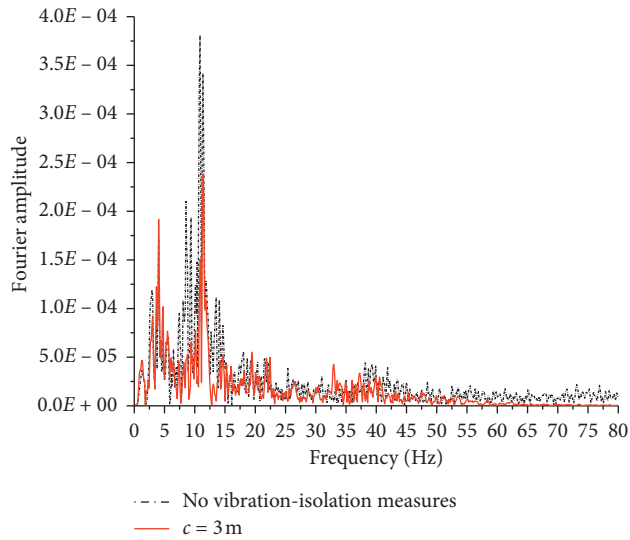
(d)

FIGURE 35: Influence of pile row number (n) on vibration-isolation effect (comparison of frequency spectra).

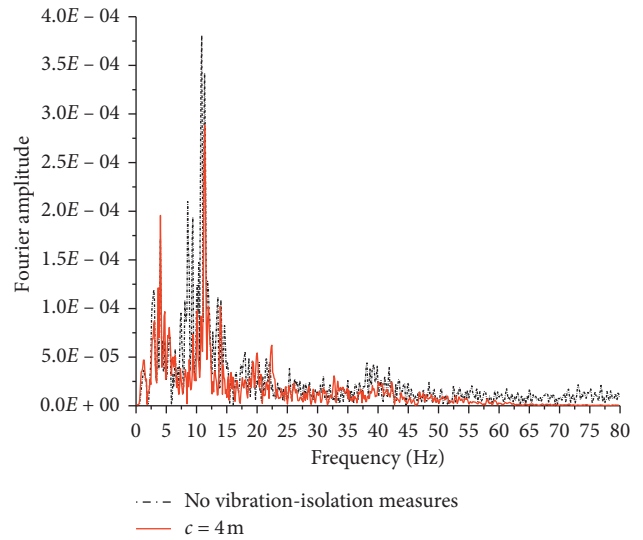
(a)



(b)



(c)



(d)

FIGURE 36: Continued.

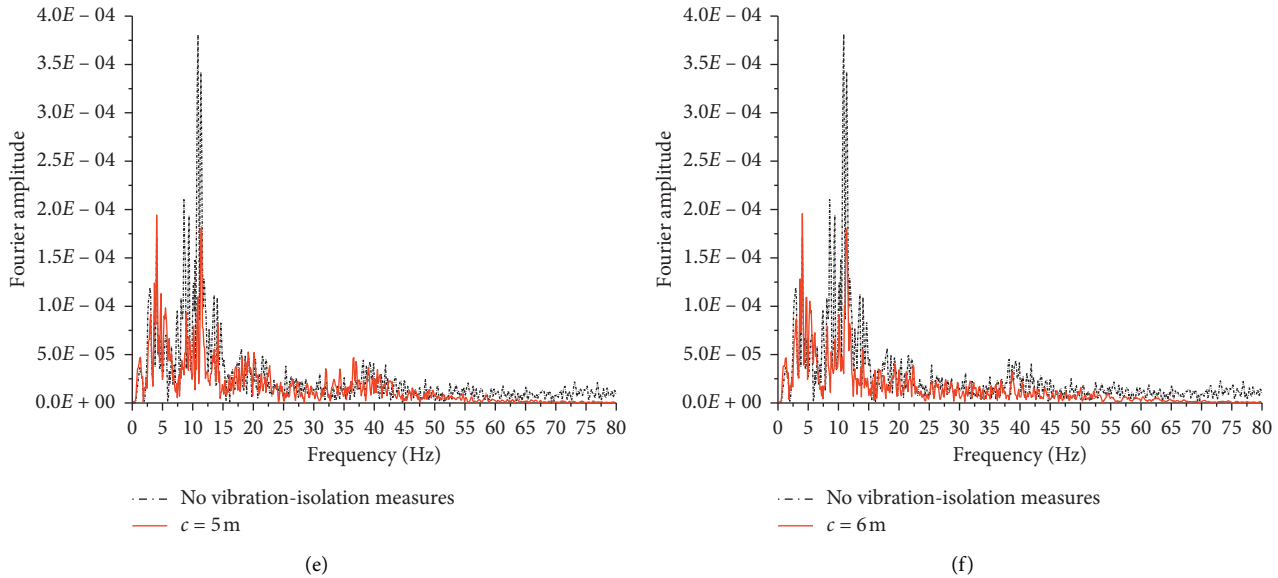


FIGURE 36: Influence of row spacing (c) on vibration-isolation effect (comparison of frequency spectra).

5. Conclusions

Based on a hard-X-ray tunnel under construction in Shanghai, relevant research was conducted on the vibration-isolation performance of a pile barrier in an area of soft soil. The main conclusions are as follows.

The vibration waves generated by the maglev, metro line 16 (viaduct part), and Luoshan Road viaduct traffic are concentrated mainly at middle and high frequencies, while those generated by the Luoshan Road ground traffic are concentrated mainly at low frequency. With increasing propagation distance and depth, the acceleration amplitude of the vibration waves is attenuated gradually. The high-frequency part of the vibration waves is attenuated rapidly in the soil, while the low-frequency part is attenuated slowly.

The attenuation law of the vibration waves in the soil as calculated by the numerical method is consistent with the field vibration measurements, thereby verifying the effectiveness of the numerical method in simulating environmental vibrations.

The pile body material, pile length, hollow ratio, filling material, and vibration-isolation position are the main factors affecting the vibration-isolation effect of the pile barrier. The vibration-isolation capacity of the pile barrier is proportional to the pile length, elastic modulus, and hollow ratio, and it is inversely proportional to the stiffness of the filling material. The pile diameter, row number, and row spacing have little influence on the vibration-isolation effect of the row piles. Increasing the pile diameter attenuates the acceleration amplitude around 10 Hz to a certain extent but basically has no influence on the acceleration amplitude around 5 Hz. With decreasing row spacing and increasing pile row number, the vibration-isolation effect of the row piles is improved slightly.

Data Availability

The data used to support the findings of this study are available from the corresponding author upon request.

Conflicts of Interest

The authors declare that they have no conflicts of interest.

Acknowledgments

This study was supported by the Shanghai Municipal Science and Technology Major Project (grant nos. 2017SHZDZX02 and 17DZ1203902).

References

- [1] S. Pennig, J. Quehl, U. Mueller et al., "Annoyance and self-reported sleep disturbance due to night-time railway noise examined in the field," *The Journal of the Acoustical Society of America*, vol. 132, no. 5, pp. 3109–3117, 2012.
- [2] M. G. Smith, I. Croy, M. Ogren, and K. P. Waye, "On the influence of freight trains on humans: a laboratory investigation of the impact of nocturnal low frequency vibration and noise on sleep and heart rate," *PLoS One*, vol. 8, no. 2, Article ID e55829, 2013.
- [3] M. Crispino and M. D'Apuzzo, "Measurement and prediction of traffic-induced vibrations in a heritage building," *Journal of Sound and Vibration*, vol. 246, no. 2, pp. 319–335, 2001.
- [4] H. Takemiya, "Field vibration mitigation by honeycomb WIB for pile foundations of a high-speed train viaduct," *Soil Dynamics and Earthquake Engineering*, vol. 24, no. 1, pp. 69–87, 2004.
- [5] S. Wolf, "Potential low frequency ground vibration (<6.3 Hz) impacts from underground LRT operations," *Journal of Sound and Vibration*, vol. 267, no. 3, pp. 651–661, 2003.

- [6] J. T. Nelson, "Recent developments in ground-borne noise and vibration control," *Journal of Sound and Vibration*, vol. 193, no. 1, pp. 367–376, 1996.
- [7] S. Gupta, W. F. Liu, G. Degrande et al., "Prediction of vibrations induced by underground railway traffic in Beijing," *Journal of Sound and Vibration*, vol. 310, no. 3, pp. 608–630, 2008.
- [8] P. Chatterjee, G. Degrande, S. Jacobs et al., "Experimental results of free field and structural vibrations due to underground railway traffic," in *Proceedings of the 10th International Congress on Sound and Vibration*, pp. 387–394, Stockholm, Sweden, 2003.
- [9] V. Aiello, D. Boiero, M. D'Apuzzo, L. V. Socco, and F. Silvestri, "Experimental and numerical analysis of vibrations induced by underground trains in an urban environment," *Structural Control and Health Monitoring*, vol. 15, no. 3, pp. 315–348, 2008.
- [10] O. von Estorff and M. Adam, "Reduction of train-induced building vibrations by using open and filled trenches," *Computers & Structures*, vol. 83, no. 1, pp. 11–24, 2005.
- [11] M. Sanayei, P. Maurya, and J. A. Moore, "Measurement of building foundation and ground-borne vibrations due to surface trains and subways," *Engineering Structures*, vol. 53, pp. 102–111, 2013.
- [12] G. Gao, N. Li, and X. Gu, "Field experiment and numerical study on active vibration isolation by horizontal blocks in layered ground under vertical loading," *Soil Dynamics and Earthquake Engineering*, vol. 69, pp. 251–261, 2015.
- [13] G. Gao, J. Chen, X. Gu, J. Song, S. Li, and N. Li, "Numerical study on the active vibration isolation by wave impeding block in saturated soils under vertical loading," *Soil Dynamics and Earthquake Engineering*, vol. 93, pp. 99–112, 2017.
- [14] M. Gao, S. P. Tian, Y. Wang et al., "Isolation of ground vibration induced by high speed railway by DXWIB: field investigation," *Soil Dynamics & Earthquake Engineering*, vol. 131, Article ID 106039, 2020.
- [15] M. Gao, X. Xu, Q. S. Chen et al., "Reduction of metro vibrations by honeycomb columns under the ballast: field experiments," *Soil Dynamics & Earthquake Engineering*, vol. 129, Article ID 105913, 2020.
- [16] S. J. Chen, X. Z. Ling, Z. Y. Zhu et al., "Field monitoring on train-induced vibration in the seasonally frozen region of daqing in spring," in *Proceedings of the International Conference on Transportation Engineering*, Chengdu, China, 2012.
- [17] D. Wei, W. X. Shi, R. L. Han et al., "Measurement and research on subway induced vibration in tunnels and buildings nearby in Shanghai," in *Proceedings of the International Conference on Multimedia Technology (ICMT)*, Hangzhou, China, July 2011.
- [18] L. Schillemans, "Impact of sound and vibration of the North-South high-speed railway connection through the city of antwerp belgium," *Journal of Sound and Vibration*, vol. 267, no. 3, pp. 637–649, 2003.
- [19] W. Gardien and H. G. Stuit, "Modelling of soil vibrations from railway tunnels," *Journal of Sound and Vibration*, vol. 267, no. 3, pp. 605–619, 2003.
- [20] S. Liao and D. A. Sangrey, "Use of piles as isolation barriers," *Journal of Geotechnical and Geoenvironmental Engineering*, vol. 104, no. 9, pp. 1139–1152, 1978.
- [21] Y. B. Yang, *Analysis on Soil Vibration Induced by High-Speed Railways*, Taiwan University, Taipei, Taiwan, 1996.
- [22] H. Xia, *Vibration Engineering of Traffic Environment*, Science Press, Beijing, China, 2010.
- [23] K. Ishihara, *Soil Behaviour in Earthquake Geotechnics*, Clarendon Press, Oxford, UK, 1996.
- [24] X. Q. Gu, J. Yang, M. S. Huang et al., "Bender element tests in dry and saturated sand: signal interpretation and result comparison," *Soils and Foundations*, vol. 55, no. 5, pp. 952–963, 2015.
- [25] B. M. Das and G. V. Ramana, *Principles of Soil Dynamics*, PWS-Kent Pub. Co., USA, 1993.
- [26] J. B. Liu, Y. Gu, and Y. X. Du, "Consistent viscous-spring artificial boundary and Viscous-spring boundary element," *Chinese Journal of Geotechnical Engineering*, vol. 28, no. 9, pp. 1070–1075, 2006.
- [27] Y. Gu, *Theoretical Analysis of the Efficient Numerical Method for Soil-Structure Dynamic Interaction and its Application*, Tsinghua University, Beijing, China, 2005.
- [28] G. Y. Gao, Z. Y. Li, C. Qiu, and Z. Q. Yue, "Three-dimensional analysis of rows of piles as passive barriers for ground vibration isolation," *Soil Dynamics and Earthquake Engineering*, vol. 26, no. 11, pp. 1015–1027, 2006.
- [29] G. Yue and Y. H. Li, "Three-dimensional analysis of a row of holes as active wave barrier in saturated soil," in *Proceedings of the GeoShanghai 2018 International Conference: Advances in Soil Dynamics and Foundation Engineering*, Shanghai, China, May 2018.

Research Article

Dynamic Reliability of Continuous Rigid-Frame Bridges under Stochastic Moving Vehicle Loads

Naiwei Lu^{1,2}, Kai Wang¹, Honghao Wang¹, Yang Liu^{1,3}, Yuan Luo³, and Xinhui Xiao³

¹Engineering Research Center of Catastrophic Prophylaxis and Treatment of Road & Traffic Safety of Ministry of Education, Changsha University of Science & Technology, Changsha 410114, China

²Industry Key Laboratory of Traffic Infrastructure Security Risk Management, Changsha University of Science and Technology, Changsha 410114, China

³School of Civil Engineering, Hunan University of Technology, Zhuzhou 412007, China

Correspondence should be addressed to Naiwei Lu; lunaiweide@163.com

Received 17 July 2020; Revised 3 September 2020; Accepted 16 September 2020; Published 25 September 2020

Academic Editor: Songye Zhu

Copyright © 2020 Naiwei Lu et al. This is an open access article distributed under the Creative Commons Attribution License, which permits unrestricted use, distribution, and reproduction in any medium, provided the original work is properly cited.

The current volume of freight traffic has increased significantly during the past decades, impacted by the fast development of the national transportation market. As a result, the phenomena of truck overloading and traffic congestion emerge, which have resulted in numerous bridge collapse events or damage due to truck overloading. Thus, it is an urgent task to evaluate bridge safety under actual traffic loads. This study evaluated probabilistic dynamic load effects on rigid-frame bridges under highway traffic monitoring loads. The site-specific traffic monitoring data of a highway in China were utilized to establish stochastic traffic models. The dynamic effect was considered in a vehicle-bridge coupled vibration model, and the probability estimation was conducted based on the first-passage criterion of the girder deflection. The prototype bridge is a continuous rigid-frame bridge with a midspan length of 200 m and a pier height of 182 m. It is demonstrated that the dynamic traffic load effect follows Gaussian distribution, which can be treated as a stationary random process. The mean value and standard deviation of the deflections are 0.071 m and 0.088 m, respectively. The dynamic reliability index for the first passage of girder deflection is 6.45 for the current traffic condition. However, the reliability index decreases to 5.60 in the bridge lifetime, accounting for an average traffic volume growth ratio of 3.6%.

1. Introduction

In the design phase of a bridge, the structural safety is usually evaluated considering design traffic loads, which were formulated according to large traffic monitoring data during the past decades [1, 2]. However, the current or future vehicle load might be beyond the design value with the rapid development of transportation industry. As a result, numerous bridges were collapsed or badly damaged due to truck overloading [3–5]. In case that growing traffic load is becoming more and more critical for in-service bridges, the bridge safety under actual traffic loads deserves investigation. The traffic load effect on a bridge is stochastic due to the random nature of traffic loads [6]. In addition, a moving vehicle leads to dynamic effects motivated by the road

roughness and the bridge deflection. In view of the above reasons, the structural dynamic reliability theory is appropriate for the safety evaluation of existing bridges under actual stochastic traffic loads. In addition, the design vehicle load model can be calibrated with the target reliability index.

In general, the dynamic effect induced by a moving vehicle can be evaluated in a vehicle-bridge interaction system [7, 8]. A great number of literatures focus on dynamic traffic load effects on both short-span and long-span bridges. Chen and Wu [9] investigated dynamic effects of a cable-stayed bridge under stochastic vehicle loads and investigated influence of the sparse and dense states of traffic loads on the probabilistic characteristics of bridge load effect. Lu et al. [10] evaluated lifetime deflection of a suspension bridge considering dynamic and growing traffic loads. Zhou

and Chen [8] investigated probabilistic characteristics of the dynamic response of a cable-stayed bridge under wind load and stochastic vehicle load. Lu et al. [11] investigated the first-passage probability of a cable-stayed bridge under stochastic vehicle loads. Obrien et al. [12] investigated the dynamic increment of extreme traffic loading on short-span bridges. Jiang et al. [13] investigated the fatigue damage of cables of cable-stayed bridge under combined effect of traffic and wind. Li et al. [14] investigated the safety of suspenders of Tsing Ma Bridge under traffic loads. However, there are relatively few studies on probabilistic dynamic traffic load effects on long-span continuous rigid-frame bridges. The unique feature for the continuous rigid-frame bridge is the high-rise piers, which are usually space-flexible, affecting the dynamic behaviour of the bridge. Thus, the probabilistic dynamic traffic load effects on continuous rigid-frame bridges deserve more investigation.

Most studies treated the traffic load effect on a bridge as a random variable. In practice, the load effect on a bridge is a time-varying random process [15]. The commonly used theoretical basis for the probabilistic dynamic analysis of bridges under vehicle load is the first-passage criterion [16, 17]. The first-passage failure probability is usually estimated based on Rice's level-crossing principle [18]. However, applications of the first-passage theory are mostly concentrated in seismic engineering, while the application to traffic load analysis is relatively insufficient. The bottleneck is that the root mean square of traffic load effects is usually evaluated in frequency domain, while the vehicle-bridge coupled vibration is mostly analysed in time domain [19]. Therefore, the key point is how to extract the probability parameters from the dynamic load effect.

This study evaluated probabilistic dynamic traffic load effects on rigid-frame bridges under highway traffic monitoring loads. The site-specific traffic monitoring data were utilized to establish stochastic traffic models. The dynamic effect was considered in a vehicle-bridge coupled vibration model, and the probability estimation was conducted based on the first-passage criterion of the girder deflection. The prototype bridge is a continuous rigid-frame bridge with mid-span length of 200 m and pier height of 182 m. It is demonstrated that the dynamic traffic load effect follows Gaussian distribution and thus can be treated as a stationary random process. Parametric studies were conducted, accounting for the road roughness condition, the bridge span length, and the traffic growth ratio.

2. Theoretical Basis of Probabilistic Traffic-Bridge Interaction Analysis

2.1. Traffic-Bridge Interaction Model. A vehicle passing on a bridge leads to the vibration of the bridge due to the road surface roughness [20]. Meanwhile, the vibration of the bridge impacts the vibration of the vehicle. Thus, the vehicle-bridge interaction is a coupled vibration system. Figure 1 shows the plane motion model of two-axle vehicle, where x represents the road roughness and C and K represent the damping and stiffness parameters, respectively. The vehicle model has four degrees of freedom

including vertical motion of two axles and the motion and rotation of the vehicle body.

Based on the simplified model as shown in Figure 1, the differential equation of motion of the vehicle-bridge coupled system can be written as [21]

$$M_v \ddot{u}_v + C_v \dot{u}_v + K_v u_v = F_{vg} + F_{vb}, \quad (1a)$$

$$M_b \ddot{u}_b + C_b \dot{u}_b + K_b u_b = F_{bg} + F_{bv}, \quad (1b)$$

where M_v and M_b represent the mass matrix of the vehicle and that of the bridge, respectively; C_v and C_b represent the damping matrix of the vehicle and that of the bridge, respectively; K_v and K_b represent the stiffness matrix of the vehicle and that of the bridge, respectively; u_v and u_b represent the displacement vector of the vehicle and that of the bridge, respectively; F_{vb} and F_{bv} represent the interaction forces between the vehicle and the bridge; F_{vg} and F_{bg} represent the weight of the vehicle and that of the bridge, respectively.

In order to consider the multiple-vehicle effect on the bridge response, this study utilized an equivalent dynamic wheel load (EDWL) approach proposed by Chen and Cai [22]. Based on the EDWL approach, the force of the j th vehicle on a bridge can be simplified as a time-varying force, which can be written as

$$\{F(t)\}_{\text{Eq}}^{\text{wheel}} = \sum_{j=1}^{n_v} \left\{ [1 - R_j(t)] G_j \cdot \sum_{k=1}^n \{h_k [x_j(t) + \alpha_k [x_j(t) d_j(t)]]\} \right\}, \quad (2a)$$

$$R_j(t) = \frac{\text{EDWL}_j(t)}{G_j}, \quad (2b)$$

$$\text{EDWL}_j(t) = \sum_{i=1}^{n_a} \left(K_{vl}^i Y_{vl}^i + C_{vl}^i \dot{Y}_{vl}^i \right), \quad (2c)$$

where R_j represents wheel weight ratio of the j th vehicle; G_j represents the GVW of the j th vehicle; x_j and d_j represent longitudinal and lateral positions on the bridge, respectively; h_k and a_k represent the k th-order vertical and torsional bending modes of the bridge; n and n_v , respectively, represent modal orders of bridges and the number of vehicles on the bridges; K_{vl}^i and C_{vl}^i represent stiffness and damping matrixes of the vehicle, respectively; Y_{vl}^i and \dot{Y}_{vl}^i , respectively, represent the vertical displacement and the velocity of the i th axle; $\text{EDWL}_j(t)$ represents the equivalent dynamic axis load of the j th vehicle at time t .

The effectiveness of EDWL approach has been verified by Wu and Chen [23] and Lu et al. [24] for long-span cable-stayed bridges and suspension bridges, respectively. This study develops the EDWL approach in probability analysis and reliability evaluation for continuous rigid-frame bridges.

2.2. First-Passage Criterion. The first-passage criterion is usually utilized for Rice's level-crossing probability analysis of a random process. The principle of Rice's level-crossing is shown in Figure 2, where t is time, x is a random process,

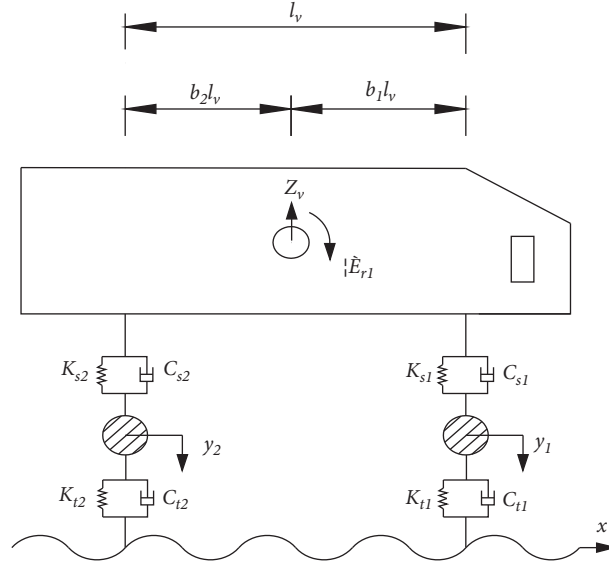


FIGURE 1: Vehicle-bridge coupled vibration system.

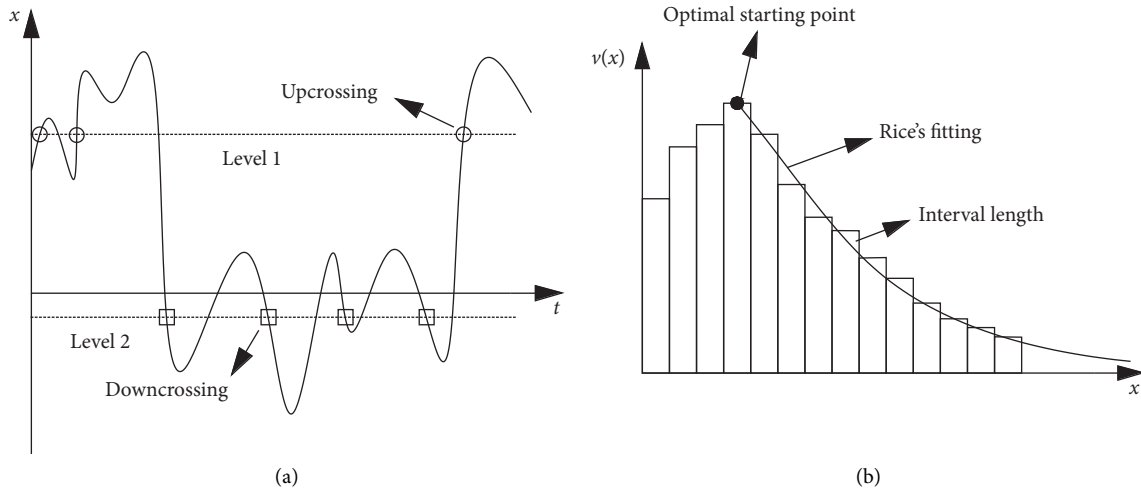


FIGURE 2: The level-crossing principle.

that is, the traffic load effect in the present study, and $v(x)$ is the level-crossing rate fitted to the histograms of the number of crossings. Thus, the critical content of the level-crossing theory is to count the number of crossings for the random process.

Suggest that the traffic load effect can be assumed as a Gaussian random process, which will be demonstrated in the case study. For a random process $x(t)$, Rice [25] provided the number of crossings for a level b during time T , which is written as

$$N_b(T) = \int_0^T \int_{-\infty}^{+\infty} |\dot{x}(t)| p_{xx}(\dot{x}, x, t) d\dot{x} dx, \quad (3)$$

where $p_{xx}(\dot{x}, x, t)$ is a joint probabilistic density function for $x(t)$ and $\dot{x}(t)$. This function is difficult to estimate for a nonstationary process. Fortunately, the traffic load effect on

a bridge can be treated as a stationary random process, as mentioned by researchers [26, 27]. On this basis, the level-crossing rate $v_b(t)$ for a threshold b can be written as

$$v_b(t) = \int_{-\infty}^{+\infty} |\dot{x}| p_{xx}(\dot{x}, x, t) d\dot{x}. \quad (4)$$

For a Gaussian stationary random process with the mean value of zero, the level-crossing probability can be simplified further as

$$v_b = \frac{1}{2\pi} \frac{\sigma_{\dot{x}}}{\sigma_x} \exp\left[-\frac{b^2}{2\sigma_x^2}\right], \quad (5)$$

where v_b is a constant for level b and σ_x is the root mean square value. In addition, the number of level-crossings of stochastic traffic load effects can be assumed as Poisson

distribution. Therefore, the probability of exceeding a threshold can be written as

$$P_r(b) = \exp[-v_b \cdot T]. \quad (6)$$

Note that the accuracy of the estimation mostly depends on the fitting to the curves as shown in Figure 2. In addition, a higher threshold b will result in a more reliable estimation. In general, the mean value of the traffic load effect on a bridge is not zero, which is different from seismic load effects. Therefore, this study developed the above procedures to a nonzero mean value process, which is rewritten as

$$v_b = \frac{1}{2\pi} \frac{\sigma_x}{\sigma_x} \exp\left[-\frac{(b - m_x)^2}{2\sigma_x^2}\right], \quad (7)$$

where m_x is the mean value of the traffic load effect.

The density of traffic loads changes with time, where the traffic will be congested and free-flowing for the day and night, respectively. Therefore, the daily vehicle flow was divided into sparse and dense states based on the density of stochastic vehicle model. The probability can be treated as the superposition of the two types of level-crossing probability, which is written as

$$P_f(b, T) = 1 - \exp[-(a_1 \cdot v_{b1} + (1 - a_1) \cdot v_{b2})T], \quad (8)$$

where v_{b1} and v_{b2} represent the level-crossing rates for the congested and free-flowing vehicle flows, respectively; a_1 and a_2 represent the proportions of the congested and free-flowing vehicle flows, respectively.

There is a relationship between the structural reliability and the first-passage probability. On this basis, the dynamic reliability can be written as

$$\beta = \Phi^{-1}(1 - P_f), \quad (9)$$

where β is the reliability index, $\Phi()$ is the cumulative distribution function (CDF) of the standard normal distribution, and $\Phi^{-1}()$ is the corresponding inverse function.

2.3. Computational Procedures. Based on the derived formulations of the vehicle-bridge coupled vibration system and the first-passage criterion, a computational framework is essential to combine the components as a system. This study presented a comprehensive framework for dynamic and probabilistic analysis for traffic load effects on rigid-frame bridges based on traffic monitoring data. Figure 3 shows the flow chart of the procedures.

As shown in Figure 3, the framework consists of three main procedures: the stochastic traffic modelling, the traffic-bridge interaction analysis, and the probability evaluation. Detailed illustrations of the procedures are shown as follows.

The first step is the stochastic traffic modelling. Initially, the screened traffic monitoring data should be collected from site-specific highways. Subsequently, all vehicles are classified as 6 groups according to the configuration associated with the number of axles. On this basis, the statistical analysis can be conducted for probability modelling of the gross vehicle weight (GVW), the driving lanes, and the

vehicle spacing. Finally, the stochastic traffic load model can be simulated utilizing the Monte Carlo simulation (MCS) approach.

The second step is the traffic-bridge interaction analysis. The critical step is to model the dynamic parameters of the vehicle model and the modal parameters of the bridge. Usually, a 2D vehicle model as shown in Figure 1 can be utilized for a relatively precise analysis. The dynamic characteristics of the bridge are considered as mode shapes and natural frequencies. Since the long-span rigid-frame bridge is more complex than a conventional-girder bridge, the numbers of mode shapes and frequencies should be considered as more as possible. Subsequently, the EDWL approach is utilized to convert the moving stochastic traffic flow into time-varying forces. Finally, the time history of traffic load effects can be simulated based on the pseudo-dynamic analysis.

The third step is the probability evaluation. This step is conducted based on Rice's level-crossing theory. Based on the time histories evaluated from the traffic-bridge interaction analysis, the number of level-crossings can be counted. The number of crossings is formed as histograms, where the level-crossing rate can be fitted accurately as shown in Figure 2(b). Subsequently, the maximum traffic load effect can be extrapolated with consideration of a return period. Finally, the first-passage probability and reliability index can be evaluated based on the assumption of Poisson distribution.

3. Stochastic Vehicle Flow Simulation Based on WIM Data

3.1. Probabilistic Modelling of WIM Measurements. Due to the truck overloading behaviour, the GVW usually follows a multimodal distribution. In this regard, this study utilized a Gaussian mixture model (GMM), which is a superposition of several Gaussian models. In practice, the GMM method is widely used in the application of data clustering [28], but it is relatively insufficient in the vehicle weight modelling.

In general, a GMM can be represented as

$$P\{w | (a_i, \mu_i, \sigma_i^2)\} = \sum_{i=1}^M a_i \cdot g(w | \mu_i, \sigma_i^2), \quad (10)$$

where w is the GVW, a_i is a weight coefficient, g is a Gaussian distribution function, and M is the number of Gaussian functions. The Gaussian is written as

$$g(w | \mu_i, \sigma_i^2) = \frac{1}{\sqrt{2\pi\sigma_i^2}} \exp\left[-\frac{1}{2\sigma_i^2}(w - \mu_i)^2\right], \quad (11)$$

where μ_i represents mean value of the i th Gaussian distribution function and σ_i represents standard deviation of the i th Gaussian distribution function. The parameters of GMMs are usually estimated based on the maximum likelihood optimization. This study utilized the Expectation-Maximization (EM) algorithm to evaluate these parameters.

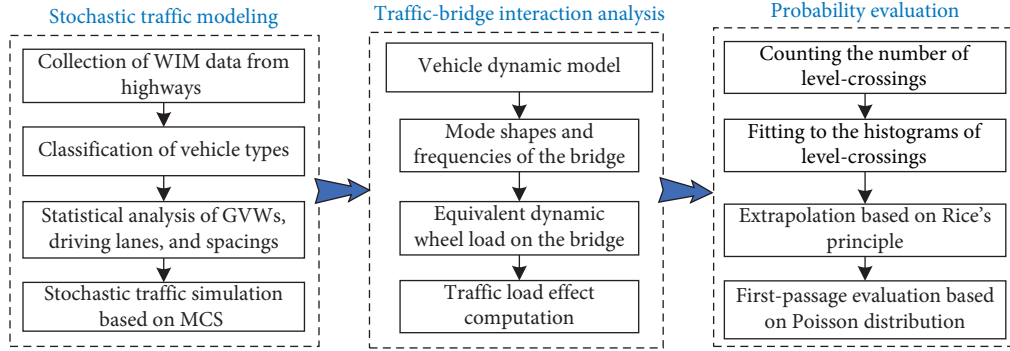


FIGURE 3: Flow chart of the proposed computational framework.

The number of components is estimated based on the Akaike information criterion (AIC) [29].

The authors have conducted extensive analyses on the probability modelling of traffic parameters as shown in the doctoral dissertation [30]. Due to the limit of article, only the probability distributions for 6-axle trucks are provided. Figure 3 plots the fitted probability distribution function (PDF) of the axle weight and the GVW, respectively. In Figure 4, W_{64} represents the second axle load of six-axle vehicle.

It is observed that the axle weight and the GVW follow bimodal distribution. In addition, the GMMs have ideally fitted to the empirical histograms. In other words, the GMM has captured the probability behaviour of truck overloading. Note that the threshold weight for 6-axle trucks is 550 kN according to the traffic law in China. It can be observed that half of the 6-axle trucks are overloaded, which is indeed a risk for existing bridges.

3.2. Stochastic Traffic Flow Simulation. With the probability models established based on the weigh-in-motion (WIM) data, this study utilized MCS to establish different types of stochastic traffic flows. The detailed procedures are summarized in Figure 5, where N_{ADT} is the total number of daily traffic. The programming package MATLAB was utilized to translate the traffic as a matrix that will be called in the subsequent vehicle-bridge interaction analysis.

The preliminary statistical analytical results of the actual traffic monitoring data indicate that the vehicle spacing between two following vehicles follows the Weibull distribution for congested traffic, while it follows Gamma distribution for free-flowing state. Figure 6 plots the sample of a free-flowing stochastic traffic flow, where V1 denotes the lightweight cars and busses, and V2–V6 denote the 2-axle to 6-axle trucks, respectively. Details of the configuration of the vehicle types can be found in [28].

The benefit of the stochastic traffic flow is the probability distribution in accordance with the site-specific traffic monitoring data. In addition, the stochastic traffic model can be updated with the consideration of the traffic volume growth and the limit of truck overloading.

4. Case Study

4.1. Backgrounds of the Prototype Bridge. Labajin Bridge, a continuous rigid-frame bridge in Yalu highway of Sichuan in China, is selected as prototype to investigate the deflection of first-passage probability. Site photos of the bridge are shown in Figure 7. The span length of the bridge is $(105 + 200 + 200 + 105)$ m. The bridge is very famous due to the highest piers in the area of Asia, where the length of pier No. 10 is 182 m. The dimensions of the cross sections of box-girders and piers are shown in Figure 8. The material of the box-girder is C60 concrete. The pier is a composite structure with concrete filled steel tube. The internal and external concrete grades are C80 and C50, respectively.

The finite element model is shown in Figure 9. All of the elements were simulated with beam elements. The boundary condition of the bridge piers is the constraint of all degrees of freedom at the bottom elements. The top nodes of mid-span piers are connected with the closest girder nodes in rigid connection. The top nodes of side-span piers are connected with the closet nodes with the compressive only connection. The top 50 vertical modes of vibration were extracted for the following vehicle-bridge interaction analysis.

4.2. Influence of RRC on Probability Distribution. Since the road roughness condition (RRC) has a significant influence on the vehicle-bridge interaction system, this study selected “good” and “poor” RRCs for the comparative study. The RRCs were simulated by an inverse Fourier transformation function and corresponding power spectral density. The coefficients for “good” and “poor” RRCs are $32 \times 10^{-6} \text{ m}^3/\text{cycle}$ and $512 \times 10^{-6} \text{ m}^3/\text{cycle}$, respectively. Figure 10 plots the time histories of the two types of RRC samples. It is obvious that the poor RRC has a wider fluctuation range compared to the one of good RRC.

The modal analysis of the bridge was conducted firstly considering the modal switches in three space directions. The first 50-order modal shape of the bridge was extracted to solve vehicle-bridge coupled vibration analysis. The damping constant of the concrete was taken as 0.05. T stochastic vehicle flow samples were transformed as equivalent time-varying concentrated forces based on EDWL method. Subsequently, the time histories of the vehicle load effects were evaluated by utilizing the proposed

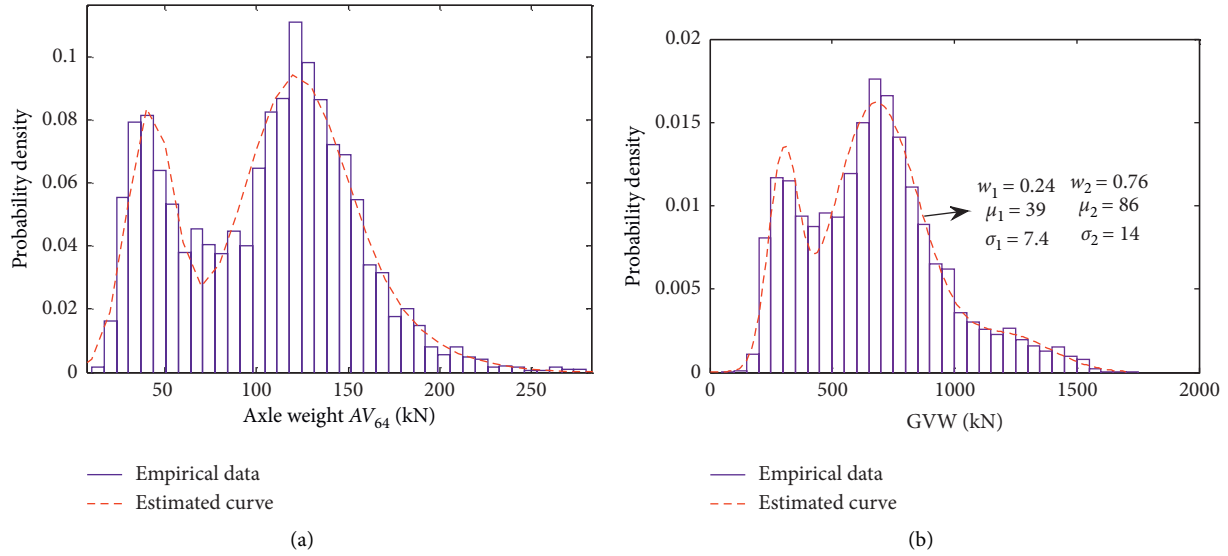


FIGURE 4: Probabilistic distribution of axle load of 6-axis trucks: (a) axle weight; (b) gross weight.

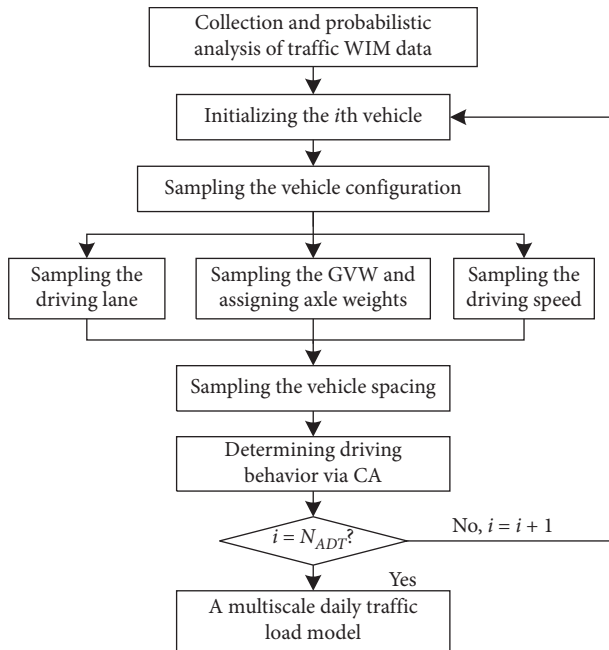


FIGURE 5: Procedures of stochastic vehicle flow simulation.

pseudodynamic approach. Figure 11 plots the vertical deflection histories of the critical point in the mid-span of the bridge accounting for both good and poor RRCs, respectively.

It is observed from Figure 10 that the poor RRC results in more deviations compared with the good RRC. The maximum deflection is located at 162 s, where several heavy trucks load on the mid-span point simultaneously. The maximum deflections for good and poor RRCs are -0.196 m and -0.246 m, respectively. Thus, it is demonstrated that the RRC has a significant influence on the maximum load effect.

Since the basis for extreme value extrapolation is the assumption of Gaussian distribution, the probability distribution should be fitted. Figure 12 plots the histograms of the deflections and the fitted PDF and CDF curves of Gaussian distribution. It is obvious that both good and poor RRCs follow Gaussian distribution. In addition, the shape of histograms for the poor RRC is more flat than that of the good RRC.

The hypothesis testing was conducted to check the fitting to Gaussian distribution. The fitting variances are 0.0028 and 0.0019 for the good and poor RRCs, respectively. It is confirmed that the samples do not refuse the Gaussian distribution. In order to capture the influence of the two types of RRCs on the probabilistic load effect, the histograms of numbers of level-crossings were counted as shown in Figure 13.

As shown in Figure 13, Rice's level-crossings were fitted to the top 30% samples. It is observed that the poor RRC leads to larger number of level-crossings compared to the good RRC. Based on the above analysis, it can be concluded that the RRC can affect the probabilistic characteristics of traffic load effects, and thus a poor RRC will amplify the maximum traffic load effect.

4.3. Influence of Bridge Span Length on the Dynamic Deflection. In order to investigate the influence of bridge span length on the deflection, both shorter-span and longer-span continuous rigid-frame bridges were selected for comparison study. The main span lengths of the three bridges are 140 m, 200 m, and 248 m, respectively. In order to make the comparison of general significance, the same traffic flow as shown in Figure 6 was utilized for the three bridges. The bridge parameters and the maximum deflections are shown in Table 1.

As observed from Table 1, the maximum deflection increases with increase of the bridge main span length.

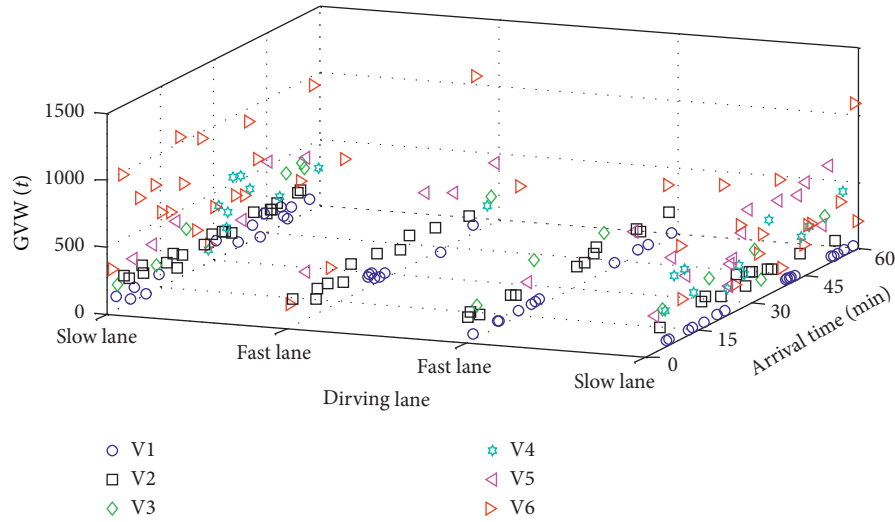


FIGURE 6: A stochastic vehicle flow sample.



FIGURE 7: In-site photos of the Labajin bridge in Yalu highway: (a) final state; (b) construction state.

However, the ratio between the good and poor RRC effects decreases with the increase of the bridge span length. This phenomenon can be explained by the theoretical basis that the bridge with a longer span length has a lower frequency, which will weaken the vehicle-bridge interaction. Therefore, the influence of the RRC on the dynamic effect is weakened with the increase of the bridge span length.

4.4. Probability Estimation. It was concluded by many researchers that dynamic response of bridges under stochastic vehicle flow can be assumed as stationary random process [31]. In order to investigate the influence of random process samples on the characteristics of stationary random processes, the mean value and the correlation coefficient in random process were analysed. Figure 14(a) plots the deflection spectrum density of the bridge girder under

stochastic traffic flow load. Figure 14(b) plots the autocorrelation coefficient of the samples in 100 s, 200 s, and 300 s, respectively.

It is observed that the mean value and standard value of the initial position are greatly affected by 7 seconds. In fact, the mean value and correlation coefficient tend to be constants with the increase of the samplings number. Therefore, if the sample is large enough, this process can be assumed as stationary random process. The random process under stochastic vehicle loads can be represented by the load effects, which was calculated by a large sample of vehicle flows.

The mean value and root mean square deflection of the continuous rigid-frame bridge were obtained by the same method. Figure 15 shows the distribution of mean value and root mean square deflection along the girders.

As observed in Figure 15, the maximum mean value and the root mean square deflection of a continuous rigid-frame

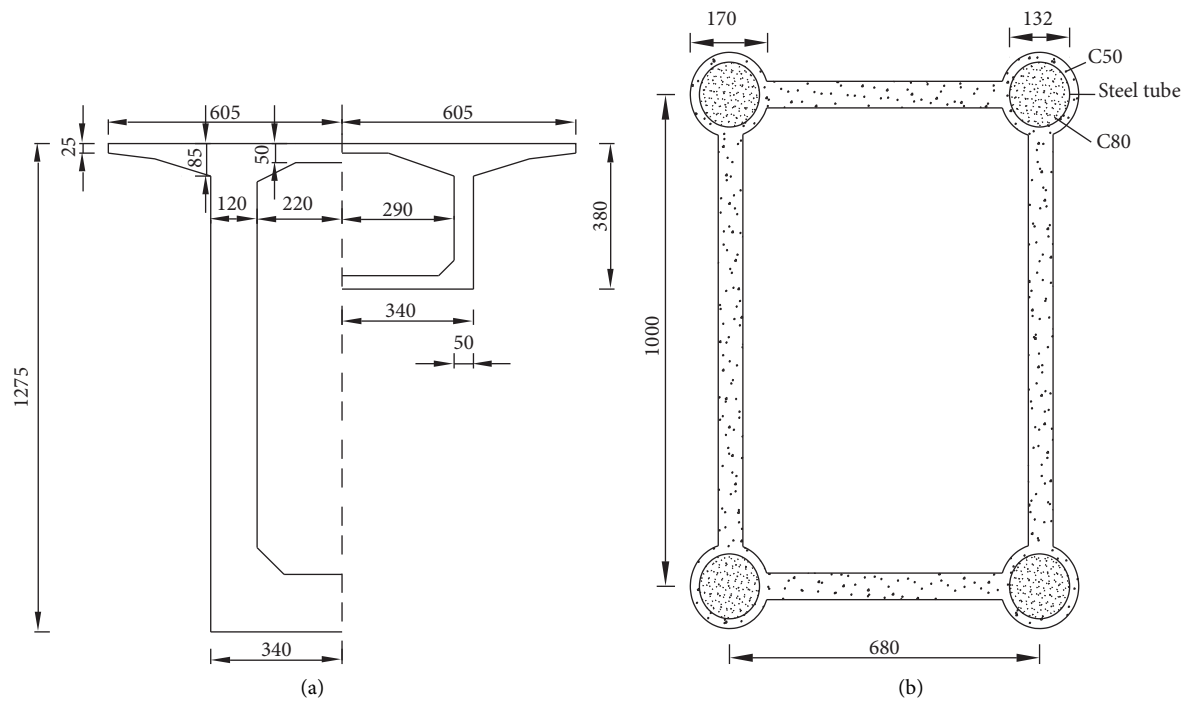


FIGURE 8: Dimensions of cross-sections of Labajin Bridge: (a) girders; (b) piers.

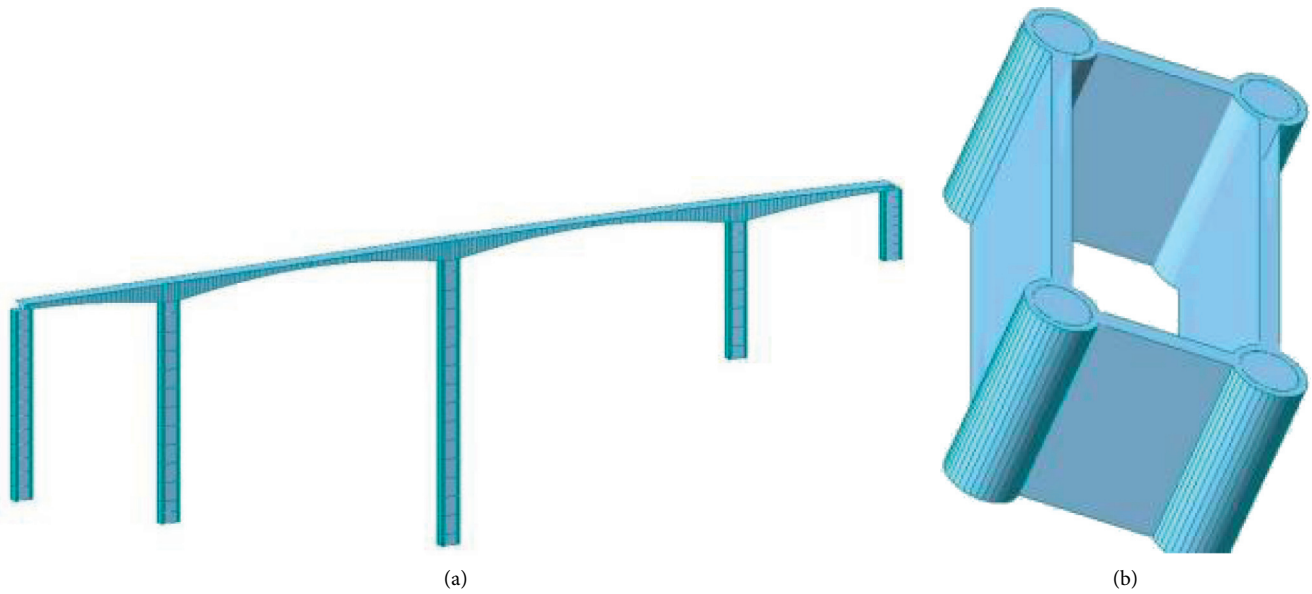


FIGURE 9: Continued.

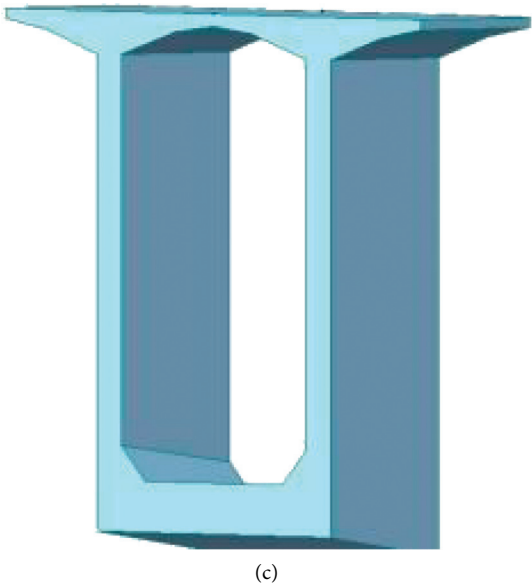


FIGURE 9: Finite element model of Labajin Bridge: (a) overall model; (b) pier element; (c) girder element.

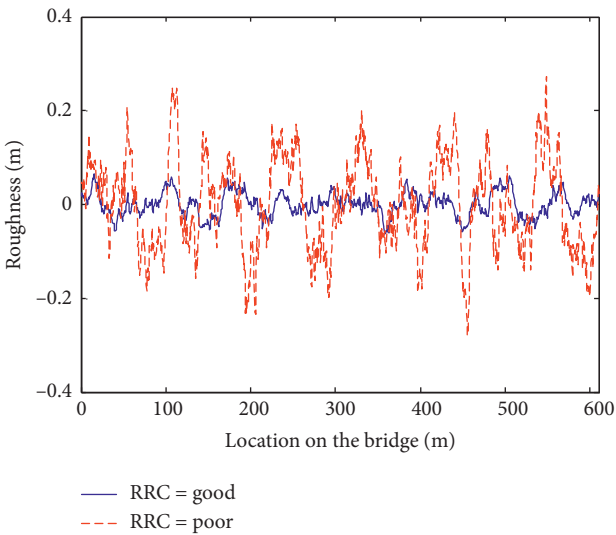


FIGURE 10: Samples of two types of road roughness conditions.

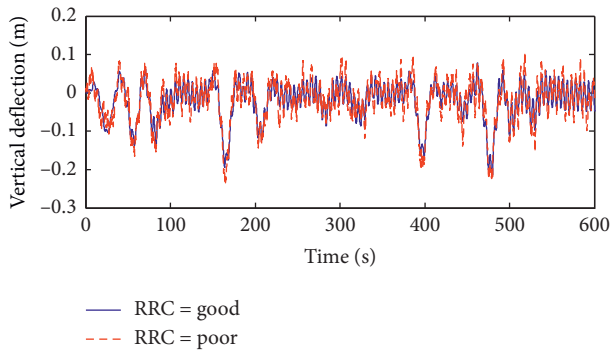


FIGURE 11: Vertical deflection histories of the critical point in the mid-span of the bridge girders in 10 min.

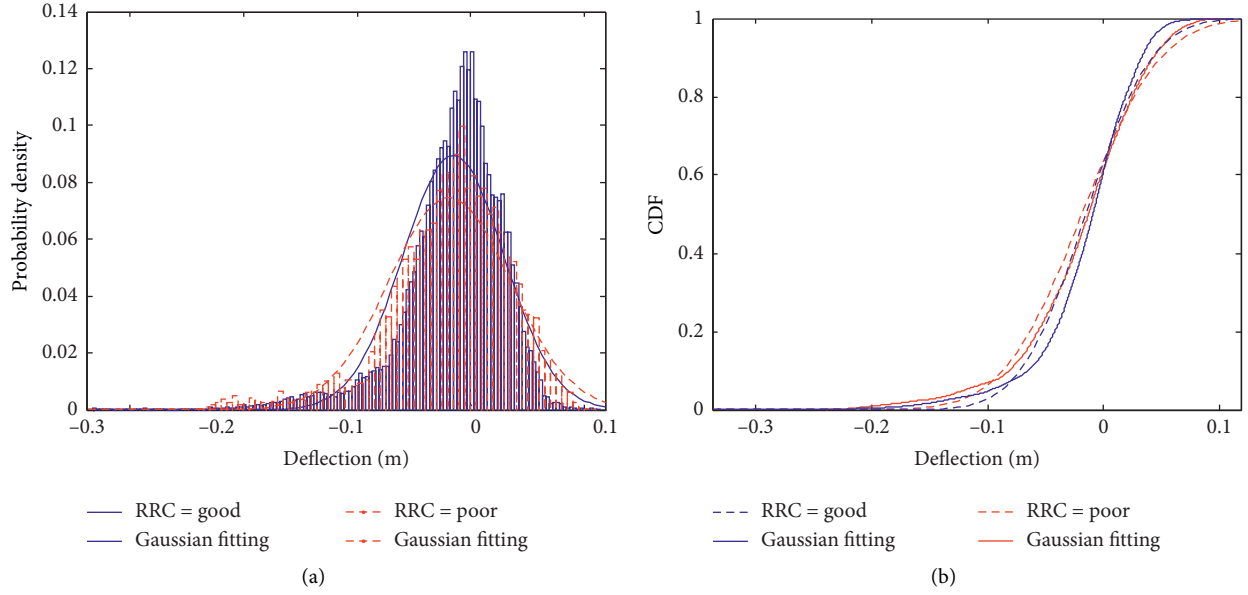


FIGURE 12: Probability distribution of the critical deflection: (a) PDF; (b) CDF.

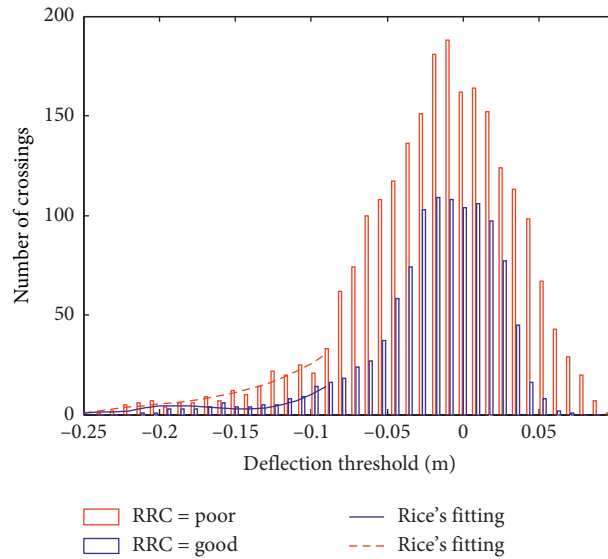


FIGURE 13: Histograms and fitting to the number of level-crossings.

bridge are -0.071 m and 0.088 m, respectively. Therefore, this study selected the mid-span point as representation. The following investigation will focus on the deflection of the critical point under stochastic traffic loads.

4.5. First-Passage Reliability Evaluation. In general, the first-passage reliability analysis can be conducted based on probabilistic model associated with maximum extrapolation. The upper threshold deflection of a continuous rigid-frame bridge is $a = L/500 = 0.4$ m according to designed codes in China. Figure 16 shows the time-varying reliability index

based on the first-passage criterion of the maximum girder deflection.

As shown in Figure 16, the initial reliability index of the bridge is 6.45. However, the reliability index decreases significantly with the time and the proportion of dense traffic flow. With consideration of the proportion of dense traffic flow as 1.2%, 2.4%, and 3.6%, the corresponding reliability indexes of the bridge in 100 years are 5.76, 5.62, and 5.60, respectively. Therefore, it is concluded that the proportion of dense vehicle flow has significant influence on the first-passage probability of the bridge deflection. Thus, the control of dense vehicle

TABLE 1: Critical parameters of three continuous rigid-frame bridges.

Bridge name	Span combination (m)	Height of the 0# segment (m)	Maximum deflection (m)		Dynamic ratio between poor and good RRCs
			RRC = good	RRC = poor	
Shizijing River Bridge	74 + 140 + 74	8.0	-0.137	-0.182	1.32
Labajin Bridge	105 + 200 + 200 + 105	12.5	-0.196	-0.246	1.25
Lengshui River Bridge	130 + 248 + 130	16.0	-0.254	-0.273	1.07

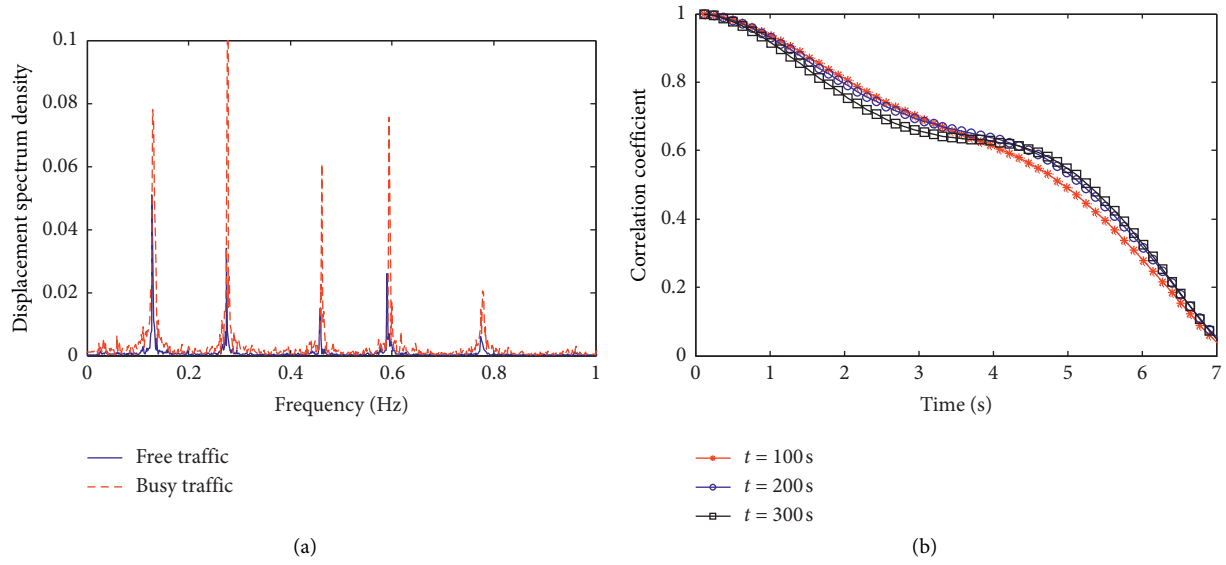


FIGURE 14: Bridge dynamic deflections in frequency domain: (a) spectrum density; (b) correlation coefficient.

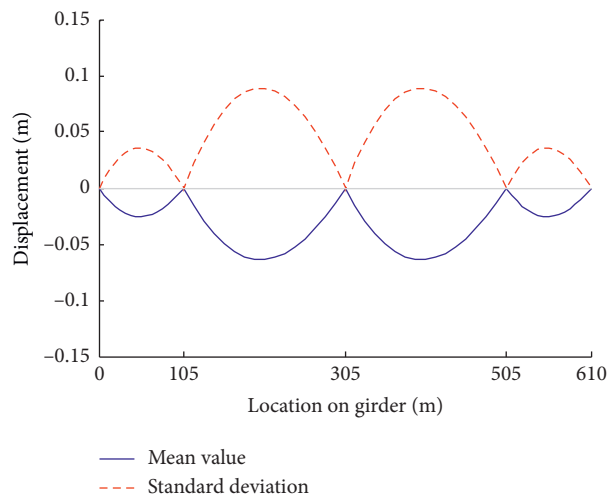


FIGURE 15: Trends of mean value and root mean square of displacement along the girders.

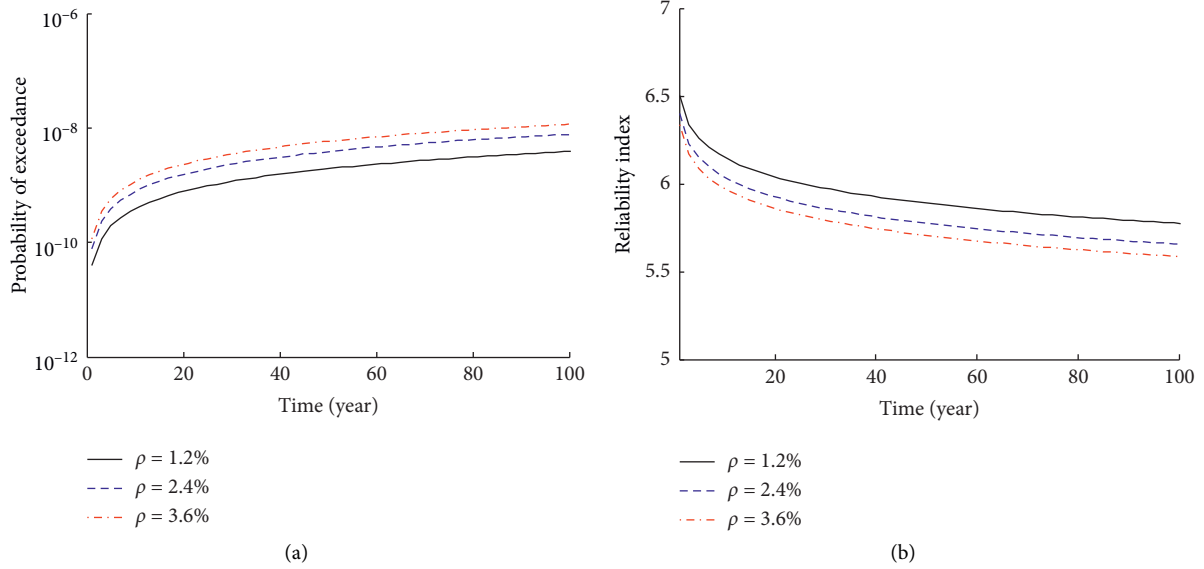


FIGURE 16: Reliability index of the continuous rigid-frame bridge based on the first-passage criterion of the girder deflection: (a) failure probability; (b) reliability index.

flow is essential for ensuring the bridge safety in service period.

5. Conclusions

This study developed the vehicle-bridge coupled vibration model to the dynamic reliability analysis of long-span bridges. A simplified analytical method was presented for evaluating probabilistic dynamic load effect induced by stochastic vehicle loads. The effectiveness of the proposed computational framework was demonstrated in the case study of a continuous rigid-frame bridge. Influence of the RRC, the bridge span length, and the traffic growth on the bridge deflection was investigated. The conclusions are summarised as follows:

- (1) The mean value and the root mean square deflections induced by stochastic traffic loads are constants, which are uncorrelated with time. Therefore, the stochastic traffic-bridge coupled vibration is demonstrated as a stationary Gaussian random process, which can be treated as a long time history.
- (2) The level-crossing is able to capture the probability characteristics of the dynamic traffic load effect and thus provides a connection between the dynamic effect and the probability model.
- (3) The RRC will impact the probabilistic characteristics of traffic load effects. A poor RRC leads to larger number of level-crossings compared to a good RRC, and thus a poor RRC will amplify the maximum traffic load effect.
- (4) The influence of the RRC on the dynamic effect is weakened with the increase of the bridge span length. This phenomenon can be explained by the theoretical basis that the bridge with a longer span length has a lower frequency, which will weaken the vehicle-bridge interaction.

- (5) With consideration of the proportion of dense traffic flow as 1.2%, 2.4%, and 3.6%, the corresponding reliability indexes of the bridge in 100 years are 5.76, 5.62, and 5.60, respectively. The proportion of dense vehicle flow has significant influence on the first-passage probability of the bridge deflection. Thus, the control of dense vehicle flow is essential for ensuring the bridge safety in service period.

Even though the proposed framework is verified for a rigid-frame bridge, it can be applied for more types of bridges. However, more studies are necessary to improve the computational efficiency and accuracy. A more refined traffic-bridge interaction analysis approach instead of the simplified EDWL approach is critical to make the simulation more reasonable. In addition, the simulated traffic load effect needs to be compared with structural health monitoring data.

Data Availability

The original traffic monitoring data are available from the authors if necessary.

Conflicts of Interest

The authors declare that there are no conflicts of interest regarding the publication of this paper.

Acknowledgments

The authors would like to acknowledge the Management Department of the Nanxi Yangtze River Bridge duo for the help with the traffic data collection. This research was funded by the National Natural Science Foundation of China (Grant no. 51908068), the Open Fund of Engineering Research Center of Catastrophic Prophylaxis and Treatment of Road and Traffic Safety of Ministry of Education (Grant no. KJF190403),

Industry Key Laboratory of Traffic Infrastructure Security Risk Management in Changsha University of Science and Technology, (Grant no. 19KF03), Open Fund of Key Laboratory of Bridge Engineering Safety Control in Department of Education in Changsha University of Science and Technology (Grant no. 19KB02), National Science Foundation of Hunan Province (Grant nos. 2020JJ5140 and 2020JJ5589), and the Innovation Platform Open Fund Project of Hunan Education Department (19K002).

References

- [1] A. S. Nowak, "Calibration of LRFD bridge code," *Journal of Structural Engineering*, vol. 121, no. 8, pp. 1245–1251, 1995.
- [2] L. Deng, W. Yan, and L. Nie, "A simple corrosion fatigue design method for bridges considering the coupled corrosion-overloading effect," *Engineering Structures*, vol. 178, pp. 309–317, 2019.
- [3] Y. Liu, X. Xiao, N. Lu, and Y. Deng, "Fatigue reliability assessment of orthotropic bridge decks under stochastic truck loading," *Shock and Vibration*, vol. 2016, Article ID 4712593, 10 pages, 2016.
- [4] Y. Ma Yafei, Z. Guo, L. Wang Lei, and J. Zhang, "Probabilistic life prediction for reinforced concrete structures subjected to seasonal corrosion-fatigue damage," *Journal of Structural Engineering*, vol. 146, no. 7, 2020.
- [5] Z. Guo, Y. Ma, L. Wang et al., "Crack propagation-based fatigue life prediction of corroded RC beams considering bond degradation," *Journal of Bridge Engineering*, vol. 25, no. 8, 2020.
- [6] D. Skokandić, A. M. Ivanković, A. Žnidarič, and M. Srbić, "Modelling of traffic load effects in the assessment of existing road bridges," *Gradevinar*, vol. 71, no. 12, pp. 1153–1165, 2019.
- [7] X. Q. Zhu and S. S. Law, "Recent developments in inverse problems of vehicle-bridge interaction dynamics," *Journal of Civil Structural Health Monitoring*, vol. 6, no. 1, pp. 107–128, 2016.
- [8] Y. Zhou and S. Chen, "Dynamic simulation of a long-span bridge-traffic system subjected to combined service and extreme loads," *Journal of Structural Engineering*, vol. 141, no. 9, pp. 1–18, 2015.
- [9] S. R. Chen and J. Wu, "Dynamic performance simulation of long-span bridge under combined loads of stochastic traffic and wind," *Journal of Bridge Engineering*, vol. 15, no. 3, pp. 219–230, 2009.
- [10] N. Lu, M. Noori, Y. Liu et al., "Lifetime deflections of long-span bridges under dynamic and growing traffic load," *Journal of Bridge Engineering*, vol. 22, no. 11, 2017.
- [11] N. Lu, M. Noori, and Y. Liu, "First-passage probability of the deflection of a cable-stayed bridge under long-term site-specific traffic loading," *Advances in Mechanical Engineering*, vol. 9, no. 1, pp. 1–10, 2017.
- [12] E. J. O'Brien, D. Cantero, B. Enright, and A. González, "Characteristic dynamic increment for extreme traffic loading events on short and medium span highway bridges," *Engineering Structures*, vol. 32, no. 12, pp. 3827–3835, 2010.
- [13] C. Jiang, C. Wu, C. S. Cai, and W. Xiong, "Fatigue analysis of stay cables on the long-span bridges under combined action of traffic and wind," *Engineering Structures*, vol. 207, Article ID 110212, 2020.
- [14] S. Li, S. Zhu, Y.-L. Xu, Z.-W. Chen, and H. Li, "Long-term condition assessment of suspenders under traffic loads based on structural monitoring system: application to the Tsing ma bridge," *Structural Control and Health Monitoring*, vol. 19, no. 1, pp. 82–101, 2012.
- [15] C. C. Caprani, "Lifetime highway bridge traffic load effect from a combination of traffic states allowing for dynamic amplification," *Journal of Bridge Engineering*, vol. 18, no. 9, pp. 901–909, 2013.
- [16] L. Shen, Y. Han, C. S. Cai et al., "Exceedance probability assessment of pedestrian wind environment based on multiscale coupling numerical simulation," *Journal of Aerospace Engineering*, vol. 33, no. 4, 2020.
- [17] P. D. Spanos and I. A. Kougiumtzoğlu, "Galerkin scheme based determination of first-passage probability of nonlinear system response," *Structure and Infrastructure Engineering*, vol. 10, no. 10, pp. 1285–1294, 2014.
- [18] F. Sloothak, V. Wachtel, and B. Zwart, "First-passage time asymptotics over moving boundaries for random walk bridges," *Journal of Applied Probability*, vol. 55, no. 2, pp. 627–651, 2018.
- [19] A. Fenerci and O. Øiseth, "Strong wind characteristics and dynamic response of a long-span suspension bridge during a storm," *Journal of Wind Engineering and Industrial Aerodynamics*, vol. 172, pp. 116–138, 2018.
- [20] D. Y. Zhu, Y. H. Zhang, D. Kennedy, and F. W. Williams, "Stochastic vibration of the vehicle-bridge system subject to non-uniform ground motions," *Vehicle System Dynamics*, vol. 52, no. 3, pp. 410–428, 2014.
- [21] X. Yin, Y. Liu, L. Deng et al., "Dynamic behavior of damaged bridge with multi-cracks under moving vehicular loads," *International Journal of Structural Stability and Dynamics*, vol. 17, no. 2, 2017.
- [22] S. R. Chen and C. S. Cai, "Equivalent wheel load approach for slender cable-stayed bridge fatigue assessment under traffic and wind: feasibility study," *Journal of Bridge Engineering*, vol. 12, no. 6, pp. 755–764, 2007.
- [23] J. Wu and S. R. Chen, "Probabilistic dynamic behavior of a long-span bridge under extreme events," *Engineering Structures*, vol. 33, no. 5, pp. 1657–1665, 2011.
- [24] N. Lu, Y. Ma, and Y. Liu, "Evaluating probabilistic traffic load effects on large bridges using long-term traffic monitoring data," *Sensors*, vol. 19, no. 22, 2019.
- [25] S. O. Rice, "Mathematical analysis of random noise," *Bell System Technical Journal*, vol. 24, no. 1, pp. 46–156, 1945.
- [26] L. Deng, W. Yan, and S. Li, "Computer modeling and weight limit analysis for bridge structure fatigue using OpenSEES," *Journal of Bridge Engineering*, vol. 24, no. 8, 2019.
- [27] W. He, T. Ling, E. J. O'Brien, and L. Deng, "Virtual axle method for bridge weigh-in-motion systems requiring no axle detector," *Journal of Bridge Engineering*, vol. 24, no. 9, 2019.
- [28] M. O'Brien, A. Khan, D. McCrum et al., "Using statistical analysis of an acceleration-based bridge weigh-in-motion system for damage detection," *Applied Sciences*, vol. 10, no. 2, 2020.
- [29] N. Lu, Y. Liu, and Y. Deng, "Fatigue reliability evaluation of orthotropic steel bridge decks based on site-specific weigh-in-motion measurements," *International Journal of Steel Structures*, vol. 19, no. 1, pp. 181–192, 2019.
- [30] N. Lu, *Probability model of dynamic responses and reliability assessment for stiffening girders of suspension bridges under random traffic flow*, Ph.D. thesis, Changsha University of Science and Technology, Changsha, China, 2014.
- [31] X. Yin, Y. Liu, G. Song et al., "Suppression of bridge vibration induced by moving vehicles using pounding tuned mass dampers," *Journal of Bridge Engineering*, vol. 23, no. 7, pp. 1–14, 2018.

Research Article

Antipenetration Performance of Honeycomb Shelter under Two Repeat Projectile Strikes

Qifan Wang,¹ Liusheng Chu²,³ Jie Li,³ Jianhu Sun,¹ Sheng Luo,¹ and Lei Mao¹

¹Department of Civil Engineering, Army Logistics University, Chongqing 401311, China

²School of Civil Engineering, Zhengzhou University, Zhengzhou 450001, China

³CMCU Engineering Co, Ltd., Chongqing 400500, China

Correspondence should be addressed to Liusheng Chu; cls981@163.com

Received 6 May 2020; Revised 2 August 2020; Accepted 25 August 2020; Published 18 September 2020

Academic Editor: Xiaonong Guo

Copyright © 2020 Qifan Wang et al. This is an open access article distributed under the Creative Commons Attribution License, which permits unrestricted use, distribution, and reproduction in any medium, provided the original work is properly cited.

Antipenetration performance of honeycomb shelter under two repeat projectile strikes is investigated via test and numerical simulation. Among them, there are two kinds of test targets: cylindrical honeycomb structure target and reinforced concrete target; a numerical simulation target is a honeycomb-structure target composed of hexagonal honeycomb unit, and the size of the target is the same as that of the honeycomb-structure target in test. The results show that the damage area of the honeycomb-structure target is smaller than that of the reinforced concrete target under projectile strikes with approximately the same velocity. The damage range of the honeycomb-structure target is limited within the hexagonal cell getting contact with projectile left other cells with no damage. During the two repeat projectile strikes, the first projectile will deflect to some extent just as single projectile strike. The deflection of the second projectile is larger and is related to the distance between the strike points of the two projectiles. The results show that honeycomb shelter performs good under two repeat projectile strikes.

1. Introduction

Relationship between weapons and protection engineering is like the relationship between spear and shield. In recent years, precision-guided weapons are getting higher in precision and larger in damage capability, [1] which lead to protection technology getting greatly developed. Therefore, in the fight against protection engineering nowadays, repeated strikes of weapons are needed to destroy the target engineering as single strike cannot destroy engineering especially deeply buried type [2]. In the Gulf War, the U.S. military had to fire two precision-guided weapons with the same trajectory to destroy underground protection engineering. In the Iraq war, an underground command center in Iraq was finally destroyed under 4 repeated penetration weapon strikes [3]. In the future, repeated strikes will be one of the major threats to the important protection engineering in war.

Concrete, metal, and other conventional materials are often unable to meet the protect requirements as for

repeated strikes. The multilevel porous structure in nature provides a way to solve the problem. Under the environment of the survival of the fittest in nature, these organisms form specific porous structures adapted to the changes of nature and get preserved, which show excellent impact resistance mechanical properties. As a typical regular porous structure, the honeycomb structure is inspired by honeybee's honeycomb. Scholars have carried out a lot of research on the impact resistance of this kind of honeycomb material. Hu et al. have studied the influence of hexagonal angle on impact performance [4], Shi et al. have studied the mechanical behavior of honeycomb and its sandwich structure under impact load [5], Shi et al. have studied the influence of loading direction on deformation mode and energy absorption characteristics of honeycomb under in-plane and out of plane loading [6], Shi et al. discussed the influence of cell irregularity and impact velocity on the honeycomb deformation mode [7], and Wang et al. carried out numerical simulation and experimental research on the single penetration performance of the honeycomb baffle structure

[8–11], mainly focusing on the single penetration performance of the honeycomb structure.

According to the current research situation, there are few research studies on the antirepeated penetration of the honeycomb structure. Repeated penetration research mainly considers the damage effects such as crater and damage area size formed by projectile penetration, which can provide research basis and experimental verification for subsequent explosion effect analysis [12]. In this paper, a kind of shielding structure composed of hexagonal concrete-filled steel tube is taken as the research object in this paper.

2. Test and FEM Simulation Specification

2.1. Test Specification. Projectiles used in the tests (Figure 1) are made of 40CrNiMoA alloy with the following specification:

Length: 70 mm

Diameter (middle): 10 mm

Ratio of length to diameter: 7

Diameter (within 60 mm length to the tail end): 15 mm

The compressive strength of concrete and the tensile strength of steel used in the tests are 90 MPa and 370 MPa, respectively. The thickness and diameter of the target are 200 mm and 640 mm, respectively. The target used in tests fall into two categories, namely, Honeycomb Shelter Target (HST for short, as shown in Figure 2) and Reinforced Concrete Target (RCT for short, as shown in Figure 3). HST is a short cylinder with diameter of 640 mm and height of 200 mm mainly composed of 7 concrete-filled steel tubes with hexagonal section, as shown in Figure 2. Each tube is made of 4 mm thickness steel plate with length of 120 mm \times 6 and width of 200 mm which means the tube is with 6 sides of 120 mm in sectional plane and height of 200 mm. RCT is also a short cylinder with diameter of 640 mm and height of 200 mm. Two layers of 70 mm \times 70 mm steel nets made of 18 mm diameter bar are set at planes off upper and lower surface of the cylinder, respectively, as shown in Figure 3.

Figure 4 is test arrangement diagram, and from the left to the right are the projectile launcher, speed measuring device, and target, respectively. Projectile speed can be adjusted by changing the amount of gunpowder charged in the projectile launcher. The speed measuring device is composed of a timer and two pieces of tinfoil arranged perpendicular to projectile trajectory with a fixed distance. Projectile speed can be calculated by distance between the two pieces of tinfoil and time of projectile moving between the two pieces of tinfoil recorded by the timer.

2.2. FEM Model Specification. The projectile is modeled with the same size as projectile used in tests by Design Modeler platform in ANSYS Workbench. The projectile model is meshed with size control (4 mm in size), as shown in Figure 5. Parameters for 40CrNiMoA alloy in AUTODYN are used for the projectile model. Johnson–Cook material strength model and linear equation of the state are also used



FIGURE 1: Projectile used in test.



FIGURE 2: Honeycomb shelter target diagram.

for the projectile model. Johnson–Cook strength model is mainly used to describe materials under large deformation, large stress, and high temperature. In this strength model, the yield stress of the material is expressed as

$$\sigma_y = (A + B\varepsilon_p^n)(1 + C\varepsilon_p^*) \left(1 - \left(\frac{\theta - \theta_t}{\theta_{\text{melt}} - \theta_t}\right)^m\right), \quad (1)$$

where σ_y is the yield stress of the material, A is the yield stress of the material under small deformation, B is the hardening constant, ε_p is the effective plastic strain, n is the hardening index, C is the strain rate constant, ε_p^* is the effective plastic strain rate, θ_{melt} is the melting temperature, and θ_t is the conversion temperature. In the linear equation of state, the material density, shear modulus, bulk modulus, and other parameters are also needed. The specific values of parameters are shown in Table 1.

The HST is modeled with the same size as target used in tests by Design Modeler platform in ANSYS Workbench. The volume sweep mesh method is adopted while generating finite element. Concrete within steel tube centered in HST is with more intensive mesh (4 mm in size) for later contact with projectile, as shown in Figure 6.

As the steel tube is made of low carbon steel, the Johnson–Cook material strength model, linear equation of state, and Johnson–Cook material failure model are used to describe the steel plate in numerical simulation, and related parameters are listed in Table 2.

The JH-2 material model is adopted for concrete in AUTODYN which is described by the Johnson–Holmquist strength model, polynomial equation of state, and Johnson–Holmquist failure model.

It is difficult to determine the parameters of polynomial equation of state by experiment, so the parameters of

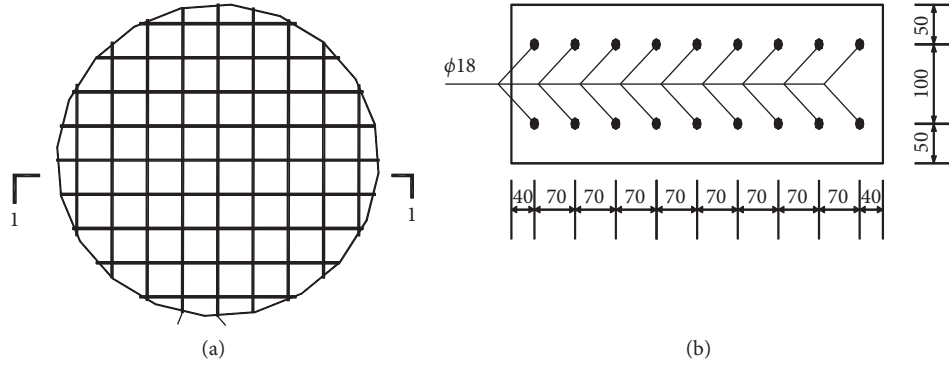


FIGURE 3: Steel nets in RCT: (a) front view and (b) 1-1 section view.

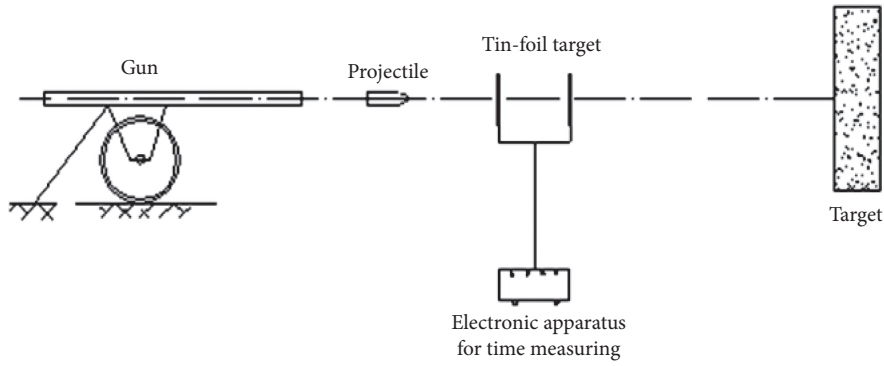


FIGURE 4: Test arrangement diagram.

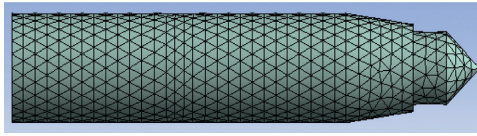


FIGURE 5: FEM model of projectile.

TABLE 1: Material parameters of the projectile body model.

ρ (kg/m ³)	G (GPa)	K (GPa)	A (GPa)	B (GPa)	n	C	m
7.83	81.8	159	0.792	0.51	0.26	0.014	1.03

concrete equation of state adopt default parameters. The parameters of the Johnson–Holmquist strength model include shear modulus, Hugoniot elastic limit, intact strength coefficient A , intact strength index N , strain rate constant C , failure strength coefficient b , failure strength index M , and maximum failure strength ratio. The parameters in the failure model include hydrostatic tensile strength ratio, damage coefficient, volume expansion coefficient, principal tensile failure stress, maximum equivalent strength, and crack-extended energy rate. These parameters are mainly determined according to the test, literature, and relevant concrete specifications [9–12]. The concrete model parameters used for numerical simulation are shown in Table 3.

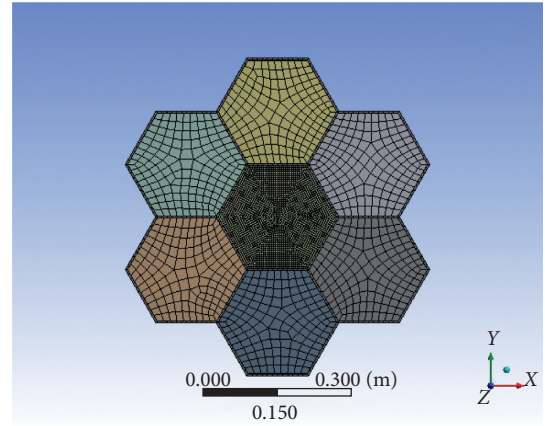


FIGURE 6: FEM model of HST.

TABLE 2: The material parameters of the steel plate model.

ρ (kg/m ³)	G (GPa)	K (GPa)	A (GPa)	B (GPa)	n	C
7.83	81.8	159	0.792	0.51	0.26	0.014
m	D_1	D_2	D_3	D_4	D_5	
1.03	-2.2	5.43	-0.47	0.016	0.63	

3. Results

3.1. Test Results. Penetration tests are carried out with HST and RCT and the penetration direction is perpendicular to target surface in all tests. The main parameters

TABLE 3: The JH-2 model of parameters of the concrete.

ρ (g/cm ³)	K (GPa)	G (GPa)	HEL (MPa)	A	N
2.5	20.45	20.09	105.81	0.79	0.63
C	B	M	MFSR	HTL (MPa)	D_1
0.007	1.61	0.63	1E20	-6.46	0.04
D_2	BCB	TF	PTFS (MPa)	MP/2 (MPa)	G_f (J/m ²)
1.0	1	Principal	8.85	1E20	116.4

TABLE 4: Test results.

Target number	v_1, v_2 (m/s)	Target failure description
HST1	377.9	Front surface: obvious funnel pit is observed and the damage area is about 374 cm ² ; one of the projectiles does not penetrate the target; cracks and other damages are not observed in other cells
	782.3	Rear surface: obvious funnel pit is observed and the damage area is about 385 cm ² ; cracks and other damages are not observed in other cells
HST2	318	Front surface: obvious funnel pit is observed and the damage area is about 390 cm ² ; cracks and other damages are not observed in other cells
	691.8	Rear surface: obvious funnel pit is observed and the damage area is about 380 cm ² ; cracks and other damages are not observed in other cells
RCT1	354.7	Front surface: obvious funnel pit is observed and the damage area is about 2830 cm ² ; There are 6 obvious cracks
	782.0	Rear surface: obvious funnel pit is observed whose depth is 9 cm and the damage area is about 4300 cm ² ; there are 17 obvious cracks

and test results are listed in Table 4, where v_1 and v_2 stand for speed of the first and second projectile, respectively. Front surface is the cylinder surface face to the projectile launcher and rear surface is the other surface of the cylinder.

Damage area of HST is smaller than that of RCT as concrete compressive strength and other performance getting improved due to restraint effect of the hexagon steel pipe surrounded. HST is divided into some cell by the hexagon steel pipe so that damage in one cell will have little influence on neighboring cells. Damage in HST will be restrained within cell getting contact with the projectile and no radioactive crack will appear. Damage of targets after tests is shown in Figure 7.

3.2. Simulation Results. Based on test results, damage in a certain cell has little influence on neighboring cells. In numerical simulation of HST under two repeat projectile strikes, two projectiles will strike at two locations within the same cell. Velocity and impact point location of projectile specifications are listed in Table 5.

In order to figure out the stress condition of the target during the projectile penetration process, several Gauge units are selected to get pressure-time history. 10# and 11# Gauge units belong to concrete within the cell getting contact with projectile. 14# and 15# Gauge units belong to concrete within the neighboring cell. 18# Gauge unit belongs to the middle steel pipe. 10#, 11#, 14#, and 18# Gauge units are within the same plane. The numerical simulation results under different configurations are shown in Figures 8–11.

4. Discussion

4.1. Analysis of Target Damage Area. It can be found from the test results that damage area of HST is far smaller than that of RCT under projectiles with appropriately the same velocity. While impact points of two projectiles with velocity 377.9 m/s and 782 m/s, respectively, are within the same cell in HST1, the damage area in the front surface and rear surface are 374 cm² and 385 cm², respectively. While impact points of two projectiles with velocities 318 m/s and 691.84 m/s, respectively, are within different cells in HST2, the damage area in the front surface and rear surface are 390 cm² and 380 cm², respectively. Under impact of two projectiles with velocity 354.7 m/s and 782.3 m/s, respectively, the damage area in the front surface and rear surface of RCT1 are 2830 cm² and 4300 cm², respectively.

Stress wave will be generated in the honeycomb structure under projectile penetration, and the stress wave will travel in the structure, and reflected wave and transmission wave will form at the interface of a different medium [8]. The stress wave caused by projectile impact will propagate through the target, both in concrete and steel, and stress wave impedance of steel is larger than that of concrete. While the incident wave arrived at the interface of concrete and steel pipe, compressed reflection wave will be formed. Due to the interaction of newly formed compression wave with other waves, the tensile stress of concrete will be reduced. Therefore, stress of concrete in the hexagonal cell which gets in contact with the projectile is smaller than stress of concrete in other hexagonal cells. Stress of the steel tube in the hexagonal cell which gets in contact with the projectile is the largest and thus the concrete damage area is small. There

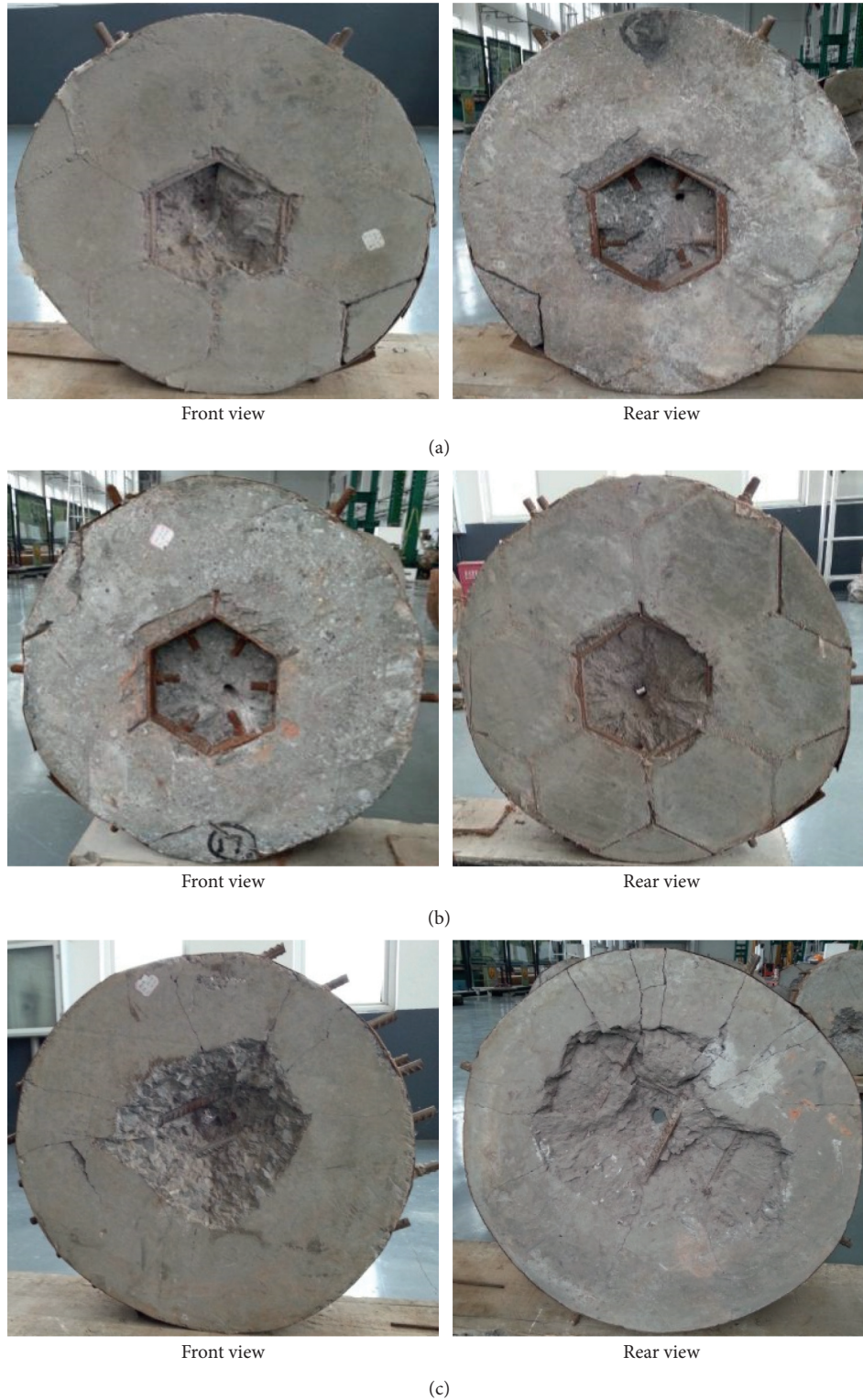


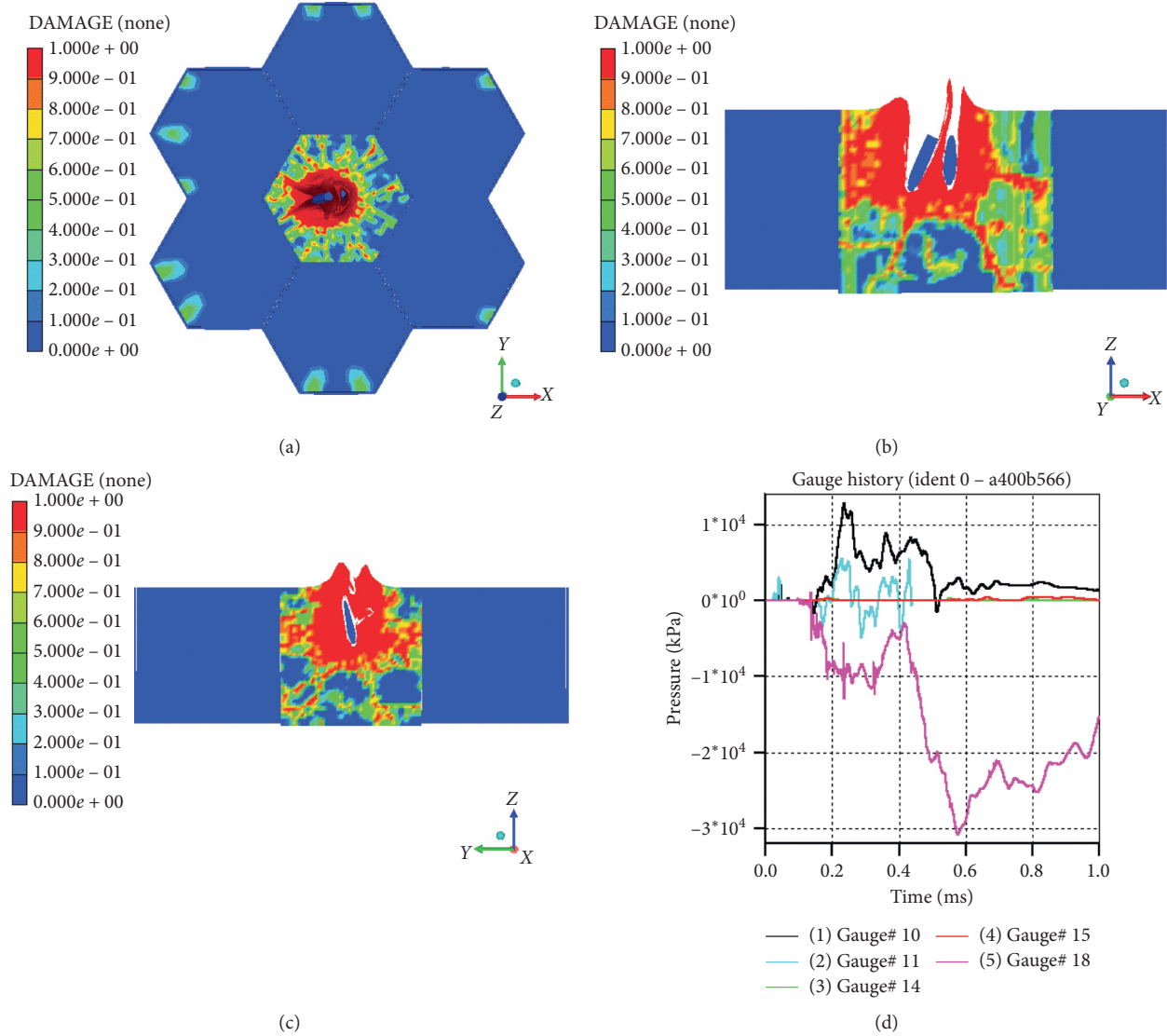
FIGURE 7: Target after test: (a) HST1 front view and rear view, (b) HST2 front view and rear view, and (c) RCT1 front view and rear view.

are only two layers of reinforced bar in reinforced concrete target, and compression reflected wave will be produced while the incident wave propagation to the face of steel bar, so the reflected wave is less and thus the failure area of concrete in the reinforced concrete target is larger.

4.2. Analysis of Target Damage Range. As the experimental results show, the damage range of the honeycomb-structure target is greatly reduced compared with that of reinforced concrete target. Damage in the front surface of HST target is within the hexagonal cell which gets in contact with the

TABLE 5: Configuration for FEM simulation.

Configuration set	Velocity of projectile 1 (m/s)	Impact point location of projectile 1	Velocity of projectile 2 (m/s)	Impact point location of projectile 2
1	400	0, 0, 0	566	-30, 0, 200
2	566	0, 0, 0	566	-30, -90, -200
3	566	-90, 0, 0	566	90, 0, 200
4	783	-60, 0, 0	783	-30, -60, 400

FIGURE 8: Target damage under configuration set 1 ($t = 1$ ms): (a) front view, (b) section view by XZ plane, (c) section view by YZ plane, and (d) gauge history.

projectile, and there is no damage in other cells. The funnel pit in the rear surface is also within the hexagonal cell which gets in contact with the projectile and no damage occur in other cells. There is a funnel pit in the area which gets in contact with the projectile and radial cracks extend to the whole target. The numerical simulation results also show that damage in the HST target are within the hexagonal cell which gets in contact with the projectile and there is no damage in other cells.

When the stress wave propagates to the free surface of the honeycomb-structure target, namely, the upper and lower surfaces of the concrete-filled steel tube cell, tensile wave will be generated as the wave impedance of air is smaller than that of the concrete or steel pipe. The tensile wave reflected and incident wave will superimpose over one another and tensile stress will be formed in the free surface of the concrete-filled steel tube. If the tensile stress is greater than that of concrete, the concrete will be damaged and flake

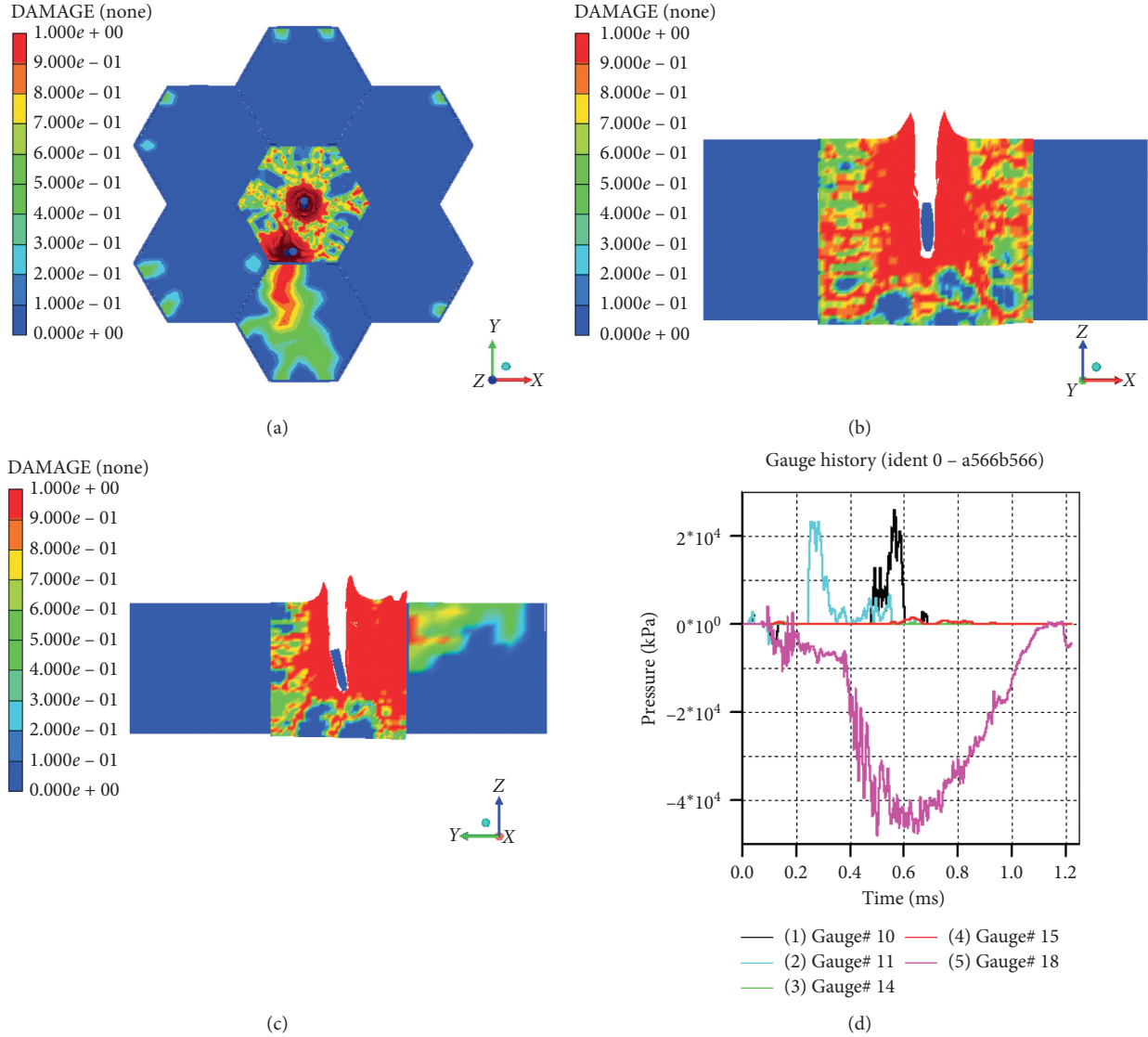


FIGURE 9: Target damage under configuration set 2 ($t = 1$ ms): (a) front view, (b) section view by XZ plane, (c) section view by YZ plane, and (d) gauge history.

or spallation will form, but the steel pipe will not peel off at the free face because of the high tensile strength of steel. New free surface will form after the formation of the first layer of concrete spallation, and then, with the penetration of the projectile, the tensile wave will form at the new free surface and will result in a new layer of spallation. All those explain the formation of impact crater and collapse crater in HST. Impact crater and collapse crater will also form in reinforced concrete targets, but the range is larger than that of the honeycomb-structure target. It is mainly due to the existence of the steel pipe in the honeycomb structure. The HST target is divided into several hexagonal cells by the steel tube, and thus wave propagation will undergo multiple reflection and transmission in the target. Damage caused by the stretch wave is limited within the hexagonal cell which gets in contact with the projectile due to the barrier effect of the steel tube. The stretch wave in other cells is smaller than the wave caused by the projectile or

target, so no damage forms in other cells. In the reinforced concrete target, the damage range is larger for there is no barrier effect of the steel tube.

4.3. Deflection of Projectile. As two projectiles strike the target in the same cell successively, the deflection of the first projectile is the same as that in single projectile strike and the deflection is related to the contact location. the deflection of the second projectile is larger than that of the first projectile and it is related to the distance between the first contact location and the second contact location. While the distance is smaller, the deflection of the second projectile will be larger. The concrete damage degree is different and the strength decreases when the first projectile penetrates the target. While the second projectile penetration into the same cell, its deflection will be influenced by the concrete around with uniform strength. The projectile body is under

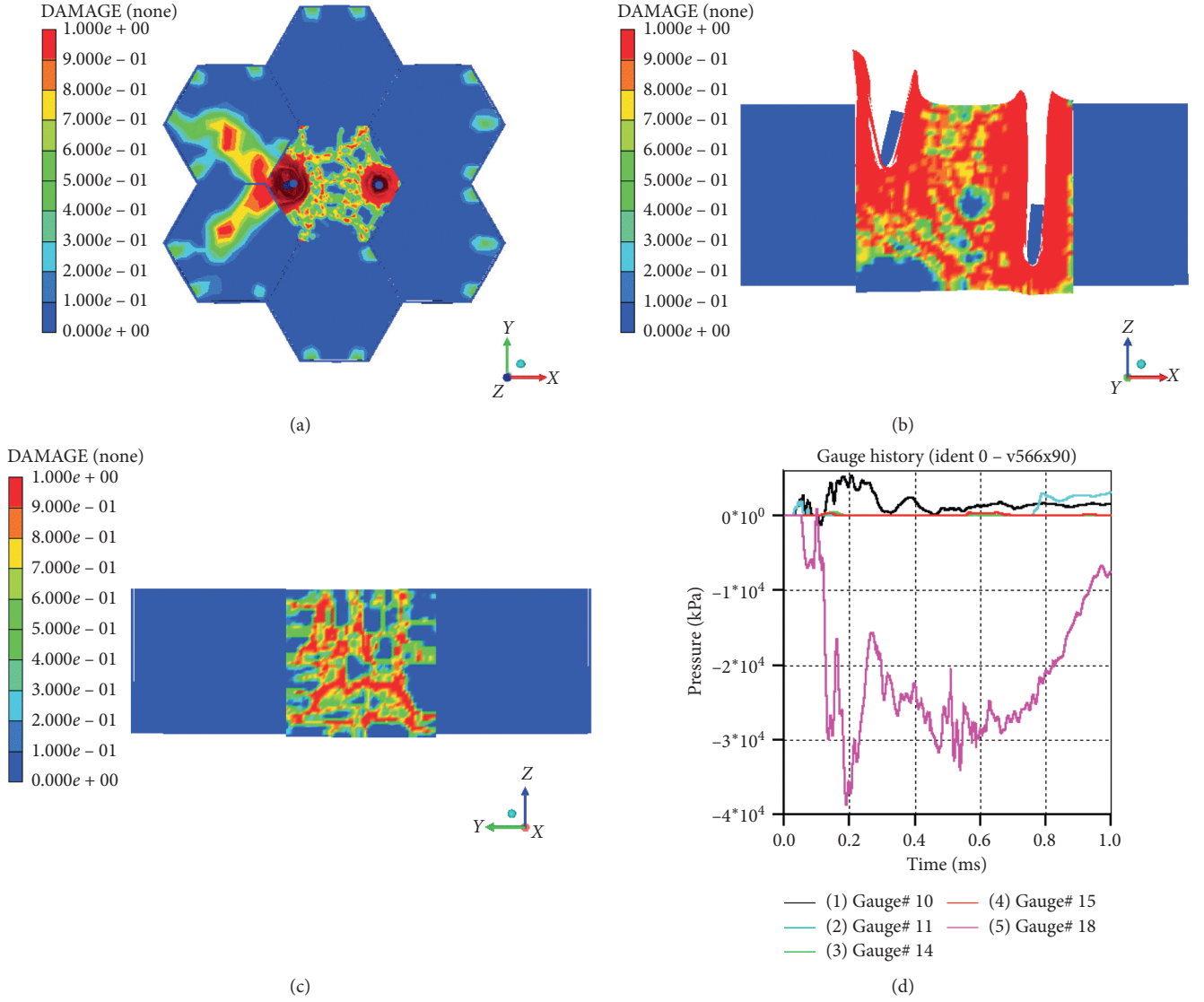


FIGURE 10: Target damage under configuration set 3 ($t = 1$ ms): (a) front view, (b) section view by XZ plane, (c) section view by YZ plane, and (d) gauge history.

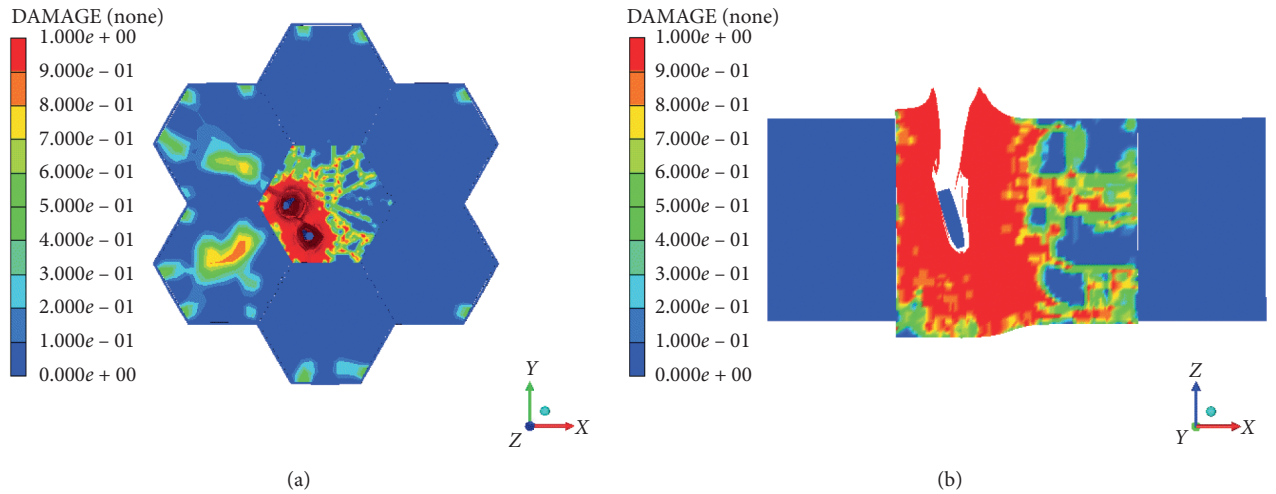


FIGURE 11: Continued.

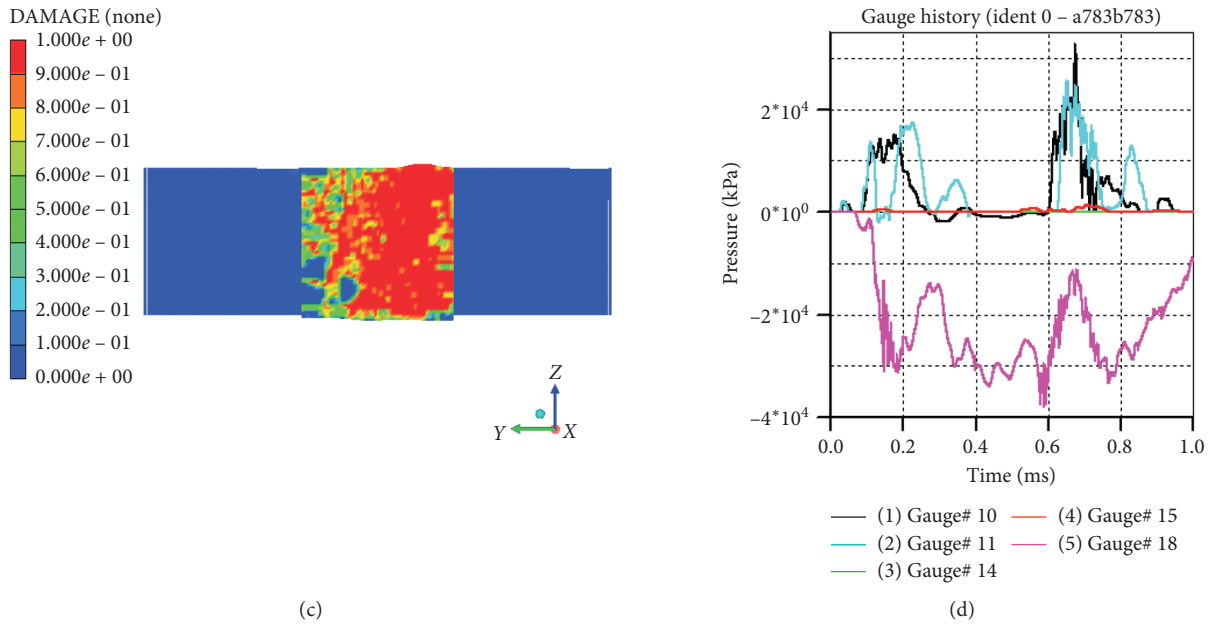


FIGURE 11: Target damage under configuration set 4 ($t = 1$ ms): (a) front view, (b) section view by XZ plane, (c) section view by YZ plane, and (d) gauge history.

asymmetric force during the penetration process, so it will undergo a large deflection.

5. Conclusion

- (1) Under two repeat projectile strikes, the damage area of the honeycomb-structure target is smaller than that of the reinforce-concrete structure because compressive strength and deformation capacity of the concrete in the honeycomb structure get improved by the steel tube.
- (2) Under two repeat projectile strikes, the damage range of the honeycomb-structure target is limited within the hexagonal cell which gets in contact with the projectile due to the barrier effect of the steel tube.
- (3) During the two repeat projectile strikes, the first projectile will deflect to some extent just as single projectile strike. The deflection of the second projectile is larger and is related to the distance between the strike point of the two projectiles.
- (4) Honeycomb shelter performs good under two repeat projectile strikes.

Data Availability

The data used to support the findings of this study are included within the article.

Conflicts of Interest

The authors declare that they have no conflicts of interest.

Authors' Contributions

Qifan Wang carried out the whole experiment and wrote the paper. Liuheng Chu designed the experiment and determined the whole structure of the paper. Jie Li carried out finite element modeling and checking calculation. Jianhu Sun carried out numerical simulation and analysis. Sheng Luo recorded and sorted out the data of repeated strike test. Lei Mao searched the relevant literature in the past five years, made corresponding revisions in the article, and helped to check grammatical errors in the text.

Acknowledgments

This project was supported by the Science and Technology Research Project of Chongqing Education Commission (no. KJZD-K201912902), China.

References

- [1] G. Ren, Z. Mu, R. Liu et al., *Penetration Effect and Engineering Protection of Precision Guided Weapons*, Science Press, Beijing, China, 2016.
- [2] Z. Wang, Y. Li, and Y. Huang, "Parameter determination of JH-2 model and numerical analysis of repeated penetration of granite," *Journal of Harbin Institute of Technology*, 2019.
- [3] G. Deng and X. Yang, "Numerical simulation analysis of multi projectile repeated strike effect in engineering rock," *Explosion and Shock*, vol. 34, no. 3, pp. 361–366, 2014.
- [4] L. Hu, F. You, and T. Yu, "Effect of cell-wall angle on the in-plane crushing behaviour of hexagonal honeycombs," *Materials & Design*, vol. 46, pp. 511–523, 2013.
- [5] S. Shi, Y. Liu, P. Yin et al., "New research on shock and explosion protection structure," *Journal of Logistical Engineering College*, vol. 20, no. 3, pp. 9–11, 2004.

- [6] S. Shi, X. Huang, Y. Liu et al., "Application of polygonal concrete-filled steel tube short component in protection engineering," *Concrete*, vol. 2005, no. 2, pp. 95–98, 2005.
- [7] S. Shi, Q. Wang, Y. Liu et al., "Study on anti penetration mechanism and numerical simulation of bionic cellular shield," *Protection Engineering*, vol. 35, no. 4, pp. 45–49, 2013.
- [8] Q. Wang, S. Shi, Z. Wang et al., "Experimental study on penetration of projectile through a honeycombed shield layer," *Explosion and Shock*, vol. 36, no. 2, pp. 253–258, 2016.
- [9] Y. Xiong, J. Chen, Y. Hu et al., "Study on key parameters of concrete Johnson-Holmquist constitutive model," *Engineering Mechanics*, vol. 29, no. 1, pp. 121–127, 2012.
- [10] X. Chai, *Because of the Concrete Target Head Shaped on the Penetration Effect*, Beijing Institute of Technology, Beijing, China, 2014.
- [11] R. Zhang, Y. Ding, W. Tang et al., "Failure strength parameters of concrete HJC and RHT constitutive models," *Proceedings of the High Pressure Physics*, vol. 25, no. 1, pp. 15–22, 2011.
- [12] Chinese Standard (2015), *Code for Design of Concrete Structures (GB50010-2010)*, China Architecture & Building Press, Beijing, China, 2015.

Research Article

Seismic Performance Analysis of Self-Centering Concentrically Braced Steel Frame Structures

Ergang Xiong¹, Kun Zu,¹ and Qian Zhang²

¹Chang'an University, Xi'an, Shaanxi Province, China

²Xi'an Eurasia University, Xi'an, Shaanxi Province, China

Correspondence should be addressed to Ergang Xiong; xerg@chd.edu.cn

Received 2 May 2020; Revised 27 May 2020; Accepted 9 June 2020; Published 9 September 2020

Academic Editor: Xing Ma

Copyright © 2020 Ergang Xiong et al. This is an open access article distributed under the Creative Commons Attribution License, which permits unrestricted use, distribution, and reproduction in any medium, provided the original work is properly cited.

To study the seismic performance of self-centering concentrically braced frame (SC-CBF) structure, the static elastoplastic analysis, low-cycle repeated loading analysis, and elastoplastic time-history analysis were conducted for a four-story SC-CBF structure, compared with the traditionally concentrically braced frame (CBF) structure. The influences of different GAP stiffnesses and cross-sectional areas of prestressed tendon were investigated on the self-centering and seismic performance of the SC-CBF structure. The results show that the SC-CBF structure has a strong lateral resistance, a small base shear under earthquake action, and a slight residual drift after unloading. The SC-CBF structure has a better ductility than the CBF structure. The displacement of the SC-CBF structure under the action of rare and extremely rare earthquakes is large, and the structure can dissipate more energy; the interstory drift is large, but the residual drift is small, exhibiting its ideal seismic and self-centering performance. However, the mechanical behavior of prestressed tendons is significantly affected by the stiffness of the GAP. The mechanical and seismic performances of the overall structure are slightly affected by the stiffness of the GAP, but the cross-sectional area of the prestressed tendons has a remarkable influence on the overall performance of the structure.

1. Introduction

The steel frame structure has so many significant advantages such as good seismic performance, lightweight, and short construction period, so it is widely used in architecture structures nowadays. However, the steel frame structure would undergo serious damages under the action of earthquake according to the earthquake disaster analysis. Meanwhile, the structure has a large residual drift after earthquake and cannot be desirably repaired [1, 2]. At present, on the basis of the seismic design idea that the structure would not collapse under major earthquakes, be repairable under moderate earthquakes, and have no damages under minor earthquakes specified in Chinese code for seismic design of buildings (GB 50011-2010) [3], the earthquake-resilient structures can recover structural function as soon as possible with some reparations after earthquake, which could well achieve the seismic resilient design goal [4–6].

As a common form of earthquake-resilient structures, the self-centering structure can effectively diminish the residual drift and recover the structures' normal function under the action of earthquake. One of the feasible ways to realize the self-centering function is to apply prestress in the steel frame structure [7]. The concentrically braced steel frame (CBF) structure can effectively improve the lateral resistance and seismic performance for the structure, thus considered to be an ideal lateral force resisting system [8]. However, the column base of the CBF structure is rigidly fixed with the foundation, which enables the structure to have a large lateral stiffness and a small lateral displacement under the horizontal earthquake action. But the structures' displacement ductility is limited, and the restrained bracings are prone to buckling, resulting in a large residual drift and technical difficulties in repairing structure after the earthquake. Ricles et al. [9] proposed the self-centering steel frame by setting horizontal prestressed steel cable in the beam and then connecting with the column, and thus, part of the shear

force is carried by the energy dissipating member. The prestressed steel cable can reduce the structure's residual deformation and provide the recovery for the structure. Due to the limitations of the CBF structure, Sause et al. [10, 11] applied the self-centering thought on the CBF structure and put forward a kind of self-centering concentrically braced steel frame structure (SC-CBF). To realize the design performance, the SC-CBF structure releases the column base and permits the column to decompress and uplift; the self-centering function can be realized by setting prestressed tendon at the column axis. Roke et al. [12] found that the SC-CBF structure can achieve the expected lateral deformation and self-centering performance by time-history analysis, considering three different prestressed tendon positions. And in the later study, it was concluded that SC-CBF structure can effectively control the structure's residual drift under the earthquake action, providing a better safety and overall deformation performance [13].

This paper aims to explore the seismic performance of self-centering concentrically braced frame (SC-CBF) structure; the static elastoplastic analysis, low-cycle repeated loading analysis, and elastoplastic time-history analysis are conducted for a four-story SC-CBF structure, compared with the traditionally concentrically braced frame (CBF) structure. Moreover, the effects of different GAP element stiffnesses and cross-sectional areas of prestressed tendon are investigated on the self-centering and seismic performance of the SC-CBF structure.

2. Working Principle and Analysis Modeling

2.1. Working Principle. The self-centering structure is originated from the application of sway column. The column can rotate freely under the horizontal force, so as to reduce the damage of members by relaxing the constraint between the foundation and structure. Based on this, it is possible to put forward the self-centering concentrically braced frame via relaxing the column base of the steel frame structure. Figure 1 shows the mechanical model of SC-CBF structure; the structural forms of SC-CBF and CBF are similar, but the SC-CBF structure has relaxed the connection of foundation and column base, which allows the column base to decompress and uplift under the action of horizontal force. Meanwhile, prestressed tendon is set vertically in the middle of the structure to provide restoring force for the structure rotation. In order to increase the structural energy dissipating capacity, the friction devices are set between the self-centering column and the gravity column or the energy dissipating element is added in the lifting part of the column base, which is different from the site of energy dissipating members for the CBF structure.

Figure 2(a) and 2(b) shows the rocking behavior of the SC-CBF structure. Figure 2 reflects the deformation and rocking of the structure under the action of moderate and rare horizontal earthquakes, respectively. SC-CBF only undergoes elastic deformation when the structure suffers a small horizontal force; the structure's column and foundation are fixed, and the top displacement is small, which is similar to the CBF structure. However, when the horizontal

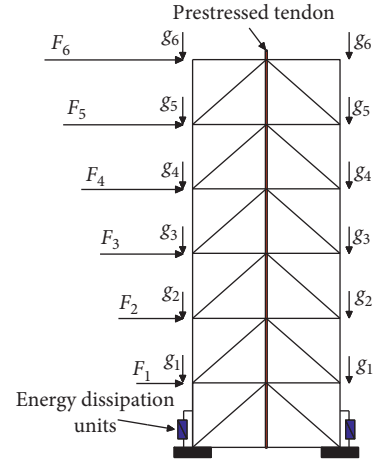


FIGURE 1: Mechanical model of the SC-CBF structure.

force is large enough, the column base and foundation would be separated, the column base is lifted, and the top displacement of the column increases the rigid body rotations of the structure. The sway change in the structure is exhibited, while the left and right column bases are lifted in Figure 2(b).

2.2. Parameters of SC-CBF Structure. The SC-CBF structure is designed as an example according to load code for building structures (GB 50009-2012) [14] and performance-based SC-CBF structure design method [15]; the floor and roof dead loads are 3.5 kN/m^2 , the live load for the floor is 2.0 kN/m^2 , and the snow load is 0.35 kN/m^2 . The welded H-shaped sections are selected for both beams, columns, and bracings. Material type is defined as Q235 whose yield strength is 235 MPa. The members' size of the structure is shown in Table 1. This SC-CBF structure has four stories. The first story height is 4.5 m, and the other story height is 3 m. The seismic fortification intensity is 8 degree, the site condition is class II, and the design earthquake classification is the 2nd group. The floor plan and elevation of the structure are shown in Figures 3 and 4, respectively.

2.3. Structural Finite Element Model. The finite element planar model of the SC-CBF structure was established by the software OpenSees 2.5.0., as shown in Figure 5. Figure 6 shows the detail of the SC-CBF structure's column base. The key difference between SC-CBF and CBF structures lies in the unrestraint of the column base and setting prestressed tendon, so the stiffness of the GAP element plays a vital role here. The stiffness of the GAP element is $880 \times 10^3 \text{ N/mm}$, the initial clearance is 0, and the critical force is $2 \times 10^{10} \text{ N}$ when the material reaches the plastic state. The default values in the OpenSees program are used for other parameters [16]. Steel 02 is adopted to simulate the steel, and beam column fiber element based on flexibility is selected; GAP element is selected for column base. The constitutive relation and axial deformation are shown in Figure 7, and the truss element is used for the simulation of the prestressed tendons.

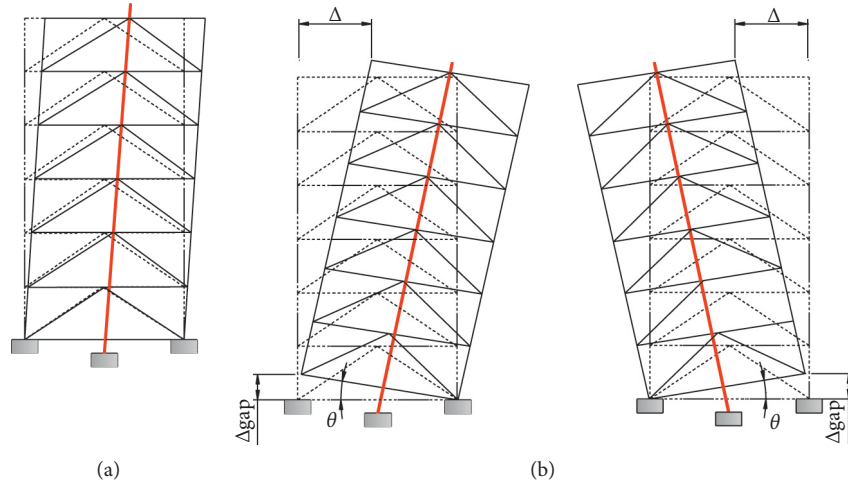


FIGURE 2: Rocking behavior of the SC-CBF structure.

TABLE 1: Sections of structure members.

Members	1 st story	2 nd story	3 rd story	4 th story
Beam	H400 × 250 × 12 × 18	H400 × 250 × 12 × 18	H400 × 250 × 12 × 15	H400 × 250 × 12 × 15
Column	H400 × 400 × 18 × 18	H400 × 400 × 18 × 18	H400 × 400 × 16 × 16	H400 × 400 × 16 × 16
Bracing	H250 × 250 × 10 × 15	H200 × 200 × 8 × 12	H200 × 200 × 12 × 15	H200 × 200 × 10 × 12

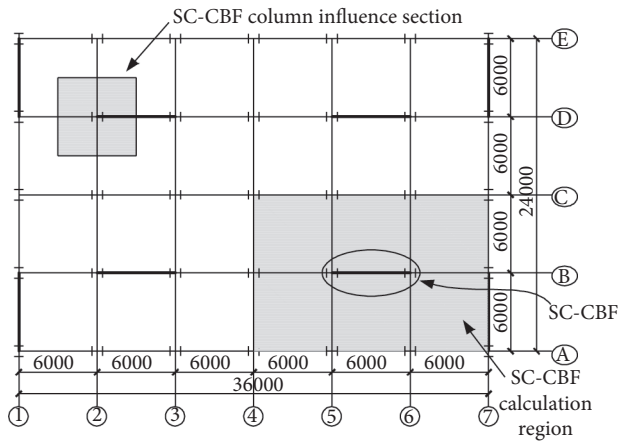


FIGURE 3: Floor plan of structure.

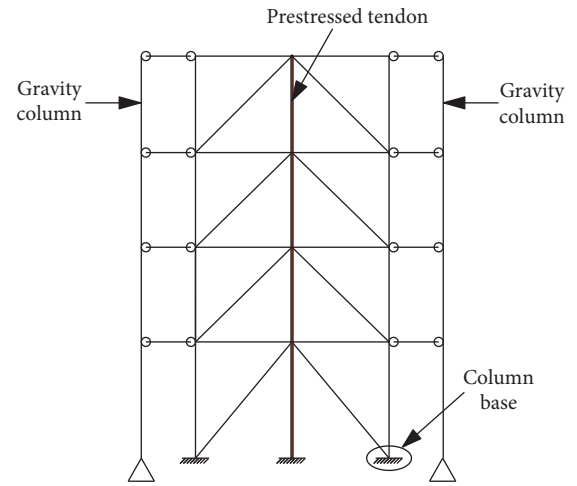


FIGURE 5: Model of the SC-CBF structure.

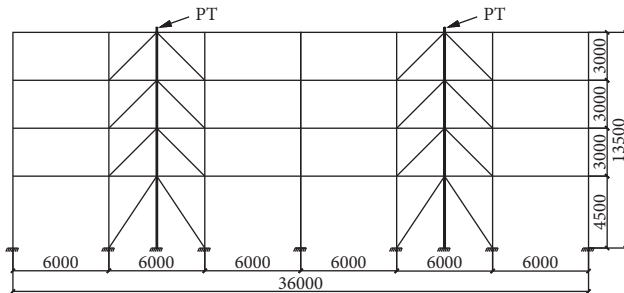


FIGURE 4: Elevation of the SC-CBF structure.

3. Nonlinear Analysis and Results

3.1. Pushover Analysis Results. The finite element model of the SC-CBF structure was established completely, and the corresponding pushover analysis was performed. The target displacement of the CBF structure is set to 270 mm (2%), while the SC-CBF structure has a large lateral deformation, so its target displacement is set as 540 mm (4%). The base shear-top displacement curves of two structures are shown in Figure 8.

It can be seen from Figure 8 that the two pushover curves have significant differences. On the one hand, the yield displacement of the two structures is quite different.

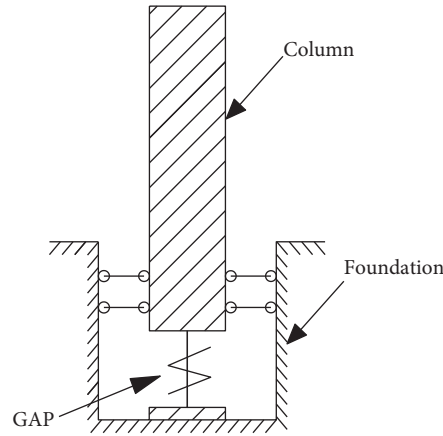


FIGURE 6: The detail of the SC-CBF structure's column base.

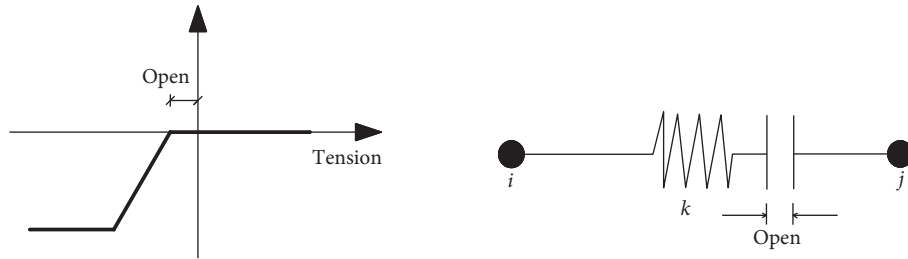


FIGURE 7: Constitutive relation and axial deformation of the GAP element.

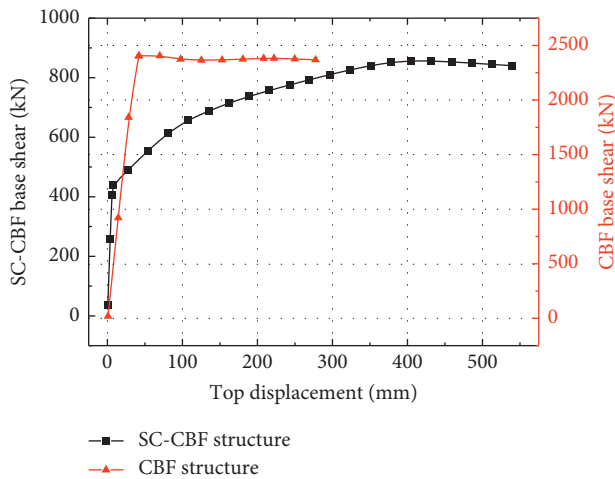


FIGURE 8: Pushover curves for SC-CBF and CBF structures.

The yield displacement of the SC-CBF structure is about 400 mm, while that of the CBF structure is only about 35 mm. Thus, SC-CBF has stronger lateral resistance than the CBF structure. On the other hand, the maximum base shear of the SC-CBF structure and CBF structure is about 800 kN and 2400 kN, respectively. The maximum base shear value of the CBF structure is almost three times that of the SC-CBF structure, which indicates that the CBF structure exhibits greater damage risk than the SC-CBF structure. Furthermore, the SC-CBF structure displays a better energy dissipating capacity due to that the structure becomes

“flexible” by loosening the column base. However, the CBF structure has a larger rigidity and can bear more seismic force due to its fixed foundation.

Figure 9 shows the pushover curve for the SC-CBF structure. Figure 10 shows the curve between the axial force of prestressed tendons and top displacement. Figures 9 and 10 show the four limit states of the SC-CBF structure under the action of earthquake. The branches A to B, B to C, and C to D in Figure 10 correspond to the column base decompression and uplift stage, decompression and uplift stage to the yield stage of prestressed tendon, and the yield to failure stage of structural members, respectively, in Figure 9.

Figure 11 is the curve of uplift displacement versus top displacement of GAP. Figure 12 is the curve of force versus deformation of GAP. The direction of the applied load here is from left to right. As for GAP, the left GAP in the structure is tensioned and experiences the uplift displacement, as shown in Figure 11. Figure 12 shows the force of the GAP drops to zero after the column base is decompressed. The right GAP is in compression, and its stiffness is large; its displacement does not change. Meanwhile, the force of the right GAP element increases with the top displacement, but the force keeps constant after the prestressed tendon yields.

3.2. Low-Cycle Repeated Loading Analysis Results. The identical finite element model is adopted to perform the cyclic pushover analysis, and the same horizontal force and

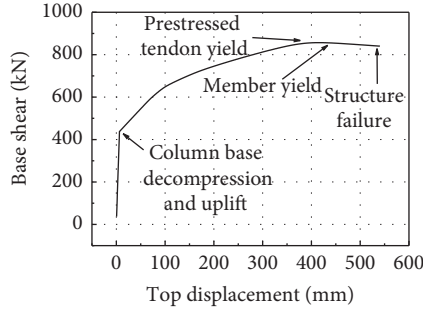


FIGURE 9: Pushover curve for the SC-CBF structure.

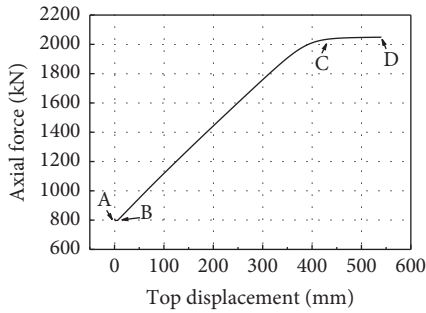


FIGURE 10: Curve between the axial force of the prestressed tendon and top displacement.

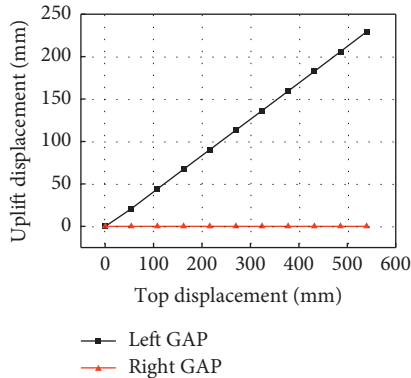


FIGURE 11: Uplift displacement versus top displacement of GAP.

maximum displacement value were used for loading as monotonic pushover analysis. The cyclic loading protocol is shown in Figure 13.

Figure 14 compares the hysteresis loops of SC-CBF and CBF structures, respectively. It can be seen from the figure that the performance of two structures is significantly different under the action of low-cycle repeated loading. However, the hysteresis loop of the SC-CBF structure is a typical flag shape, which is basically consistent with the expectation. Before the top displacement of the structure reaches 400 mm and the structure displays a good lateral resisting ability, there is no obvious structural stiffness degradation. During the unloading, the deformation recovers quickly, and the residual drift of SC-CBF structure is

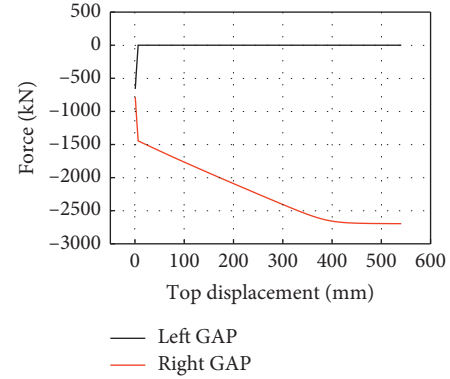


FIGURE 12: Force versus deformation of GAP.

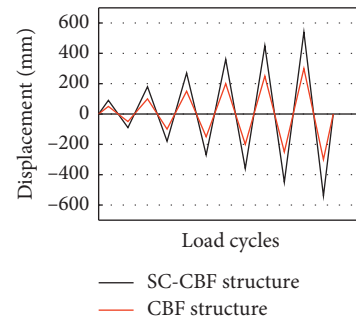


FIGURE 13: Cyclic loading protocol.

close to zero, achieving the self-centering expectation smoothly. Meanwhile, good energy dissipation can be observed corresponding to the shuttle shape exhibited in the hysteresis loop of CBF structure, but the recovery of structural deformation is small when unloading, and there is a significant recovery of deformation hysteresis phenomenon. After that, the slope of the curve gradually decreases with the increase in load, which indicates the structure undergoes stiffness degradation obviously, while the structural residuals drift is large after unloading.

The prestressed tendons stress-top displacement curve of the SC-CBF structure during the cyclic loading are shown in Figure 15. However, the prestressed tendon has some losses of prestress before yielding of the prestressed tendon. However, the loss of prestress gradually increases with the increase in the top displacement after the prestressed tendon yields, and the increment is more significant especially when the structure's top displacement reaches 540 mm; the loss of prestress arrives at the largest, about 550 MPa. In this case, the prestressed tendon can be seen as ineffective, which is corresponding to the fortification goals of life safety under the rare earthquake.

It can be seen from Figure 16 that the base shear of the structure increases along with the uplift displacement of GAP. When the uplift displacement of GAP is removed, the base shear change in the structure is small, which is because the prestressed tendon always provides a vertical tensile force for structure. Furthermore, the stress of GAP in Figure 17 increases with the increase in the top displacement; it

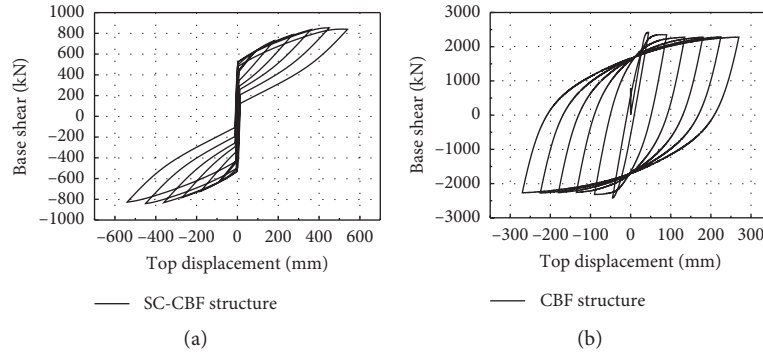


FIGURE 14: Hysteresis loops of structures.

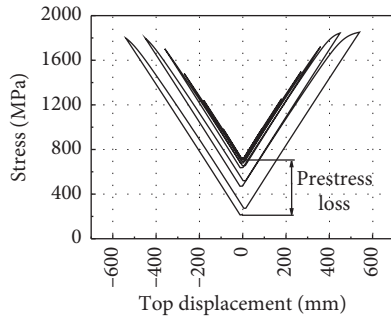


FIGURE 15: Curve of prestressed tendons stress versus top displacement.

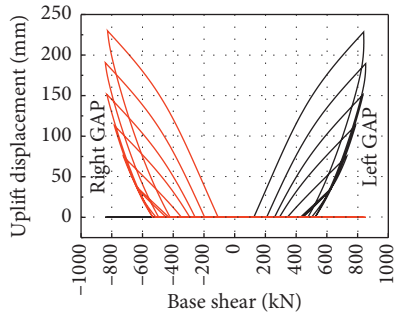


FIGURE 16: Curve of uplift displacement versus base shear of GAP.

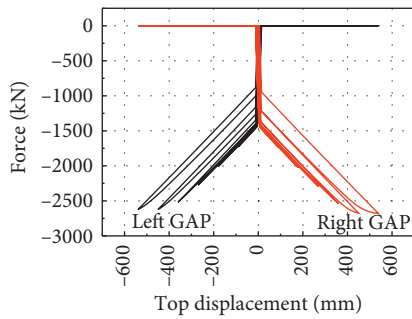


FIGURE 17: Curve of force versus top displacement of GAP.

suddenly increases when the top displacement starts to change, and then, the amplitude becomes smaller. When the top displacement of the structure reaches 400 mm, the force of

GAP degenerates during unloading. This is caused by yields of the prestressed tendon, which leads to the change in the overall mechanical performance of the SC-CBF structure.

3.3. Elastoplastic Time-History Analysis Results. The elastoplastic time-history analysis has advantages in observing the whole seismic response process of the structure under the earthquake action, so the seismic response and self-centering performance analysis for SC-CBF and CBF under rare earthquake and extremely rare earthquake is performed by elastoplastic time-history analysis in OpenSees software. The peak value of the earthquake accelerograms in the time-history analysis is determined by the Chinese standard and code [5, 17]. The selected earthquake waves are El Centro wave, Taft wave, and artificial wave, and the design basis acceleration is 0.20 g. The peak accelerations are 0.40 g and 0.60 g corresponding to intensity 8 rare earthquake and extremely rare earthquake, respectively.

It can be seen from Figures 18 and 19 that the top displacement of the SC-CBF structure is nearly twice than that of the CBF structure. This is due to the unrestrained column base of the SC-CBF structure, reducing the rigidity of the structure, which provides a greater lateral drift under the earthquake forces. Owing to the prestressed tendon's tensile recovery effect, the SC-CBF structure's drift curves have more peak points than the CBF structure, as shown in Figure 19(b); SC-CBF structure has three peak drift points at 7 s, 14 s, and 24 s, which makes the top displacement of structure change greatly under the action of earthquake.

The peak interstory drift for the two structures is about 0.6% in Figure 20, which is less than the code's limit value of 2%. This is due to the large size of the frame selected in the calculation analysis here to fully study the recovery capacity of the prestressed tendon in SC-CBF, thus providing a great stiffness for the structure. At the same time, the structure can effectively meet strength requirements under the earthquake action. The interstory drift of the SC-CBF structure is larger than that of CBF, owing to the SC-CBF structure's small stiffness. However, it can be seen from Figure 21 that the residual drift of the SC-CBF structure is far smaller than that of CBF under different earthquake actions. In general, the good self-centering performance of the SC-CBF structure is fully demonstrated.

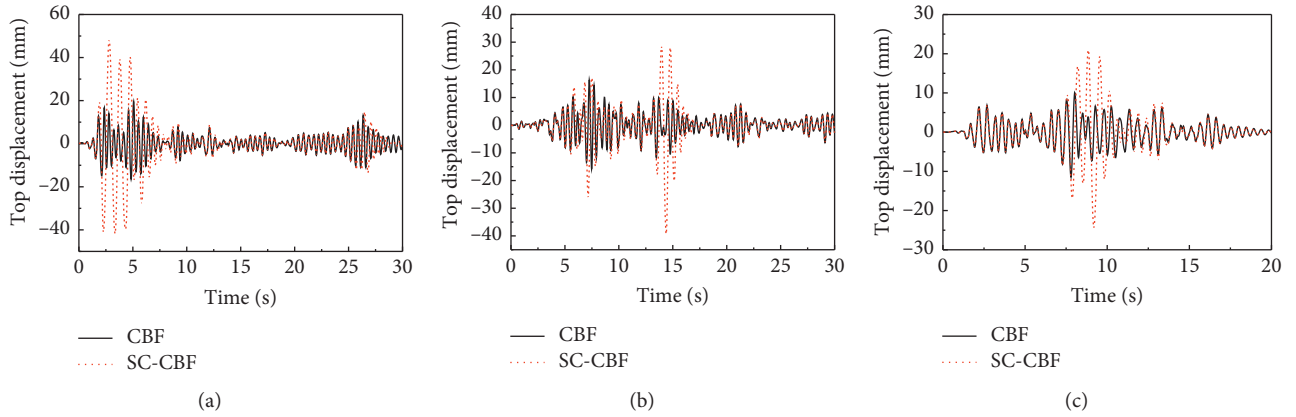


FIGURE 18: Top displacement versus time curves of the structure under rare earthquake: (a) El Centro wave; (b) Taft wave; (c) artificial wave.

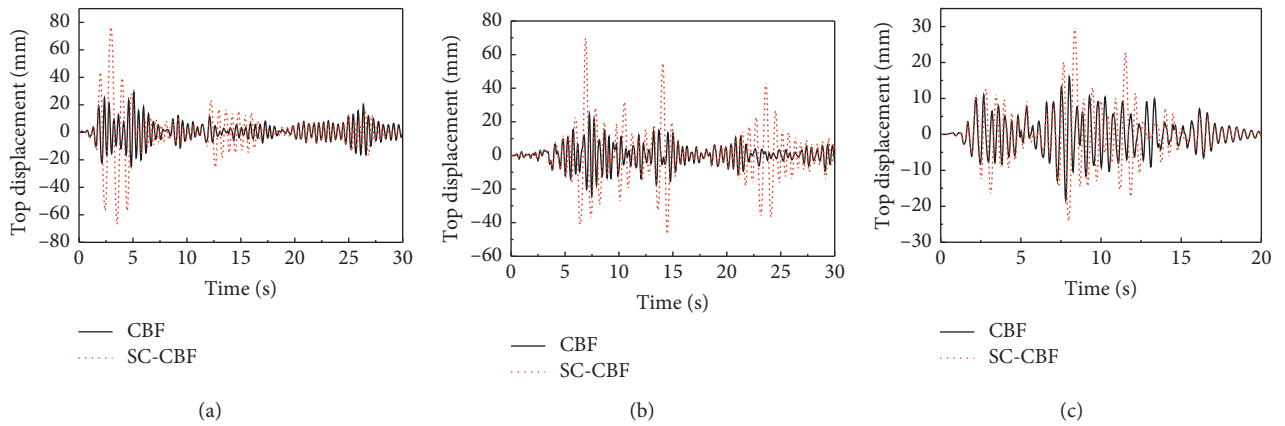


FIGURE 19: Top displacement versus time curves of the structure under extremely rare earthquake: (a) El Centro wave; (b) Taft wave; (c) artificial wave.

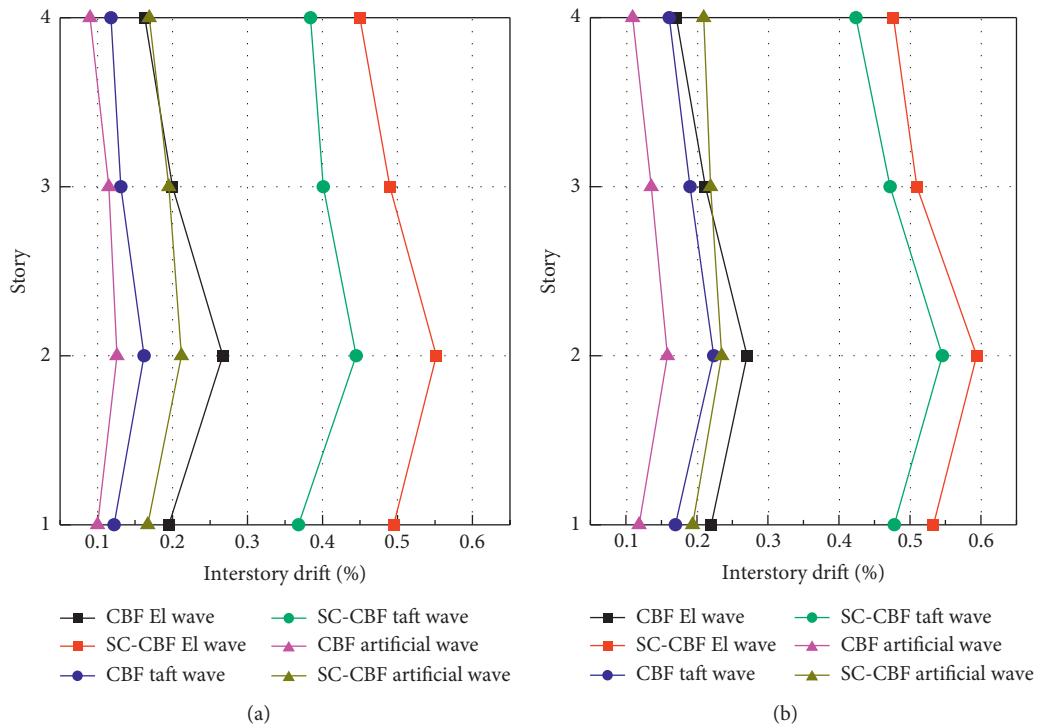


FIGURE 20: Peak interstory drift of 4-story structure under earthquake actions: (a) rare earthquake; (b) extremely rare earthquake.

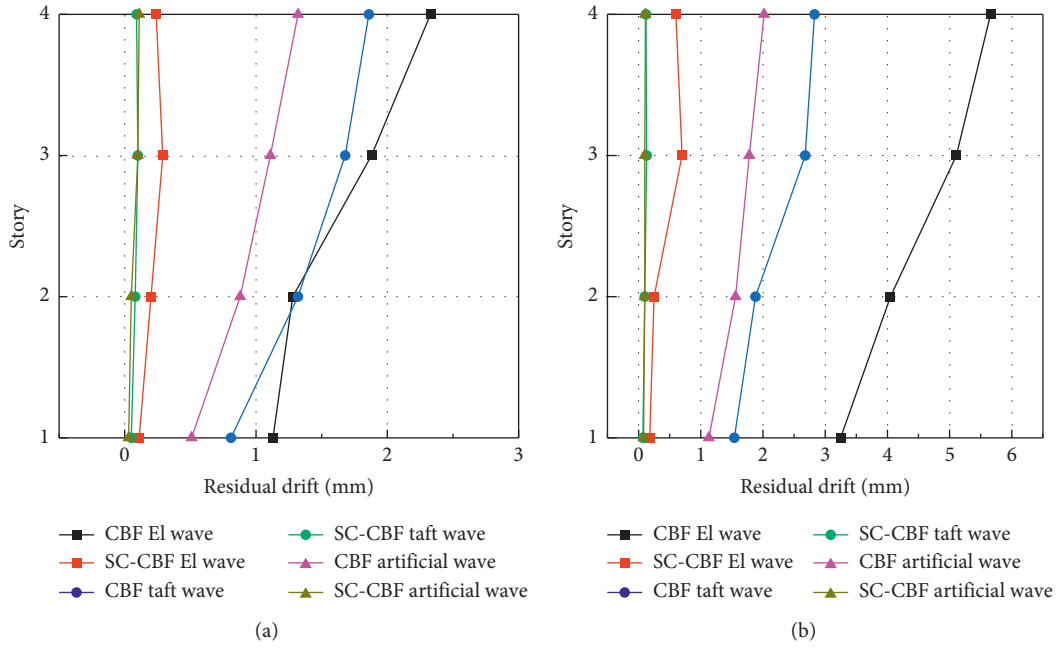


FIGURE 21: Residual drift response of 4-story structure under earthquake actions: (a) rare earthquake; (b) extremely rare earthquake.

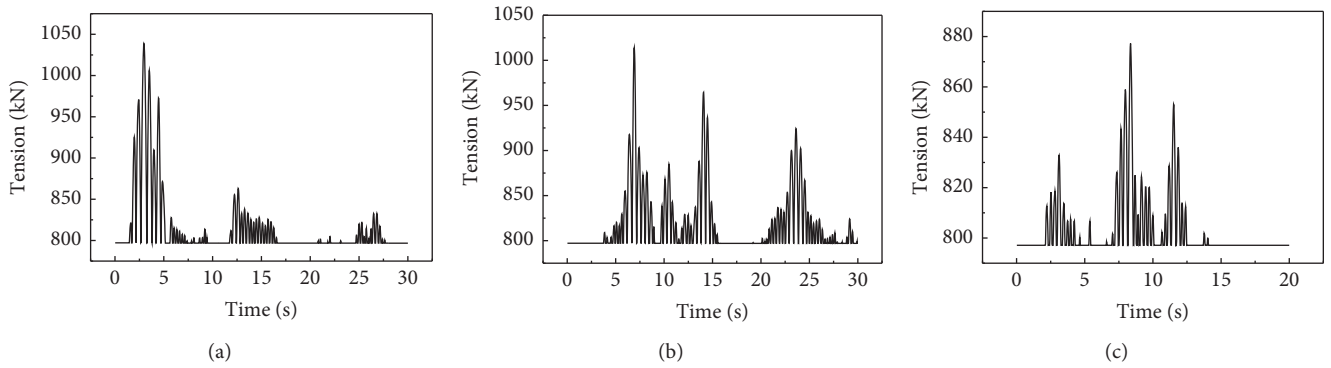


FIGURE 22: Axial tension time-history curves of prestressed tendons under extremely rare earthquake: (a) El Centro wave; (b) Taft wave; (c) artificial wave.

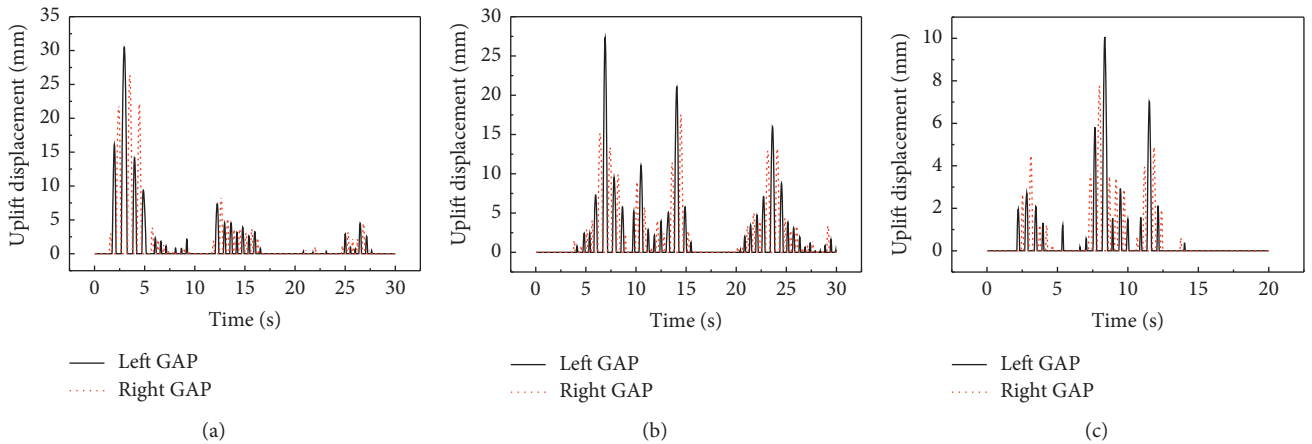


FIGURE 23: Time-history curves of GAP's uplift displacement under extremely rare earthquake: (a) El Centro wave; (b) Taft wave; (c) artificial wave.

The time-history analysis results of structures' members under extremely rare earthquakes are shown in Figures 22 and 23. Wherein, Figure 22 shows that the peak axial force of prestressed tendon reaches the maximum 1040 kN under earthquake, and the prestressed tendon does not yield in this case, which can provide a sufficient restoring force for the structure. In addition, it can be seen from Figure 23 that GAP element would experience a certain uplift displacement under earthquake, which provides a good rocking behavior and overall displacement ductility for the structure. The uplift displacement of the left GAP element is obviously larger than that of the right side, which is due to the earthquake waves inputted from left to right. After left-side GAP has undergone the earthquake, the SC-CBF structure has dissipated a certain amount of earthquake energy, and the right GAP's uplift displacement would decrease in this case. As the amplitude of GAP uplift displacement increases, the axial tension of prestressed tendon increases. Because the prestressed tendon does not yield all the time, SC-CBF structure exhibits a good seismic performance.

4. Parametric Analysis of SC-CBF Structure

The mechanical behavior of the SC-CBF structure under earthquakes is complicated. In order to understand the SC-CBF structure's self-centering characteristic and seismic performance comprehensively, it is necessary to analyze the structural performance under different design parameters. Thus, the stiffness of the GAP element and the cross-sectional area of prestressed tendon are selected for parameter analysis in this section, which is because the relaxation of column base and the application of prestressed tendon will significantly influence the structural performance.

4.1. Effect of Stiffness for GAP. To explore the influence of different GAP on the seismic performance of structure, the stiffness of the GAP was selected as K , $1/2K$, and $1/4K$, respectively, and the low-cycle repeated loading analysis was carried out here.

Figures 24 and 25 are the hysteresis loop of the base shear versus top displacement and its skeleton curve, respectively. Figure 24 manifests that three hysteresis loops become a typical flag shape, and the envelope of the loops is basically identical under different GAP stiffnesses, which verifies the good self-centering performance of the SC-CBF structure. It can be seen from Figure 25 that the slope of skeleton curve decreases along with the gradual decline in GAP stiffness until the decompression and uplift of column base. In addition, the GAP stiffness also has a great impact on the yield displacement. From Figure 25, the structures' top displacement with stiffness of K , $1/2K$, and $1/4K$ of GAP is 400 mm, 450 mm, and 520 mm, respectively, when structure yields, which can be explained from the stress change in the prestressed tendons.

The yield displacement of prestressed tendons has a significant difference under different GAP stiffnesses in Figure 26. The smaller the GAP stiffness is, the larger the yield displacement is, and the larger the lateral drift of the

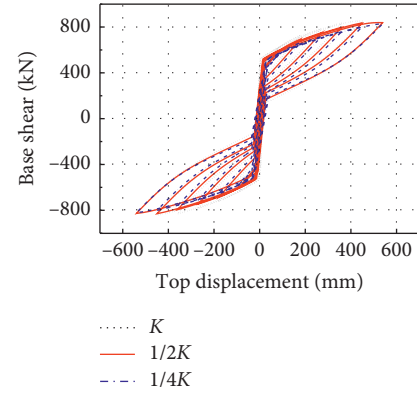


FIGURE 24: Hysteresis loop of the base shear versus top displacement.

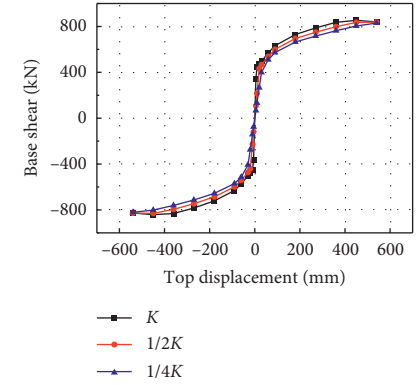


FIGURE 25: Skeleton curve.

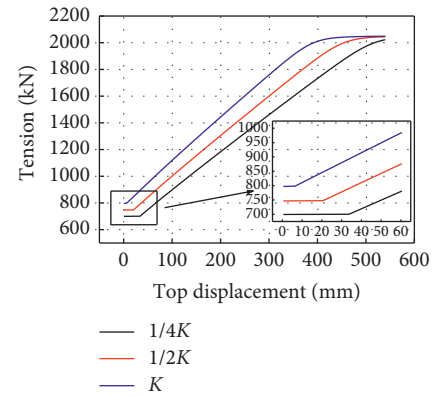


FIGURE 26: Prestressed tendon axial force-top displacement curve.

structure is, which also leads to the change in the yield point for the SC-CBF structure. The smaller the initial prestress of the prestressed tendons, the smaller the GAP stiffness in the initial mechanical phase. Although the same initial prestress has been defined in the analysis, the difference of the initial prestress would also exist due to the constitutive properties of GAP. When the stiffness of GAP is K , the prestressing

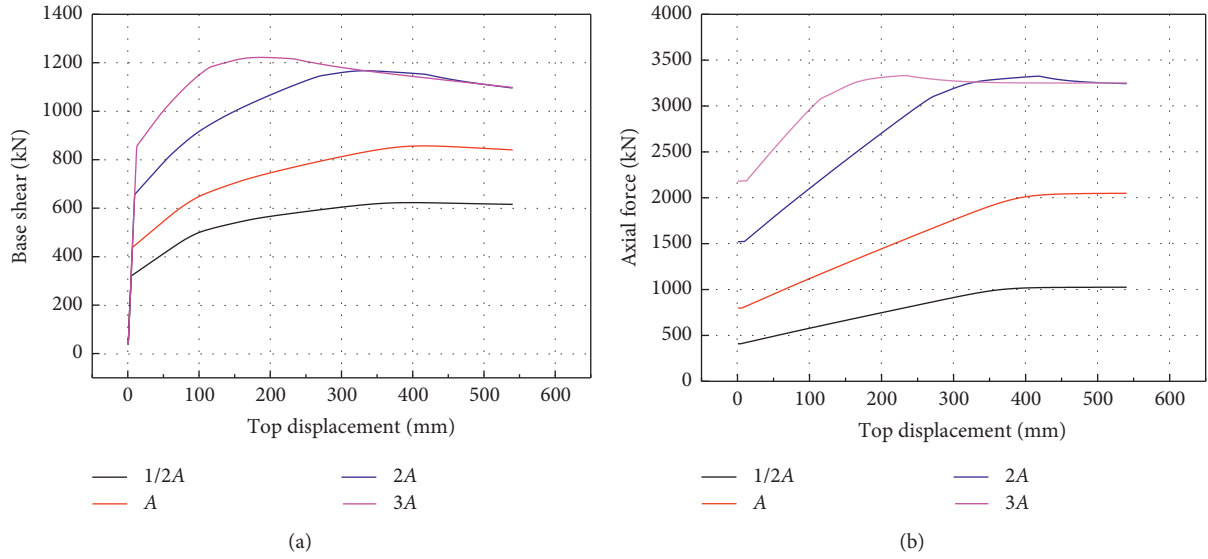


FIGURE 27: (a) Pushover curve of base shear versus top displacement; (b) pushover curve of axial force versus top displacement.

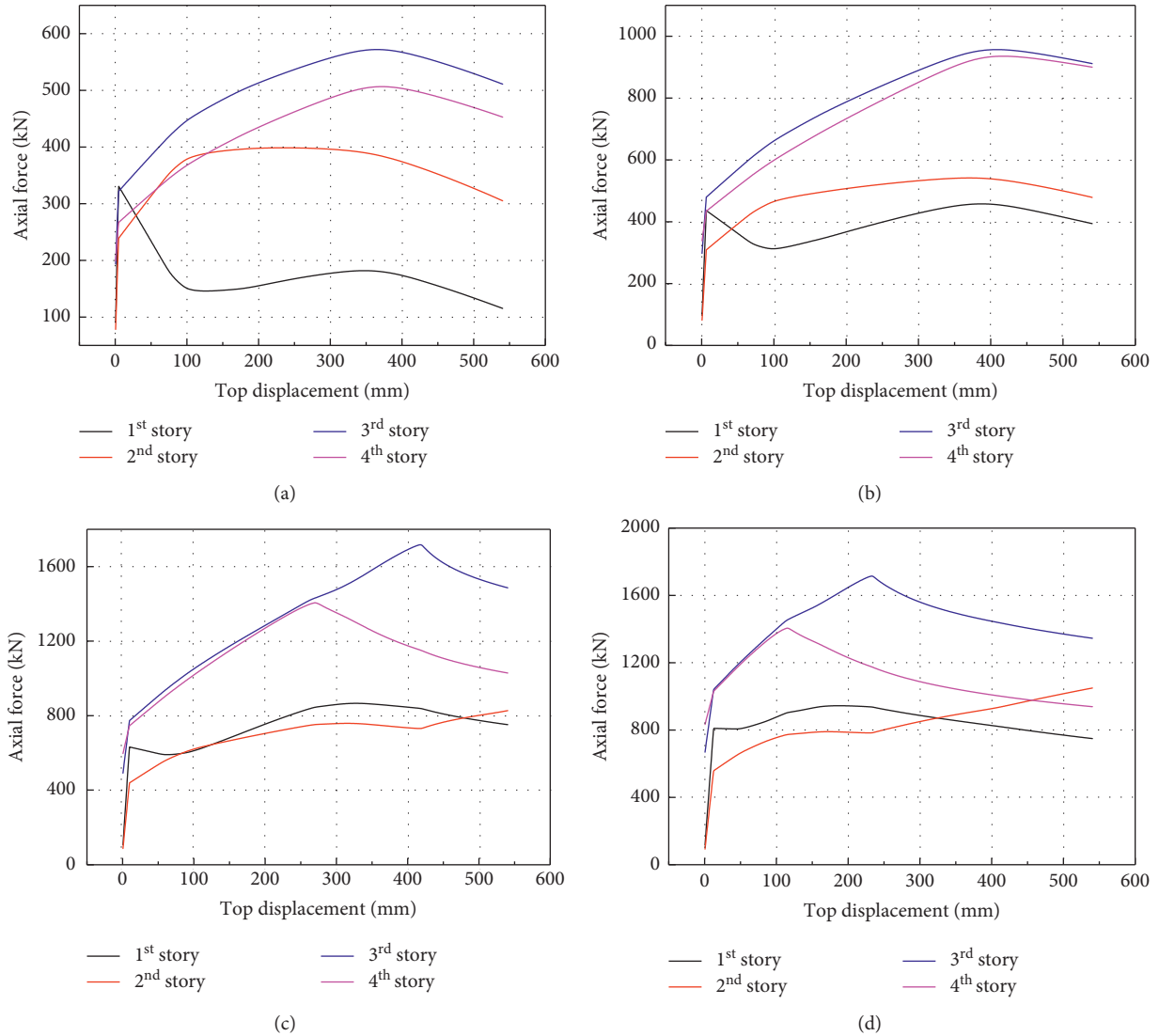


FIGURE 28: Pushover results of bracing axial force versus top displacement with different areas in each story: (a) 1/2A; (b) A; (c) 2A; (d) 3A.

force begins to increase when the top displacement is 6 mm, and then the prestressed tendon begins to extend; the corresponding displacement is 20 mm and 34 mm, respectively, when the stiffness is $1/2K$ and $1/4K$.

4.2. Effect of the Prestressed Tendons Cross-Sectional Area. As we know, the prestressed tendon can provide self-centering force for the SC-CBF structure, but the performance would display some differences with variable cross-sectional tendon. The cross-sectional area for tendons were selected as A , $2A$, and $3A$, respectively, to analyze the seismic performance for the SC-CBF structure.

4.2.1. Pushover Analysis. Pushover analysis was performed here to study the influence of different sections of prestressed tendon on the limit state for the SC-CBF structure. Figure 27 exhibits the pushover results of base shear and axial force versus top displacement for different section areas of prestressed tendons, respectively. For different sections of the prestressed tendon, the curves of axial force-top displacement for bracings at each story are shown in Figure 28. In the illustration, A is the cross-sectional area of prestressed tendon.

In Figure 27(a), the pushover curve of the SC-CBF structure keeps the same tendency with the cross-sectional areas of $1/2A$, A , and $2A$, but the maximum base shear occurs at small yield displacement as the area is $3A$. In case of the prestressed tendon cross-sectional area being less than $2A$, the base shear of the structure increases gradually with the increase in the cross-sectional areas of the prestressed tendon, and there would exist an obvious difference in the maximum base shear. Nevertheless, the difference in maximum base shear is small when the cross-sectional area is between $2A$ and $3A$, which indicates that the design of the prestressed tendons must fully consider the structural overall performance.

As is shown in Figure 27(b), the peak axial tensile force of prestressed tendon is about 1000 kN and 2000 kN, respectively, with tendons' cross-sectional areas of $1/2A$ and A , which has reached the yield point. Furthermore, when the structure is with $2A$ and $3A$ cross-sectional areas, the peak axial tension of prestressed tendon is about 3250 kN, and the prestressed tendon has not yielded in this case.

The influence of cross-sectional areas of prestressed tendons on the limit state of the structure can be analyzed according to the bracing's axial force reflected in Figure 28. It can be seen from Figures 28(a) and 28(b) that the force of bracings in each story is relatively small, and the bracing has not yielded before the prestressed tendons yield, which conforms to the ideal sequence of limit state for the SC-CBF structure. The bearing capacity of the structure reduces when the prestressed tendons yield, and the bearing capacity of the bracing decreases gradually. Therefore, the bracing's axial force decreases with the increase in the top displacement. In Figures 28(c) and 28(d), the third and fourth story bracings' forces are about 1700 kN and 1400 kN, and it has reached the value of yield now. The pushover results show a significant

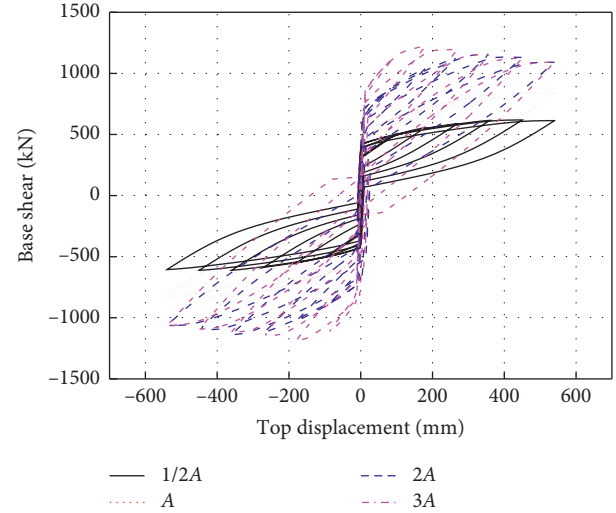


FIGURE 29: Hysteresis loop of base shear versus top displacement.

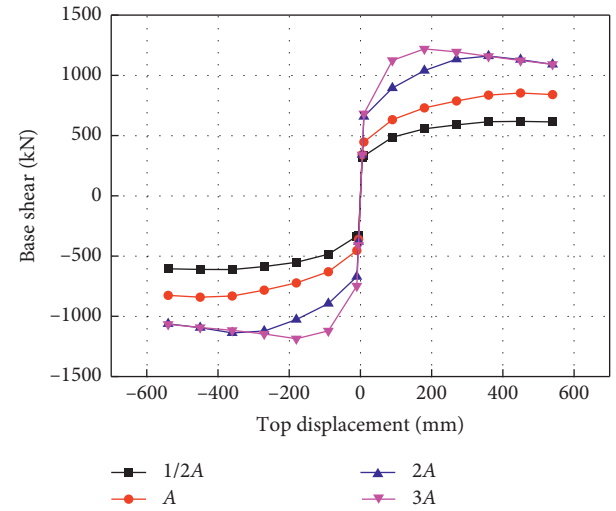


FIGURE 30: Skeleton curve.

decline tendency, which is different from the decline of bracing's axial force in Figures 28(a) and 28(b). At the yield of the third and fourth story bracings, the prestressing force of the prestressed tendon also decreases gradually, leading to the sequence changes in the limit state of the SC-CBF structure, and the members yield after the column base decompresses and uplifts, which cannot meet the requirements of the performance-based design method.

4.2.2. Low-Cycle Repeated Loading Analysis. To explore the seismic and energy dissipating performance of the SC-CBF structure with different cross-sectional areas of prestressed tendon, the low-cycle repeated loading analysis was carried out in this section. Figures 29 and 30 are the hysteresis loop of the base shear versus top displacement and its skeleton

curve for four different tendon's cross-sectional areas, respectively.

The prestressed tendons would provide the restoring force for the structure, and it does not change with the difference in tendons' cross-sectional areas. The hysteresis loop presents a flag shape, and the envelope area of the loop increases along with the increase in the tendons' cross-sectional areas, indicating that the ability of energy dissipation is significantly affected by the cross-sectional areas. However, the structure has a large residual drift when the cross-sectional area is $3A$ in case of the yielding of the bracings. The bracing's yield induces the improvement in the energy dissipation, but the members undergo an unrecoverable plastic deformation after unloading. Figure 30 shows that the structure's base shear increases with the increasing areas of tendons, and the displacement increases during the column decompression. Moreover, the decline of base shear becomes more obvious just as the base shear reaches the peak value, and the structure stiffness decreases greatly during reloading and unloading. Especially, when the cross-sectional area is $3A$, the stiffness decreases most significantly.

5. Conclusion

In this paper, through the OpenSees program, the mechanical and seismic performances are researched for the SC-CBF and CBF structures by the static elastoplastic analysis, low-cycle repeated loading analysis, and elastoplastic time-history analysis. Some conclusions can be drawn from the results of this investigation:

- (1) Pushover analysis results of the SC-CBF structure verify its mechanical properties and four-stage limit states. SC-CBF structure has a stronger lateral resistance capacity, a small base shear, and a good displacement ductility under earthquake action, compared with the CBF structure, which can ensure the structure safety effectively.
- (2) The hysteresis loop of the SC-CBF structure presents a flag shape with a prominent self-centering performance. The residual drift of the structure is small, and the prestress loss is small when the prestressed tendon is unloaded before yielding. However, the CBF structure hysteresis loop is full of "Shuttle," displaying a good energy dissipation, but the residual drift is large when unloading, and the stiffness degradation phenomenon is obvious.
- (3) Under the rare and extremely rare earthquakes, the SC-CBF structure experiences a larger drift response, the maximum interstory drift is about 2-3 times than that of CBF structure, but the residual drift when unloading is just 1/10 of CBF structure according to the elastoplastic time-history analysis result, which fully reflects its good ductility and self-centering performance.
- (4) When the stiffness of GAP decreases by 1/2 and 3/4, the top displacement increases for 12.5% and 30%, and the structural lateral drift increases meanwhile.

With the decrease in GAP stiffness, the initial stress of prestressed tendon decreases, but the yield displacement of prestressed tendon increases.

- (5) The base shear and the axial force of the prestressed tendon increase with the increase in the sectional areas of the prestressed tendons, the hysteresis loop becomes full, and the energy dissipation capacity is increased with the change in areas. When the increment of the cross-sectional areas arrives to a certain extent, the failure mechanism of the SC-CBF structure would change, which is because the prestressed tendons have not yet yielded when the components yield, so the overall performance of the structure must be considered when designing the prestressed tendons for the structure.

Data Availability

The data used to support the study can be available upon request to the corresponding author.

Conflicts of Interest

The authors declare that there are no conflicts of interest regarding the publication of this paper.

Acknowledgments

This research was funded by the National Natural Science Foundation of China (Grant nos. 51808046 and 51108035), Natural Science Basic Research Plan in Shaanxi Province of China (Grant nos. 2020JQ-917, 2017JQ5061, 2016JM5007, and 2013JM7030), Special Fund for Basic Scientific Research of Central College (Grant nos. 310828162017, 310828161009, and 310841171001), and Scientific Research Fund of Xi'an Eurasia University (Grant no. 2018XJZK03).

References

- [1] A. Dall'Asta, G. Leoni, F. Morelli, W. Salvatore, and A. Zona, "An innovative seismic-resistant steel frame with reinforced concrete infill walls," *Engineering Structures*, vol. 141, pp. 144–158, 2017.
- [2] Y. Li, R. Song, and D. L. J. W. Van, "Collapse fragility of steel structures subjected to earthquake mainshock-aftershock sequences," *Journal of Structural Engineering*, vol. 140, no. 12, Article ID 04014095, 2014.
- [3] China Architecture and Building Press, *Code for Seismic Design of Buildings: GB 50011-2010*, China Architecture and Building Press, Beijing, China, 2010, in Chinese.
- [4] M. Bruneau, S. E. Chang, R. T. Eguchi et al., "A framework to quantitatively assess and enhance the seismic resilience of communities," *Earthquake Spectra*, vol. 19, no. 4, pp. 733–752, 2003.
- [5] Resilient City Report, *Defining What San Francisco Needs from its Seismic Mitigation Policies*, The San Francisco Planning and Urban Research Association, San Francisco, CA, USA, 2009.
- [6] M. Grigorian, A. S. Moghadam, H. Mohammadi, and M. Kamizi, "Methodology for developing earthquake-resilient structures," *The Structural Design of Tall and Special Buildings*, vol. 28, no. 2, Article ID e1571, 2019.

- [7] C. C. Chou and J. H. Chen, "Development of post-tensioned self-centering structures for earthquake resistance," *International Journal of Structural Engineering*, vol. 3, no. 1-2, pp. 1-17, 2012.
- [8] A. Hassanzadeh and S. Gholizadeh, "Collapse-performance-aided design optimization of steel concentrically braced frames," *Engineering Structures*, vol. 197, Article ID 109411, 2019.
- [9] J. M. Ricles, R. Sause, M. M. Garlock, and C. Zhao, "Post-tensioned seismic-resistant connections for steel frames," *Journal of Structural Engineering*, vol. 127, no. 2, pp. 113-121, 2001.
- [10] D. Roke, R. Sause, J. M. Ricles, C. Y. Seo, and K. S. Lee, "Self-centering seismic-resistant steel concentrically-braced frames," in *Proceedings of 5th International Conference on Behaviour of Steel Structures in Seismic Areas*, pp. 85-90, Yokohama, Japan, 2006.
- [11] R. Sause, J. M. Ricles, Y. C. Lin, C. Y. Seo, D. Roke, and N. B. Chancellor, "Self-centering damage-free seismic-resistant steel systems," in *Proceedings of 7CUEE & 5ICEE*, pp. 39-48, Tokyo, Japan, 2010.
- [12] D. Roke, R. Sause, J. M. Ricles, and N. Goner, "Design concepts for damage-free seismic-resistant self-centering steel concentrically-braced frames," in *Proceedings of 2009 ASCE Structures Congress*, pp. 1-10, Reston, VA, USA, 2009.
- [13] R. Sause, J. M. Ricles, D. Roke, N. B. Chancellor, and N. Goner, "Large-scale experimental studies of damage-free self-centering concentrically-braced frame under seismic loading," in *Proceedings of 2010 ASCE Structures Congress*, pp. 1495-1509, Reston, VA, USA, 2010.
- [14] China Architecture and Building Press, *Load Code for the Design of Building Structures: GB 50009-2012*, China Architecture and Building Press, Beijing, China, 2012, in Chinese.
- [15] L. W. Yang, *Seismic Performance Analysis of Self-Centering Steel Concentrically Braced Frames Based on OpenSees*. Master Dissertation, Chang'an University, Xi'an, China, 2018, in Chinese.
- [16] D. Roke, *Damage-free seismic-resistant self-centering concentrically-braced frames*, Ph.D. thesis, Lehigh University, Bethlehem, PA, USA, 2010.
- [17] Standards Press of China, *Seismic Ground Motion Parameter Zonation Map of China: GB 18306-2015*, Standards Press of China, Beijing, China, 2015, in Chinese.

Research Article

Seismic Response Study of Tunnels Running underneath a Subway Station in Parallel

Fuxue Sun,¹ Guo-bo Wang ,¹ Xiang-jun Peng,² Zhou-zhou Jin,¹ Xiao-chun Li,³ and Jie-lin Zhao ²

¹Department of Wenzhou University, College of Civil Engineering and Architecture, Wenzhou, China

²Department of Wuhan University of Technology, Hubei Key Laboratory of Roadway, Wuhan, China

³Department of Shanghai Tunnel Engineering Co., Ltd., Shanghai, China

Correspondence should be addressed to Guo-bo Wang; wgb16790604@126.com

Received 20 March 2020; Revised 2 June 2020; Accepted 20 June 2020; Published 27 July 2020

Academic Editor: Xiaonong Guo

Copyright © 2020 Fuxue Sun et al. This is an open access article distributed under the Creative Commons Attribution License, which permits unrestricted use, distribution, and reproduction in any medium, provided the original work is properly cited.

A tunnel passing below a metro station is taken as the object of our study, and a two-dimensional plane model is established to study the effects of their dynamic interaction to seismic excitation. Comparative analysis is used to obtain the influence law between the underground structures and on the soil. The results show that (1) the influence of the underground structure on the soil response is related to structure depth. The range of influence of the station structure on the surface is approximately five times the width of the station, and the surface response is obviously significant within this range. (2) The existence of the tunnel is conducive to reducing the acceleration of the column in the station. It increases the displacement difference between the stations, but the impact on the internal force of the station is not significant. (3) The influence of the station on the dynamic response of the tunnel is consistent with regard to tunnel acceleration, difference in displacement between the top and bottom of the tunnel, and internal force. The presence of the station will reduce the dynamic response of the tunnel.

1. Introduction

With increased development and utilization of urban underground space and the expansion and transformation of existing underground structures, underground engineering structures inevitably appear to pass each other at close distances, and cross-shaped and X-shaped traverse have emerged. As underground structures play an important role in the daily operation of the city, it is very critical to study the seismic performance of closed underground tunneling structures. Because an underground structure is buried in the soil, it is bound by the surrounding soil during an earthquake. The earthquake resistance mechanism of an underground structure is inevitably different from that of a surface structure: the seismic response of the surface structure is mainly controlled by the inertial force, whereas that of the underground structure is affected by the surrounding soil and mainly controlled by soil deformation. It is generally believed that the seismic performance of underground structures is superior to that of surface

structures; therefore, the seismic problems of underground structures are often ignored. However, numerous underground structures have been seriously damaged in a series of large earthquakes around the world in the recent years. For example, the destruction of subway stations and tunnels caused by the Hanshin earthquake and Wenchuan earthquake indicates that underground structures are not absolutely safe, and their seismic performance needs to be studied [1–3].

Presently, there are many research studies on seismic resistance of underground structures, which have yielded constructive results. In terms of theoretical research, Lee and Trifunac [4] studied the dynamic response of tunnels during the early stage of an earthquake. The analytical solution of the tunnel dynamic response during an earthquake was derived through theoretical analysis and reasonable assumptions. In addition, the effects of soil–structure stiffness and tunnel depth on the dynamic response of the tunnel were analyzed. Bourouaiah et al. [5] revealed that soil properties have a great impact on soil–structure interactions,

and the behavior at the interface between the soil and the structure depends directly on the soil properties, but the horizontal and vertical directions are affected differently. In terms of numerical simulation, Anastasopoulos et al. [6] simulated the immersed tunnel segment joints with nonlinear superelastic elements and studied the seismic response law of multisegment long-span tunnels under nonuniform seismic excitation. The analysis considered that the tunnel joint can effectively “absorb” a part of the deformation, and increasing the thickness of the joint gasket or reducing the length of the joint makes the structure more resistant to earthquakes. Pitilakis and Tsinidis [7] and Pitilakis et al. [8] analyzed the deformation behavior of rectangular underground structures during nonuniform earthquakes and pointed out that the special characteristics of underground structures make their seismic performance different from that of aboveground structures. Maugeri et al. [9] studied the performance of the shallow tunnel lining under seismic loading through numerical simulation and metaheuristic techniques. The results showed that genetic algorithm can be used to evaluate the safety performance of the tunnel lining. Wen et al. [10] studied the plastic failure behavior of tunnels, and the results showed that the plastic failure of the upper cross section of the tunnel was more serious than that of the lower part. Presently, there are numerous research results on the lateral response of structures, and the longitudinal response of the structure is gradually receiving attention. Park et al. [11] performed pseudostatic three-dimensional finite element analysis of tunnel structures under the action of spatially varied ground motion. It was pointed out that the spatial ground motion will cause the tunnel to bend longitudinally and increase the longitudinal axial force of the tunnel. Chen et al. [12] carried out a model shaking table test of the tunnel structure. It was considered that the dynamic response of the tunnel structure under nonuniform seismic excitation was greater than that under uniform seismic excitation. Therefore, the spatial effect of seismic excitation should be considered in the tunnel design. A related test by Cilingir and Gopal Madabhushi [13, 14] found that the ground motion response of the tunnel structure depends on the peak acceleration of the seismic excitation, and the change in the buried depth does not affect the tunnel deformation mode; it mainly affects the tunnel acceleration and internal force. Moghadam and Baziar [15] studied the mode of influence of the tunnel on the ground dynamic response during an earthquake by using a combination of the shaking table test and numerical simulation. Hashash et al. [16] reviewed the current state of seismic analysis and design of underground structures, introduced the quantitative methods used by engineers to assess the seismic action on underground structures, and expounded the deterministic and probabilistic methods for seismic hazard analysis. Numerical analysis tools such as the finite element method or finite difference method are used to analyze the dynamic soil-structure interactions. The effects of the relative structural flexibility of soil on the structural deformation and other properties have been studied, and calculation methods have been proposed. Abate and Massimino [17] studied the effects of the tunnel depth, aboveground structure position,

and input seismic waveform on the dynamic interaction of the tunnel-soil-ground structure system based on an actual case in Italy. The system was fully coupled and analyzed. Thirty different recorded accelerations were analyzed based on the time domain, frequency domain, seismic bending moment, and axial force on the tunnel lining.

Most of the existing related researches are directed to a single simple structure, such as a rectangular subway station or circle tunnel, and the influencing factors (seismic excitation amplitude and type, structural depth, structure size, and form) are relatively simple. There is a lack of research on multiple structural systems, such as tunnels crossing each other, subway stations crossing each other, and tunnels crossing subway stations from below or above. In addition, their interactions have not been sufficiently explored, and it is difficult to draw a systematic general law. The purpose of this paper is to establish a two-dimensional model to study the influence of different positional relationships between structures on the dynamic response of the structures in a traversing system and draw some general conclusions.

2. Calculation Models

There are many engineering cases of tunnels passing through subway stations in China. In order to reflect the generality, the research object of this article is not a specific engineering case, but an abstract general model from actual projects, which can obtain a general research result.

2.1. Calculation Range and Boundary Conditions. This paper studies the seismic response of tunnels running underneath a metro station structure. Because the tunnel and station structure are not changed along the longitudinal section, the problem can be simplified to a plane problem under the action of seismic waves perpendicular to the longitudinal direction of the tunnel and the metro station. Therefore, this paper establishes a two-dimensional plane model, and the calculation software used is ABAQUS.

The subway station is a two-story and two-span frame structure with a cross-sectional dimension of $24\text{ m} \times 14\text{ m}$, side wall width of 0.8 m , center pillar width of 0.6 m , top plate and bottom plates are both of 0.9 m , and a middle floor slab thickness of 0.4 m . The outer diameter of the tunnel is 6 m , inner diameter is 5.3 m , thickness of the lining is 0.35 m , and the distance between the centers of the two tunnels is considered as $0.5D$, D , $2D$, and $3D$ (D is tunnel diameter). The tunnel depth is 17.5 m or 26 m , corresponding to shallow buried tunnels and deep buried tunnels, respectively. Based on existing research results [18], the width of the calculation model is 7 times the width of the station (three times the width of each station on the left and right sides), that is, 168 m , and the depth is 50 m to the bedrock surface.

The established station and tunnel models are shown in Figure 1. The finite element model includes a free-field model, spatially varying ground motion soil-station model, soil-double hole tunnel model, and soil-tunnel-station model, as shown in Figure 2.

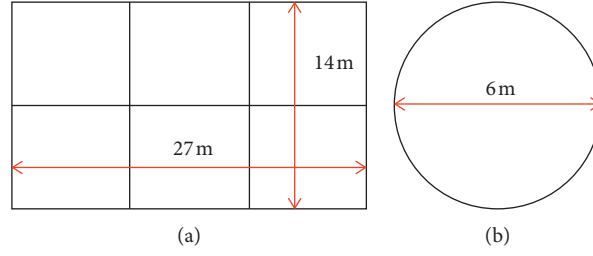


FIGURE 1: Underground structure model. (a) Station structure. (b) Tunnel structure.

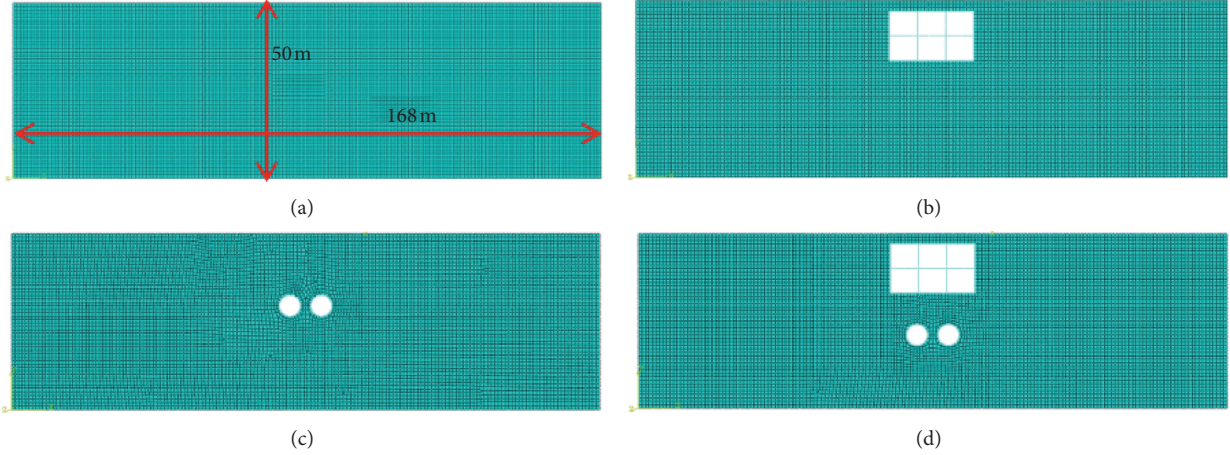


FIGURE 2: Finite element model. (a) Free-field model. (b) Soil-station model. (c) Soil-tunnel model. (d) Soil-tunnel-station model.

The size requirement of the grid unit is $L \leq \lambda/10 = v/10f$, where λ is the shortest wavelength, v is the equivalent shear wave velocity of the soil, and f is the maximum frequency within the range of the ground motion energy to be considered. According to the soil material parameters, the equivalent shear wave velocity of the soil is approximately 220 m/s, and the ground motion energy is mainly concentrated within 10 Hz. Considering $f = 10$ Hz, we obtain $L \leq 2.2$ m. Therefore, the size of the grid unit is 1 m.

Because the modal analysis is performed first, the vibration characteristics of the system are determined, and then, the transient analysis is performed. The boundary conditions of the modal analysis are as follows: the bottom of the model is set as the fixed boundary, the side is set to the vertical displacement constraint (i.e., the lateral slip boundary), and the top is free. In the transient analysis, in order to input the horizontal transverse seismic wave at the bottom of the model, the horizontal constraint of the bottom of the model is removed; the other aspects of the analysis are the same as in the modal analysis.

2.2. Constitutive Model. In this paper, the equivalent linear model, called the Davidenkov model, is used to consider the nonlinear characteristics of soil. Chazelas et al. [19] realized the secondary development of this model based on ABAQUS. The Davidenkov model can be described as

$$\frac{G_d}{G_{\max}} = 1 - \left[\frac{(\gamma_d/\gamma_r)^{2B}}{1 + (\gamma_d/\gamma_r)^{2B}} \right]^A, \quad (1)$$

$$\frac{\lambda}{\lambda_{\max}} = \left[\frac{1 - G_d}{G_{\max}} \right],$$

where A and B are fitting constants; γ_r is the reference shear strain; γ_d is the instantaneous dynamic shear strain; G_d and λ are the instantaneous dynamic shear modulus and damping ratio; and G_{\max} and λ_{\max} are the maximum dynamic shear modulus and maximum damping ratio. When $A = 1$, $B = 0.5$, the Davidenkov model degenerates into the common Hardin–Drnevich model. Based on the existing dynamic test data of soil, different types of soils are selected with different A and B values, and the initial damping ratio is 0.003.

The soil body adopts the solid element, and the unit type is CPE4R [20]. Because the equivalent nonlinear Davidenkov model is employed, the damping characteristics are considered in the model. The tunnel structure and station structure adopt the beam unit of unit type B21 [20], and the tunnel and the station adopt the elastic model. The calculation parameters of each material are shown in Table 1. The soil and station and the soil and tunnel are in tie contact, that is, the relative displacement of the contact interface is not considered.

TABLE 1: Calculation parameters of each material.

Material	Density (kg/m ³)	Elastic modulus (MPa)	Poisson's ratio
Soft soil (0–40 m)	1800	208	0.45
Hard soil (40–50 m)	2000	917	0.3
Concrete (station and tunnel)	2500	3.5×10^4	0.2

2.3. Input Seismic Wave. The famous El-Centro wave is selected firstly in the paper, and the amplitude of the input seismic wave was adjusted to 0.1 g (g is the gravitational acceleration) according to Chinese Code. Then, in order to compare the seismic response of the tunnel-soil-station system under different seismic excitations, Kobe wave is selected for comparison, whose time history and spectrum curves are shown in Figure 3.

The calculation uses the display algorithm; the step time of the calculation is taken as 0.002 s, and the calculation time is taken uniformly as 30 s.

3. Calculation Conditions

3.1. Test Conditions. El-Centro wave (near-field wave) ground motion is selected in the seismic response analysis. The acceleration time-history curve of the seismic wave and its Fourier spectrum curve are shown in Figure 3. The seismic response law of the structural system under the action of seismic waves is analyzed. The specific working conditions are shown in Table 2. There are 18 working conditions. In Tables 2, S represents the net spacing between the two tunnels, and H represents the net distance between the top of the tunnel and the bottom of the station.

3.2. Test Points Program of Models. To monitor the seismic response of the soil and structure, the measuring points are arranged at equal intervals on the surface and in the depth direction of the soil, and the acceleration, velocity, and displacement response of the soil and structure are mainly monitored. The specific arrangement of the test points is shown in Figure 4. Due to the symmetrical structure, the surface test points are only on the semistructure and are arranged as one point every 4 m; the arrangement in the depth direction is one point every 2 m. The station measurement point is on the middle column, and the tunnel measurement points are at the top and bottom.

4. Verification of Numerical Analysis

In order to ensure the accuracy of the numerical simulation, this section verifies the tunnel shaking table test in reference [15].

4.1. Verification of Modal Analysis. In order to verify the calculation model thoroughly, two models are both used in the paper. According to the actual size of the model box in reference [15], a $1\text{ m} \times 1.6\text{ m}$ model is established (Figure 5(a)), and a prototype with a size of $160\text{ m} \times 32\text{ m}$ is

established according to the similarity relationship (Figure 5(b)). The calculation model is established as discussed in Section 2, and the soil parameters are obtained according to the values in the reference. The first-order frequencies of the model and the prototype are 36.948 Hz and 2.748 Hz, respectively. This shows a good agreement with the theoretical calculations of 37 Hz and 2.74 Hz; the relative errors are 0.14% and 0.29%, respectively, indicating the correctness of the modal analysis process.

4.2. Verification of Dynamic Analysis. Because the input seismic excitation selected in the shaking table test in the literature cannot be obtained, the classical El-Centro wave is used to verify the relationship diagram shown in Figure 21 (Figure 6(a) in this paper) in reference [15]. A free-field model (FF model) and a model containing an underground tunnel (SF model) are established, and the amplification factor at $V_S = 100\text{ m/s}$ is obtained, as shown in Figure 6(b).

It can be seen from Figure 6 that the simulation results in this paper are similar to those in reference [15]. When the dimensionless distance $X/a = 0$, the amplification factor is the smallest; when $X/a = 3$ (or 2), the amplification factor is the largest; and when $X/a > 6$, the amplification factor tends to 1. Despite the influence of different factors such as input seismic waves, the calculation results in this paper and the experimental data in [15] show only a slight difference in amplitude. They maintain a good agreement on the regular trend, and the differences are within the acceptable error range. Therefore, the dynamic analysis model and the method followed in this paper can be considered reasonable and feasible and can be used for subsequent parameter analysis.

5. Analysis of Calculation Results

5.1. Modal Analysis. The modal analysis of the established model is carried out to determine the vibration frequency characteristics of each working condition. The first 3 frequencies of the free field, soil-station model, soil-shallow buried tunnel model, and the corresponding soil-station-shallow buried tunnel model are shown in Table 3.

It can be seen from the Table 3 that (1) $f = 1.1\text{ Hz}$ is calculated based on the theoretical formula $f = V/4H$ for the self-vibration characteristics of the free-field soil. It is closer to the frequency of the model in the table, indicating the correctness of the model. (2) The fundamental frequencies of the working conditions are similar, and the underground structure has no significant influence on the dynamic characteristics of the system. Its influence is considered negligible from the engineering point of view.

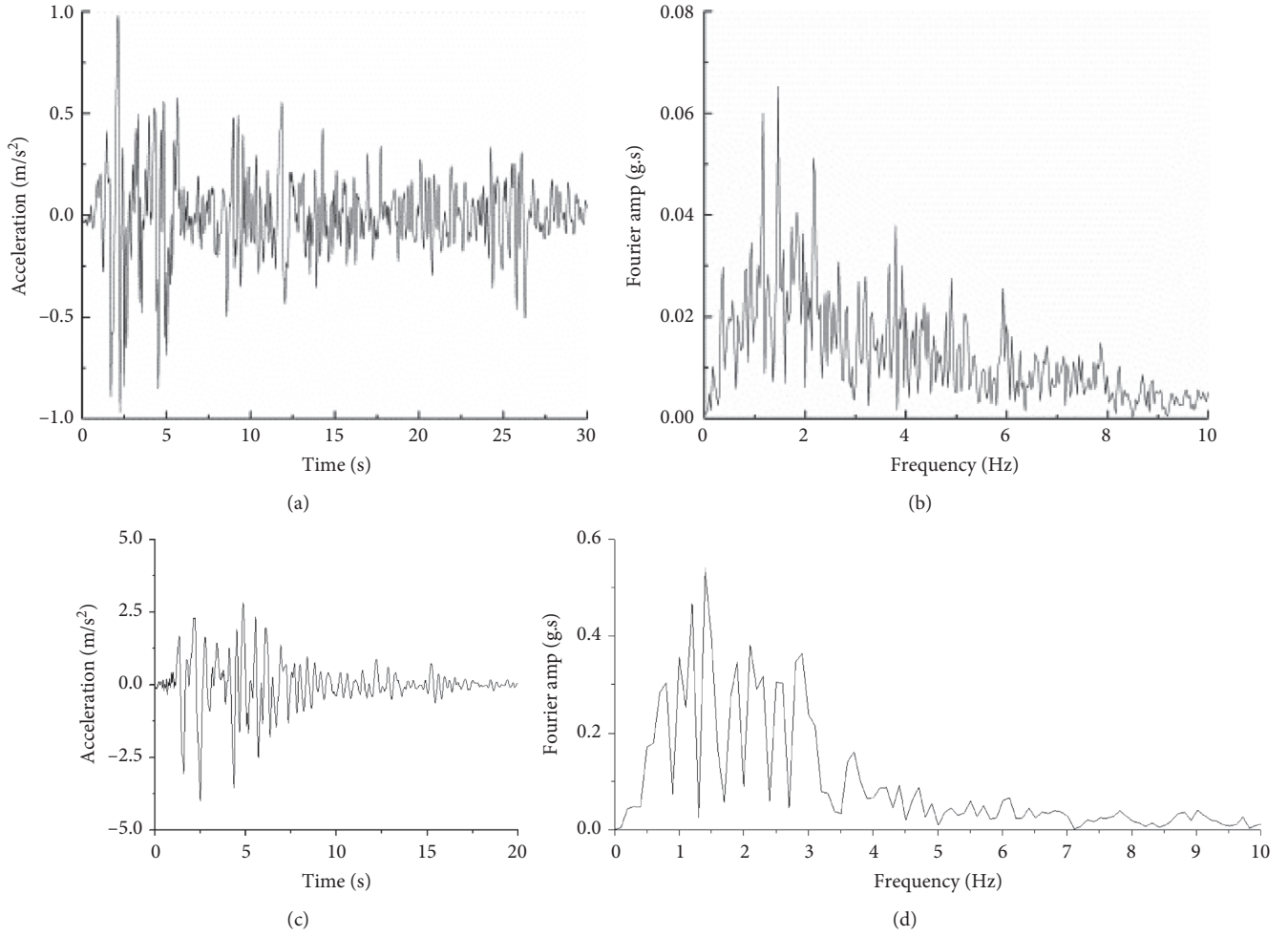


FIGURE 3: Time history and spectrum curves of El-Centro wave and Kobe wave. (a) Time history curve of El-Centro wave. (b) Frequency curve of El-Centro wave. (c) Time history curve of Kobe wave. (d) Frequency curve of Kobe wave.

TABLE 2: Calculation conditions.

Set	Model type	Parameters (m)	Input motion	
SS1	Soil-station	Buried depth is 3	El-Centro wave and its amplitude are adjusted to 0.1 g.	
ST2				$S = 3$
ST3				$S = 6$
ST4		Buried depth is 17.5		$S = 12$
ST5				$S = 18$
ST6				$S = 3$
ST7		Buried depth is 26		$S = 6$
ST8				$S = 12$
ST9				$S = 18$
STS10 STS11	Soil-tunnel-station	$S = 3$	$H = 0.5$	
			$H = 9$	
STS12 STS13		$S = 6$	$H = 0.5$	
			$H = 9$	
STS14 STS15		$S = 12$	$H = 0.5$	
		$H = 9$		
STS16 STS17		$S = 18$	$H = 0.5$	
			$H = 9$	
FF18	Free-field		Kobe wave (0.1 g)	
FF19	Free-field			
SS20	Soil-station	Buried depth is 3		

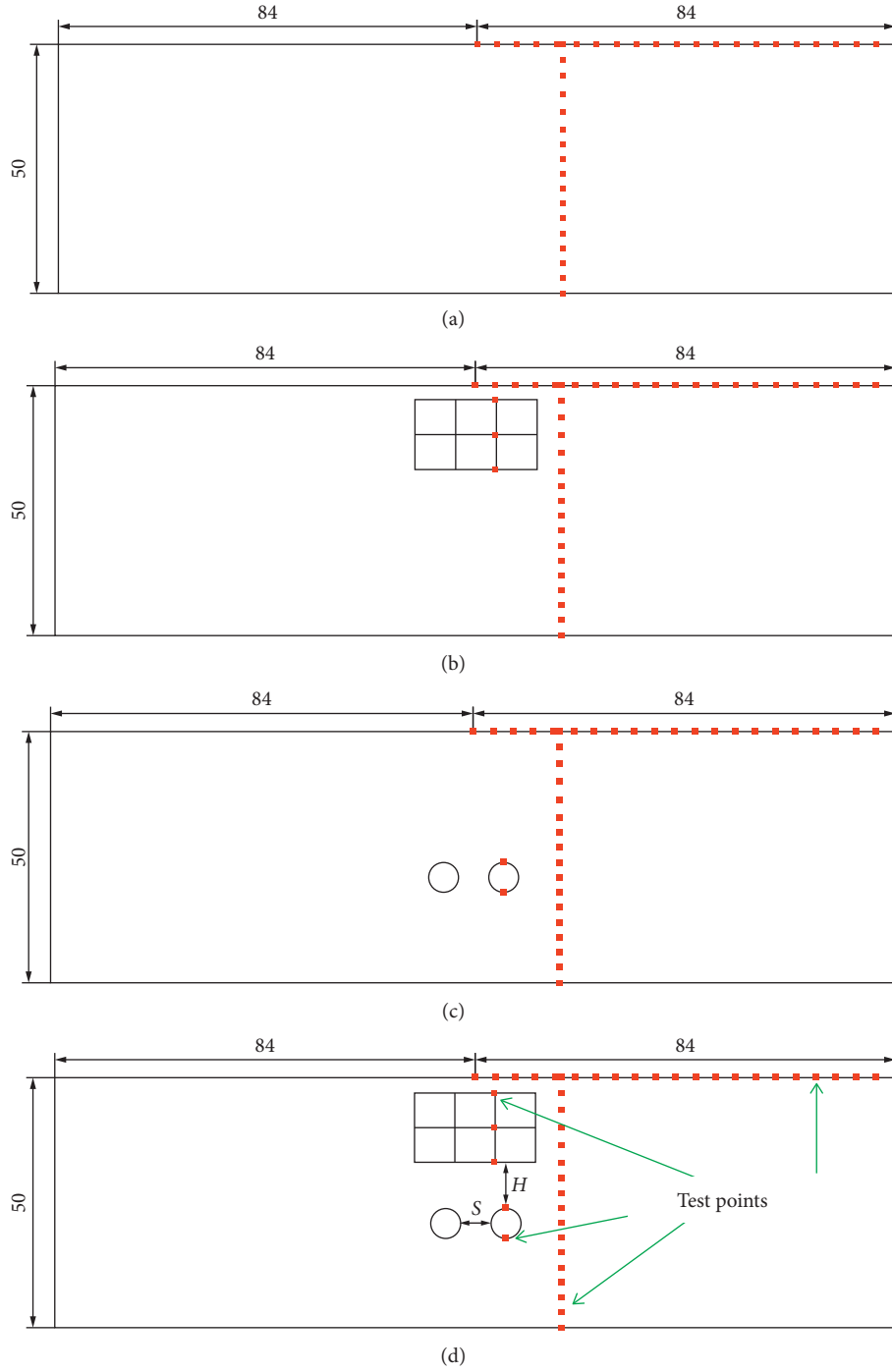


FIGURE 4: Arrangement of test points (unit: m). (a) Free-field model. (b) Soil-station model. (c) Soil-tunnel model. (d) Soil-tunnel-station model.

5.2. Soil Response Analysis

5.2.1. Acceleration Analysis of the Midpoint of the Surface.

Figure 7 shows the acceleration-time history diagram of the midpoint of the surface of the free field under the action of 0.1 g El-Centro wave. The magnitudes of the acceleration at the midpoint of the ground are listed in Table 4 and compared with those of the free field. To facilitate

quantitative analysis, the influence coefficient of the underground structure on soil is defined as

$$R_1 = \frac{(A_{CS} - A_0)}{A_0}, \quad (2)$$

where A_0 represents the positive acceleration amplitude of the center of the free-field table, and A_{CS} represents the

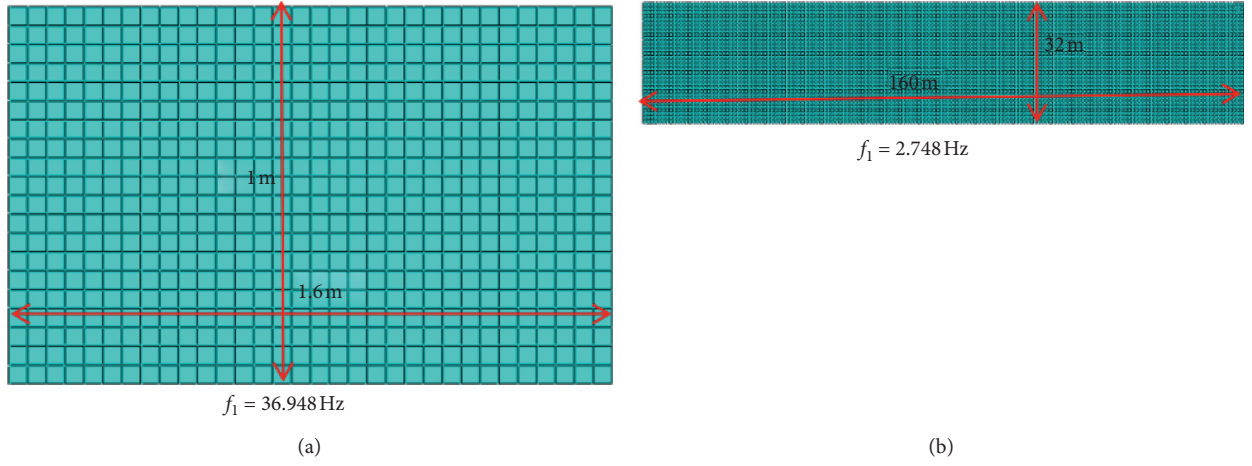


FIGURE 5: Numerical model and frequency. (a) Model. (b) Prototype.

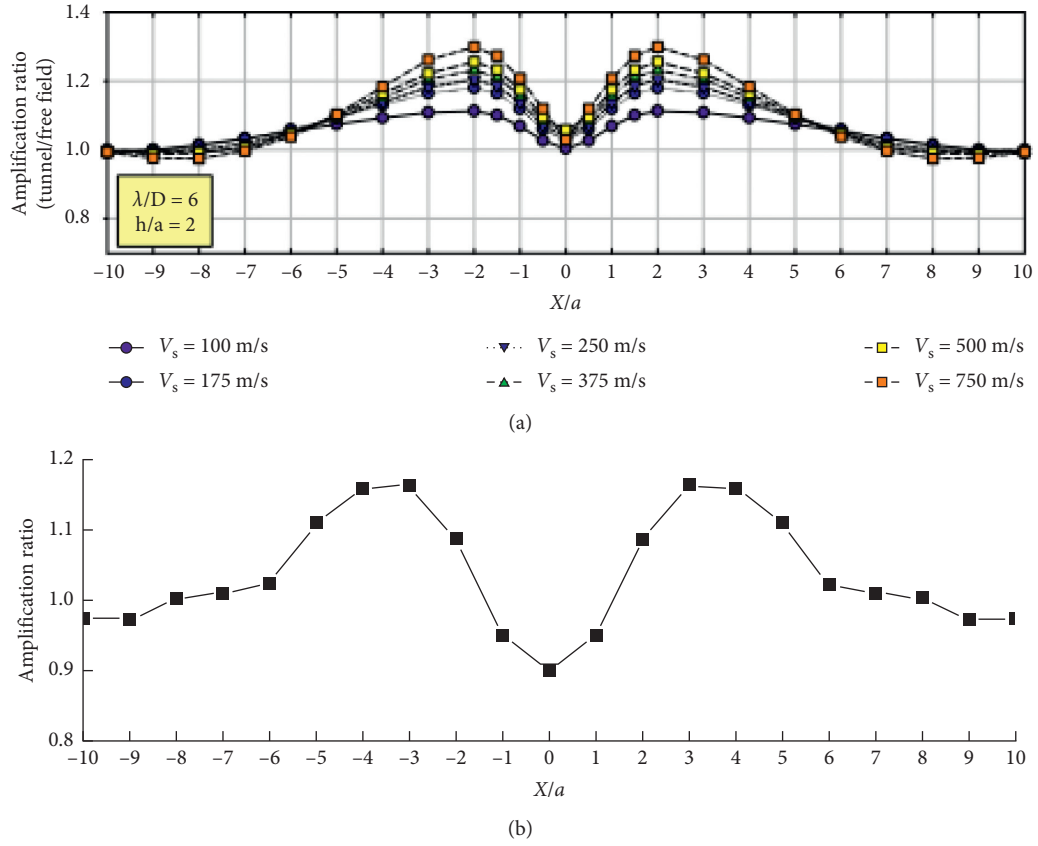


FIGURE 6: Comparison of simulation results. (a) Results in Reference [15]. (b) Simulation results of this paper.

TABLE 3: First three orders of natural frequency under different conditions (unit: Hz).

Set	First order	Second order	Third order
SS1	1.203	1.723	2.256
ST2	1.184	1.618	2.216
STS10	1.204	1.723	2.266
FF18	1.187	1.566	2.148

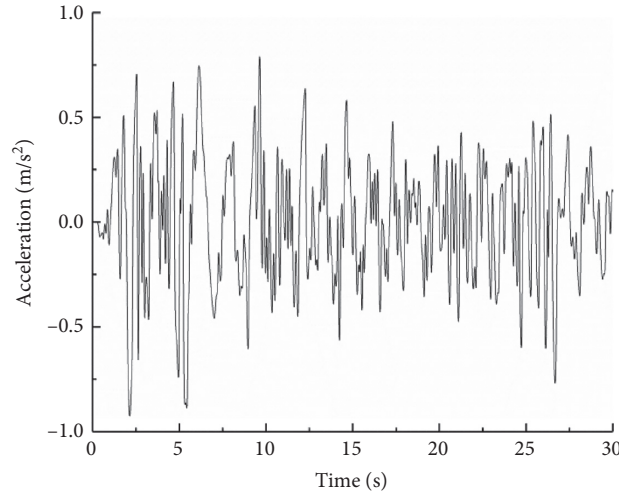


FIGURE 7: Comparison of simulation results.

TABLE 4: Surface midpoint acceleration under different conditions.

Set	S (m)	Acceleration amplitude (m/s^2)	R_1 (%)
FF18		0.925	
SS1		1.174	26.918
ST2	3	0.925	0
ST3	6	0.933	0.864
ST4	12	0.913	-1.29
ST5	18	0.929	0.432
ST6	3	0.927	0.216
ST7	6	0.926	0.108
ST8	12	0.924	-0.108
ST9	18	0.924	-0.108
STS10	3	1.170	26.486
STS12	6	1.167	26.162
STS14	12	1.163	25.729
STS16	18	1.157	25.081
STS11	3	1.157	25.081
STS13	6	1.158	25.189
STS15	12	1.162	25.622
STS17	18	1.160	25.405

positive acceleration amplitude of the center of the surface when the underground structure exists.

It can be seen from the Table 4 that the station structure has small buried depth and large cross-sectional size, which have a great influence on the surface acceleration. The station structure significantly increases the acceleration of the surface center, and the impact amplitude is approximately 25%. However, owing to the large depth and small size of the tunnel, the impact on the surface acceleration is small, which can be neglected.

5.2.2. Influence of Underground Structure on Soil Response.

Taking the deep buried tunnel as an example, the effects of the underground structure on the surface acceleration response and soil displacement along the depth of the soil are explored. The surface acceleration amplitude curves of the four systems (Figure 8) and the soil displacement map in the depth direction (Figure 9) are presented.

It can be seen from the figure that the degree of influence of the station on the ground surface acceleration is greater than that of the tunnel; the influence of the station on the surface acceleration is approximately five times the station width (60 m on both sides of the center of the earth's surface). In this range, the surface acceleration is obviously larger than the free field, and the surface acceleration outside this range is different much to free field. Based on the displacement of the soil in the depth direction, the existence of the underground structure is beneficial in reducing the lateral displacement of the soil, and the influence of the station structure is greater than the influence of the tunnel structure. The influence of the station structure plays a major role when the station and the tunnel exist simultaneously.

5.2.3. Influence of the Seismic Wave Type.

The soil and structural responses may be different for different types of seismic waves. The soil response is taken as an example to

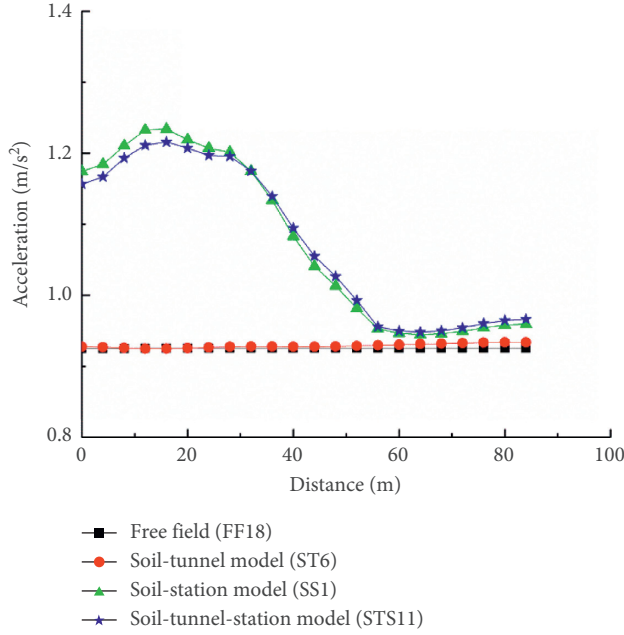


FIGURE 8: Surface acceleration amplitude under El-Centro wave.

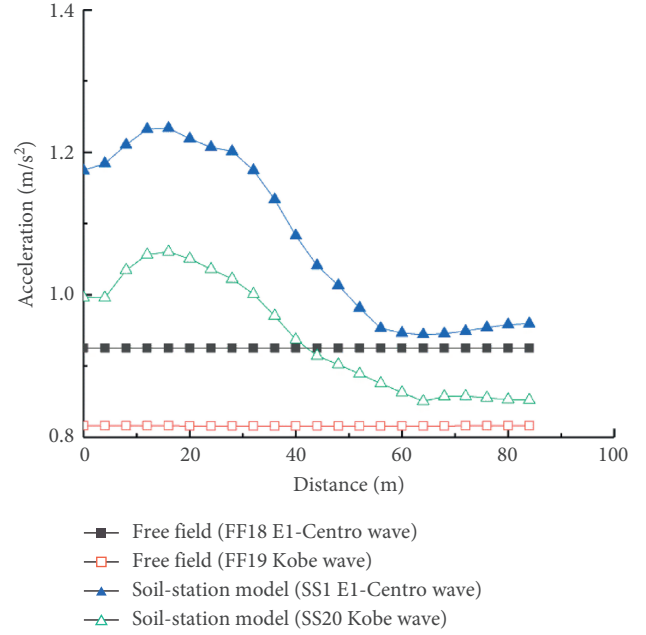


FIGURE 10: Surface acceleration under different seismic waves.

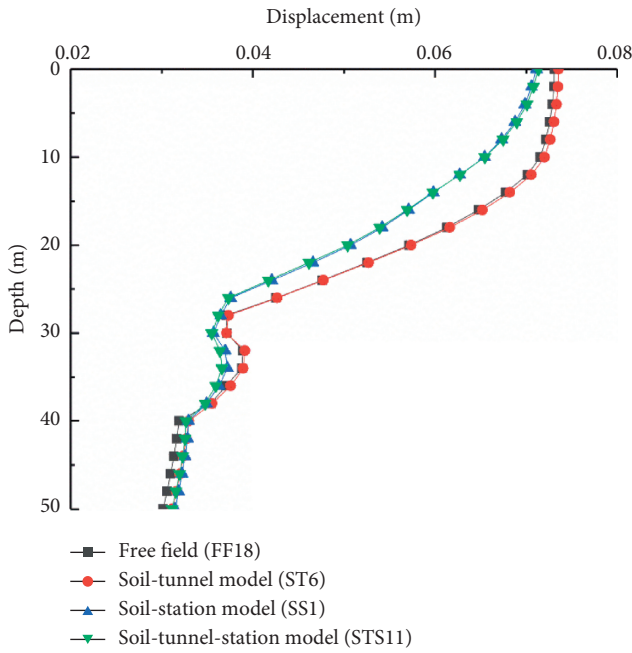


FIGURE 9: Soil displacement in the depth direction under El-Centro wave.

analyze the effects of different types of seismic waves and the surface acceleration of the free field, and the soil-station model (Figure 10) and soil displacement map are obtained in the depth direction (Figure 11) under different seismic waves.

It can be seen from the figure that the influence law and degree of influence of different seismic waves on the soil response are different. Based on the surface acceleration response and soil displacement response, the influence of the El-Centro wave is larger than that of the Kobe wave.

5.3. Analysis of the Influence of Tunnel on Station Response. This section compares the different aspects of the seismic response of the station with and without tunnels. To facilitate the analysis of the problem, the influence coefficient of the tunnel on the station is defined as

$$R_2 = \frac{C_{CS} - C_C}{C_C}, \quad (3)$$

where C_C represents the response of the station in the earth-station system, and C_{CS} represents the response of the station in the earth-tunnel-station system.

5.3.1. Acceleration Analysis of the Top of the Middle Column of the Station. In order to explore the influence of the acceleration response at the top of the column in the station with the tunnel passing underneath, the acceleration response of the station center column is given for the case when only the station structure is present (Figure 12). Table 5 lists the acceleration amplitudes for the station structures with and without the tunnel.

It can be seen from the Table 5 that the existence of the tunnel can reduce the acceleration of the column in the station by approximately 10%. Generally, the influence of the net spacing between the tunnels is not obvious. The greater the distance between the tunnel and the station, the smaller the acceleration of the column in the station.

5.3.2. Analysis of the Displacement Angle between Floors of the Station. There are three measuring points on the column in the station, which are located at the top, middle, and bottom of the column. The displacement response of these points can provide the difference in the interlayer displacement between the upper and lower layers and the

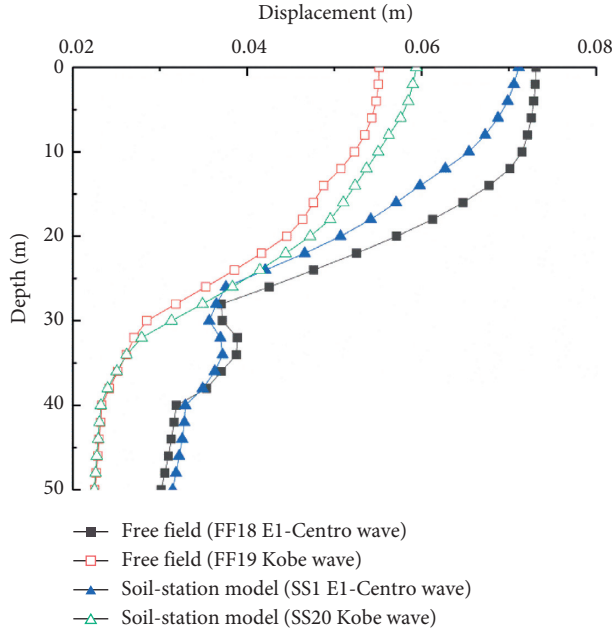


FIGURE 11: Displacement of soil in depth direction under different seismic waves.

displacement angle between the layers. The time-history map of the displacement angle between the stations is shown in Figure 13 when only the station structure is present. The maximum displacement angle between the stations in other systems is given in Table 6.

It can be seen from the graph that the interlayer displacement angle of the lower layer of the station structure is large; the existence of the tunnel structure increases the interlayer displacement angle of the station structure. The smaller the spacing between the tunnel and the station and the smaller the spacing between the tunnels, the greater the increase in the displacement angle between the stations. When the distance between the tunnel and the station is large, the change in the net spacing between the tunnels will not cause a large change in the displacement angle between the stations.

5.3.3. Internal Force Analysis of the Station. By observing the bending moment cloud diagram of the station structure, it is found that the maximum bending moment always appears at the corner of the station at 2.180 s. The bending moment cloud at 2.18 s is shown in Figure 14. The maximum values (absolute value) of the bending moment of the left corner of the station for other conditions are listed in Table 7.

It can be seen from the graph that the bending moment at the corner of the station structure is large and stress concentration can easily occur. When the distance between the tunnel and the station is small, the existence of the tunnel increases the bending moment of the station, but the overall impact is not significant.

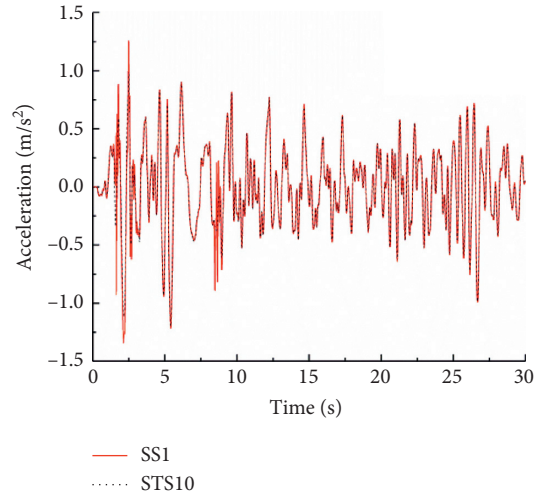


FIGURE 12: Acceleration at the top of the station.

TABLE 5: Acceleration at the top of the interior column.

Set	S (m)	Acceleration amplitude (m/s ²)	R ₂ (%)
SS1		1.345	
STS10	3	1.207	-10.260
STS12	6	1.204	-10.483
STS14	12	1.201	-10.706
STS16	18	1.201	-10.706
STS11	3	1.198	-10.929
STS13	6	1.199	-10.855
STS15	12	1.200	-10.781

5.4. Analysis of the Influence of the Station on Tunnel Response. This section analyzes the response of the tunnel and discusses the impact of the station on the dynamic response of the tunnel. To facilitate the analysis of the problem, the influence coefficient of the station on the tunnel is defined as

$$R_3 = \frac{S_{CS} - S_S}{S_S}, \quad (4)$$

where S_S represents the response of the tunnel in the soil-tunnel system and S_{CS} represents the response of the tunnel in the corresponding soil-tunnel-station system.

5.4.1. Analysis of Acceleration at the Top of the Tunnel. Taking the soil-shallow buried tunnel with a tunnel spacing of 3 m as an example, the acceleration diagram of the top of the tunnel is shown in Figure 15. The maximum accelerations of the top of the tunnel under other conditions are shown in Table 8.

It can be seen from the chart that stations influence shallow buried tunnels and deep buried tunnels differently. In the case of a shallow buried tunnel (distance between the shallow buried tunnel and station is 0.5 m), the presence of a station slightly enlarges the acceleration of the tunnel top. The amplification is between 2% and 4%;

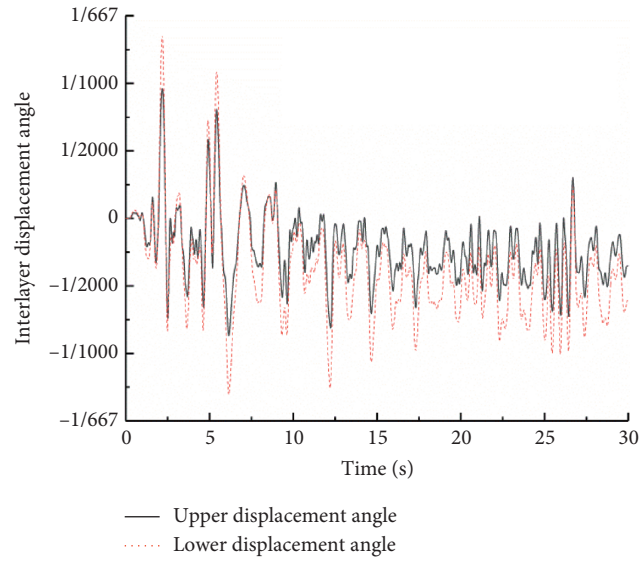


FIGURE 13: Interlayer displacement angle of the station structure.

TABLE 6: Interlayer displacement angle of station structure for various conditions.

Set	S (m)	Maximum displacement angle		R_2 (%)	
		Upper layer	Lower layer	Upper layer	Lower layer
SS1		1/1041	1/739		
STS10	3	1/1013	1/712	2.813	3.769
STS12	6	1/1013	1/716	2.813	3.178
STS14	12	1/1015	1/714	2.604	3.474
STS16	18	1/1016	1/718	2.500	2.882
STS11	3	1/1026	1/733	1.458	0.813
STS13	6	1/1026	1/733	1.458	0.813
STS15	12	1/1026	1/731	1.458	1.034
STS17	18	1/1026	1/731	1.458	1.034

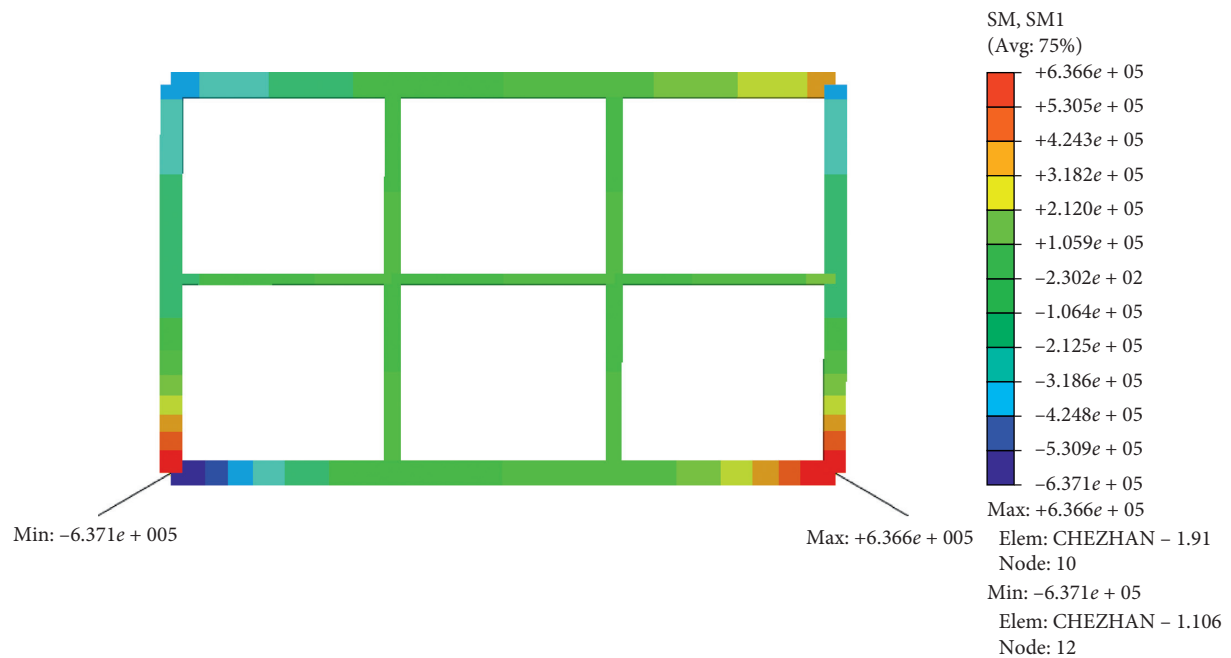


FIGURE 14: Bending moment cloud diagram of the station structure.

TABLE 7: Maximum bending moment at the corner of the station.

Set	S (m)	Maximum bending moment (N·m)	R_2 (%)
SS1		637063	
STS10	3	655808	2.942
STS12	6	648061	1.726
STS14	12	647094	1.575
STS16	18	641156	0.642
STS11	3	638948	0.296
STS13	6	636342	−0.113
STS15	12	634166	−0.455
STS17	18	634791	−0.356

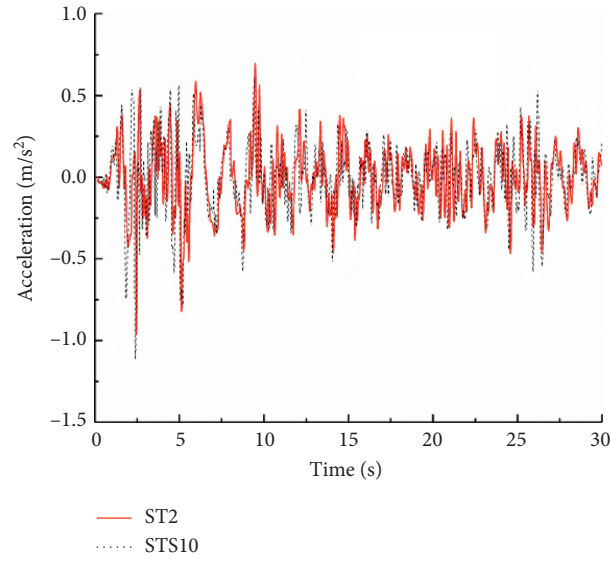


FIGURE 15: Acceleration at the top of the tunnel.

TABLE 8: Acceleration at the top of the tunnel under different conditions.

Set	S (m)	Acceleration (m/s ²)	R_3 (%)
ST2		0.961	
STS10	3	0.979	1.873
ST3		0.984	
STS12	6	1.004	2.033
ST4		1.002	
STS14	12	1.026	2.395
ST5		0.998	
STS16	18	1.037	3.908
ST6		1.217	
STS11	3	1.115	−8.381
ST7		1.232	
STS13	6	1.144	−8.81
ST8		1.257	
STS15	12	1.182	−7.143
ST9		1.264	
STS17	18	1.189	−5.934

the larger the net spacing between the tunnels, the more obvious the amplification effect. In the case of a deep buried tunnel, the presence of the station weakens the

acceleration response at the top of the tunnel by 5%–9%; the degree of attenuation decreases as the spacing between the tunnels increases.

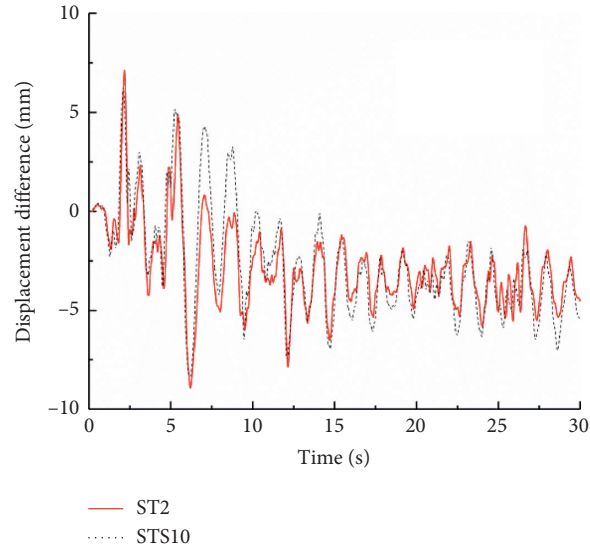
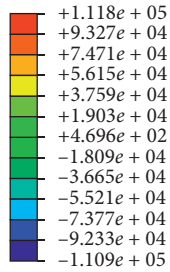


FIGURE 16: Relative displacement between the top and bottom of the tunnel.

TABLE 9: Displacement difference between the top and bottom of the tunnel under various conditions.

Set	S (m)	Relative displacement (mm)	R_3 (%)
ST2	3	8.925	-14.756
STS10		7.608	
ST3	6	9.135	-10.662
STS12		8.161	
ST4	12	9.271	-8.715
STS14		8.463	
ST5	18	9.347	-4.119
STS16		8.962	
ST6	3	11.367	-26.515
STS11		8.353	
ST7	6	11.532	-24.957
STS13		8.654	
ST8	12	11.602	-20.067
STS15		9.277	
ST9	18	11.753	-16.651
STS17		9.796	

SM, SM1
(Avg: 100%)



Max: +1.118e+05
Node: SUIDAO - 1.11
Min: -1.109e+05
Node: SUIDAO - 1.17

Max: +1.118e+005
Min: -1.109e+005

FIGURE 17: Bending moment cloud diagram of the tunnel structure.

TABLE 10: Maximum bending moment of the tunnel structure under various conditions.

Set	S (m)	Maximum bending moment (N·m)	R_3 (%)
ST2	3	111846	8.289
STS10		121117	
ST3	6	113982	1.835
STS12		116074	
ST4	12	114694	-11.753
STS14		101214	
ST5	18	117130	-9.873
STS16		105566	
ST6	3	135637	-15.88
STS11		117046	
ST7	6	139212	-13.706
STS13		123486	
ST8	12	140029	-10.364
STS15		125517	
ST9	18	141635	-11.681
STS17		125090	

5.4.2. *Analysis of the Displacement Difference between the Top and Bottom of the Tunnel.* Taking the soil-shallow buried tunnel with a tunnel spacing of 3 m as an example, the displacement difference between the top and bottom of the tunnel is shown in Figure 16. The maximum displacement differences between the top and bottom of the tunnel for various conditions are shown in Table 9.

It can be seen from the chart that the station reduces the difference in the horizontal displacement between the top and bottom of the tunnel, and the degree of attenuation decreases with an increase in the spacing between the tunnels. However, the impact amplitudes of the shallow tunnel and deep tunnel are different. The attenuation for the shallow tunnel is 4%–15%, whereas that for the deep tunnel is 16%–27%.

5.4.3. *Internal Force Analysis of the Tunnel.* By observing the bending moment cloud diagram of the tunnel structure, it is found that the maximum bending moment appears in the 45° direction of the tunnel structure. The bending moment cloud diagram of the tunnel structure in the soil-shallow buried tunnel system (when the tunnel spacing is 3 m) is shown in Figure 17. The maximum value of the bending moment of the working tunnel structure is shown in Table 10.

It can be seen from the graph that the maximum bending moment of the tunnel structure appears in the 45° direction of the tunnel section. The larger the spacing between the tunnels, the larger the bending moment on the tunnel; the influence of the station structure on the tunnel bending moment is inconsistent. In general, the presence of a station can reduce the bending moment of the tunnel structure.

6. Conclusions

In this paper, a two-hole tunnel underpass station model was established. The ABAQUS finite element software was used to analyze the seismic response. The seismic response law of the

cross-underground structure was discussed. The following rules were obtained from the calculation and analysis:

- (1) Influence of the underground structure on the dynamic response of soil: the station structure has a great impact whereas the tunnel structure has less impact on the surface response. The range within which the station structure has a great impact on the surface response is five times the width of the station. Within this range, the surface acceleration response increases significantly, whereas the influence outside this range is small. The tunnel has a large buried depth, and its influence on the surface response is basically negligible. The station depth is small because of which it has a great influence on the surface response. When the station and the tunnel structure exist simultaneously, the influence of the station structure plays a major role. Overall, the presence of underground structures reduces the horizontal displacement of the soil.
- (2) Impact of the tunnel on the dynamic response of the station: the existence of the tunnel can reduce the acceleration of the column in the station by approximately 10%; the impact of the net spacing between the tunnels is not obvious. When the distance between the tunnel and the station is large, the acceleration of the column in the station is greatly weakened. The existence of the tunnel structure increases the interlayer displacement angle of the station structure; the smaller the distance between the tunnel and the station and the smaller the spacing between the tunnels, the greater the increase in the displacement between the stations. The impact of the tunnel on the internal force response of the station is not significant.
- (3) Impact of the station on the dynamic response of the tunnel: the station influences the acceleration of the shallow buried tunnel and the deep buried tunnel differently. In the case of the shallow buried tunnel, the existence of the station slightly amplifies the acceleration response at the top of the tunnel. In the case of the deep buried tunnel, the presence of the station weakens the acceleration response at the top of the tunnel. As the spacing between the tunnels increases, the degree of attenuation decreases. The presence of the station reduces the difference in displacement between the top and bottom of the tunnel, and with an increase in the spacing between the tunnels, the degree of attenuation decreases. The presence of the station is conducive to reducing the internal force of the tunnel.

At present, the research on seismic resistance of complex underground structure is limited, and the related research still needs further improvement. Underground structures tend to be large in size and traverse different strata. Moreover, they do not exist independently and have a complex environment. Therefore, it is

necessary to consider more influencing factors, such as structural characteristics, changes in soil parameters, seismic excitation characteristics, spatial effects of ground motion effects, and aboveground buildings.

Data Availability

No data were used to support the findings of the study.

Conflicts of Interest

The authors declare that they have no conflicts of interest.

Authors' Contributions

Fuxue Sun conducted investigation on existing research results extensively and deeply and supervised the development of research work. Wang Guo-bo conceptualized the actual project, determined the reasonable modeling method, and acquired funds to ensure the success of the research work. Xiang-jun Peng was responsible for modelling and simulating actual engineering problems through software and data analysis. Zhou-zhou Jin verified the correctness and reliability of the results and wrote the original draft. Xiaochun Li administrated the actual project and provided necessary resources for the research. Jie-lin Zhao was responsible for reviewing and editing the original draft to improve overall English language usage, readability, clarity, grammar, and spelling.

Acknowledgments

This research work was supported by the National Natural Science Foundation of China (Grant nos. 51878529 and 51678465) and the Research Project of Study on Key Technology of Large-Diameter Shield Tunnel Construction in biogas-rich soft ground. The support is gratefully acknowledged.

References

- [1] G. Chen, H. Zhuang, and G. Shi, "Analysis on the earthquake response of subway station based on the substructure subtraction method," *Journal of Disaster Prevention and Mitigation Engineering*, vol. 24, no. 4, pp. 396–401, 2004.
- [2] M. Singh, M. N. Viladkar, and N. K. Samadhiya, "Seismic analysis of Delhi metro underground tunnels," *Indian Geotechnical Journal*, vol. 47, no. 1, pp. 67–83, 2017.
- [3] D. Ulgen, S. Saglam, and M. Y. Ozkan, "Dynamic response of a flexible rectangular underground structure in sand: centrifuge modeling," *Bulletin of Earthquake Engineering*, vol. 13, no. 9, pp. 2547–2566, 2015.
- [4] V. W. Lee and M. D. Trifunac, "Response of tunnels to incident," *SH-waves—Journal of the Engineering Mechanics Division*, vol. 105, no. 4, pp. 643–659, 1979.
- [5] W. Bourouaiah, S. Khalfallah, and S. Boudaa, "Influence of the soil properties on the seismic response of structures," *International Journal of Advanced Structural Engineering*, vol. 11, no. 3, pp. 309–319, 2019.
- [6] I. Anastasopoulos, N. Gerolymos, V. Drosos, R. Kourkoulis, T. Georgarakos, and G. Gazetas, "Nonlinear response of deep immersed tunnel to strong seismic shaking," *Journal of Geotechnical and Geoenvironmental Engineering*, vol. 133, no. 9, pp. 1067–1090, 2007.
- [7] K. Pitilakis and G. Tsinidis, *Performance and Seismic Design of Underground Structures—Earthquake Geotechnical Engineering Design*, pp. 279–340, Springer International Publishing, Cham, Switzerland, 2014.
- [8] K. Pitilakis, G. Tsinidis, and A. M. Leanza, "Seismic behaviour of circular tunnels accounting for above ground structures interaction effects," *Soil Dynamics and Earthquake Engineering*, vol. 67, pp. 1–15, 2014.
- [9] A. Maugeri, R. Mikaeil, and S. S. Haghshenas, "Integration of finite difference method and genetic algorithm to seismic analysis of circular shallow tunnels (case study: Tabriz urban railway tunnels)," *KSCE Journal of Civil Engineering*, vol. 22, no. 5, pp. 1–13, 2017.
- [10] K. Wen, H. Shimada, T. Sasaoka et al., "Numerical study of plastic response of urban underground rock tunnel subjected to earthquake," *International Journal of Geo-Engineering*, vol. 8, no. 1, pp. 1–15, 2017.
- [11] D. Park, M. Sagong, D. Y. Kwak et al., "Simulation of tunnel response under spatially varying ground motion," *Soil Dynamics and Earthquake Engineering*, vol. 29, no. 11–12, pp. 1417–1424, 2009.
- [12] J. Chen, X. Shi, and J. Li, "Shaking table test of utility tunnel under non-uniform earthquake wave excitation," *Soil Dynamics and Earthquake Engineering*, vol. 30, no. 11, pp. 1400–1416, 2010.
- [13] U. Cilingir and S. P. Gopal Madabhushi, "A model study on the effects of input motion on the seismic behaviour of tunnels," *Soil Dynamics and Earthquake Engineering*, vol. 31, no. 3, pp. 452–462, 2011.
- [14] U. Cilingir and S. P. G. Madabhushi, "Effect of depth on the seismic response of square tunnels," *Soils and Foundations*, vol. 51, no. 3, pp. 449–457, 2011.
- [15] M. R. Moghadam and M. H. Baziar, "Seismic ground motion amplification pattern induced by a subway tunnel: shaking table testing and numerical simulation," *Soil Dynamics and Earthquake Engineering*, vol. 83, pp. 81–97, 2016.
- [16] Y. M. A. Hashash, J. J. Hook, and B. J. Schmidt, "Seismic design and analysis of underground structures," *Tunnelling and Underground Space Technology*, vol. 16, no. 4, pp. 247–293, 2001.
- [17] G. Abate and M. R. Massimino, "Parametric analysis of the seismic response of coupled tunnel-soil-aboveground building systems by numerical modelling," *Bulletin of Earthquake Engineering*, vol. 15, no. 1, pp. 443–467, 2017.
- [18] G. Tsinidis, E. Rovithis, and K. J. L. Pitilakis, "Seismic response of box-type tunnels in soft soil: experimental and numerical investigation," *Tunnelling and Underground Space Technology*, vol. 59, pp. 199–214, 2016.
- [19] H. Chazelas, Z. Hu, X. Wang, and G. Chen, "Seismic responses of a large underground structure in liquefied soils by FEM numerical modelling," *Bulletin of Earthquake Engineering*, vol. 13, no. 12, pp. 3645–3668, 2015.
- [20] ABAQUS, *6.12 Documentation*, Dassault Systemes, Providence, RI, USA, 2014.